UNIVERSIDAD DE CHILE
FACULTAD DE CIENCIAS FÍSICAS Y MATEMÁTICAS
DEPARTAMENTO DE FÍSICA

ORDER AND DENSITY FLUCTUATIONS IN THE VICINITY OF A GRANULAR SOLID-LIQUID-LIKE PHASE TRANSITION

TESIS PARA OPTAR AL GRADO DE DOCTOR EN CIENCIAS MENCIÓN FÍSICA

GUSTAVO EMILIO CASTILLO BAUTISTA

PROFESOR GUÍA:
NICOLÁS MUJICA FERNANDEZ

MIEMBROS DE LA COMISIÓN:
CLAUDIO MOISÉS FALCÓN BEAS
LUIS EUGENIO HAMM HAHN
DINO ENZO RISSO ROCCO
RODRIGO ANTONIO SOTO BERTRÁN

SANTIAGO DE CHILE

JUNIO, 2013

Resumen

Esta tesis se dedica al estudio de las fluctuaciones de densidad, orden y de capilaridad en la vecindad de una transición de fase granular tipo sólido-líquido que ocurre en una monocapa granular vibrada de geometría cuasi-bidimensional. En la Parte I introducimos las bases teóricas del trabajo con los conceptos y definiciones que serán usadas para describir, analizar y discutir los resultados experimentales más adelante. En el capítulo 1 se repasan los modelos microscópicos más importantes usados para describir la materia granular. Además, se presenta una breve revisión sobre teoría cinética e hidrodinámica granular. El capítulo 2 aborda los conceptos escenciales para entender la teoría de las transiciones de fase, tales como la noción de un parámetro de orden y la definición de exponentes críticos. En la Parte II se presentan en detalle los montajes experimentales usados para estudiar el problema, junto con los métodos experimentales usados, en particular la detección de partículas y la detección de la interfase tipo sólido-líquido. En la Parte III, la cual a su vez está dividida en 3 capítulos, se presentan los resultados. En el capítulo 5 se presenta la descripción estática de la transición y su caracterización en términos de un parámetro de orden. Se muestra que esta transición fuera del equilibrio puede ser de primer o segundo tipo dependiendo de la altura de la celda y la densidad de llenado. Además, ésta se caracteriza por el parámetro de orden orientacional Q_4. Cuando la transición resulta ser de segundo orden, la longitud de correlación asociada ξ_4, el tiempo de relajación τ_4, la susceptibilidad estática de Q_4, la función de correlación de pares de Q_4, y la amplitud del parámetro de orden obedecen leyes de potencias críticas, con saturaciones debido a efectos de tamaño finito. Con esto, la transición continua presenta un comportamiento crítico, con exponente dinámico z consistente con el modelo C de la teoría de fenómenos críticos dinámicos. Luego, en el capítulo 6 se presentan los resultados concernientes a las fluctuaciones de la interfase sólido-líquido. En particular se muestra que estas fluctuaciones resultan estar bien descritas por la teoría de ondas capilares, lo que permite medir la tensión superficial γ, y la movilidad M una vez determinada la energía térmica granular. También se presenta el comportamiento de la tensión de superficie como función del parámetro de control Γ, mostrando que para la transición continua esta disminuye a medida que el sistema se acerca al punto crítico, mientras que para el caso de la transición abrupta esta es aproximadamente constante. Finalmente, en el capítulo 7 se presentan los resultados obtenidos a través del estudio de funciones de correlación dinámicas. En particular, se encuentra la presencia de ondas en el sistema y se obtienen la velocidad de fase y de grupo, tanto de las ondas longitudinales como transversales. Las conclusiones y perspectivas para el trabajo futuro son presentadas en el capítulo final.

Abstract

In this thesis we study the density, order and capillary fluctuations in the vicinity of the solid-liquid-like transition that occurs in a quasi-two-dimensional vibrated granular monolayer. In Part I we introduce a brief theoretical background with the main concepts and definitions that will be used to describe, analize and discuss the experimental results. In Chapter 1 we review the most important microscopic models used to describe granular matter. In addition, we present a brief and simple review on kinetic theory and the basics of the granular hydrodynamics equations. In Chapter 2 we deal with the main concepts in the theory of phase transitions, such as the notion of an order parameter and the definition of the critical exponents. In Part II we present in detail the experimental setups used to study the problem, along with the experimental methods developed, concerning the detection of particles and the solid-liquid interface. Part III, which in turn is divided into three chapters, is about the presentation and discussion of results obtained. In Chapter 5 we present the static description of the transition and its characterization in terms of an order parameter. Here we show that the non-equilibrium solid-liquid transition can be of either first- or second-order type depending on the vertical height and filling density. Besides, this is characterized through the bond-orientational order parameter Q_4. When the transition is a second-order type, the associated correlation length ξ_4, the relaxation time τ_4, the zero k limit of Q_4 fluctuations (static susceptibility), the pair correlation function of Q_4, and the amplitude of the order parameter obey critical power laws, with saturations due to finite size effects. Hence, the continuous transition presents critical-like behavior, with dynamic exponent z consistent with model C of dynamical critical phenomena. Then, in Chapter 6 we show the results concerning the fluctuations of the solid-liquid interface by means of a coarse-graining procedure. In particular we demonstrate that these fluctuations turn out to be well described by the capillary wave theory, which allows us to measure the solid-liquid interface surface tension γ, and mobility M once the granular thermal kinetic energy is determined. We also present the behavior of the surface tension γ as function of the acceleration Γ, showing that for the continuous transition, γ decreases as we approach the transition, whereas for the abrupt transition γ is almost constant. Finally, in Chapter 7 we present results obtained through the analysis of density, order and current dynamical correlation functions. In particular we demonstrate the presence of waves in the system, and measure the phase and group speeds of longitudinal and transverse waves. Concluding remarks along with perspectives for future work are given in the last chapter.

« The secret of success is making your vocation your vacation. »

Mark Twain

Acknowledgements

Foremost, I would like to express my sincere gratitude to Nico for the continuous support of my Ph.D study and research, for his patience, motivation, enthusiasm, and immense knowledge. His guidance helped me in all the time of research and writing of this thesis. I could not have imagined having a better advisor for my Ph.D study. He was not only important in the strictly academical issues, he was also very supportive when I had problems or when I was having tough times. I want also to thank Rodrigo and Li-Hua, with whom it was a pleasure to work.

I thank my fellow labmates Andrea, Caro, David, Camilo, Monica and all the people that I had the chance to share with during these four years, especially to Jocelyn, Suomi, Loreto, Tania and Leo. I am going to miss the long lunches with all of you where we used to talk and laugh about anything.

Last but not the least, I would like to thank my huge family and Javiera: my parents for supporting during all my life, my brothers Rodrigo and Karla and my cousin Cristian for being always with me through thick and thin; I would also like to thank my grandmother and granduncle who are not among us now, but I am sure they would be happy to know that I finally made it. I thank especially to Javi, who with all her love has given me the strenght and support that I needed to finish this thesis.

This research is supported by Fondecyt Grants No. 1090188 and No. 1120211, and Anillo Grant ACT 127.

Contents

Introduction

« In science there is only physics, all the rest is just stamp collecting. »

Lord Kelvin

Granular materials are ubiquitous in our daily lives. We see them every day; a truck transporting cement, kids playing with sand in the beach, and even in the kitchen if we think of rice. They are also very important in pharmaceutical industry, as well as in many minning processes. Nevertheless. its proper understanding still remains a challenge [1]. But, what is a granular medium? A granular medium is a collection of macroscopic particles that may interact through many different forms. The interactions go from dissipative, hard corelike collisions, to capilary bridges in wet sands, van der Waals forces in most powders, and even electrostatic and magnetic forces when we speak of long-ranged interactions. In order to give a thorough description of the phenomenon of *jamming*, in which the dynamics of a system slows down dramatically as we increase the density or confining pressure, is necessary to include soft interactions. In our research, we are interested in a dry granular medium, with only disspatives contact forces involved.

Accordingly, in order to study the dynamics of granular media, the injection of energy is imperative, and thus in average there is a balance between dissipated and injected power. The injection of energy is usually made through vibrations or by means of injection of airflows. Despite this seeming simplicity, properties of granular materials are often different from conventional solids, liquids, and gases due to the dissipative nature of forces acting on interacting grains, such as inelastic collisions and friction. They behave as solids, liquids, or gases depending on the nature of the forces that act upon them and the energy injection rate [1, 2, 3]. These systems present phase transitions and coexistence. Simple examples are a thin layer of vibrated sand, which for small driving amplitudes remains solid but can be completely fluidized for larger accelerations, and an avalanche driven by gravity where a thin layer of grains flows above an almost solid pile (see Fig. 0.0.1).

Granular systems are therefore excellent candidates for studying nonequilibrium phase transitions [4, 5]. In vibrated thin layers, energy is transferred from the top and bottom lids to the vertical motion of the grains, which later transfer the energy to the horizontal motion at collisions that are also dissipative. The sequence breaks the detailed balance, keeping the system out of equilibrium.

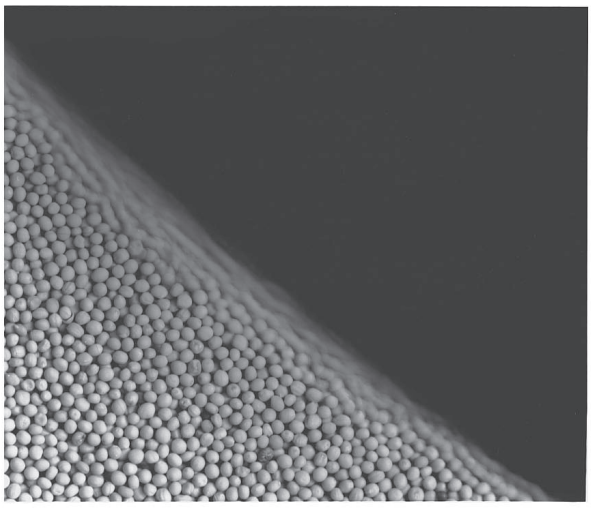

Figure 0.0.1.: A pile of mustard seeds that is tilted to an angle slightly above the angle of repose, thus creating an avalanche [2]. Note that the flow ocurrs only in a thin layer of particles, while deeper inside the pile, the particles do not move.

Recently, several granular systems that undergo phases transitions have been reported [6, 7, 8, 9, 10]. For example, the equilibrium Kosterlitz–Thouless–Halperin–Nelson–Young (KTHNY) theory has proven useful in the two dimensional (2D) melting of granular monolayers [10, 11]. In the KTHNY scenario, the two-dimensional melting consists of two continuous transitions, the first from a crystalline phase (algebraically decaying positional order and long-range orientational order) to an hexatic phase (short-range positional order and algebraically decaying orientational order) by means of the unbinding of dislocation pairs. Then the hexatic phase melts into an isotropic phase (liquid with only short-range order) by unbinding of disclination pairs [12].

One particular system is a vibrated fluidized granular monolayer composed of N hard spheres of diameter d confined in a shallow cell of height $L_z < 2d$ (typically $L_z \approx 1.7d$–$1.9d$). Under proper conditions, solid and liquid phases can coexist at mechanical equilibrium. Considering that the parameters to vary in the system are the particle density and the dimensionless acceleration imposed on the system, this transition occurs at low densities for high accelerations, and high densities for low accelerations, indicating a clear line between a "pure fluid" region from the region of solid-liquid coexistence [6, 9]. The solid clusters can present different order symmetries, like square or hexagonal, depending on forcing, geometrical, and particle parameters. It has been reported that for $L_z \approx 1.7d$–$1.9d$ and for a large range of filling densities, the most compact structure in quasi two dimensions is made of two layers of square symmetry. The more compact hexagonal structure formed by two layers needs a larger vertical gap or larger densities [9]. In this thesis we present an experimental study of this solid-liquid granular phase transition. In Fig. 0.0.2 we observe an time-averaged image showing this two-phase coexistence.

The physical mechanism behind this transition was unknown until some years ago, when it was found that the solid-liquid granular transition is macroscopically triggered by a negative compressibility

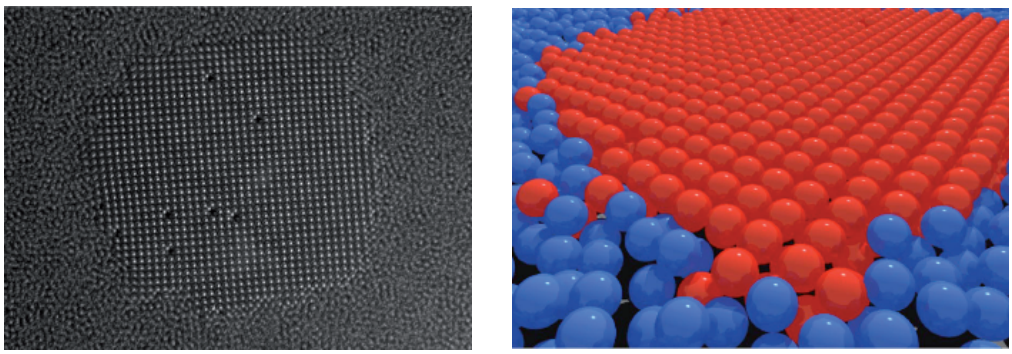

Figure 0.0.2.: Left: Time-averaged image of particle positions showing the two-phase coexistence. Right: 3D rendering of instantaneous particle positions [6].

like in the van der Waals phase coexistence, even though the system does not satisfy the hypothesis used in atomic systems [8]. Aditionally, it was also shown that the transition is mediated by waves, and that the crystals in the system interact through them. Moreover, due to inelasticy and friction these waves decay rapidly. By means of a coarse-graining procedure the waves were found to have a group velocity of $c = 5 - 50$ cm/s.

After important breakthroughs towards the understanding of the problem were done in the lasts years [6, 8, 9], several interesting questions remained unanswered. Hence, the main objectives of this thesis are to characterize the true nature of the transition; in other words we would like to find *the right* order parameter that characterizes the transition, in order to decide whether the transition is a first or second order kind. If it turns out to be a second order phase transition, are there critical exponents that can be measured experimentally? If so, can we describe the critical exponents by means of the standard theory of critical phenomena? On the other hand, we would also like to provide a physical description of the liquid-solid-like interface, that is, we would like to characterize the interface by means of an effective surface tension as it is done in condensed matter physics when studying classical solid to liquid interfaces. We would also like to obtain a more quantitative description of the dynamical properties of the system, namely relaxation rates and wave propagation therein. Is there a more trustworthy method for obtaining the sound speeds in the system?

0.1. Objectives

Accordingly, the main objectives of our research are:

- To study the role of both order and density fluctuations near the solid-liquid granular transition, given that they seem to be fundamental for the transition that takes place.

- To find one or more order parameters that characterize the solid-liquid granular transition. Once this is achieved, to make a thorough analysis of the behavior of the order parameter near the critical point, thus deciding whether it is a continuous or abrupt phase transition.

- In the case of an abrupt phase transition, to study hysteresis cycles such as the case of classical first order phase transitions.
- In the case of a continuous phase transition, to characterize it by means of the theory of critical phenomena by finding the critical amplitudes and exponents.
- Once the system is above the critical point, to describe the fluctuations of the solid-liquid interface by means of an effective surface tension.
- To study the dynamical properties of the system, that is, to obtain relaxation times and to derive dispersion relations and wave speed in a quantitative way.

0.2. Outline

The thesis has the following organization: in Part I we introduce a brief theoretical background with the main concepts and definitions that will be used to describe, analize and discuss the experimental results. In Chapter 1 we review the most important microscopic models used to describe granular matter. In addition, we present a brief and simple review on kinetic theory and the basics of the hydrodynamics equations. In Chapter 2 we deal with the main concepts in the theory of phase transitions, such as the notion of an order parameter and the definition of the critical exponents. In Part II we present in detail the experimental setups used to study the problem, along with some experimental methods developed, concerning the detection of particles and the solid-liquid interface. Part III, which in turn is divided into three chapters, is about the presentation and discussion of results obtained. In Chapter 5 we present the static description of the transition and its characterization in terms of an order parameter. Then, in Chapter 6 we show the results concerning the fluctuations of the solid-liquid interface by means of a coarse-graining procedure. Finally, in Chapter 7 we present the dynamical results obtained through the analysis of some dynamical correlation functions. Concluding remarks are given in the last chapter.

Part I.

Theoretical background

1. Models of granular matter

« Whenever anyone says, "theoretically", they really mean, "not really".»

Dave Parmas

In this chapter we introduce the basic concepts of granular matter and its dynamics by means of the collision rules that account for the behavior of single particles, then we extend the description to a mesoscopic scale by introducing concepts of kinetic theory and finally provide a set of hydrodynamic equations which emerge naturally from kinetic theory for a certain limit. In order to know the resulting velocities of two colliding particles we should know what are the details of the interaction, whether this interaction conserves energy or not, and specifically on what parameters the force depends on. In this chapter we review in some detail the different types of interaction in a constructive way, from the simplest case to more complex and realistic ones. From this microscopic view, it is also possible to derive a mesoscopic description in the context of kinetic theory, which deals with probabilities and distribution functions, that turns out to be a very useful tool when dealing with dilute systems. Moreover, kinetic theory provides a firm theoretical base in the derivation of a hydrodynamical theory that, as in the case of molecular fluids, gives a description of the system through macroscopic fields such as density, temperature and velocity. We also discuss briefly the validity and limitations of these theories and how applicable they are.

1.1. Microscopic properties of granular matter

Granular matter is a very diverse field which incorporates many concepts in physics that go from elasticity to statistical physics. In order to have a good understanding of the variety phenomena that granular matter displays, it is necessary to have a proper description of the interaction among grains. These interactions may be of different nature, and many theoretical approaches have been proposed. Deformation in solids are described by a strain-stress relation. The simplest case is given by Hooke's law, which describes pure elastic deformations where the stress depends linearly on the strain. If we want to give a more accurate description it is necessary to incorporate other factors such as the deformation rate, which accounts for dissipation in the interaction. That is the case of *viscoelastic deformations*, which are characterized by a stress tensor that is the sum of the elastic

stress and the dissipative stress, where the elastic stress depends linearly on the deformation and the dissipative stress depends linearly on the deformation rate.

By supposing isotropy and homogeneity, the elastic properties of a viscoelastic material are characterized just by its Young's modulus Y, and the Poisson's ratio ν. The Young's modulus describes the resistance of the material against compression and extension, whereas the Poisson's ratio accounts for the transverse deformation when an object is compressed or stretched [13]. To describe the dissipative stress it is also necessary to know the viscosities $\eta_{1,2}$ [1]. Therefore, the interaction forces between particles may be obtained as a function of the elastic constants of the material, the radii of the particles, their relative position and their relative velocity.

1.1.1. Elastic forces

The most simple collision interaction model that we can think of is the one which involves elastic deformations. In other words, grains deform each other due to static or quasi-static contacts and the deformations are small compared to the radii of the particles. Elastic deformation also implies that after the collision the particles recover their original shape and size, *i.e.*, there are no plastic deformations (see Appendix A for details). Using these assumptions, the force between two spheres is given by

$$F_{el} = \rho \xi^{3/2}. \tag{1.1.1}$$

where $\rho \equiv \frac{2Y}{3(1-\nu^2)}\sqrt{R^{eff}}$, $R^{eff} \equiv \frac{R_1 R_2}{R_1+R_2}$ and $\xi(t) = R_1 + R_2 - |\vec{r}_1(t) - \vec{r}_2(t)|$ is the the time-dependent deformation, whereas in the 2D case the force becomes

$$F_{el} \propto \xi. \tag{1.1.2}$$

This contact problem was solved for the first time by Heinrich Hertz in 1882 [14]. From 1.1.1 it is possible to calculate that the maximum deformation h, for a sphere of radius R and density ρ, colliding at a speed U_0, with a semi-infinite plane is given by

$$h = 2.2\rho^{2/5}\frac{RU_0^{5/5}}{\overline{Y}^{2/5}}, \tag{1.1.3}$$

where $\overline{Y}$ is the effective Young modulus and is defined as $1/\overline{Y} = \left(1-\nu_1^2\right)/Y_1 + \left(1-\nu_2^2\right)/Y_2$. The collision time τ_c reads

[1] The constants η_1 and η_2 are the two independent components of the *viscosity tensor* η_{iklm} for an isotropic body [13].

$$\tau_c = 6.46\rho^{2/5}\frac{R}{U_0^{1/5}Y^{2/5}}. \tag{1.1.4}$$

For stainless steel spheres of radius $R = 0.5$ mm, colliding with a glass plate at a speed $U_0 \sim 1$ cm/s, the compression distance turns out to be $h \sim 1\,\mu$m, while the collisional time is $\tau_c \sim 0.1$ ms.

1.1.2. Viscous forces

When two particles collide, the deformation changes in time, and a dissipative force arises. The simplest model that one can think of is the one where the dissipative stress tensor is proportional to the deformation rate tensor. After some calculations that go beyond the scope of this thesis, the dissipative force between two spheres of identical material due to viscous effects of the collision F_{diss}, is found to be:

$$F_{diss} = \frac{3}{2}A\rho\sqrt{\xi}\dot{\xi}, \tag{1.1.5}$$

with

$$A \equiv \frac{1}{3}\frac{(3\eta_2 - \eta_1)^2}{(3\eta_2 + 2\eta_1)}\left[\frac{(1-\nu^2)(1-2\nu)}{Y\nu^2}\right]. \tag{1.1.6}$$

and ρ as defined above, and where A is a function which depends on the elastic constant of the bodies and also on the viscous constants η_1, η_2, and determines basically the relation between the stress tensor and the deformation rate tensor. It is important to remark at this point that this approach also has some limitations. Equation 1.1.6 is valid only if the approaching velocities between the particles is small compared to the speed of the sound c in the material. Another important issue has to do with the assumption of the plasticity of the deformation. That is, it is not necessarily true that after the collision the bodies recover their shape. There have been several attempts to tackle this, and it is still a matter of debate (see [15] and references therein).

1.1.3. Adhesion forces

If we want to push things a little further, it should be noticed that under some conditions there exists another force which gives an extra complication to the problem . If the particles are small ($\lesssim 100\,\mu$m), the assumption that the contact force goes to zero when tensile stress is applied is no longer valid. We pointed out in the previous section (Sec. 1.1.1) that when the overlapping distance is ξ, the force exerted on a particle is $F \propto \xi^{3/2}$ for spheres, and $F \propto \xi$ for disks. But if the overlapping distance ξ is comparable to the typical length scale of the van der Waals attraction

force, an additional adhesion force appears. Attard & Parker [16] extended the Hertz approach by modeling the adhesion force using a Lenard-Jones potential yielding

$$F_a = \frac{H}{6\pi\delta^3}\left(\frac{\delta_0^6}{\delta^6} - 1\right), \tag{1.1.7}$$

where δ is distance between the surfaces, δ_0 is the equilibrium distance, and H is the Hamaker constant of the van der Waals interaction [17].

There is also another type of interaction between grains that becomes particularly important in powders[2]. When there is interstitial fluid present, the so-called capillary liquid bridges provide adhesion which is usually absent in dry granular media. There are several works on the effects of adhesion forces in the behavior of granular media. It is believed to be responsible of increasing the repose angle in sandpile avalanches and also responsible of producing a complete new rheology of granular matter. For details see [15].

Obviously the forces that we have dealt so far are not the only ones that play a role in a collision. There should be taken into consideration non-plastic deformations, other types of interaction for adhesive forces, and maybe more importantly the effect of the shape of the particles, which is probably the most complex issue to deal with.

1.1.4. Restitution coefficient

Until now we have dealt with different types of forces that are present when two particles collide. In turn, these forces provide the kinematics of particles. From now on, we assume that no adhesion nor electrostatic force are present, so that particles only interact through elastic and viscous forces. Let the colliding particles be spheres of identical material and also assume that they do not exchange tangential momentum. As stated before, the time-dependent deformation reads

$$\xi\left(t\right) = R_1 + R_2 - \left|\vec{r}_1\left(t\right) - \vec{r}_2\left(t\right)\right|, \tag{1.1.8}$$

where $\vec{r}_1\left(t\right)$ and $\vec{r}_2\left(t\right)$ are the position of the particle centers at time t. The relative motion of two colliding particles may be described by the motion a point particle whose mass is

$$m_{eff} \equiv \frac{m_1 m_2}{m_1 + m_2}. \tag{1.1.9}$$

Hence, the equation of motion of this point particle reads

$$\ddot{\xi} - \frac{\rho}{m_{eff}}\left(\xi^{3/2} + \frac{3}{2}A\sqrt{\xi}\dot{\xi}\right) = 0. \tag{1.1.10}$$

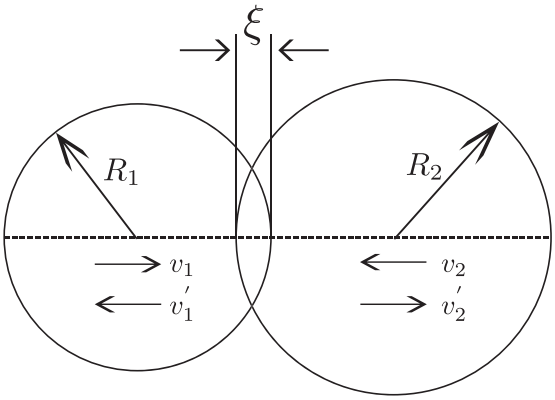

Figure 1.1.1.: Head-on collision of two spheres.

With $\xi(0) = 0$ and $\dot{\xi}(0) = u$.[3] After the collision part of the energy is lost in the interaction, and the (normal) restitution coefficient quantifies this. Its definition is:

$$\epsilon \equiv -\frac{\dot{\xi}(t_c)}{\dot{\xi}(0)} = -\frac{\dot{\xi}(t_c)}{u}, \tag{1.1.11}$$

with t_c defined as the duration of the collision. Using this definition, provided momentum conservation, it is possible the derive the final velocities of the particles after colliding, yielding:

$$\begin{aligned} \vec{v}_1' &= \vec{v}_1 - \frac{m_{eff}}{m_1}(1+\varepsilon)(\vec{v}_{12}\cdot\vec{e})\,\vec{e} \\ \vec{v}_2' &= \vec{v}_2 + \frac{m_{eff}}{m_1}(1+\varepsilon)(\vec{v}_{12}\cdot\vec{e})\,\vec{e}. \end{aligned} \tag{1.1.12}$$

Where $\vec{e}$ is a unit vector pointing from the center of particle 1 to particle 2.
A simple derivation of the restitution coefficient may be performed by doing simple dimensional analysis. A general form for elastic and dissipative forces is

$$F_{el} = m_{eff}K_1\xi^{\alpha}, \qquad F_{diss} = m_{eff}K_2\xi^{\gamma}\dot{\xi}^{\beta}, \tag{1.1.13}$$

With these, the equation of motion reads

$$\ddot{\xi} + D_1\xi^{\alpha} + D_2\xi^{\gamma}\dot{\xi}^{\beta} = 0, \qquad \xi(0) = 0, \qquad \dot{\xi}(0) = u. \tag{1.1.14}$$

[2]The standard definition of powders refers to grains of less than 10 μm diameter.
[3]In this notation, $u \equiv v_1(0) - v_2(0)$.

It is possible to define a typical or characteristic length of the collision, and this can be done in the case of pure elastic deformation ($K_2 = 0$) by equating the kinetic energy $m_{eff}u^2/2$ with the potential energy $m_{eff}K_1\xi^{\alpha+1}/(\alpha+1)$. Hence,

$$\xi_0 \equiv \left(\frac{\alpha+1}{2K_1}\right)^{1/(\alpha+1)} u^{2/(\alpha+1)}. \tag{1.1.15}$$

From this, it is possible to define a characteristic time which is simple the time required for particle to cover the distance ξ when traveling at a speed u. That is, $\tau_0 \equiv \xi/u$. Therefore, we define the new dimensionless variables as:

$$\lambda \equiv \frac{\xi}{\xi_0} \qquad \dot{\lambda} \equiv \frac{\dot{\xi}}{u} \qquad \ddot{\lambda} \equiv \left(\frac{\xi_0}{u^2}\right)\ddot{\xi}. \tag{1.1.16}$$

And inserting 1.1.16 into 1.1.14 implies,

$$\ddot{\lambda} + \chi\lambda^{\gamma}\dot{\lambda}^{\beta} + \frac{1+\alpha}{2}\lambda^{\alpha} = 0, \qquad \lambda(0) = 0, \qquad \dot{\lambda}(0) = 1. \tag{1.1.17}$$

Where the function χ is defined by

$$\chi(u) \equiv K_2\left(\frac{1+\alpha}{2K_1}\right)^{(1+\gamma)/(1+\alpha)} u^{2(\gamma-\alpha)/(1+\alpha)+\beta}. \tag{1.1.18}$$

It is clear from 1.1.17 that material properties or impact velocity just come into play in the function χ, *i.e.* all the dynamics is captured in the function χ. Accordingly, any dependence of the restitution coefficient on the particular parameters of the collision should be of the form $\varepsilon = \varepsilon[\chi(u)]$. Now, we may study some cases:

I. If the restitution coefficient does not depend on the impact velocity u, then 1.1.18 implies that

$$2(\gamma-\alpha) + \beta(1+\alpha) = 0. \tag{1.1.19}$$

For small $\dot{\xi}$ it is kind of realistic to assume that the viscous force has a linear dependence on $\dot{\xi}$ ($\beta = 0$), hence

- As said before, $F_{el} \propto \xi$ for disks, *i.e.* $\alpha = 1$ which implies that $F_{diss} \propto \dot{\xi}$, *i.e.* $\gamma = 0$.
- In the 3D case, Hertz law states $F_{el} \propto \xi^{3/2}$, *i.e.* $\alpha = 3/2$ and thus $F_{diss} \propto \xi^{1/4}\dot{\xi}$.

But there are not physical arguments in favor of this last relation, whereby the assumption that $\epsilon = const$ is only applicable to 2D mechanics, whereas for the 3D case the result leads to unphysical phenomena. One of the most remarkable results concerning this unphysical consequence is the so-called *inelastic collapse,* which occurs in event-driven simulations of hard inelastic particles with fixed ε. McNamara and Young [18] showed that a constant value of ε leads to a divergence in the number of collisions between two particles in a finite time, dissipating completely the energy of the relative motion making the particles to move as a cluster. Of course, in reality the number of interparticle collisions remains finite, because eventually the interval between collisions becomes comparable to the collision time, and hence the assumption of *hard particles* is no longer valid.

II. On the other hand, in the case of a viscoelastic interaction the coefficients are $\alpha = 3/2$, $\beta = 1$, $\gamma = 1/2$, and therefore $\chi(u)$ becomes:

$$\chi(u) = \frac{3}{2}\left(\frac{5}{4}\right)^{3/5} A\left(\frac{\rho}{m_{eff}}\right)^{2/5} u^{1/5} \Longrightarrow \varepsilon = \varepsilon\left[A\left(\frac{\rho}{m_{eff}}\right)^{2/5} u^{1/5}\right]. \tag{1.1.20}$$

Now if we assume that $\varepsilon(u)$ is a well-behaved and smooth function, then we can expand it as a Taylor series with $\varepsilon(0) = 1$, thus

$$\varepsilon = 1 - C_1 u^{1/5} + C_2 u^{2/5} \mp \ldots \tag{1.1.21}$$

which was derived using very simple arguments, but has also been obtained from a more thorough analysis [19].

1.1.5. Friction

Hitherto the analysis made has neglected the role of friction in the interparticle interaction, but it is widely known that it plays a very important role in the behavior of granular systems. Thus, in order to give a meticulous description of what happens when two particles collide, it becomes imperative to take into account the effects of friction. It has been an active field of research for the last decades [20, 21], and it has been proven to be key to understanding many phenomena (see [22] for a review).

Friction arises from complicated intermolecular and surface forces between particles, and it is known to be hysteretic and strongly non-linear, making its analysis extremely difficult. A simple approach to grasp the problem is the *Coulomb law* that is a phenomenological law which states that two grains are in rest relative to each other if the ratio of the tangential force F^t to the normal force F^n is less than the amount μ_s, known as the *static friction coefficient.* That is,

$$\left|F^t\right| \leq \mu_s \left|F^n\right|. \tag{1.1.22}$$

Once the particles set into motion, the tangential force F^t becomes exactly proportional to F^n,

$$\left|F^t\right| = \mu_d \left|F^n\right|, \tag{1.1.23}$$

where μ_d is defined as the *dynamic friction coefficient.* Tab. 1.1.5 shows these coefficients for different materials.

Material	ϵ	μ_s	μ_d
Steel	0.6	0.78	0.42
Glass	0.9	0.9-1.0	0.4
Cooper	0.5	1	0.3
Rubber	0.8	1-2	-
Teflon	0.72	0.04	-
Nylon	0.88	0.15-0.25	-

Table 1.1.: Coefficient of restitution ϵ, static friction coefficient μ_s, and dynamic friction coefficient μ_d for different materials. Friction coefficients are provided for contact between the same materials [23].

It is important to remark that the Coulomb's law is just an approximation. There are plenty of factors that were not taken into consideration. It is well known that when there is contact among three or more particles, the friction forces are undetermined given that constraints equations are fewer than stress components. However, there have been several attemps to make contributions in this subject (see [24] and references therein for a review). Besides, real particles have rotational degrees of freedom whereby a sliding motion may become a stick-slip motion depending on the angular speed of the particles. Moreover, non spherical particles complicate things out even more. Accordingly, in order to simplify things, we introduce the *tangential restitution coefficient* which is defined by

$$\varepsilon^t \equiv \frac{u'^t}{u^t}, \tag{1.1.24}$$

where u^t and u'^t are the relative tangential velocities of the particles before and after the collision respectively. In general ε^t takes values between $-1 < \varepsilon^t < 1$. And unlike the normal restitution coefficient, it depends on both normal and tangential velocities.

1.2. Kinetic theory and hydrodynamics

Given the resemblance of ordinary molecular gases and dilute colliding particles, it is very tempting to push the analogy a little further by setting into motion all the well-devoleped machinery of statistical mechanics to describe granular gases. Although there are many fundamental differences between both systems. As already mentioned, real granular media are composed of inelastic particles, and it is well known in the literature that even with slightly ineslatic particles, the behavior of the systems is markedly different. Besides, in granular gases there is no equipartion theorem; Luding and

McNamara [25, 26] showed numerically that the mean rotational energy differs from translational kinetic energy for monodisperse spheres. Also, it has been shown that the velocity distribution of granular gases is non-Maxwellian, and instead it is characterized by a stretched exponential [27, 28, 29]. However, in spite of all these complications, it is possible the give an approximate statistical description of granular gases, which ultimately gives rise to the Boltzmann-Enskog equation [15].

1.2.1. Boltzmann equation

The main ingredient for the formulation of a kinetic theory is the *distribution function* $f(\vec{r},\vec{v},t)$ which is defined such that $f(\vec{r},\vec{v},t)\,\mathrm{d}\vec{r}\,\mathrm{d}\vec{v}$ gives the number of particles whose positions lie within the infinitesimal volume $\mathrm{d}\vec{r}$ about $\vec{r}$, and their velocities lie within $\mathrm{d}\vec{v}$ at $\vec{v}$. So, from its definition follows that when integrated over the whole phase space,

$$\int f(\vec{r},\vec{v},t)\,\mathrm{d}\vec{r}\,\mathrm{d}\vec{v} = N, \tag{1.2.1}$$

where N is the particles number of the system. The derivation we present next was first obtained by Boltzmann in 1896, and then generalized by Enskog in 1917, but we follow a more intuitive or phenomenological approach based on the work by Chapman & Cowling [30]. Now, for the sake of simplicity we consider identical particles of radius σ.

During a time interval Δt the number of particles $f(\vec{r}_1,\vec{v}_1)\,\mathrm{d}\vec{r}_1\mathrm{d}\vec{v}_1$ in the volume of the phase space $\mathrm{d}\vec{r}_1\mathrm{d}\vec{v}_1$ centered at $(\mathrm{d}\vec{r}_1,\mathrm{d}\vec{v}_1)$ can split up into two sources. *Direct collisions* are collisions in which particles in this interval are involved. In general, these collisions lead to velocities that are *out* of the volume considered, and thus direct collision tend to decrease the number of particles in the volume $\mathrm{d}\vec{r}_1\mathrm{d}\vec{v}_1$. Contrary, *inverse collisions* are collisions of particles that lie outside the velocity interval $(\vec{v}_1,\vec{v}_1+\mathrm{d}\vec{v}_1)$, but after the collision they belong to this interval. Hence, inverse collisions in general tend to increase the number of particles in the considered phase-space volume. In order to quantify this, we must take the collision rule 1.1.12 using $m_1=m_2$, leading to

$$\begin{aligned} \vec{v}_1' &= \vec{v}_1 - \frac{(1+\epsilon)}{2}\left(\vec{v}_{12}\cdot\vec{e}\right)\vec{e}, \\ \vec{v}_2' &= \vec{v}_2 + \frac{(1+\epsilon)}{2}\left(\vec{v}_{12}\cdot\vec{e}\right)\vec{e}. \end{aligned} \tag{1.2.2}$$

In Fig. 1.2.1 is depicted the scheme of a collision of identical particles. Each scatterer has a well-defined collision cylinder that accounts for all possibles collisions within the infinitesimal solid angle $\mathrm{d}\vec{\Omega}\equiv\mathrm{d}\vec{e}$. From the figure we can see that the volume of the collision cylinder V_{cc} is:

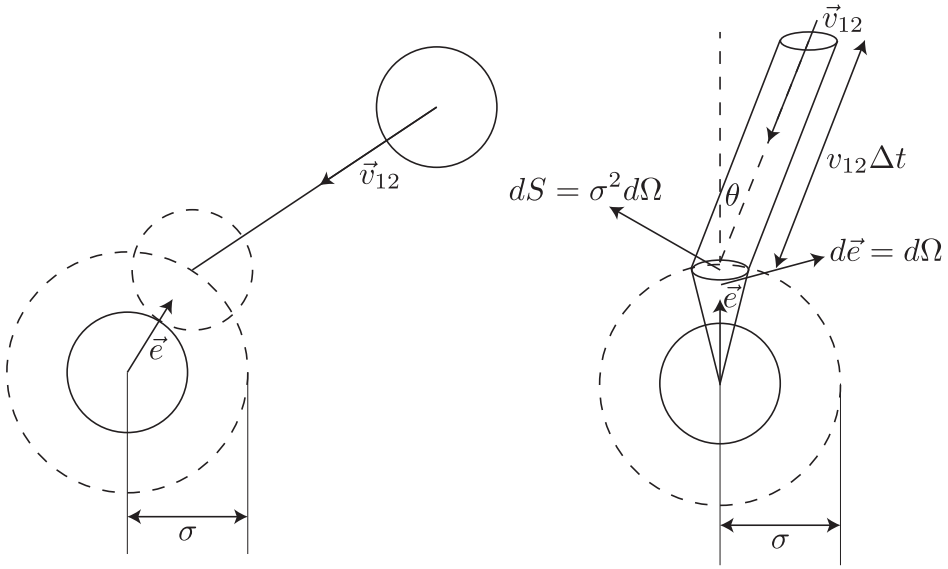

Figure 1.2.1.: Collision cylinder for the scattering of particles colliding at a relative velocity $\vec{v}_{12} \equiv \vec{v}_1 - \vec{v}_2$. The cylinder accounts for all the particles that hit the surface at a small spot around $\vec{e}$.

$$\begin{aligned} V_{cc} &= \mathrm{d}\vec{S} \cdot \vec{v}_{12}\Delta t, \\ &= \sigma^2 \mathrm{d}\vec{\Omega} \cdot \vec{v}_{12}\Delta t, \\ V_{cc} &= \sigma^2 \left|\vec{v}_{12} \cdot \vec{e}\right| \Delta t. \end{aligned} \tag{1.2.3}$$

The number of scatterers in the volume $\mathrm{d}\vec{r}_1$ is $f\left(\vec{v}_2, t\right) \mathrm{d}\vec{r}_1\, \mathrm{d}\vec{v}_2$. Besides, according to the definition of the velocity distribution function, the number of particles with velocity $\vec{v}_1$ in the collisional cylinder is $f\left(\vec{v}_1, t\right) d\vec{v}_1\, V_{cc}$. Therefore, the total number of collisions during the interval Δt is

$$\nu^{-}\left(\vec{v}_1, \vec{v}_2, \vec{e}, t\right) = f\left(\vec{v}_1, t\right) f\left(\vec{v}_2, t\right) \mathrm{d}\vec{r}_1\, \mathrm{d}\vec{v}_1\, \mathrm{d}\vec{v}_2\, \sigma^2 \left|\vec{v}_{12} \cdot \vec{e}\right| \Delta t. \tag{1.2.4}$$

Inverse collisions are defined as collisions of particles with velocities $\vec{v}_1'$ and $\vec{v}_2'$ that after the impact yield particles with velocities $\vec{v}_1$ and $\vec{v}_2$. So, according to 1.1.12 we have

$$\begin{aligned} \vec{v}_1 &= \vec{v}_1' - \frac{(1+\epsilon)}{2}\left(\vec{v}_{12}' \cdot \vec{e}\right)\vec{e}, \\ \vec{v}_2 &= \vec{v}_2' + \frac{(1+\epsilon)}{2}\left(\vec{v}_{12}' \cdot \vec{e}\right)\vec{e}. \end{aligned} \tag{1.2.5}$$

Using the same reasoning as before, we can write the number of direct collisions:

$$\nu^+\left(\vec{v}_1', \vec{v}_2', \vec{e}, t\right) = f\left(\vec{v}_1', t\right) f\left(\vec{v}_2', t\right) \mathrm{d}\vec{r}_1 \, \mathrm{d}\vec{v}_1' \, \mathrm{d}\vec{v}_2' \, \sigma^2 \left|\vec{v}_{12}' \cdot \vec{e}\right| \Delta t. \tag{1.2.6}$$

But, in order to have ν^+ as a function of $\vec{v}_1$ and $\vec{v}_2$, instead of $\vec{v}_1'$ and $\vec{v}_1'$ we can invert the relations of equations 1.2.5,

$$\begin{aligned} \vec{v}_1' &= \vec{v}_1 - \frac{(1+\varepsilon)}{2\varepsilon}\left(\vec{v}_{12} \cdot \vec{e}\right)\vec{e}, \\ \vec{v}_2' &= \vec{v}_2 + \frac{(1+\varepsilon)}{2\varepsilon}\left(\vec{v}_{12} \cdot \vec{e}\right)\vec{e}, \end{aligned} \tag{1.2.7}$$

and for the particular case of $\epsilon = const$ we get

$$\nu^+\left(\vec{v}_1', \vec{v}_2', \vec{e}, t\right) = \frac{1}{\varepsilon^2} f\left(\vec{v}_1', t\right) f\left(\vec{v}_2', t\right) \mathrm{d}\vec{r}_1 \, \mathrm{d}\vec{v}_1 \, \mathrm{d}\vec{v}_2 \, \sigma^2 \left|\vec{v}_{12} \cdot \vec{e}\right| \Delta t. \tag{1.2.8}$$

In a more general case, instead of having the term $1/\epsilon^2$ we have a more complicated function of ε, namely $\chi(\epsilon)$.
So far we have the direct and inverse collision rate, and by integrating over all possibles velocities $\vec{v}_2$ and over all directions $\vec{e}$ that correspond to an actual impact, it is possible to calculate to total amount of collisions. Now, it is important to note that for direct collisions, only directions with $\vec{v}_{12} \cdot \vec{e} < 0$ lead to an impact, whereas for inverse collisions only directions such that $\vec{v}_{12}' \cdot \vec{e} > 0$ should be taken into account. Hence the increment in the number of particles in the interval Δt is

$$\Delta \left|f\left(\vec{v}_1, t\right)\right| \mathrm{d}\vec{r}_1 \, \mathrm{d}\vec{v}_1 = \int \mathrm{d}\vec{v}_2 \mathrm{d}\vec{e} \left(\Theta\left(-\vec{v}_{12}' \cdot \vec{e}\right) \nu^+\left(\vec{v}_1', \vec{v}_2', \vec{e}, t\right) - \Theta\left(-\vec{v}_{12} \cdot \vec{e}\right) \nu^-\left(\vec{v}_1, \vec{v}_2, \vec{e}, t\right)\right), \tag{1.2.9}$$

where Θ is the Heaviside function,

$$\Theta(x) = \begin{cases} 1 & \text{if } x \geq 0 \\ 0 & \text{if } x < 0. \end{cases} \tag{1.2.10}$$

From the collision rule 1.2.5 it is possible to derive that $\vec{v}_{12} \cdot \vec{e} = -\varepsilon \vec{v}'_{12} \cdot \vec{e}$, thus implying that $\Theta\left(\vec{v}'_{12} \cdot \vec{e}\right) = \Theta\left(-\vec{v}_{12} \cdot \vec{e}\right)$, and noting that changing the $\vec{e} \to -\vec{e}$ does not change the first integral in 1.2.9, using 1.2.8 and 1.2.4 we finally obtain the Boltzmann equation after dividing both sides of the equation by $\mathrm{d}\vec{r}_1 \mathrm{d}\vec{v}_1 \Delta t$ and taking the limit $\Delta t \to 0$,

$$\frac{Df}{Dt}\left(\vec{v}_1, t\right) = \sigma^2 \int \mathrm{d}\vec{v}_2 \int \mathrm{d}\vec{e}\, \Theta\left(-\vec{v}_{12} \cdot \vec{e}\right) \left|\vec{v}_{12} \cdot \vec{e}\right| \left[\chi\left(\varepsilon\right) f\left(\vec{v}'_1, t\right) f\left(\vec{v}'_2, t\right) - f\left(\vec{v}_1, t\right) f\left(\vec{v}_2, t\right)\right], \tag{1.2.11}$$

$$\frac{\partial f}{\partial t}\left(\vec{v}_1, t\right) + \vec{v}_1 \cdot \nabla f \equiv I\left[f\right]. \tag{1.2.12}$$

In the derivation of equation 1.2.12 we made several approximations that are not necessarily true. One of the most strong assumptions was that the velocities of two colliding particles are not correlated, whereby the joint probability $f_2\left(\vec{r}_1, \vec{r}_2, \vec{v}_1, \vec{v}_2, t\right)$ for two colliding particles is just the product of the corresponding single-particle distribution functions. This assumption is known as *the hypothesis of molecular chaos* or *Stosszahlansatz* according to its historical name given by Boltzmann. This hypothesis is not always satisfied, and neglecting correlations of velocities should only be appropriate for molecular dilute gases, and even for dilute granular gases there is evidence that velocity correlations are not negligible [31, 32, 33, 34]. The main sources of the observed correlations are the inelasticity of the collisions, and more importantly the finite-volume effects. It was Enskog at the beginning of the 20th century who came up with a solution to these problems giving an improved, but still approximated, relation for the joint probability $f_2\left(\vec{r}_1, \vec{r}_2, \vec{v}_1, \vec{v}_2, t\right)$:

$$f_2\left(\vec{v}_1, \vec{v}_2, t\right) \simeq g\left(\sigma\right) f\left(\vec{v}_1, t\right) f\left(\vec{v}_2, t\right), \tag{1.2.13}$$

where $g\left(\sigma\right)$ is just the value taken by the *pair distribution function* $g\left(r\right)$ evaluated at $r_{12} = \sigma$, and is also known as the *Enskog factor* (see Sec. 2.4 for more details). In general $g\left(\sigma\right)$ is written in terms of the packing fraction ϕ, and its specific form depends on the type of interaction that is taken into consideration[4]. In physical terms, the Enskog factor accounts for an increment in the collisional rate due to excluded-volume effects. Thus, the *Boltzmann-Enskog equation* reads,

$$\frac{\partial f}{\partial t}\left(\vec{v}_1, t\right) + \vec{v}_1 \cdot \nabla f = g\left(\sigma\right) I\left[f\right]. \tag{1.2.14}$$

From 1.2.14 it can be shown that for elastic particles ($\varepsilon = 1$), a possible solution for an isolated system is $f\left(\vec{v}, t\right) \to f_{MB}\left(\vec{v}\right)$, where $f_{MB}\left(\vec{v}\right)$ is the well-known Maxwell-Boltzmann distribution function. But for inelastic particles ($\varepsilon < 1$), the Maxwellian is no longer a stationary solution and finite correlations exist.

Despite this straightforward generalization, there are still phenomena that are not not fully captured by 1.2.14 such as the the alignment of neighboring particles yielding vortices in an otherwise homogeneous granular state [35, 36, 37], and the behavior of polyatomic gases, where interactions are not

[4] For hard-spheres, $g\left(\sigma\right) = \frac{(2-\phi)}{2(1-\phi)^3}$.

only mediated through interparticle distance, but also through their orientation. Besides there is another complication, by incorporating the extra rotational and vibrational degrees of freedom that play an important role in the collision rule [38], which we have ignored altogether. As an important remark, we should say that standard kinetic theory can be formally derived from the *BBGKY hierarchy (Bogoliubov–Born–Green–Kirkwood–Yvon hierarchy)* [39, 40, 41] and leads to the Boltzmann equation at low densities. This thesis does not pretend to give a full and detailed picture of kinetic theory but just a glimpse.

As a final comment, it should be said that in the more general context of the *BBGKY hierarchy*, the s-particle distribution function $f^{(s)}(\vec{v},t)$ is written as an expansion in a power series of $\lambda \equiv n\sigma^3$, such that this distribution is assumed to be $f^{(s)}(\vec{v},t) = f_0^{(s)}(\vec{v},t) + \lambda^2 f_1^{(s)}(\vec{v},t) + \ldots$, and where equation 1.2.14 is only valid for $f_0^{(s)}(\vec{v},t)$, whereas higher order moments must fulfill other recursive relations (see [40] and references therein for further details). The problem arises due the set of equations is not closed, that is, the equation for a given moment depends on a higher order moment, and then in order to have closure the distribution function is conjectured to be a Maxwellian multiplied by factors that depend on local gradients of hydrodynamical fields.

1.2.2. Granular hydrodynamics

As in the case of molecular gases (or liquids), we can define macroscopic fields for granular gases such as the number density $n(\vec{r},t)$, the velocity $\vec{V}(\vec{r},t)$ and the temperature $T(\vec{r},t)$ by taking moments of the Boltzmann function $f(\vec{v},t)$ as follows:

$$n(\vec{r},t) \equiv \int \mathrm{d}\vec{v} f(\vec{r},\vec{v},t), \tag{1.2.15}$$

$$\vec{V}(\vec{r},t) \equiv \frac{1}{2n(\vec{r},t)} \int \mathrm{d}\vec{v}\,\vec{v} f(\vec{r},\vec{v},t), \tag{1.2.16}$$

$$T(\vec{r},t) \equiv \frac{m}{dn(\vec{r},t)} \int \mathrm{d}\vec{v} \left(\vec{v}-\vec{V}\right)^2 f(\vec{r},\vec{v},t), \tag{1.2.17}$$

where d is the spatial dimension and m is the mass of the particles. The concept of granular temperature has encountered some opposition in the past, due to concerns about the real meaning of temperature in systems out-of-equilibrium, since in granular systems it is not associated to a conserved quantity (energy), but it seems now that the physical community has agreed about its importance [42, 43]. Provided the distribution function, it is possible to write down conservative equations of mass, momentum, and energy:

$$\frac{Dn}{Dt} = -n\nabla\cdot\vec{v}, \tag{1.2.18}$$

$$mn\frac{D\vec{v}}{Dt} = -\nabla\cdot\boldsymbol{\sigma} + n\vec{g}, \tag{1.2.19}$$

$$nc_V\frac{DT}{Dt} = -\boldsymbol{\sigma}:\dot{\gamma} - \nabla\cdot\vec{q} - \Gamma_E, \tag{1.2.20}$$

where $D/Dt = \partial_t + \vec{v}\cdot\nabla$ is the material derivative, $\vec{g}$ is the gravity acceleration and c_V is the specific heat at constant volume. The stress tensor $\boldsymbol{\sigma}$, the energy flux vector $\vec{q}$, the energy dissipation rate Γ_E are defined by

$$\sigma_{ij} = \int \mathrm{d}\vec{v}\, V_i V_j f\left(\vec{r},\vec{v},t\right), \tag{1.2.21}$$

$$\vec{q} = \frac{1}{2}\int \mathrm{d}\vec{v}\, V^2\vec{V} f\left(\vec{r},\vec{v},t\right), \tag{1.2.22}$$

$$\Gamma_E = \frac{\pi\left(1-\epsilon^2\right)\sigma^2}{8n}\iint \mathrm{d}\vec{v}_1\,\mathrm{d}\vec{v}_2\, v_{12}^3 f\left(\vec{r}_1,\vec{v}_1\right) f\left(\vec{r}_2,\vec{v}_2\right). \tag{1.2.23}$$

The form of these balance equations is the same as for fluids with elastic collisions, except for the last term in 1.2.20 which is a "sink term" that turns out to be proportional to $1-\epsilon^2$ and is identified as the cooling rate. Now, in order to give a complete description of the hydrodynamic fields, constitutive equations should be provided. For molecular fluids there is no ambiguity about what these relations should be, however it is unclear whether such a closure exists for granular matter, if the processes are Markovian or have memory, or even if the interactions are local. For dilute systems, these constitutive equations for the stress tensor $\boldsymbol{\sigma}$ and the energy flux $\vec{q}$ are found to be:

$$\sigma_{ij} = \left[p + \left(\eta - \eta_b\right)\mathrm{Tr}\dot{\gamma}\right]\delta_{ij} - \eta\dot{\gamma}_{ij}, \tag{1.2.24}$$

$$\vec{q} = -\kappa\nabla T - \mu\nabla n, \tag{1.2.25}$$

where p is the isotropic pressure; η and η_b[5] are the shear and bulk viscosity respectively; κ is the thermal conductivity of the granular material; $\mu\left(\epsilon\right)$ is a new transport coefficient coupling the heat flux to a density gradient, which vanishes as $\varepsilon \to 1$; and $\dot{\gamma}_{ij}$ is the strain rate tensor defined as $\dot{\gamma}_{ij} \equiv \left(\partial_i v_j + \partial_j v_i\right)/2$.

We can notice that the functional form of the stress tensor is the same as that for fluids with elastic collisions, except that now $\eta\left(\varepsilon\right)$ depends on the normal restitution coefficient, as well as $\kappa\left(\epsilon\right)$ does in the Fourier's law of equation 1.2.25. There have been several attempts to give an equation of state,

[5]The bulk viscosity η_b vanishes at low densities.

along with expressions for the transport coefficients that could catch the wide variety of phenomena present in granular media. Carnahan & Starling [44], and Luding *et. al.* [45], propose equations of state for dilute and high-density regimes respectively that have proven to be useful in their range of validity.[6]

Granular hydrodynamics has been widely used in the physics community as a tool for describing a variety of behaviors, such as instabilities, granular convection, patterns in vibrated granular media, segregation, etc. On the contrary, granular hydrodynamics has not been able to explain the effects of force chains, nor hysteretic phase transitions from solid to fluid phases (see [46, 2, 47] and references therein). We should say also that in granular media there is absence of a scale separation, that is, the ratio between a microscopic time scale τ and a macroscopic time scale, lets say $\dot{\gamma}^{-1}$, is an $\mathcal{O}(1)$ quantity, unless the particles are nearly elastic ($\varepsilon \approx 1$) [48]. Hence, the particular system we study, which is in a high-density regime with inelastic collisions as will be clear later, could be of great importance to test granular hydrodynamics and could be fundamental to know what are the ingredients we need to add to it to capture adequately these phenomena.

[6] In the dilute limit $p = nT$.

2. Phase transitions and critical phenomena

> *« The scientist does not study nature because it is useful; he studies it because he delights in it, and he delights in it because it is beautiful. If nature were not beautiful, it would not be worth knowing, and if nature were not worth knowing, life would not be worth living. »*
>
> *Henri Poincaré*

We know from everyday experience that matter presents itself in different *states or phases*, and from elementary school we were taught that they were three states of matter; namely *solid, liquid and gas,* but thousands of years ago ancient people believed that there were four: *earth, wind, fire and water.* With the development of science in the last centuries, specially in the last one, there have been discovered many new states. Superfluids and superconductors are startling new states, liquid crystals used as displays of a great variety of electronic devices is another remarkable example found in everyday life, along with an immense family of different crystalline states with distinct structures. The variety of states that a system may be on, depend upon conditions of pressure and temperature, and hence by varying these conditions the system undergo a *phase transition.* A simple case is observed when we boil water in the kitchen: by heating the container where the liquid water is, we increase the temperature turning liquid water into vapor.

But talking about states of matter and phase transitions there are some questions that naturally arise; How do we actually define a state of matter? Maybe more importantly, how do we differentiate two phases? How do you tell that oil and water are in the same state or phase? What is the signature that a phase transition has taken place? In these chapter we try to answer these questions by giving a description of some phase transitions in nature and then studying some simple theories, though approximated, help us capture most of the main features of phase transitions. In the end we also approach the theory of critical phenomena in some detail.

2.1. States of matter and broken symmetries

In order to have a clear idea of how phase transitions take place, lets think for a while in the case of water, which is something common to us. Under ambient conditions of pressure and temperature, water is liquid and its molecules have large kinetic energy. The distance among particles is a trade-off between the repulsive and attractive parts of the interaction. The molecules move by diffusion and

the density is isotropic and homogeneous, although there are some density fluctuations spreaded out through the fluid, which are very short-lived. As we lower the temperature, these density fluctuations increase in intensity, and persisting for longer times. At even lower temperatures, molecules have less kinetic energy, the attractive part of the interaction becomes more dominant than before yielding some bonds among molecules that now begin to appear, besides interparticle distance is smaller. Consequently, density fluctuations increase in intensity even further and begin to form domains with certain order that span large portions of the fluid. Finally, at some particular value (0^oC), the attraction among particles becomes stronger, increasing the density of the system. The bonds are stronger and rigid, and now these domains convert into a single one that covers the whole system having a well-defined order. This rigid structure or *crystal* is made up of molecules whose kinetic energy is negligible and it is just vibrational energy. Accordingly, as temperature drop below a critical value, the system undergoes a *phase transition*. Above the critical temperature, water is in the liquid phase which is isotropic and homogeneous, which means there is rotational as well as translational symmetry. But the solid phase *does not* have those symmetries. Thus, we say there was an *spontaneous break of symmetry*. This kind of phase transitions is known as structural transition, that is, when there is symmetry breaking. Another example of this type of phase transitions is what happens with the isotropic and nematics phases in some fluids[1]. We should remark though, that not all structural phase transitions are disorder-order transitions. There are also solid-solid transitions, that is, where both phases are ordered but the symmetries of the crystals are not the same. However, not all phase transitions in nature are associated to any broken symmetry such as the case of the liquid-vapor transition. In that case, even though there are important differences between them, both phases have the same symmetries and the principal physical quantity distinguishing the liquid and the gas phases is their density. Phase transitions that take place between two phases with the same symmetries are called *isostructural transitions*. In other words, the system is in a state that has less symmetry than the Hamiltonian, which in general is invariant under translations and rotations.

Symmtery-breaking transitions may in general be described by an *order parameter*, which is a variable that quantifies the degree of order of the phase, and it is usually defined in such a way that it is zero in the phase with greater symmetry. There are cases, though, where it is not posssible to define an order parameter, such as the solid-solid transition, since this can be done only if the symmetry group of one phase is a subgroup of the symmetry group of the other phase.

The order parameter is a field, scalar or vectorial, meaning that it is defined at each point of the system. To clarify this, lets think of a magnet. At each point $\vec{x} = (x, y, z)$ we have the local direction of the magnetization vector $\vec{M}(\vec{x})$. Thus, the magnetization can be visuallized as little vectors attached to each point in space. We know that at given temperature, the magnitude of the vector $\vec{M}$ is almost constant, $|\vec{M}| \approx M_0$, basically depending only on the material itself, but its direction changes in different parts of the material. We take the magnetization $\vec{M}$ as the order parameter that describes the state of the system. By the end of the 19th century, Pierre Curie studied the magnetic properties of matter for his PhD thesis and was able to explain succesfuly the paramagnetic transition. He showed that if a ferromagnetic material[2] is heated above certain critical temperture, so-called *Curie Point*, it looses its magnetic properties since the magnetization vector

[1] Isotropic-nematic phase transitions occurs when the systems is composed of non-spherical particles whose shape has some preferred direction.

[2] A ferromagnetic material is defined as being able to hold spontaneous magnetization.

$\vec{M}$ is no longer oriented in a particular direction, but it becomes isotropic. This transition has been extensively studied, it is known to be reversible. Whereby when we cooled down the material below T_c, it becomes a magnet by breaking the rotational symmetry.

This rather intuitive example of a phase transition and its order parameter might lead you to think that defining an order parameter is an easy task, but it is not. The choice of the order parameter is not always easy, because once you have figured out what is really going on in the phase transition, you have more chances of guessing the right order parameter. Moreover, there are several cases where there is more than one order parameter, such as the case of the gas-liquid transition on a binary fluid, or the case of Heisenberg antiferromagnet [49]. In general, there are more than one order parameter that couple with each other. In Sec. 2.5 we study in some detail the underlying standard theory of dynamical phase transitions where there is more than one order parameter involved.

2.2. Abrupt and continuous phase transitions

Having clarified what a phase transition is, we now may proceed to clasify them. In the previous section we discussed about the symmetries that some phases posses, and thus a straightforward way to clasify them is *structural* (with symmetry breaking), or *isostructural* (without symmetry breaking). On the other hand, we could also clasify them depending on whether they have an associated *latent heat*. The latent heat is simply the heat released or absorbed by a body when it undergoes a process without a change in temperature. In particular, this process could be a phase transition, and we can have a phase transition without latent heat ($l_Q = 0$), or a transition whit latent heat ($l_Q \neq 0$) where it is said to be *endothermic* or *exothermic* depending on the sign of l_Q[3]. From an experimental point of view, it is more convenient to use this classification given that in general it is far easier to measure l_Q than a change in symmetry. Now, lets remember the well-known Clausius-Clapeyron equation, which is widely used in thermodynamics,

$$\frac{dp\,(T)}{dT} = \frac{s_1 - s_2}{v_1 - v_2}, \tag{2.2.1}$$

where s_i and v_i are the entropy and volume per particle on each phase. We know also that for a reversible process $\delta Q = l_Q = T\Delta S$, thus, if $l_Q \neq 0 \Rightarrow s_1 \neq s_2$ which implies that the first derivatives of the Gibbs free energy are discontinuous ($S = -\partial G/\partial T$, $V = \partial G/\partial p$). Hence, this led Paul Ehrenfest to introduce a new clasification which is based on the continuity of the thermodynamic potential. According to Ehrenfest, a phase transition is said to be of order n, if the n-th derivative of the thermodynamic potential is the first quantity to present a discontinuity. Accordingly, if $l_Q \neq 0$ we have a *first-order phase transition,* whereas if $l_Q = 0$ it is at least a *second-order phase transition.* By definition a point in the (p, T) plane that corresponds to a phase transition in which $l_Q = 0$ is called *critical point.* An analogous thermodynamical definition is that it is an inflection point of an isotherm curve on a pV diagram.

[3] By convention $l_Q > 0$ if the system release energy into its sorroundings, and $l_Q < 0$ if it absorbes energy from its sorroundings.

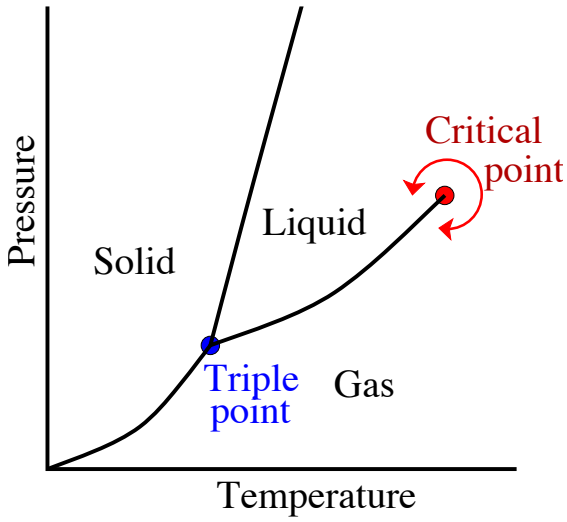

Figure 2.2.1.: Typical phase diagram showing the coexistence curves for the different phases, the triple point where the three phases coexist, and also the critical point that is the point beyond which it is not possible to distinguish the liquid and gaseous phases. As a simple comment we might say that the solid-liquid coexistence line has negative slope in the case of water, which is an anomalous case, and is responsible for the well-known fact that ice floats on liquid water, among many other phenomena

Thereby, given that the transition between solid and liquid corresponds to a symmetry breaking, the coexistence boundary cannot end. Nevertheless, there are systems where this is not true, such is the case of confined water nanofilms where the transition to a solid phase can be either of first or second order, depending on the filling density [50]. The reason for this, is the confinement of ths system. As we lower the spatial dimension of a system, the fluctuations increase in intensity becoming much more important, allowing to pass from one phase to another continuously above a critical point. However, as we saw earlier this is not the case for the liquid-gas boundary, and it is possible to go continuously from one phase to the other, as is depicted in Fig. 2.2.1. The fact that first order phase transitions have a discontinuity implicate that in general they show hysteresis and consequently are rate-dependent on the input, meaning in the particular case of the solid-liquid phase transition that the melting and freezing point *do not* agree, they just agree if the change of temperature is performed slow enough for the system to order itself and reach its equilibrium point. This will be clearer in the next section. Another important difference between first and second order phase transitions is that given that the later involves a critical point beyond which the two phases in consideration are basically the same, the fluctuations become increasingly important as the critical point is approached, thus implying that some physical quantities such as the susceptibility or the correlation length diverge at the critical point[4]. This remarkable fact is maybe what makes second-order phase transitions and critical phenomena so fascinating and have attracted so much attention in the last decades [2, 51, 52, 53, 8].

[4]Of course we do not mean a divergence in a sense strictly mathematical, but a physical divergence because of finite-size effects.

2.3. Equilibrium critical phenomena

2.3.1. van der Waals model

In order to deepen a little further into the features of phase transition and critical phenomena, lets take a look at the well-known model proposed by van der Waals to describe the behavior of fluid systems. Basically we can describe this model as an improvement of the *ideal gas law* by taking into account finite-size effects and the attraction among particles, but still in the dilute regime. Hence, the van der Waals state equation for gases is

$$\left(p + \frac{a}{V^2}\right)(V - b) = Nk_bT, \tag{2.3.1}$$

where the first term accounts for a reduction of the pressure due to the attractive part of the interaction potential, whereas the $(V - b)$ term comes from estimating the "free volume" available for the molecules by excluding a hard core contribution. The van der Waals potential that is used to derive this equation of state is

$$U(r) = \begin{cases} \infty & r \leq d \\ \sim -\left(\frac{\sigma}{r}\right)^6 & r \geq d, \end{cases} \tag{2.3.2}$$

where σ is the typical size of the molecules. Thus, $U(r)$ corresponds to a hard-core potential for distances smaller than d, and a decaying attractive potential for larger r.

Fig. 2.3.1 shows three diferent isotherms sketched in the pV space. As pointed out earlier, above the critical temperature T_c the liquid and vapor phases are undistinguishable, and the isotherms for $T \gg T_c$ approach the ideal gas law $pV = Nk_bT$, being independent of the microscopic interation parameters a and b. As we drop the temperature, the isotherms develop an inflection point that turns into a saddle point with horizontal tangent. When the system is below the critical temperature T_c, which is defined from the *spinodal curve*[5], the system is in the liquid state if we are at small volumes, or in gaseous state if we are at high volumes. In other words, the liquid phase is stable to the left of (A) whereas the vapor phase is stable to the right of (D). But, it can be shown that in the $(B - C)$ region the system is unstable, while the regions $(A - B)$ and $(C - D)$ are where the liquid and the gas are metastable phases. This can be derived from the stability criteria, that is, we can show that the condition $\left(\partial^2 U/\partial V^2 \geq 0\right)$ is equivalent to $(\partial P/\partial V)_T \leq 0$. Thus, in Fig. 2.3.1, zones of positive slope correspond to unstable regions. Clearly we do not observe the unstable solutions, and thus the physical solution below the spinodal curve is the horizontal dashed curve, which implies that the chemical potentials are the same in both phases, and so thermodynamical as well as mechanical equilibrium is satisfied[6]. Therefore this non-analyticity of the pressure $p(V)$

[5] A spinodal curve is defined such is the limit of stability of a solution, denoting the boundary of a region of instability in a phase diagram.

[6] It can be shown that this statement is equivalent to say that the two bounded areas formed by the isotherm and the horizontal dashed line are equal.

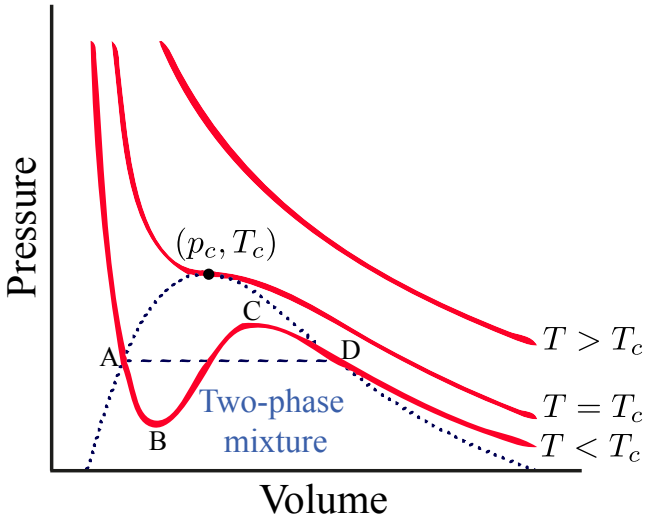

Figure 2.3.1.: The van der Waals isotherms sketched. The curve that has an inflection point is the critical isotherm, and thus below the spinodal curve (dashed line) the two phases coexist.

implies that as we increase the pressure at constant temperature, there is a *discontinuous jump* of the volume, or correspondingly, of the density; and hence the associated change in the entropy per particle s releases a latent heat $l_Q = T\,(s_g - s_l)$. Accordingly, for $T < T_c$, the van der Waals equation describes a *first order phase transition.* Notice now that the coexistence region does not extend beyont T_c, and from Fig. 2.3.1 it is clear that at precisely $T = T_c$ the discontinuous jump becomes zero, or in other words the latent heat at the critical point vanishes and the liquid-gas phase transition becomes a *second order phase transition.* Now, we proceed to study what actually occurs near T_c. From Fig. 2.3.1 it is easy to observe that we can define the critical point such that

$$p_c = p\,(p_c, V_c)\,, \qquad \left.\frac{\partial p}{\partial V}\right|_{T_c,V_c} = 0, \qquad \left.\frac{\partial^2 p}{\partial V^2}\right|_{T_c,V_c} = 0. \tag{2.3.3}$$

But this is equivalent to

$$\begin{aligned} p_c &= \frac{N k_b T_c}{V_c - b} - \frac{N^2 a}{V_c^2}, \\ \left.\frac{\partial p}{\partial V}\right|_{T_c,V_c} &= -\frac{N k_b T_c}{(V_c - b)^2} + \frac{2N^2 a}{V_c^2} = 0, \\ \left.\frac{\partial^2 p}{\partial V^2}\right|_{T_c,V_c} &= \frac{2N k_b T_c}{(V_c - b)^3} - \frac{6N^2 a}{V_c^4} = 0. \end{aligned} \tag{2.3.4}$$

By solving this three equations, we straightforwardly obtain (p_c, T_c, V_c):

$$p_c = \frac{a}{27b^2}, \qquad k_b T_c = \frac{8a}{27b}, \qquad V_c = \frac{b}{3}. \tag{2.3.5}$$

Fluid	T_c [K]	$p_c[atm]$	$\rho_c \left[g \cdot cm^{-3}\right]$
Water	647.5	218.5	0.325
Alcohol	516.6	63.1	0.28
Ether	476.0	35.5	0.26
Carbon dioxide	304.2	72.8	0.46
Oxygen	154.6	49.7	0.41

Table 2.1.: Critical point parameters for some fluids [54].

Now, by defining $p^* \equiv (p - p_c)/p_c$, $\epsilon \equiv (T - T_c)/T_c$, $\varphi \equiv (V - V_c)/V_c$, we can write the dimensionless form of the van der Waals equation, which turns out to be

$$1 + p^* = \frac{4(1+\epsilon)}{1 + 3\varphi/2} - \frac{3}{(1+\varphi)^2}. \tag{2.3.6}$$

From equation 2.3.6, we can conclude that this state equation is independent of the microscopic parameters a and b, and thus if we measure the pressure, volume and temperature in terms of their critical values respectively, then the equation of state is the same for all fluids. Accordingly, all the properties derived from this equation are universal. In other words, according to 2.3.6 *any* two fluids with the same p^*, ϵ, φ may be said to be in the *corresponding states*. Let us take a look at the relations of 2.3.5. It is straightforward to deduce

$$Z = \frac{p_c V_c}{k_b T_c} = \frac{3}{8} = 0.375. \tag{2.3.7}$$

For ideal fluids we have $Z = 1$. However, for real fluids the experimental value is $Z = 0.2 - 0.3$. Hence, we may say that even though van der Waals theory has achieved some improvements in the description of real fluids, it is a rather simplistic approach, and does not provide a final quantitative accurate result.

Returning to the calculations, from the cubic equation for φ in 2.3.6 it is possible to show that:

- if $\pi = 0$ and $\epsilon = 0$, we obtain $\varphi = 0$ as expected.
- if $\epsilon > 0$, there is just one real solution.
- if $\epsilon < 0$, there are three solutions, but only two of them are stable, as shown in Fig. 2.3.1.

From 2.3.6 we can derive some properties in the vicinity of the critical point by expandig the equation and retaining only the lowest-order nonvanishing terms, yielding

$$p^* \approx 4\epsilon - 6\epsilon\varphi + 9\epsilon\varphi^2 - \frac{3}{2}\varphi^3. \tag{2.3.8}$$

Hence, the cubic critical isotherm ($\epsilon = 0$) is readily obtained,

$$p^* \approx -\frac{3}{2}\varphi^3. \tag{2.3.9}$$

Accordingly, if we define the critical exponent δ through the relation $|p^*| = p_\pm |\varphi|^\delta$, δ turns out to be $\delta = 3$.

Besides, we can also compute the *vapor pressure curve*, because of the antisymmetry near V_c we may just set $\varphi = 0$ into (2.3.6), and obtain $p_0 = 4\epsilon$. This pressure sets the reference for determining the change in volume at the phase transition. The coexistence curve is defined as the projection onto the pV plane of the Fig. 2.3.1, thus $0 \approx -6\epsilon\varphi + 9\epsilon\varphi^2 - \frac{3}{2}\varphi^3$, implying

$$\varphi_g = -\varphi_l = \begin{cases} 0 & \epsilon \geq 0 \\ \approx (-4\epsilon)^{1/2} + \mathcal{O}(\epsilon) & \epsilon < 0 \end{cases} \tag{2.3.10}$$

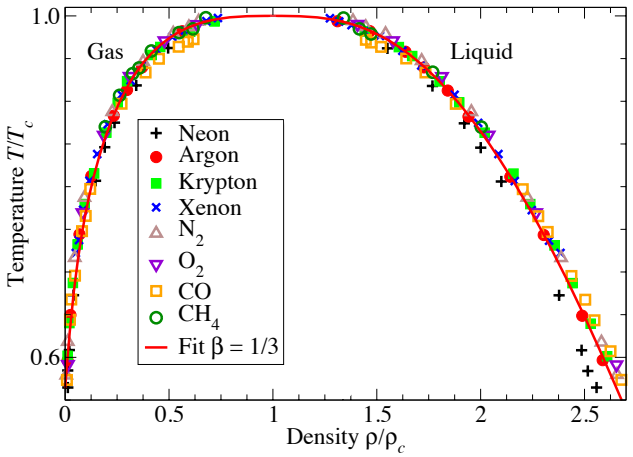

Figure 2.3.2.: Law of corresponding states. The liquid-gas coexistence lines near the critical point for a variety of atoms showing universality, but where the exponent is not the same as predicted by van der Waals. The curve is a fit to the argon data, $\rho/\rho_c = 1 + s(1 - T/T_c) \pm \rho_0 (1 - T/T_c)^\beta$, with $s = 0.75$, $\rho_0 = 1.75$, and $\beta = 1/3$ [54].

In Fig. 2.3.2 we observe the law of corresponding states for a variety of gases showing that they follow $\rho/\rho_c = 1 + s(1 - T/T_c) \pm \rho_0 (1 - T/T_c)^\beta$, with $s = 0.75$, $\rho_0 = 1.75$ and $\beta = 1/3$.

The difference $\varphi_g - \varphi_l = 2\varphi_g$ which is continuous at $\epsilon = 0$ may serve as a definition of the *order parameter* that describes this transition.[7] Experimental and numerical results do not agree with this result, but they show that $\Delta\varphi \sim (-\epsilon)^{\beta}$, with $\beta \simeq 0.35$, which differs from the value $\beta = 1/2$ predicted by the van der Waals theory. The reason of the disagreement is that the hard-core repulsion is just an approximation, and neither another functional form of the potential does give accurate results. The answer is given by the renormalization theory, which takes into account the effect of the fluctuations in the system [55]. In the same way, the isothermal compressibility turns out to be:

$$\chi_T = -\left(\frac{\partial\varphi}{\partial p}\right)_{\epsilon} \approx \frac{1}{6\epsilon + \frac{9}{2}\varphi^2} \approx \begin{cases} \frac{1}{6\epsilon} & \epsilon > 0 \\ \\ \frac{1}{12|\epsilon|} & \epsilon < 0. \end{cases} \tag{2.3.11}$$

Which means $\chi_T = \chi_{\pm}\left|\epsilon\right|^{-\gamma}$, where $\gamma = 1$, diverges on both sides of the critical point, but with different amplitudes $\chi_+/\chi_- = 2$. By using the thermodynamical relation

$$\chi = \frac{V\left(\Delta N\right)^2}{N k_b T}, \tag{2.3.12}$$

we can conclude that near the critical point there are large density fluctuations. These fluctuations cause strong light scattering in the system, a phenomenon known as *critical opalescence* (see [56, 51] and references therein). As a last result on this section, we calculate how the specific heat behaves. From thermodynamics we know that

$$C_V = T\frac{\partial S}{\partial T} = \frac{\partial F}{\partial T}, \tag{2.3.13}$$

but from the van der Waals equation of state, we can compute the Helmholtz free energy: $p = \frac{\partial F}{\partial V}$ implies that

$$F = \int p\mathrm{d}V \tag{2.3.14}$$

$$= \int \left(\frac{N k_b T}{V - b} - \frac{N^2 a}{V^2}\right)\mathrm{d}V \tag{2.3.15}$$

$$F = N k_b T \ln\left(V - b\right) + \frac{N^2 a}{V} + f\left(T\right), \tag{2.3.16}$$

hence, it is clear that in the van der Waals gas the specific heat is the same as in the ideal gas, since C_V just depends on the derivative of the constant of integration. So,

[7] Though in the literature you will find that is far more common to use the difference of densities instead of volumes as the order parameter, but it is basically the same.

$$C_V = C_V^{ideal} = \left(\frac{\partial U}{\partial T}\right)_V = \frac{3}{2} N k_b T, \tag{2.3.17}$$

whereby C_V does not diverge, and following the same idea as before, by writing $C_V = C_\pm \left|\epsilon\right|^{-\alpha}$ we have $\alpha = 0$.

As a summary, we may say that at the critical isotherm $T = T_c$ the system undergoes a second-order phase transition and where some physical quatities become non-analitic, in particular they diverge with some *critical exponents*. In the van der Waals model for this particular system we could find explicitly these exponents, which are $\alpha = 0$, $\beta = 1/3$, $\gamma = 1$ and $\delta = 3$. A summary of these results is shown in 2.3.2. In the next sections, we take a more phenomenological approach to determine relations between these exponents, but that gives us a more intuitive notion about critical phenomena.

2.3.2. Critical exponents

Until now we have not told the whole story. Actually, there are more than just the four exponents that we have just presented so far. Besides α, β, γ and δ, there are two others exponents associated to spatial correlations. We define the exponents ν and η related to the behavior of the pair correlation function and its structure factor. Since a more extensive discussion about $g(r)$ is presented in Sec. 2.4, here we only give a brief definition of the exponents themselves. The *correlation length* ξ is a measure of the range of the correlation function $g(r)$ *near the critical point.* In the vicinity of the critical point, the pair correlation function (in a 3D system) follows

$$g(r) \sim \frac{e^{-r/\xi}}{r}, \tag{2.3.18}$$

where the correlation length ξ diverges with exponent $\nu_\perp$,

$$\xi \sim \left|\epsilon\right|^{\nu_\perp}. \tag{2.3.19}$$

The van der Waals model predicts this exponent takes the value $\nu = 1/2$. In most cases, *at the critical point* ($T = T_c, p = p_c$), the pair correlation function decays with increasing distance r in a power-law form

$$g(r) \sim \frac{1}{r^{D-2+\eta}}, \tag{2.3.20}$$

thereby defining the *anomalous exponent* η (D is the dimensionality of the system).[8]

Everything we have done so far can be put into a more general context. In the particular case of the liquid-gas phase transition the order parameter that describes the transition may be defined as the difference of densities between both phases, $\psi = \rho_l - \rho_g$, which is zero above the critical point

[8] The reason for this name will be clear in Sec. 2.4.

Exponent	Definition	Description	Value
α	$C_V = \frac{\partial F}{\partial T} = C_{\pm} \left\vert\epsilon\right\vert^{-\alpha}$	Specific heat at constant volume $V = V_c$	0
β	$V_g - V_l \sim \left\vert\epsilon\right\vert^{\beta}$	Order parameter (shape of coexistence curve)	1/2
γ	$\chi_T = -\frac{1}{V}\left(\frac{\partial V}{\partial p}\right)_T \sim \left\vert\epsilon\right\vert^{-\gamma}$	Isothermal compressibility	1
δ	$\left\vert p - p_c\right\vert \sim \left\vert V - V_c\right\vert^{\delta}$	Critical isotherm	3
η	$g\left(r\right) \sim r^{-(D-2+\eta)}$	Correlation function (at $T = T_c$)	0
$\nu_{\perp}$	$g\left(r\right) \sim e^{-r/\xi}/r \rightarrow \xi \sim \left\vert\epsilon\right\vert^{\nu_{\perp}}$	Correlation length	1/2

Table 2.2.: Critical exponents of the liquid-gas transition according to the van der Waals theory

because we have just one phase; and takes a non-zero value below T_c. Accordingly, in order to extend the definitions of the critical exponents, lets think in a general order parameter ψ. Thus, instead of having the specific heat defined as $C_V = (\partial F/\partial T)$, but now where the Helmholtz free energy F is now a function of the order parameter ψ; analogously now we have $\psi \sim \left\vert\epsilon\right\vert^{\beta}$and consequently, we may do the same with the other definitions. This generalization is shown in Tab. 2.3.

Exponent	Definition
α	$\frac{\partial F[\psi]}{\partial \epsilon} \sim \left\vert\epsilon\right\vert^{-\alpha}$
β	$\psi \sim \left\vert\epsilon\right\vert^{\beta}$
γ	$S\left(0\right) \approx \langle \psi_k \psi_k^* \rangle \sim \left\vert\epsilon\right\vert^{-\gamma}$
δ	$\psi \sim h^{1/\delta}, \quad \text{at } \epsilon = 0$
η	$g\left(r\right) \approx \langle \psi\left(r\right) \psi\left(0\right) \rangle \sim r^{-(D-2+\eta)}$
$\nu_{\perp}$	$g\left(r\right) \sim e^{-r/\xi}/r \rightarrow \xi \sim \left\vert\epsilon\right\vert^{\nu_{\perp}}$

Table 2.3.: Extended definitions for the critical exponents. ψ is the order parameter, and h is an external field.

This generalization will be very useful later when dealing with more generic second order phase transitions, and when we compute and compare the critical exponents using different theories.

As a final remark, we should say that measuring critical exponents is an extremely difficult task

from an experimental point of view. One of the reasons is because in general the physical quantities that we can actually measure do not follow exactly a power-law, instead they follow

$$f(t) = A_0 |\epsilon|^{-\vartheta} \left(1 + A_1 |\epsilon|^{\theta} + \ldots\right) \qquad \theta > 0, \tag{2.3.21}$$

where ϑ may be $\{\alpha, \beta, \gamma, \delta, \eta, \nu_\perp\}$. Therefore, the critical exponent is defined as limiting power law

$$k \equiv \lim_{\epsilon \to 0} \frac{\log f(\epsilon)}{\log |\epsilon|}. \tag{2.3.22}$$

The corrections at the critical point vanish, but they may become important for $\epsilon > 0$. Hence if we want reliable values for the actual critical exponent, these corrections cannot be neglected. When measuring a critical exponent there are others difficulties arising. One is related to the finite-size of the experimental system. The fact that the system in question is not infinite yields a rounding of the divergence. In adition, normally there is a slightly varying background which has not singular behavior near T_c, thus a curve fitting is necessary in order to substract this effect. One last problem comes from the phenomenon *critical slowing down*, which means that as $T \to T_c$ the system takes longer and longer to equilibrate. As we saw, when the system approaches the critical point, the correlation length diverges, and so the fluctuating regions become bigger and bigger. Therefore the system takes longer to relax (correlation time diverges) implying that the experimentalist must wait for large times to be certain that equilibrium has been reached. A more extensive discussion about this last point will be given in Sec. 2.5 where we study the dynamics of phase transitions.

2.3.3. Universality and scaling

We have seen in the last two sections that there are several critical exponents, but not all of them are independent. For example, γ is always of order $2\nu_\perp$ and $\alpha + 2\beta + \gamma$ is of order 2. These relations are a result of scaling properties of correlations functions and thermodynamics quantities near the critical point and can be derived using a renormalization group. The renormalization group introduced by Kenneth Wilson in the 70s provided a method for calculating the exponents and established that in general they depend on the spatial dimension and the symmetry of the order parameter, but not on the details of the interaction. This was already pointed out for the case of the van der Waals model. Thus, we say there exist *Universality classes*, and all transitions in the same univerality class have the same critical exponents. An easy approach to derive the relations among the exponents is provided by the *scaling hypothesis*.

In order to make the derivations of the scaling hypothesis we focus for a while in the ferromagnetic transition, but the relations obtained will be completely general. The scaling hypothesis states that the Gibbs potential $G(\epsilon, h)$ is a generalized homogeneous function.[9] Thus, this is equivalent to the

[9] A homogeneous function is a function with multilpicative scaling behaviour, *i.e.* there exist exponents a and b, such that $f\left(\lambda^a x, \lambda^b y\right) = \lambda f(x, y)$ for any λ.

requirement that there exist two parameters y_ϵ and y_h, such that

$$f(\epsilon, h) = b^{-d} f\left(b^{y_\epsilon}\epsilon, b^{y_h} h\right) \tag{2.3.23}$$

for any value of the number b. This means that all the critical exponents can be expressed as a function of y_t and y_h, and that if two critical exponents are provided, all others can be determined.

As the the number b can take any value, let us take it to be $b = |\epsilon|^{-1/y_\epsilon}$. Then 2.3.23 takes the form,

$$\begin{aligned} f(\epsilon, h) &= |\epsilon|^{\frac{d}{y_\epsilon}} f\left(\pm 1, |\epsilon|^{-\frac{y_h}{y_\epsilon}} h\right) \\ &= |\epsilon|^{\frac{d}{y_\epsilon}} \phi\left(|\epsilon|^{-\frac{y_h}{y_\epsilon}} h\right), \end{aligned}$$

where we have defined $\phi_\pm(x) = f(\pm 1, x)$. Now lets take a look at the magnetization. From the Ising model we know that $M \sim \epsilon^\beta$, thus

$$M \equiv \frac{1}{k_B T} \left.\frac{\partial f}{\partial h}\right|_{h=0} \tag{2.3.24}$$

$$= \frac{1}{k_B T} |\epsilon|^{\frac{d-y_h}{y_\epsilon}} \phi'\left(|\epsilon|^{-\frac{y_h}{y_\epsilon}} h\right) \tag{2.3.25}$$

$$M \sim |\epsilon|^{\frac{d-y_h}{y_\epsilon}} \tag{2.3.26}$$

which implies

$$\beta = \frac{d - y_h}{y_\epsilon}. \tag{2.3.27}$$

On the other hand, M must be finite as $\epsilon \to 0$ and thus $\phi'(x) = x^{\frac{d}{y_h}-1}$, because then

$$M \sim |\epsilon|^{\frac{d-y_h}{y_\epsilon}} \frac{h^{\frac{d-y_h}{y_\epsilon}}}{|\epsilon|^{\frac{y_h(d-y_h)}{y_h y_\epsilon}}} \Longrightarrow M \sim h^{\frac{d-y_h}{y_\epsilon}}. \tag{2.3.28}$$

And using the fact that the critical isotherm is $M \sim h^{1/\delta}$, we obtain

$$\delta = \frac{y_h}{d - y_h}. \tag{2.3.29}$$

Looking at the specific heat (from the previous section we have $C_V \sim |\epsilon|^{-\alpha}$) we have

$$C_V \equiv \left.\frac{\partial^2 f}{\partial \epsilon^2}\right|_{h=0} \sim |\epsilon|^{\frac{d}{y_\epsilon}-2} \Longrightarrow \alpha = \frac{d}{y_\epsilon} - 2 \tag{2.3.30}$$

In the same way, by using the usual definition for the susceptibility and noting that $\chi \sim |\epsilon|^{-\gamma}$ near

the critical point we get

$$\chi = \frac{1}{k_B T} \left. \frac{\partial^2 f}{\partial h^2} \right|_{h=0} \sim |\epsilon|^{\frac{d-2y_h}{y_\epsilon}} \Longrightarrow \gamma = \frac{2y_h - d}{y_\epsilon}. \tag{2.3.31}$$

By following a straightforward renormalization procedure we can also obtain the normalized pair correlation function [55],

$$g(r) = b^{-2(d-y_h)} g\left(\frac{r}{b}, b^{y_\epsilon}\epsilon\right) \tag{2.3.32}$$

$$g(r) = |\epsilon|^{\frac{2(d-y_h)}{y_\epsilon}} \Phi\left(r/|\epsilon|^{-1/y_\epsilon}\right). \tag{2.3.33}$$

As we saw earlier $\xi \sim |\epsilon|^{-\nu_\perp}$, and finally we obtain

$$\nu_\perp = \frac{1}{y_\epsilon}. \tag{2.3.34}$$

And to obtain the last relation we impose $b = r$ and $\epsilon = 0$ in 2.3.32,

$$g(r) = r^{-2(d-y_h)} \sim r^{-(d-2-\eta)} \Longrightarrow \eta = d + 2 - 2y_\epsilon. \tag{2.3.35}$$

Summarizing we have obtained 6 equations for the exponents,

$$\begin{aligned} \alpha &= \frac{d}{y_\epsilon} - 2 \\ \beta &= \frac{d - y_h}{y_\epsilon} \\ \gamma &= \frac{d - 2y_h}{y_\epsilon} \\ \delta &= \frac{y_h}{d - y_h} \\ \nu_\perp &= 1/y_\epsilon \\ \eta &= d + 2 - 2y_\epsilon \end{aligned} \tag{2.3.36}$$

By solving this set of equations and canceling the terms y_ϵ and y_h, which do not have any physical relevance, we obtain 4 relations among the exponents that are shown in Tab. 2.4.

Relation	Law
$\alpha + 2\beta + \gamma = 2$	Rushbrooke's law
$\gamma = \beta(\delta - 1)$	Widom's law
$\gamma = \nu_\perp (2 - \eta)$	Fisher's law
$\nu_\perp d = 2 - \alpha$	Josephson's law

Table 2.4.: Summary of the scaling laws.

2.4. The pair distribution function and the Ornstein-Zernike theory

2.4.1. Pair distribution function

Let us first consider the density of a fluid confined in a volume V

$$n(\vec{r}) \equiv \sum_{i=1}^{N} \delta(\vec{r} - \vec{r}_i) \tag{2.4.1}$$

at the point $\vec{r}$ in the fluid, where $\vec{r}_i$ is the position of the i-th particle. We know that if the system is uniform, then $\langle n(\vec{r})\rangle = \left\langle \frac{N}{V} \right\rangle \equiv n$, where

$$\langle n(\vec{r})\rangle = \frac{1}{\mathcal{Z}} \sum_{N=0}^{\infty} \frac{1}{N! h^{3N}} \int \mathrm{d}^N \vec{r}\, \mathrm{d}^N \vec{p}\, n(\vec{r})\, e^{-\beta(U_N - \mu N)}, \tag{2.4.2}$$

and we use the notation $\mathrm{d}^N \vec{r} = \mathrm{d}\vec{r}_1 \mathrm{d}\vec{r}_2 \ldots \mathrm{d}\vec{r}_N$, and $\mathrm{d}^N \vec{p} = \mathrm{d}\vec{p}_1 \mathrm{d}\vec{p}_2 \ldots \mathrm{d}\vec{p}_N$. Besides, we use the grand canonical ensemble, which partition function is given by

$$\mathcal{Z} = \sum_{N=0}^{\infty} \frac{e^{\beta\mu N}}{N! h^{3N}} \int \mathrm{d}^N \vec{r}\, \mathrm{d}^N \vec{p}\, e^{-\beta U_N(\vec{r}_i, \vec{p}_i)}. \tag{2.4.3}$$

Now, lets take a look at the quantity defined by

$$\left\langle n(\vec{r})\, n\left(\vec{r}'\right)\right\rangle = \frac{1}{\mathcal{Z}} \sum_{N=0}^{\infty} \frac{1}{N! h^{3N}} \int \mathrm{d}^N \vec{r}\, \mathrm{d}^N \vec{p}\, n(\vec{r})\, n\left(\vec{r}'\right) e^{-\beta(U_N - \mu N)}, \tag{2.4.4}$$

whose properties gives us microscopic information of the system. Hence, we have that the quantity $\left\langle n\left(\vec{r}\right) n\left(\vec{r}^{\,\prime}\right)\right\rangle$ is proportional to the probability of finding a particle in $\vec{r}$ given that we know that there is a particle in $\vec{r}^{\,\prime}$.

By defining

$$g(\vec{r},\vec{r}^{\,\prime}) \equiv \frac{\left\langle n\left(\vec{r}\right) n(\vec{r}^{\,\prime})\right\rangle}{n^2}, \tag{2.4.5}$$

which measures the correlations of the fluctuations of the density, we have that if the system is *spatially uniform*, *i.e.* it is invariant under translations, then we can write $g(\vec{r},\vec{r}^{\,\prime}) = g(\vec{r}-\vec{r}^{\,\prime})$ and $\langle n\left(\vec{r}\right)\rangle = \langle n(\vec{r}^{\,\prime})\rangle$. Hence, the *radial distribution function* becomes

$$g\left(\vec{r}-\vec{r}^{\,\prime}\right) = \frac{\left\langle n\left(\vec{r}\right) n(\vec{r}^{\,\prime})\right\rangle}{n^2}. \tag{2.4.6}$$

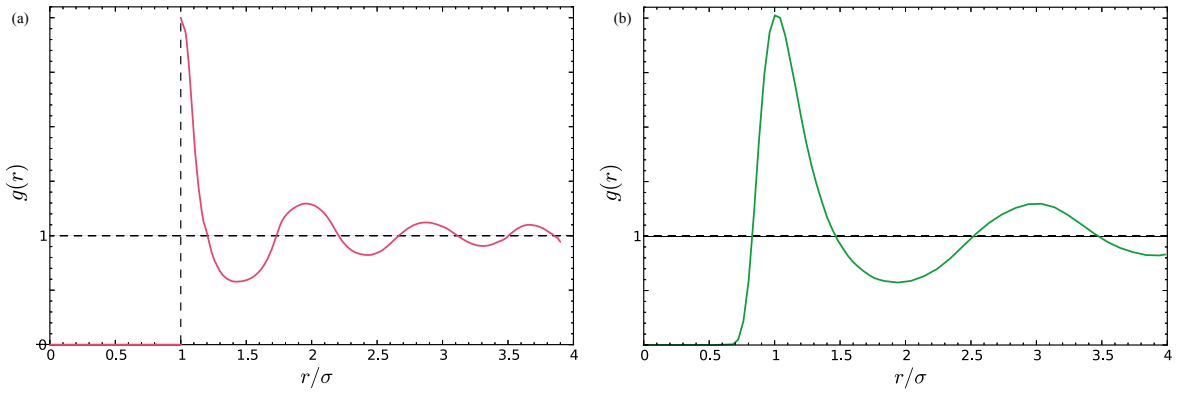

Figure 2.4.1.: (a) Sketch of the radial distribution function for the hard-core model of fluid. (b) Sketch of $g\left(r\right)$ for the Lennard-Jones model ($U\left(r\right) \sim ar^{-12} - br^{-6}$).

2.4.2. Compressibility and fluctuations

Lets take a look now at the fluctuations of the total number of particles N:

$$\begin{aligned} \left\langle \left(N - \langle N\rangle\right)^2 \right\rangle &= \left\langle N^2\right\rangle - \left\langle N\right\rangle^2 \\ &= \left(k_b T\right)^2 \left(\frac{\partial^2 \ln \mathcal{Z}}{\partial \mu^2}\right)_{T,V} \end{aligned} \tag{2.4.7}$$

and from thermodynamics we know that $\ln \mathcal{Z} = \frac{pV}{kT}$, and thus

$$\begin{aligned}\left\langle (N-\langle N\rangle)^2 \right\rangle &= (k_bT)^2 \left\{ \frac{\partial^2 (pV/kT)}{\partial \mu^2} \right\}_{T,V} \\ &= k_bTV \left(\frac{\partial^2 p}{\partial \mu^2} \right)_{T,V}.\end{aligned} \tag{2.4.8}$$

But,

$$\left(\frac{\partial p}{\partial \mu} \right)_{T,V} = \frac{\langle N\rangle}{V} = n, \tag{2.4.9}$$

then 2.4.8 becomes

$$\begin{aligned}\left\langle (N-\langle N\rangle)^2 \right\rangle &= k_bTV \left\{ \frac{\partial \left(\langle N\rangle / V \right)}{\partial \mu} \right\}_{T,V} \\ &= -\frac{\langle N\rangle k_bTV}{V^2} \left(\frac{\partial V}{\partial \mu} \right)_{T,N}.\end{aligned} \tag{2.4.10}$$

Where we have used

$$\left(\frac{\partial \omega}{\partial y} \right)_x = \left(\frac{\partial \omega}{\partial y} \right)_z + \left(\frac{\partial \omega}{\partial z} \right)_y \left(\frac{\partial z}{\partial y} \right)_x. \tag{2.4.11}$$

By defining the isothermal compressibility

$$\begin{aligned}\chi_T &\equiv -\frac{1}{V} \left(\frac{\partial V}{\partial p} \right)_{T,N} \\ &= -\frac{1}{\langle N\rangle} \left(\frac{\partial V}{\partial \mu} \right)_{T,N},\end{aligned} \tag{2.4.12}$$

then 2.4.10 becomes

$$\left\langle (N-\langle N\rangle)^2 \right\rangle = \langle N\rangle \, nk_bT\chi_T. \tag{2.4.13}$$

For an ideal gas, $\chi_T^0 = 1/nkT$, hence

$$\frac{\chi_T}{\chi_T^0} = \frac{\left\langle (N-\langle N\rangle)^2 \right\rangle}{\langle N\rangle}. \tag{2.4.14}$$

On the other hand, lets notice that

$$\begin{aligned}\left\langle (N-\langle N\rangle)^2 \right\rangle &= \left\langle \int \mathrm{d}\vec{r}\left\{ n\left(\vec{r}\right) - \left\langle n\left(\vec{r}\right)\right\rangle \right\} \int \mathrm{d}\vec{r}^{\,\prime}\left\{ n(\vec{r}^{\,\prime}) - \left\langle n(\vec{r}^{\,\prime})\right\rangle \right\} \right\rangle \\ &= \int \mathrm{d}\vec{r} \int \mathrm{d}\vec{r}^{\,\prime}\, g\left(\vec{r}-\vec{r}^{\,\prime}\right) \\ &= V \int \mathrm{d}\vec{r}^{\,\prime\prime}\, g\left(\vec{r}^{\,\prime\prime}\right)\end{aligned} \tag{2.4.15}$$

Finally, 2.4.14

$$\frac{\chi_T}{\chi_T^0} = \frac{1}{n}\int \mathrm{d}\vec{r}\, G\left(\vec{r}\right) \tag{2.4.16}$$

As is clearly visible in 2.4.16, a divergent behavior of χ_T near the critical point T_c corresponds mathematically to an increase in the range of the pair correlation function $g(\vec{r}-\vec{r}^{\,\prime})$. In the air, the correlation length near T_c becomes as large as the wavelength of light, and thus the density inhomogeneities scatter light strongly; this phenomenon is known as *critical opalescence* which was observed for the first time in 1869, but explained by A. Einstein in 1910 [57].

2.4.3. Ornstein-Zernike theory

Here we give a simple deduction of the Ornstein-Zernike relation, deduce first in 1914. In order to do so, we must make use of the pair correlacion function $g\left(\vec{r}\right)$ defined in the previous section. By inserting 2.4.1 into 2.4.6 we get

$$g\left(\vec{r}-\vec{r}^{\,\prime}\right) = \left\langle \sum_{i=1}^{N}\sum_{j=1}^{N} \delta\left(\vec{r}-\vec{r}_i\right)\delta\left(\vec{r}^{\,\prime}-\vec{r}_j\right)\right\rangle - n^2. \tag{2.4.17}$$

By spliting up $g\left(\vec{r}-\vec{r}^{\,\prime}\right)$ into a term cooresponding to the correlation of one particle with itself, and a second term corresponding to the correlation between different particles we have

$$g\left(\vec{r}-\vec{r}^{\,\prime}\right) \equiv n\delta\left(\vec{r}-\vec{r}^{\,\prime}\right) + n^2\Gamma\left(\vec{r}-\vec{r}^{\,\prime}\right). \tag{2.4.18}$$

We now introduce the *direct correlation function* $C\left(\vec{r}\right)$ through its Fourier transform $\hat{C}\left(\vec{q}\right)$, where

$$\hat{C}\left(\vec{q}\right) \equiv \int C\left(\vec{r}\right) e^{-i\vec{q}\cdot\vec{r}}\mathrm{d}\vec{r} \equiv \frac{\hat{\Gamma}\left(\vec{q}\right)}{1+n\hat{\Gamma}\left(\vec{q}\right)}, \tag{2.4.19}$$

and $\hat{\Gamma}\left(\vec{q}\right)$ is the Fourier transform of $\Gamma\left(\vec{r}\right)$. An important property is that with this definition of $\hat{C}\left(\vec{q}\right)$ does not depend strongly on temperature. At high temperatures, $\hat{\Gamma}\left(\vec{q}\right)$ is almost zero, then from 2.4.19 we get $\hat{C}\left(\vec{q}\right) \sim \hat{\Gamma}\left(\vec{q}\right)$. And near the critical point $(T \to T_c)$ we know from 2.4.18 that

$\hat{\Gamma}(\vec{q}=0)$ must diverge, then $\hat{\Gamma}(\vec{q}=0) \to \infty \Longrightarrow \hat{C}(\vec{q}=0) = \int C(\vec{r})\,\mathrm{d}\vec{r} \sim 1/n$. Accordingly, the function $C(\vec{r})$ must remain relatively short-ranged even near the critical point.

By Fourier transforming 2.4.19 we obtain:

$$\Gamma\left(\vec{r}-\vec{r}^{\,\prime}\right) = C\left(\vec{r}-\vec{r}^{\,\prime}\right) + n\int C\left(\vec{r}-\vec{r}^{\,\prime\prime}\right)\left(\vec{r}^{\,\prime\prime}-\vec{r}^{\,\prime}\right)\mathrm{d}\vec{r}^{\,\prime\prime}. \tag{2.4.20}$$

This last equation is often referred to as the *Ornstein-Zernike integral equation*, and it may well serve as a definition for $C(\vec{r})$.

If we define the *static strucure factor* $S(\vec{q})$ through the Fourier transform of $g(\vec{r})$,

$$S(\vec{q}) \equiv \int \mathrm{d}\vec{r}\, e^{-i\vec{q}\cdot\vec{r}} g(\vec{r}), \tag{2.4.21}$$

by using 2.4.18 and 2.4.21 it is straightforward to show that

$$S(\vec{q}) = n + n^2\hat{\Gamma}(\vec{q}). \tag{2.4.22}$$

Thus,

$$\frac{1}{n}S(\vec{q}) = 1 + n\hat{\Gamma}(\vec{q}) = \frac{1}{1-n\hat{C}(\vec{q})}. \tag{2.4.23}$$

By following the argument of Ornstein and Zernike, we assume that $\hat{C}(\vec{q})$ can be expanded around $\vec{q}=0$ for all temperatures right up to T_c. For an isotropic system

$$\hat{C}(q) = \hat{C}(0) + \sum_{l=0}^{\infty} \varepsilon_l(n,T)\, q^l, \tag{2.4.24}$$

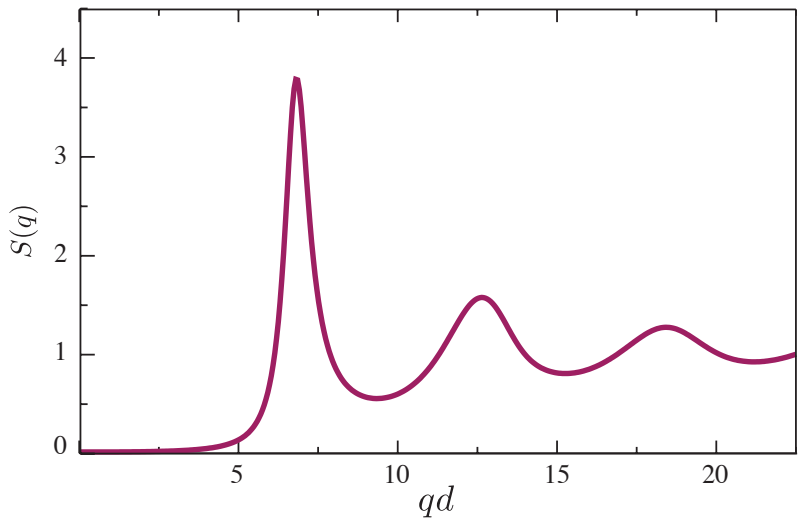

Figure 2.4.2.: Typical behavior of the static structure factor $S(q)$ in a Lennard-Jones fluid [58].

where the coefficients $\varepsilon_l(n,T)$ are given by the Maclaurin's expansion[10],

$$\varepsilon_l(n,T) = \frac{1}{l!}\left\{\frac{\partial^l \hat{C}(q)}{\partial q^l}\right\}_{q=0} \propto \frac{i^l}{l!}\int_{-1}^{1} u^l \mathrm{d}u \int_0^{\infty} r^{l+2} C(r)\,\mathrm{d}r. \tag{2.4.25}$$

Now we need to make one final assumption; even though we know from its definition that $C(r)$ must be integrable at $T = T_c$, there is no reason to think that all the coefficients $\varepsilon_l(n.T)$ must be finite. For now, we just assume it so. Accordingly, by truncating the series we have

$$\frac{n}{S(q)} = 1 - n\hat{C}(q) = n\left\{\hat{C}(0) + \varepsilon_2(n,T)\,q^2 + \mathcal{O}\left(q^4\right)\right\} \tag{2.4.26}$$

$$= \varepsilon_2(n,T)\left\{\frac{1 - n\hat{C}(0)}{\varepsilon_2(n,T)} - nq^2 + \mathcal{O}\left(q^4\right)\right\} \tag{2.4.27}$$

$$= R^2\left(\kappa_1^2 + q^2 + \mathcal{O}\left(q^4\right)\right), \tag{2.4.28}$$

where R^2 is proportional to the second moment of $C(r)$,

$$R^2 \equiv -n\varepsilon_2(n,T) \propto \int r^2 C(r)\,\mathrm{d}\vec{r}, \tag{2.4.29}$$

and κ is related to the zeroth moment,

$$\kappa_1^2 \equiv \frac{1 - C(0)}{R^2}. \tag{2.4.30}$$

Therefore we find that $S(q)$ at $\mathcal{O}\left(q^2\right)$ follows a Lorentzian,

$$\frac{S(q)}{n} = \frac{R^{-2}}{\kappa_1^2 + q^2}. \tag{2.4.31}$$

As a small remark, from 2.4.16 we have

$$\frac{\chi_T}{\chi_T^0} = \frac{1}{n}\int g(\vec{r})\,\mathrm{d}\vec{r} = \frac{1}{n}S(\vec{q}=0). \tag{2.4.32}$$

Hence we obtain the relation

$$S(q=0) = n^2 k_b T \chi_T. \tag{2.4.33}$$

[10] $\varepsilon_l(n,T)$ is zero for odds values of l, which is clear from the first integral in 2.4.25, that comes from an angular integration.

2.4.4. Failure of Ornstein-Zernike theory and Fisher's solution

By inverting 2.4.21 and using the d-dimensional Fourier transform we have

$$g(\vec{r}) = \int S(\vec{q})\, e^{-\vec{q}\cdot\vec{r}} \mathrm{d}\vec{q}, \tag{2.4.34}$$

where the element of volume is $\mathrm{d}\vec{q} = q^{d-1}\mathrm{d}q(\sin\theta_1)^{d-2}\,\mathrm{d}\theta_1\mathrm{d}\Omega_{d-1}$, $q = |\vec{q}|$ and $\mathrm{d}\Omega_{d-1}$ is the solid angle in $d-1$ dimensions. Hence, for an isotropic system 2.4.34 becomes

$$g(r) = \int S(q) \left\{ \int_0^\pi e^{iqr\cos\theta} (\sin\theta_1)^{d-2}\, \mathrm{d}\theta_1 \right\} \mathrm{d}\Omega_{d-1} q^{d-1}\mathrm{d}q \tag{2.4.35}$$

$$g(r) \propto \int_0^\pi S(q) \frac{J_{d/2-1}(qr)}{(qr)^{d/2-1}} q^{d-1}\mathrm{d}q. \tag{2.4.36}$$

Where we have used the Bessel function of the first kind $J_l(x)$[11]. It was Fisher in 1962 who made a detailed analysis of this last expression, obtaining:

- Fixed $T > T_c$, but let $r \to \infty$,

$$g(r) \propto \frac{e^{-\kappa r}}{r^{(d-1)/2}} \left(1 + \mathcal{O}\left(\frac{d-3}{\kappa r}\right)\right). \tag{2.4.37}$$

- Fixed r, but let $T \to T_c^+$,

$$g(r) \propto \begin{cases} (\ln r)\, e^{-\kappa r} \left(1 + \mathcal{O}\left(\frac{1}{\ln \kappa r}\right)\right) & d = 2 \\ \frac{e^{-\kappa r}}{r} & d = 3 \\ \frac{e^{-\kappa r}}{r^{d-2}} \left(1 + \mathcal{O}(\kappa r)\right) & d > 3 \end{cases} \tag{2.4.38}$$

We see that for $d = 3$ the higher order terms vanish identically in 2.4.37. Hence both cases presented give the same answer, $g(r) \propto e^{-\kappa r}/r$.

Accordingly, from 2.4.38 for $r \to \infty$ we have

$$g(r)\Big|_{T\to T_c^+} \propto \begin{cases} \ln r & d = 2 \\ \frac{1}{r^{d-2}} & d \geq 3. \end{cases} \tag{2.4.39}$$

Therefore, the Ornstein-Zernike theory predicts that in $d = 2$ the correlation increases with distance, which is clearly a non-physical result. In order to settle this issue, Fisher came up with the solution

[11] It is possible to define this function by means of a Taylor expansion: $J_\alpha(x) = \sum_{m=0}^{\infty} \frac{(-1)^m}{m!\Gamma(m+\alpha+1)} \left(\frac{x}{2}\right)^{2m+\alpha}$.

by assuming that in the hydrodynamic regime ($d/\xi \lesssim kd \ll 1$) $S(q)$ behaves as

$$S(q)\Big|_{T\to T_c^+} \propto q^{\eta-2}. \tag{2.4.40}$$

Thus introducing this new exponent η, which is known by the name *anomalous exponent.* Consequently, by inverting 2.4.40 we obtain for large r,

$$g(r)\Big|_{T\to T_c^+} \propto r^{-(d-2+\eta)}. \tag{2.4.41}$$

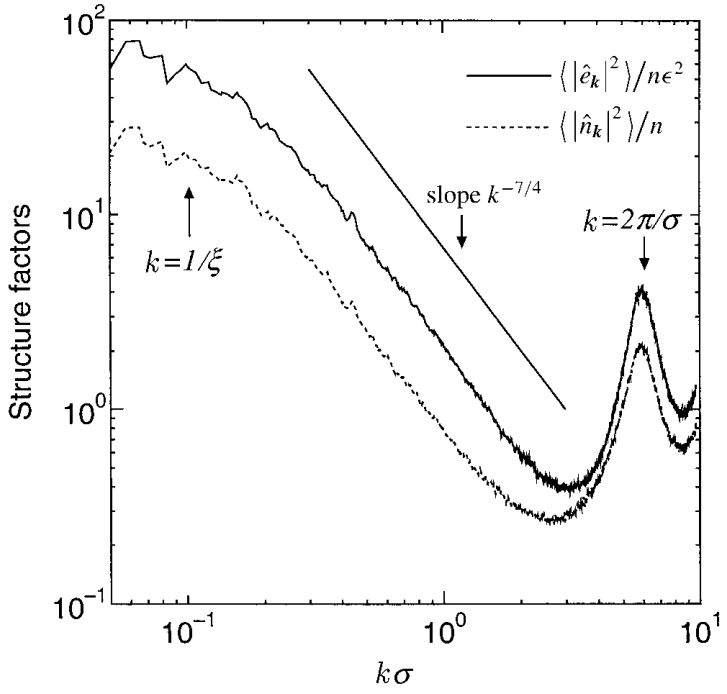

Figure 2.4.3.: Anomalous exponent. The structure factors of the density and energy fluctuations as a function of kd for a 2D Lenard-Jones fluid close to the gas–liquid critical point. The long-wavelength parts ($kd \leq 1$) represent the critical fluctuations. A line with a slope of $\eta - 2 = -7/4$ is included as a guide [56].

2.5. Phase transition dynamics

As explained earlier in this chapter, we know there are 6 critical exponents: α, β, γ, δ, η and $\nu_\perp$, which definition is given in Tab. 2.3. Nevertheless, not all of these exponents are independent of each other, but there are some simple relations among them (see Tab. 2.4). Therefore, as pointed out earlier, there exist only 2 independent exponents. A fundamental property of the second-order phase transitions is their so called *universality* (see Sec. 2.3.3); *i.e.* the fact that systems very different from each other may share the same set of critical exponents. This indicates that the critical behavior does

not depend on microscopic details of the intreactions involved, but only on some general features of the degrees of freedom, such as the symmetry of the order parameter, the dimensionality, and whether it is a conserved quantity or not. Therefore, we can assign all system to *classes,* each with its own set of exponents.

It was in the early 70s that Hohenberg and Halperin first introduced the *theory of dynamical critical phenomena* to study relaxation in equilibrium states [49, 59]. In order to describe the dynamical properties of a system near its critical point, some aditional exponents had to be introduced. For example, the critical characteristic time of the order parameter ψ is related to the correlation length by means of the *dynamical critical exponent* z,

$$\tau \sim \xi^z, \tag{2.5.1}$$

that is, by defining the exponent $\nu_\parallel$ through the relation $\tau \propto \varepsilon^{-\nu_\parallel}$, then an equivalent definition of z is

$$z \equiv \frac{\nu_\parallel}{\nu_\perp}. \tag{2.5.2}$$

For several years it was believed that there were only 3 independent exponents (2 static exponents), but this was proven wrong. Actually, recent developments have introduced 3 new dynamical exponents (see [60] and references therein), but its study is beyond the scope of this thesis, and we'll just focus on z. In the next section we give a brief and summarized review of some of the features of the dynamical theory of phase transitions.

2.5.1. Ginzburg-Landau free energy

First, we start our analysis by assuming that the phase transition is described by an n-component real order parameter $\psi_\alpha(\vec{x}, t)$. It is also assumed that the variations of $\psi_\alpha(\vec{x}, t)$ have wave-vectors smaller than a specified cutoff Λ. The free energy is given by

$$\mathcal{H}/T = \int \left[\frac{1}{2} r_0 \psi^2(x) + \frac{1}{2} |\nabla\psi|^2 + \frac{u_0}{4!}\psi^4(x)\right] \mathrm{d}^d r + \frac{F_0(T)}{T}, \tag{2.5.3}$$

where

$$\psi^2 \equiv \sum_{\alpha=1}^{n} \psi_\alpha^2, \qquad |\nabla\psi|^2 = \sum_{\alpha=1}^{n} |\nabla\psi_\alpha|^2, \tag{2.5.4}$$

and r_0, u_0 and F_0 are regular functions of the temperature T. The time-dependent Ginzburg-Landau model is chosen in such a way that, in abscence of noise, the system relaxes towards a minimum of energy; in other words the system reaches the equilibrium probability function

$$P[\psi] = \frac{1}{\mathcal{Z}} \exp\left(-\mathcal{H}[\psi]/T\right), \tag{2.5.5}$$

where

$$\mathcal{Z} = \int \mathrm{d}\{\psi\} \exp\left(-\mathcal{H}[\psi]/T\right), \tag{2.5.6}$$

is the partition function. Accordingly, this leads to the Markovian equations of motion

$$\frac{\partial \psi_\alpha}{\partial t}(x,t) = -\frac{\Gamma}{T}\frac{\delta \mathcal{H}}{\delta \psi_\alpha(x,t)} + \Gamma h_\alpha(x,t) + \zeta_\alpha(x,t), \tag{2.5.7}$$

where $h_\alpha(x,t)$ is an arbitrary external field, and $\zeta_\alpha(x,t)$ is a Gaussian white noise with correlations

$$\begin{aligned} \langle \zeta_\alpha \rangle &= 0 \\ \langle \zeta_\alpha(x,t)\zeta_{\alpha'}(x',t') \rangle &= 2\Gamma\delta(x-x')\delta(t-t')\delta_{\alpha\alpha'}. \end{aligned} \tag{2.5.8}$$

The first term in 2.5.7 causes ψ_α to relax towards equilibrium, whereas the noise ζ_α ensures the fluctuation-dissipation theorem is satisfied [49].

The properties of this model at low frequencies depend crucially on the function Γ.

- *Case* A: Non-conserved order parameter
  By doing $\Gamma = -\lambda_0\nabla^2$, then $\int \psi(x,t)\mathrm{d}^d x$ is independent of time, and hence ψ is a conserved quantity. Moreover, any perturbation of ψ will relax very slowly if the wavelength of the disturbance is large.

- *Case* B: Conserved order parameter
  If Γ is constant λ_0, then the temporal derivative of $\int \psi(x,t)\mathrm{d}^d x$ is in general finite, thus at any $T > T_c$, a fluctuation of ψ relaxes to zero at a finite rate.

Now, it is clear to see that after applying the equation of motion 2.5.7, in both cases A and B, the energy dentity ϵ_ψ *is not* conserved[12]. One way to satisfy energy conservation is achieved by introducing the energy as a separate field $\epsilon(x)$ coupled to the order parameter ψ. In the literarure this is known as the *C-model* and will be explained later [49, 60, 61, 62].

In order to study how the model behaves, lets consider the simplest case (Gaussian model) $u_0 = 0$ and $h_\alpha(x,t) = 0$. From 2.5.7 we can write the equations of motion in Fourier space:

$$\frac{\partial \Psi_k}{\partial t} = -\Gamma_k(k^2 + r_0)\Psi_k + \zeta_k, \tag{2.5.9}$$

where

$$\langle \zeta_k(t)\zeta_{k'}{}^*(t') \rangle = 2\Gamma_k\delta(k-k')\delta(t-t'). \tag{2.5.10}$$

By taking the average of 2.5.9 we get

$$\frac{\partial \langle \Psi_k \rangle}{\partial t} = -\Gamma_k(k^2 + r_0)\langle \Psi_k \rangle. \tag{2.5.11}$$

Now, two possibilities arise:

[12] It is straightforward to show that the energy density has the form $\epsilon_\psi(x) = c_1(T) - \frac{1}{2}r_0^{(1)}\psi^2(x)$, where $r_0^{(1)}$ is a constant and c_1 is defined by $c_1 \equiv -T^2(F_0/T)'$.

- *A-model* (non-conserved order parameter)
  In this case we have $\Gamma_k = \lambda_0$, and thus is clear to see from 2.5.11 that the characteristic decay time for the mode k is given by

$$\tau_k \sim \frac{1}{\lambda_0 \left(k^2 + r_0\right)}. \tag{2.5.12}$$

  Hence, in the hydrodynamic limit ($k \sim \xi^{-1}$), $\tau_k \sim \xi^2$. Therefore, the dynamical exponent in the *A-model* is $z = 2$.

- *B-model* (conserved order parameter)
  Here $\Gamma_k = \lambda_0 k^2$, and we obtain for this case,

$$\tau_k \sim \frac{1}{\lambda_0 k^2 \left(k^2 + r_0\right)}. \tag{2.5.13}$$

  Accordingly, in the hydrodynamic limit $\tau_k \sim \xi^4$, and thus $z = 4$.

As stated above, the simplest model that takes into account conserved densities is the *C-model*, which comprises a static coupling between a non-conserved order parameter ψ_n and a scalar conserved density m. In the abscene of any mode coupling the dynamics of m is purely diffusive, whereas the dynamics of the order parameter is purely relaxational. Thence, the dynamical equations are

$$\frac{\partial \vec{\psi}}{\partial t}(x,t) = -\Gamma \frac{\delta \mathcal{H}}{\delta \vec{\psi}(x,t)} + \eta_\psi(x,t), \tag{2.5.14}$$

$$\frac{\partial m}{\partial t}(x,t) = -\lambda \nabla^2 \frac{\delta \mathcal{H}}{\delta m(x,t)} + \eta_m(x,t), \tag{2.5.15}$$

where,

$$\left\langle \eta_{\psi_i}(x,t)\eta_{\psi_j}(x',t')\right\rangle = 2\Gamma\delta(x-x')\delta(t-t')\delta_{ij}, \tag{2.5.16}$$

$$\left\langle \eta_m(x,t)\eta_{m'}(x',t')\right\rangle = -2\lambda\nabla^2\delta(x-x')\delta(t-t'). \tag{2.5.17}$$

Here Γ, known as the *kinetic exponent*, and λ known as the *Onsager exponent*, are the relaxation rate and the difussive constant of ψ and m respectively. In this model, the free energy is given by

$$\mathcal{H} = \int \left\{ \frac{1}{2}\bar{r}_0\psi^2 + \frac{1}{2}\left|\nabla\psi\right|^2 + \frac{\bar{u}_0}{4!}\psi^4(x) + \frac{1}{2}a_m m^2 + \frac{1}{2}\gamma m\psi^2 - h_m m \right\} \mathrm{d}^d r. \tag{2.5.18}$$

With this, the partition function is

$$\mathcal{Z} = \int \mathrm{d}\{\psi\}\mathrm{d}\{m\} \exp\left(-\mathcal{H}[\psi,m]/T\right). \tag{2.5.19}$$

Like in the previous models, $\mathcal{Z}$ is the functional integral of all ψ_n and m whose variations have wavenumbers smaller than some cutoff values Λ and Λ_m respectively. Given that the energy density itself m represents a noncritical variable entering the Hamiltonian only quadratically, it can be integrated out exactly in the partition function 2.5.19. Thus, $\int \mathcal{H}[\psi,m]d\{m\} \to \mathcal{H}[\psi]$, and defining

the function $f(\psi) = \frac{1}{2}\bar{r}_0\psi^2 + \frac{1}{2}|\nabla\psi|^2 + \frac{\bar{u}_0}{4!}\psi^4$ we obtain

$$\begin{aligned}
\mathcal{H}[\psi] &= \int \left[f(\psi) + \frac{1}{2}a_m m^2 + \frac{1}{2}\gamma m\psi^2 - h_m m \right] \mathrm{d}^d r \mathrm{d}m && (2.5.20)\\
&= \int \left[f(\psi) + \frac{a_m}{2}\left(m^2 + 2m\left(\frac{\gamma}{2a_m}\psi^2 - \frac{h_m}{a_m} \right) \right) \right] \mathrm{d}^d r \mathrm{d}m && (2.5.21)\\
&= \int \left[f(\psi) + \frac{a_m}{2}\left(\left(m + \left(\frac{\gamma}{2a_m}\psi^2 - \frac{h_m}{a_m} \right) \right)^2 - \frac{\gamma^2}{4a_m^2}\psi^4 \right.\right. && (2.5.22)\\
&\qquad \left.\left. + \frac{\gamma h_m}{a_m^2}\psi^2 - \frac{h_m^2}{a_m^2} \right) \right] \mathrm{d}^d r \mathrm{d}m \\
&= \int \left[f(\psi) + \frac{\gamma h_m}{2a_m}\psi^2 - \frac{\gamma^2}{8a_m}\psi^4 \right] \mathrm{d}^d r && (2.5.23)\\
\mathcal{H}[\psi] &= \int \left[\frac{1}{2}\left(\bar{r}_0 + \frac{\gamma h_m}{a_m} \right)\psi^2 + \frac{1}{2}|\nabla\psi|^2 + \frac{1}{4!}\left(\bar{u}_0 - \frac{3\gamma^2}{a_m} \right)\psi^4 \right] \mathrm{d}^d r. && (2.5.24)
\end{aligned}$$

Hence, by defining r_0 and u_0 in such a way that

$$\begin{aligned}
r_0 &\equiv \bar{r}_0 + \frac{\gamma h_m}{a_m}, \\
u_0 &\equiv \bar{u}_0 - \frac{3\gamma^2}{a_m}.
\end{aligned} \qquad (2.5.25)$$

Therefore, this choice of parameters merely shifts the coupling between the fields but implies that all the static properties derived from 2.5.18 are equivalent to the corresponding static properties of a system with just one order parameter ψ_n. Nevertheless, this coupling may modify the dynamical critical behavior. By using techniques of renormalization theory it is possible the conclude that there exist two different regimes for this *C-model* [59, 61, 63, 64]. If we have a one-component order paramter ($n = 1$), one finds what is called "strong scaling", *i.e.*

$$z_\psi = z_m = 2 + \frac{\alpha}{\nu_\perp}, \qquad (2.5.26)$$

where α is the exponent related to the specific heat, and $\nu_\perp$ is the critical exponent of the correlation length ξ. The second regime corresponds to the n-component order parameter ($n \geq 2$), in which the Langevin equations for ψ_n and m are effectively decoupled, leading to a purely diffusive behavior for the conserved field m ($z_m = 2$), whereas the order parameter is described by the *A-model* with a dynamical exponent given by

$$z_\psi = 2 + c\eta, \qquad (2.5.27)$$

where η is the anomalous exponent already defined and c is a constant defined by $c = 6\ln(4/3) - 1 + \mathcal{O}(\epsilon = 4 - d)$ [61, 62].

Part II.

Experimental methods

3. Physical setup

« No amount of experimentation can ever prove me right; a single experiment can prove me wrong. »

Albert Einstein

In this chapter we describe the main features of the experimental setup. In Sec. 3.1 we give details of the basic setup used in the first part of the research, whereas in Sec. 3.2 we deal with a more advanced setup that tried to solve some of the problems that the first one possesed. Both experimental setups share many features and turned out to give very reliable results. Actually, the main difference have to do with the way the experimentalist has to perform the levelling of the cell, and accordingly with the how long the cell stays leveled. Also, some issues concerning the ITO layer of the glass plates are discussed, along with reproducibility issues that the system presents under some circumstances.

3.1. Basic setup

In this research we used two different configurations that in the end turned out to be fundamental for our results. The granular system is composed of $N \sim 10^4$ stainless steel spherical particles of mass $m = 4.45 \cdot 10^{-3}$ g. In order to study the different possible transitions, first- or second-order type, two configurations are used: $L_z = 1.83d \pm 0.02d$ and $N = 9878$, or $L_z = 1.94d \pm 0.02d$ and $N = 11504$. We call these 2 configurations (C1) and (C2) respectively. The quasi-two-dimensional box has lateral dimensions $L_x = L_y \equiv L = 100d$, with $d = 1$ mm. The box consists of two 10 mm thick ITO coated glass plates to dissipate electrostatic charges, separated by a square frame. For configuration 1 (C1), L_z is fixed by using a steel frame; for configuration 2 (C2), a thin mylar sheet frame is added. The box is fixed to a base by four posts placed at each corner of the cell. The base supports an array of high intensity light emitting diodes. An accelerometer, fixed to the base, allows the measurement of the imposed forcing amplitude. The main advantage of this setup is that particles are illuminated from below. They are then visualized as dark circles on a white background. This allows to detect particles in dense clusters, even when particles are partially mounted on top of each other.

The whole setup is forced sinusoidally with an electro-mechanical shaker, with displacement $z(t) = A\sin(\omega t)$. Top view images are obtained with a high-speed camera (MotionPro X3) at 10 or 500

fps, depending on the particular quantity we wish to measure. For static quantities we measure at 10 fps given that we want uncorrelated data to take averages, however we acquired the images at 500 fps when we need to track some quantities in time. The images acquired have a typical resolution of $1020 \times 1020\,\mathrm{pix}^2$, thus we obtain particles of 10 pix diameter approximately. Particle positions are determined at subpixel accuracy using an algorithm implemented on *C++ & CUDA*, and will be explained in Chapter 4. Results have been obtained by fixing the particle number N, cell height L_z, and driving frequency $f = \omega/2\pi = 1/T = 80$ Hz. The dimensionless acceleration $\Gamma = A\omega^2/g$ is varied in the range 1–6.

The sinusoidal signal used to induce the motion of the electromechanical shaker was generated by a waveform generator (Agilent 3322A). This devise provides a signal with a maximum aplitude of 10 V. The current is measured by means of an ammeter connected in series to the system. Thus, we control the maximum current the shaker can bear, which is approximately 10 A. The signal is then sent to a sound amplifier (SKPRO MaxG-1000) which supplies the necessary power for the proper functioning of the shaker.

The acceleration is measured by means of a piezoelectric accelerometer (B&K 4393) attached at the bottom of the cell, which sends the acceleration signal to a charge amplifier (B&K 2635), which in turn sends the amplified signal to a lock-in amplifier (Standford Research SR830). By using a GPIB (General Purpose Interface Bus), the lock-in amplifier is connected to a computer that saves the acceleration data and where they are analyzed using the sofware LabView. This sofware computes the value of the acceleration $\langle\Gamma\rangle$ with the corresponding standard deviation, which is about 0.02% of $\langle\Gamma\rangle$. A diagram of the setup is shown in Fig. 3.1.1.

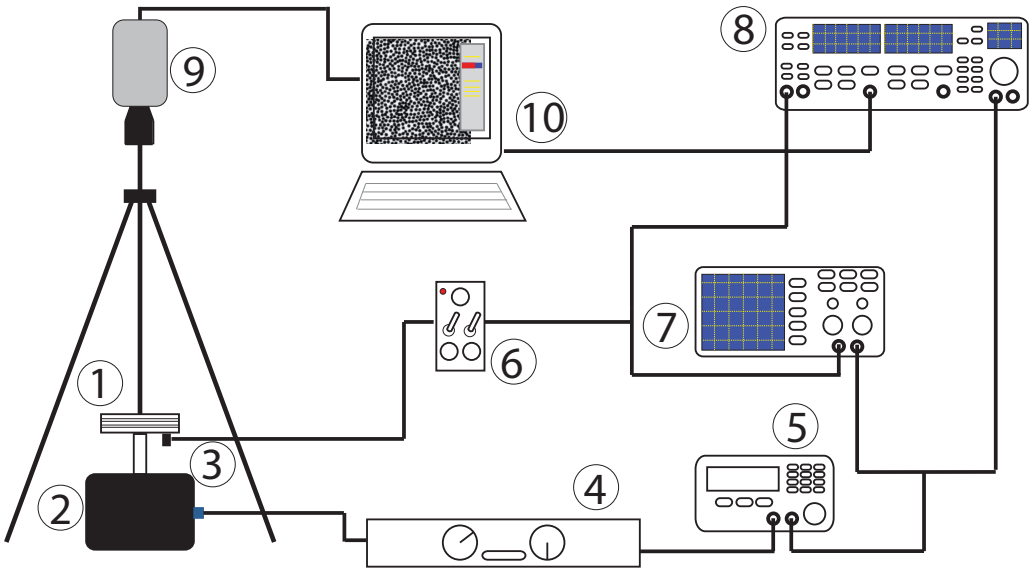

Figure 3.1.1.: Diagram of the experimental setup. (1) Cell; (2) Electromechanical shaker; (3) Acceleremeter; (4) Amplifier; (5) Wave generator; (6) Charge amplifier; (7) Osciloscope; (8) Lock-in amplifier; (9) High-speed camera; (10) Computer.

The surface coverage is defined by the filling fraction $\phi = N\pi d^2/4L^2$. For the two different configu-

rations, $\phi_{C1} = 0.776$ and $\phi_{C2} = 0.904$. In addition to ϕ, a different surface coverage parameter that is usually used in this system is $\rho = N/N_{max}$, where $N_{max} = 2L^2/\left(\sqrt{3}d^2\right) = 11547$ is the maximum number of particles that fit in a single hexagonally close-packed layer at rest on the bottom plate. A sketch of the configuration which defines N_{max} is presented in Fig. 3.1.2.

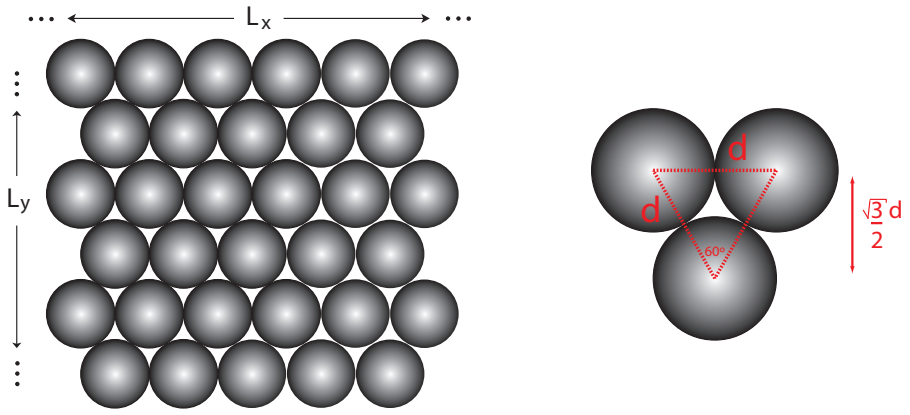

Figure 3.1.2.: Scheme of the hexagonal monolayer that defines the maximum filling density $\rho = 1$.

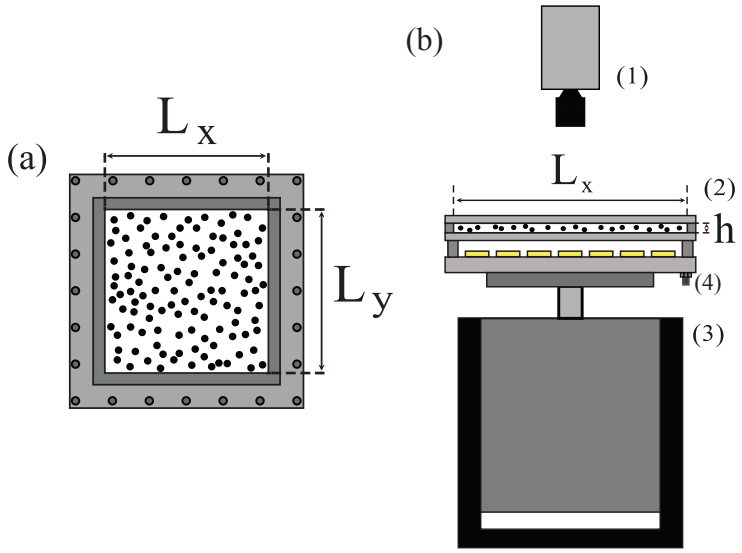

Figure 3.1.3.: Basic experimental setup. (a) Top view of the system. (b) Side view. (1) high-speed camera, (2) cell, (3) shaker, (4) accelerometer.

Because $\phi = \pi\rho/\left(2\sqrt{3}\right)$, then a single hexagonal close-packed layer corresponds to $\phi \approx 0.907$. Thus, for the two configurations, $\rho = 0.856$ and $\rho = 0.997$ respectively. It should be noticed that the system is not strictly 2D. At the high accelerations explored, particles do overlap partially, so care

must be taken when comparing our filling fractions with those used in real 2D systems. Another possible relevant parameter is the volume filling fraction $\phi_{3D} = N4\pi r^3/\left(3L^2L_z\right) = \phi 2d/\left(3L_z\right)$. For the two configurations, $\phi_{3D} = 0.283$ and $\phi_{3D} = 0.311$ respectively, indicating that the system is far from the jamming regime. A sketch of the experimental setup is shown in Fig. 3.1.3.

An important issue is the homogeneity of L_z through the experimental cell. This height is measured at a given horizontal position with an optical microscope with the following procedure: (i) both interior surfaces of each glass plate are marked with a permanent thin pen with short lines, perpendicular between them (forming a cross when projected); (ii) one surface is focused on the microscope; (iii) the microscope stage is moved vertically until the other surface is focused; (iv) the distance L_z is computed by counting the number of marks on the stage's vertical control knob (100 μm per turn, 1 μm per division). Following this procedure, L_z was measured at nine horizontal positions, placed in a regular grid, three times for each position. Within experimental errors the glass plates are indeed parallel, where for C1 the height turns out to be $L_z = 1.83d \pm 0.02d$, whereas for C2 is $L_z = 1.94d \pm 0.02d$. The error bars reported before correspond to the standard deviation of all 27 measurements for each configuration. The measurements for configuration C1 are shown in Tab. 3.1.

	A	B	C	D	E	F	G	H	I
first measurement	1.84	1.89	1.80	1.82	1.80	1.77	1.80	1.81	1.84
second measurement	1.83	1.83	1.85	1.83	1.87	1.77	1.82	1.88	1.87
third measurement	1.85	1.85	1.86	1.81	1.82	1.81	1.81	1.82	1.90

Table 3.1.: Measurements of the height L_z (in mm) of the cell in 9 different points for configuration C1. The position of the points were the measurements were performed is shown in Fig. 3.1.4.

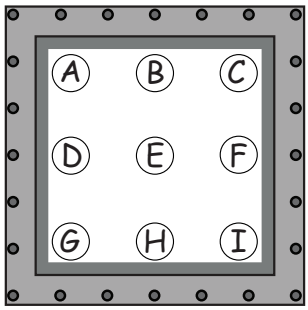

Figure 3.1.4.: Scheme depicting where the 9 measurements of the height's cell were made. The points in the borders are placed approximately at 1.5 cm from the edges.

A second and very important experimental consideration is to minimize electrostatic effects. We have used two sets of ITO (indium tin oxide) coated glass plates. One set of resistivity 7.5 $\mu\Omega$m and thickness 25 nm (Diamond Coatings Limited), whereas the second set 750 nm thickness, same

resistivity. This ITO coating works very well for many hours of experimental runs. Eventually, it does however get damaged by particle collisions. All data presented in this thesis correspond to reproducible runs where no important damage was noticeable in the ITO coating. In fact, a surface damaged ITO coating is manifested in important changes of the measured quantities with respect to those obtained for a new pair of ITO coated glass plates. We conjecture that damage occurs because of erosion of the ITO coating, which in turn affects particle interactions by an increase of electrostatic forces and contamination of the system by dust formed from the ITO coating. In order to characterize the damage due to the particle colisions, some surface images were obtained with an atomic force microscope (AFM). We believe it was because we were looking in a scale too small for some imperfections to be noticeable. In order to insure reproducibility, glass plates were changed periodically during the time duration of all the experimental runs, and all parts of the experiments are cleaned in an ultrasonic bath before mounting the experimental cell again, including the particles. Finally, for fixed geometry, particle density and vibration frequency we perform vibration amplitude ramps, from $\Gamma \gtrsim 1$ in the liquid phase, increasing A going through the solid-liquid transition that is reached at $\Gamma \equiv \Gamma_c$. In order to verify the existence of hysteresis, for some runs we also perform decreasing amplitude ramps starting slightly above Γ_c.

It is important to note that during the research we have used two sets of ITO coated glass plates. Most of the results presented in the next chapters were obtained with the thin coating, unless stated otherwise. After we run out of these glass plates we had to use the thick ITO coating by keeping constant all the other parameters (the definitions of C1 and C2 do not vary). It turned out to be of great importance in the analysis because we could actually verify whether the transition observed was still present once we change microscopic quantities, such as the restitution and friction coefficients. For the new glass plates we showed that solid-liquid transition takes places at a different acceleration Γ_c, given that we changed dissipation in the system.

A third important issue is the mechanical leveling of the whole setup. For the initial experiments a simple mechanical leveling stage was used. The leveling procedure was quite good and it was verified through the isotropy of $S(\vec{k})$ and the Fourier components $\left\langle \hat{\rho}(\vec{k}) \right\rangle$ for each experimental run. When this quantities are plotted versus k_x and k_y, there is no preferential direction. For example $S\left(k_x, k_y\right)$ shows the characteristic symmetric circular annular shape at $kd \approx 2\pi$ and also at the position of the pre-peak. In order to ensure a proper level for longer times we designed and implemented another experimental setup that allowed us to improve this issue.

3.2. Improved setup

The new setup intended to solve the issue that after approximately 24 hours of experimental runs the level of the whole system tended to be lost. Consequently a new setup was developed. It was decided that a proper solution would be to put an air-bearing system in place, mounted on an optical table. In this new configuration we use a an optical table with a hole in the center, through which the air-bearing system is placed. The air bearing system is mechanically connected through the shaker by means of a 30 cm long threaded rod. For proper functioning, the air-bearing system is connected to an air-compressor, supplying a pressure of 60 psi. The scheme of this new setup is

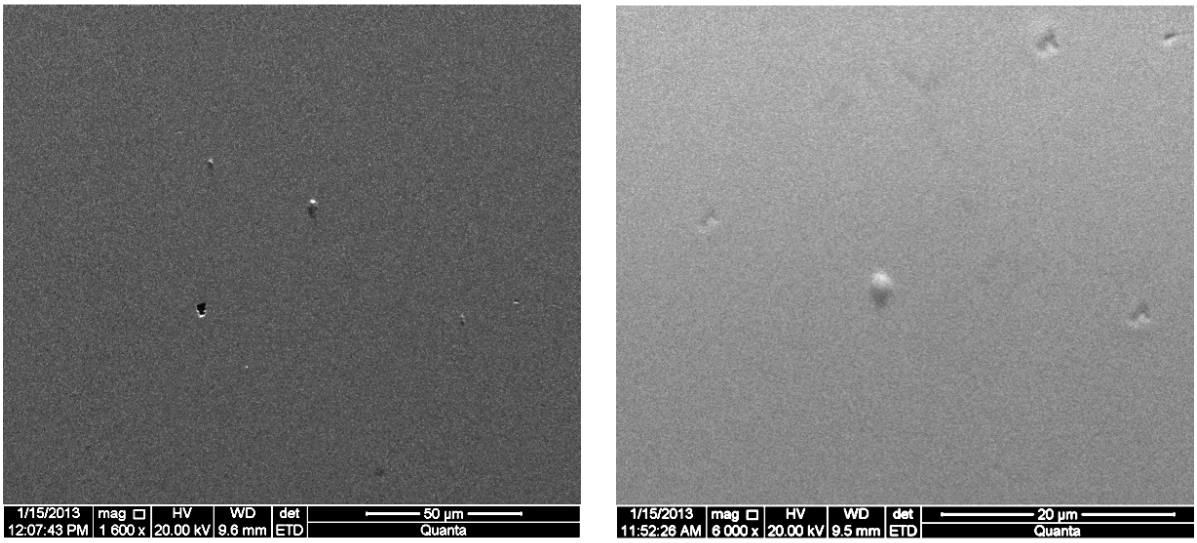

Figure 3.1.5.: Images obtained from the AFM at two different scales (50 μm and 20 μm) for a piece of glass that has not been very used (approximately 15 hours). Notice some holes and impurities produced by the collisions.

shown in Fig. 3.2.1. Given that the air-bearing has a cylindrical shape and eventually it can rotate, the system has an extra degree of freedom. Hence, in order to avoid this, we placed four posts, each one of them attached to a ball of teflon (6mm diameter), in contact in the corners the cell. The balls of teflon were chosen due to the small friction with steel, thus, without affecting the vertical motion.

The leveling is carefully done using the same procedure as before. The results with and with out the air-bearing and optical table system are the same, the main difference is that in the latter case the leveling is achieved more easily and stays constant for much longer times.

One disadvantage here is that with all the parts added between the cell and the shaker, the system is much heavier. Thus, we have reduced the maximal acceleration the shaker can provide. For the actual capabilities of the shaker we use (VTS-100), the maximal force is 100 lbf $\approx$ 444.8 N, hence the maximum acceleration peak-to-peak is approximately

$$\Gamma_{max} = \frac{100 \text{ lbf}}{5,5 \text{ kg}} \approx 8g, \tag{3.2.1}$$

which is fine for the typical accelarations explored in our research, but it is rather limited if we intend to increase the size of the cell.

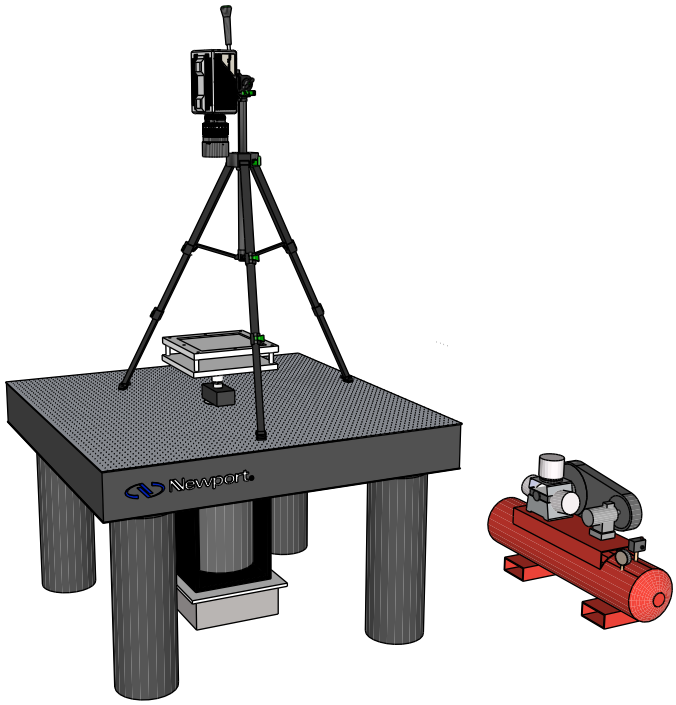

Figure 3.2.1.: Final experimental setup showing the cell mounted on the optical table. In this setup, the cell is mechanically connected to the shaker by means of a threaded rod. The air-bearing system is connected to an air-compressor, supplying a pressure of 60 psi.

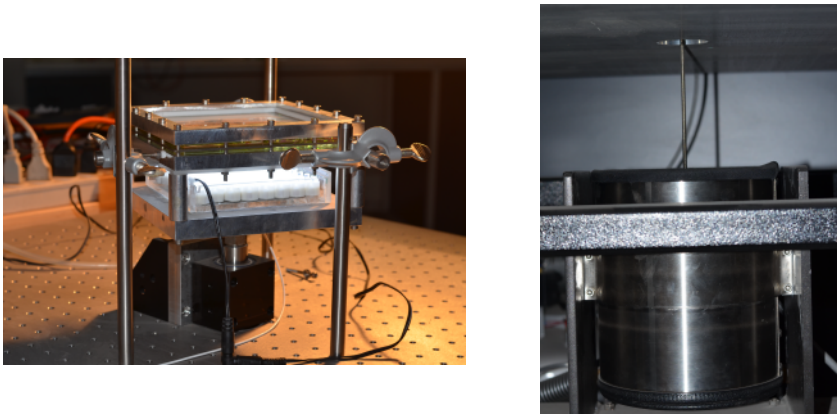

Figure 3.2.2.: Actual pictures of the setup. Left: Side view showing the air-bearing system attached to the optical table, along with the four poles used to avoid the rotation of the cell. Right: Threaded rod conecting the shaker to the air-bearing (not shown).

4. Particle and interface detection

« The function of an expert is not to be more right than other people, but to be wrong for more sophisticated reasons. »

David Butler

In this chapter we explain in some detail the basic principles of the algortihm of particle detection as well as the interface detection. The particle detection used is a least-square fit algorithm and, and as was pointed out earlier, it is a modification of an open source Matlab code [65]. Some improvements added to the original code are also discussed, along with some comments on the computing times required and the upgrades in this regard. We also discuss the details of the detection of the interface once the system has approached the transition, when both liquid and solid phases are present. We explain in some detail the different criteria that can be used to detect the interface and also present the coase-graining procedure which is used to describe it.

4.1. Particle detection

Our array of ilumination, of high intensity light emitting diodes, allows to know with sub-pixel accuracy the center of almost all the particles in the system, missing about ~ 10 out of 10000. This is achieved by running a code with input parameters the particle diameter, D, and a parameter ω which determines how abrupt is the change between the particle and the white background. The parameter ω is intimately related to the focus of the image, thus a very sharp image would have a value $\omega \approx 1\,\text{pix}$, while an image that is not so well focused would have $\omega > 1\,\text{pix}$. The main idea of the algortihm is that we can describe an ideal particle by the function

$$I_p\left(\vec{x}; D, \omega\right) = \left[1 - \tanh\left(\frac{|\vec{x}| - D/2}{\omega}\right)\right]/2. \tag{4.1.1}$$

Fig. 4.1.1 shows this function and an image of the particle obtained from this function.

Then, we find the center of the particles using a least-square fit. Thus, we define the function χ^2,

$$\chi^2\left(\vec{x}_0; D, \omega\right) \equiv \int W\left(\vec{x} - \vec{x}_0\right)\left[I\left(\vec{x}\right) - I_p\left(\vec{x} - \vec{x}_0; D, \omega\right)\right]^2 \mathrm{d}\vec{x}, \tag{4.1.2}$$

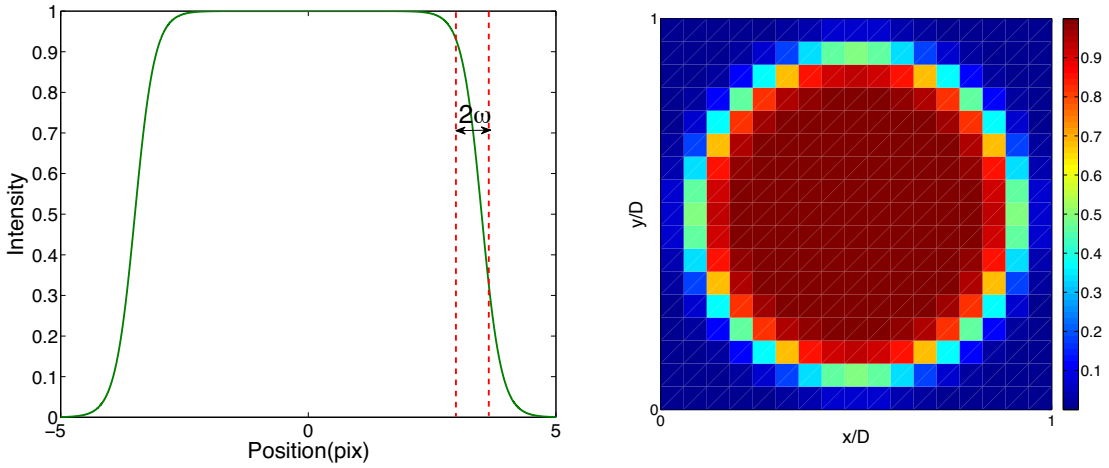

Figure 4.1.1.: Particle detection. Left: Function which defines the intensity of an ideal particle. Right: Image of an ideal particle.

where $W(\vec{x}-\vec{x}_0)$ is a weight function. The domain of integration is over the area of the experimental image. With all of this, we can obtain the function χ^2, which minima correspond to the position of the center of the particles. So the process of finding the particles is equivalent to finding all of the minima of chi-squared. We can use convolution to do this easily. By expanding 4.1.2 we get

$$\chi^2 = I^2 \otimes W - 2I \otimes (WI_p) + \left\langle WI_p^2 \right\rangle, \tag{4.1.3}$$

where

$$f \otimes g = [f \otimes g](\vec{x}_0) = \int f(\vec{x})\, g(\vec{x}-\vec{x}_0)\, \mathrm{d}\vec{x}, \tag{4.1.4}$$

and

$$\langle f \rangle = 1 \otimes f. \tag{4.1.5}$$

For the images we have, we use $W(\vec{x}-\vec{x}_0) = I_p$, then 4.1.3 becomes

$$\chi^2 = I^2 \otimes I_p - 2I \otimes I_p^2 + \left\langle I_p^3 \right\rangle \tag{4.1.6}$$

Hence, by computing the convolutions we get the function χ^2 throughout the image. Later, we invert the function χ^2 and establish that every maximum of $1/\chi^2$ whose intensity is larger than its

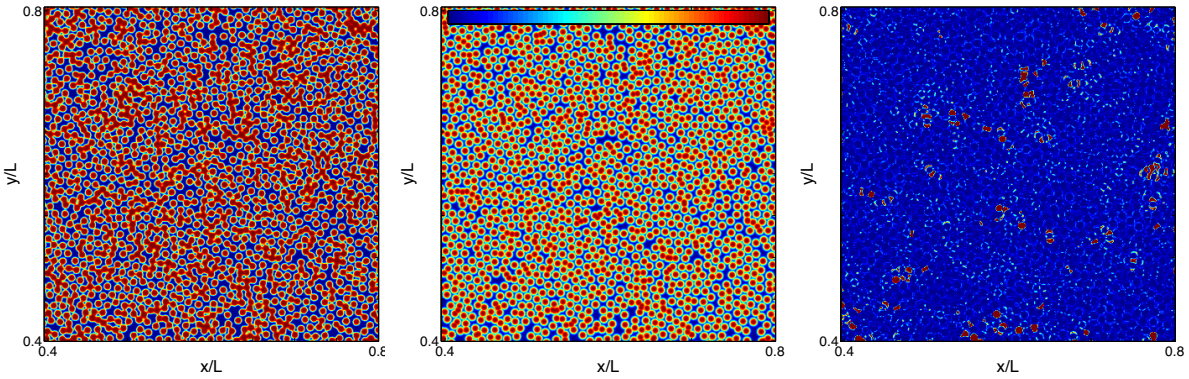

Figure 4.1.2.: From left to right: Real, calculated and χ^2 shown for a region of an entire image of our system. The images are normalized, so that the intensities are approximately 1 inside, and 0 outside of the particles.

8 neighbors and some threshold would be consider a particle. Thus far, we obtain the center of the particles with pixel resolution.

In order to obtain sub-pixel accuracy for the particles poistion, we define a new function χ^2 that is now dependent on the particles center,

$$\chi^2\left(\vec{x}_n; D, \omega\right) \equiv \int \left[I\left(\vec{x}\right) - I_c\left(\vec{x} - \vec{x}_n\right)\right]^2 \mathrm{d}\vec{x}, \tag{4.1.7}$$

where $I\left(\vec{x}\right)$ is the image to be tracked and $I_c\left(\vec{x} - \vec{x}_n\right)$ is defined by

$$I_c\left(\vec{x} - \vec{x}_n\right) \equiv \sum_n W_n\left(\vec{x}\right) I_p\left(\vec{x} - \vec{x}_0; D, \omega\right). \tag{4.1.8}$$

$W_n\left(\vec{x}\right)$ takes the value 1 if $\vec{x}$ is inside the Voronoi area of particle n, and 0 otherwise. By minimazing this function with respect to the positions $\vec{x}_n$, we get the particles center with sub-pixel resolution.

$$\frac{\partial \chi^2\left(\vec{x}_n^*; D, \omega\right)}{\partial \vec{x}_n} = 0 \tag{4.1.9}$$

Similarly, we then find the parmeters D and ω according to the real image, instead of the approximated values. In this regard, we now minimize the new function χ^2 with respect to D^* and ω^*. With this pair of new values we repeat the process of finding the particles center with sub-pixel accuracy, and finally obtain the position of the particles for each image.

With this procedure, for our actual images, the algorithm works quite well in the fluidized regime (loosing 10-20 particles of 10000); but when the system presents both fluid and solid phases the

rutine tended to miss many particles in dense zones, in particular where the top layer particles are placed in the valleys that the bottom particles form. Accordingly, a final step to the algorithm was added. To find these missed particles, the new step in the routine looks at the difference image, *i.e.* the image constructed from the "found particles" substracted from the real image. In this difference image, particles that were missed will appear as dots on a white background (*i.e.* the difference image will have "particles" where the difference between the real and constructed image is high). We then run all the previous routine until the minimization of D and ω on this difference image, and appends the found particle locations to the original position array. This process is repeated until either no more new particles are found (usually in one or two iterations) or 7 iterations have been achieved (an empirically stable upper bound).

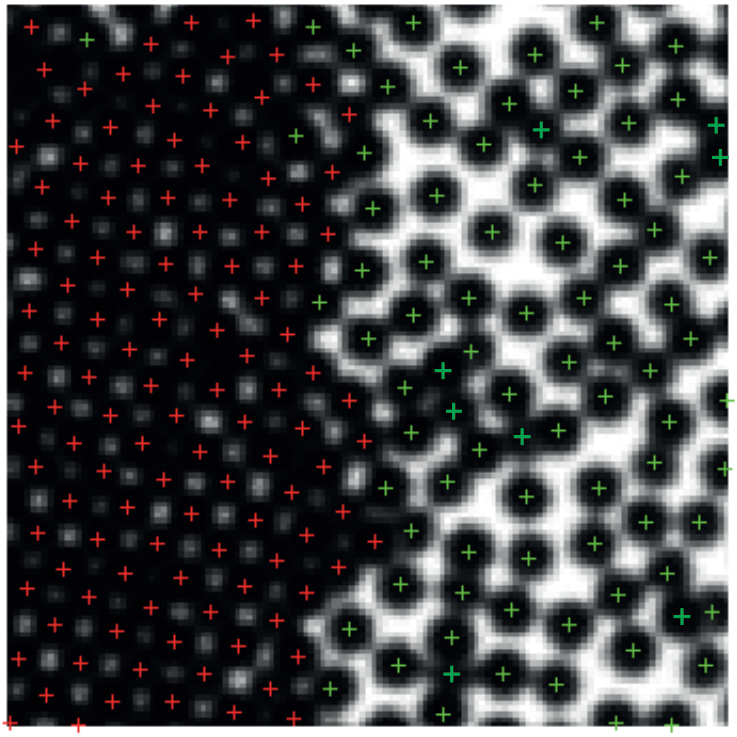

Figure 4.1.3.: Particle detection. Test image showing the particle detection. Green crosses correspond to particles in the liquid phase, whereas red crosses correspond to particles in the solid phase.

In Fig. 4.1.3 we present a zoomed image showing the interface between the liquid and solid phases illustrating the position of the particles found through the algorithm explained above. After establishing some criterion (that will be explained in detail in Chapter 6) we can also distinguish whether the particle is in the "solid phase" or in the "liquid phase". When the system presents the dense solid cluster, the routine provides very good results, though not perfect. In average, for each image we miss about 0.1-0.2% of the total amount of particles.

In the beginnings of the experiment the original Matlab code was translated to *C* language by Mauricio Cerda due mainly that the *C* code allowed much more faster calculations, but we still required

almost 2 weeks to compute the positions of one-day of experimental runs (typical experimental runs consist of at least 30 video acquisitions, one for each A, of about 3300 images each. Hence, the complete number of images to analyze for a single experimental run is about 10^5.) and therefore another improvement was done. Thanks to Juan Silva we could implement a modified *C++ & CUDA* code that allows faster computation for large number of particles and also the parallelization of the particle detection image analysis using a cluster of computers, reducing computation time to about 100 images per minute [66, 67].

4.2. Bond-orientational order parameter and interface detection

In the quasi-2D geometry the solid phase consists of two square interlaced layers instead of the single hexagonal layer that is characteristic of 2D systems [9]. These interlaced square lattices, when projected in 2D, result also in a square lattice. If particles in the solid phase are permanently in contact such that grains are close packed, then the unit cell per layer should have an area $d \times d$, implying that the projected lattice should have a Voronoi area equal to $d^2/2$. Two local parameters can be used to analyze the system. For each particle we can compute its Voronoi cell area, A_v, which is inversely proportional to the local density, and also the 4-fold local order parameter, Q_4, that is defined as [53]

$$Q_4^j = \frac{1}{N_j} \sum_{s=1}^{N_j} e^{4i\alpha_s^j}. \tag{4.2.1}$$

Here, N_j is the number of nearest neighbors of particle j and α_s^j is the angle between the neighbor s of particle j and the x axis. For a particle in a square lattice, $|Q_4^j| = 1$ and the complex phase measures the square lattice orientation respect to the x axis. For computing Q_4^j, the information of nearest neighbors is obtained by Voronoi tessellation. However, the square lattice is particularly unstable; for a perfect square lattice, a small amount of noise in particle positions would induce many particles to finish with more that four nearest neighbors in the Voronoi construction. This results in pairs of neighbors that share within their Voroinoi cells one side of length much shorter than the one in a perfect square lattice. As a consequence, even if the local structure is almost square based, $|Q_4^j|$ would be considerably lower than 1. Thus, an additional condition is used: neighbors of a given particle that share a Voronoi edge whose length is shorter than $d/4$ are discarded as nearest neighbors in the computation of Q_4^j. This ensures that $|Q_4^j| \approx 1$ in those dense clusters that visually present a square symmetry.

Fig. 4.2.2 presents the probability distribution function (PDF) of normalized Voronoi areas $2A_v/d^2$ and local order parameter $|Q_4|$ obtained from 3000 images, for which the system is indeed phase separated. The Voronoi area, A_v, is normalized by $d^2/2$, the corresponding Voronoi area for closed packed two square interlaced layers. Fig. 4.2.3 shows the marginal PDF, defined as

$$\mathrm{PDF}(A_v) = \int \mathrm{PDF}(|Q_4|, A_v) dA_v, \tag{4.2.2}$$

$$\mathrm{PDF}(|Q_4|) = \int \mathrm{PDF}(|Q_4|, A_v) d|Q_4|. \tag{4.2.3}$$

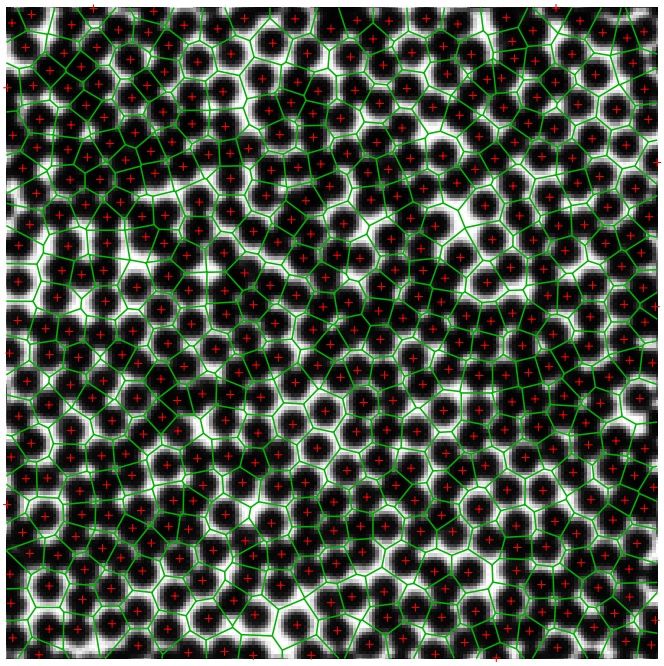

Figure 4.2.1.: Typical Voronoi tesselation for a zoomed image.

From the joint and marginal PDFs (Fig. 4.2.2 and Fig. 4.2.3 respectiveley) we can state that there is clearly a superposition of three distributions: a wide distribution related to the liquid phase, around $|Q_4| \approx 0.2$ and $2A_v/d^2 \approx 2$; another more localized and stronger peak related to the solid phase, close to $|Q_4| = 1$ and $2A_v/d^2 \approx 1.3$; and a third small peak of more ordered particles in a dense phase, with $|Q_4| \approx 0.55$ and $2A_v/d^2 \approx 1.4$, which correspond to small density and order fluctuations in the system. In general, the normalized Voronoi area of particles in the solid phase is larger than 1, implying that particles are slightly separated (in average). A separation distance of $0.15d$ is enough to shift this peak from 1 to 1.3. For classifying particles in the solid or liquid phase three simple criteria can be established. The first one is to use only A_v, defining a critical value A_v^c ($2A_v^c/d^2 \approx 1.5$) such that particles with A_v lower (larger) than this value are labelled as solid (liquid) particles. A second criterion is to use only local order. If $|Q_4| \geqslant Q_4^c$ ($|Q_4| < Q_4^c$), then the particle is in the solid (liquid) phase. A third possibility is to use both quantities, such that if $A_v \leqslant A_v^c$ and $|Q_4| \geqslant Q_4^c$ are both satisfied, then the particle is considered to be in the solid phase. We have verified that our results are not sensitive to which condition we use (see Sec. 6.5), and for simplicity we choose the second condition, with $|Q_4^c| = 0.7$. However, the first criterion also detects particles that are less ordered but dense, adding a thin liquid-like layer, with intermediate order, around the solid cluster.

As it it will be clear in Chapter 5 we conclude that Q_4 is a more appropriate order parameter to characterize the liquid to solid transition, compared to the local density. Indeed the correlations of

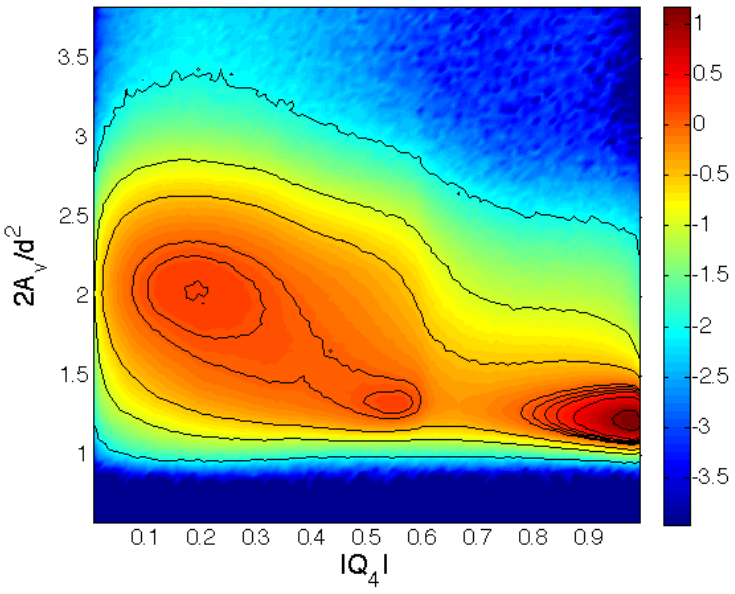

Figure 4.2.2.: Probability density function of normalized Voronoi areas $2A_v/d^2$ and local order parameter $|Q_4|$ obtained from 3000 images (about 2.8×10^6 pairs of A_v and $|Q_4|$ values), for which the system is indeed phase separated. The criterion for solid-liquid identification relies on the valley obtained around $|Q_4| = 0.7$ that is almost independent of A_v. The color code indicated in the vertical bar is the logarithm (base 10) of the PDF. Contour plots are shown for $\log_{10}[\mathrm{PDF}(|\mathrm{Q_4}|, \mathrm{A_v})] = -2$, -1, -0.5, 0, 0.1, 0.2, 0.3, 0.5, 1.

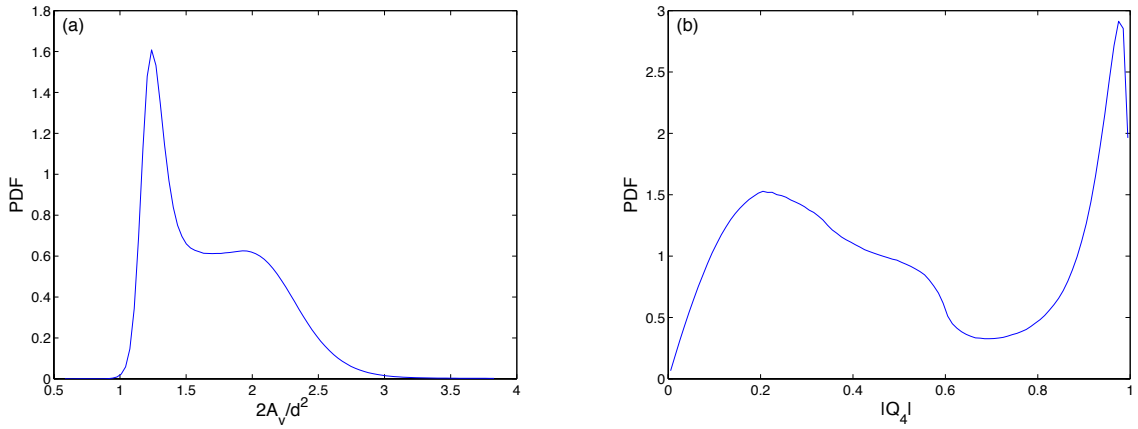

Figure 4.2.3.: Projected probability density functions of normalized Voronoi areas $2A_v/d^2$ (a) and local order parameter $|Q_4|$ (b) obtained from 3000 images. The minimum obtained for $|Q_4| = 0.7$ is chosen as criterion for solid-liquid identification.

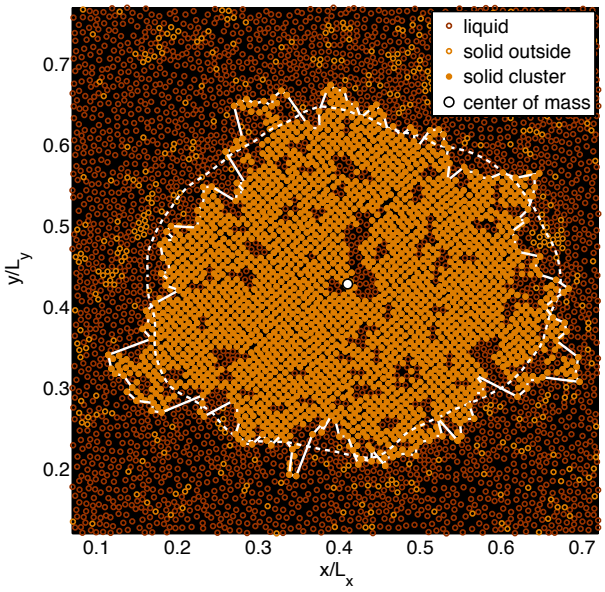

Figure 4.2.4.: Map of $|Q_4^j|$ in real space. Particles are classified in the solid or liquid phase using the criterion defined in the text. The solid line with dots shows the interface detection. The dashed line corresponds to the average interface obtained from 7000 images acquired at 500 fps. The solid white circle shows the center of mass of particles in the largest solid cluster.

Q_4 showed critical divergencies at the critical point, while those of the local density were insensitive to the transition.

Fig. 4.2.4 shows a typical example of the solid-liquid interface detection. For each image, particles that are in a solid or liquid phase are labeled using the previously defined criterion. Also for each image, particles belonging to the same cluster are identified, as well as the largest cluster in each image. This cluster of course corresponds to the largest, most stable, solid cluster that is present when the driving acceleration exceeds the critical value. Then, for each image the center of mass of particles that belong to the largest solid cluster is determined. Using all the centers of masses from a stack of images, the global center of mass is determined.

The next step then corresponds to detect those particles that are at the solid-liquid interface of the largest solid cluster for each image. This is done by an angle coarse-graining procedure. From the position of the global center of mass, the position of the solid particle that is the most distant from this center of mass within an angle $\Delta\theta$ is determined. This is done from $\theta_1 = 0°$ until $\theta_N = 360° - \Delta\theta$, following $\theta_i = \theta_1 + (i-1)\Delta\theta$. Thus, for each θ_i, there is a pair of coordinates (x_i^b, y_i^b) of the particle that is in the largest solid cluster and that is the most distant to the global center of mass, thus at the solid-liquid boundary. For simplicity, we describe each of these particles by the coordinates (θ_i^b, r_i^b), which are polar coordinates of each particle respect to the reference system fixed at the global center of mass. The final step is to interpolate these coordinates to a set where the angles are equally spaced, such that $\theta_i^{\text{int}} = \theta_1 + (i-1)\Delta\theta/2$, and we end up with the set of coordinates $(\theta_i^{\text{int}}, r_i^{\text{int}})$. It is this set of coordinates that is used for the Fourier analysis presented in this study. Fig. 4.2.4

also shows that in general the interface is rather smooth, except for some "jumps". These jumps are artificial, as they arise because we force the interface to be described by a single-evaluated function $r_i^{\mathrm{int}} = r_i^{\mathrm{int}}(\theta_i^{\mathrm{int}})$, which is not always the case. Because of the adopted procedure for the interface determination, we necessarily end with a few of these jumps for each image. However, theses jumps do not contribute to the low wavenumber modes that turn out to be relevant for this study. This is explicitly shown in Sec. 6.6, where we discuss the validity of the small slope approximation.

Part III.

Results

5. Static analysis and critical phenomena

« It is a capital mistake to theorize before one has data. Insensibly one begins to twist facts to suit theories instead of theories to suit facts. »

Sherlock Holmes

We present some of the results of the study on density and order fluctuations in the vicinity of the solid-liquid- like transition that occurs in a vibrated quasi-two-dimensional granular system. The two-dimensional projected static and dynamic correlation functions are studied. We show that density fluctuations, characterized through the structure factor, increase in size and intensity as the transition is approached, but they do not change significantly at the transition itself. The dense, metastable clusters, which present square symmetry, also increase their local order in the vicinity of the transition. This is characterized through the bond-orientational order parameter Q_4, which in Fourier space shows an Ornstein-Zernike-like behavior. Depending on the filling density and vertical height, the transition can be of first- or second- order type. In the latter case, the associated correlation length ξ_4, the relaxation time τ_4, the zero k limit of Q_4 fluctuations (static susceptibility), the pair correlation function of Q_4, and the amplitude of the order parameter obey critical power laws, with saturations due to finite size effects. Their respective critical exponents are $\nu_\perp = 1$, $\nu_\parallel = 2$, $\gamma = 1$, $\eta = 0.67$ and $\beta = 1/2$, whereas the dynamical critical exponent $z = \nu_\parallel/\nu_\perp = 2$. These results are consistent with model C of dynamical critical phenomena, valid for a nonconserved critical order parameter (bond-orientation order) coupled to a conserved field (density). We also discuss at the end of the chapter the universality of the exponents, and whether the concepts formulated in Sec. 2.3.3 can be applied.

5.1. Overview

Recently, several granular systems that undergo interesting phase transitions have been reported [8, 68, 9, 69, 70, 71, 72, 73, 6, 10, 74]. One particular system is a vibrated fluidized granular monolayer composed of N hard spheres of diameter d confined in a shallow cell of height $L_z < 2d$ (typically $L_z \approx 1.7d - 1.9d$). Under proper conditions, solid and liquid phases can coexist at mechanical equilibrium [68, 9, 6, 74]. The solid clusters can present different order symmetries, like square or hexagonal, depending on forcing, geometrical, and particle parameters. It has been reported that for $L_z \approx 1.8d - 1.9d$ and for a large range of filling densities, the most compact structure in quasi

two dimensions is made of two layers of square symmetry. The more compact hexagonal structure formed by two layers needs a larger vertical gap or larger densities [9]. The critical amplitude above which there is coexistence decreases with increasing density. Many of the previous works on granular phase transitions focus on the similarities or comparisons of such nonequilibrium systems with equilibrium phase transitions [68, 9, 6, 10, 74, 75]. For example, the equilibrium KTHNY theory has proven useful in the two dimensional (2D) melting of granular monolayers [10]. Here we focus on a dynamical critical phase transition in a nonequilibrium quasi-2D granular system. We present an experimental study of the solid-liquid phase transition in a vibrated fluidized granular monolayer. The solid phase consists of two square interlaced layers, stabilized by the collisions with the top and bottom walls and the confining pressure exerted by the liquid phase [8, 9]. We focus on density and bond-orientation order fluctuations in the vicinity of the transition. We show that the transition can be continuous or abrupt depending on the cell's height and filling density. Density fluctuations show a crossover behavior at the transition, whereas the order shows strong fluctuations. In the continuous case several magnitudes show critical-like behavior making it possible to measure five independent critical exponents. These results are consistent with model C of dynamical critical phenomena [49], valid for a nonconserved critical order parameter (bond- orientation order) coupled to a conserved field (density).

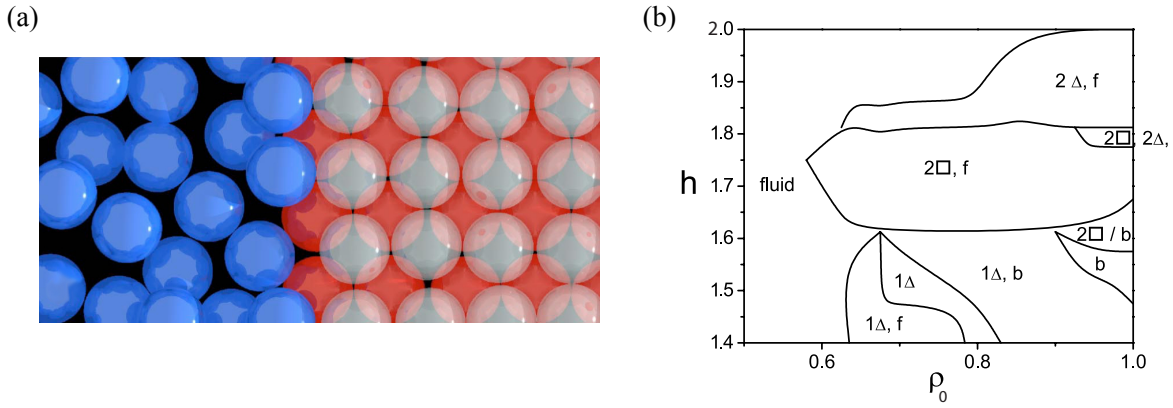

Figure 5.1.1.: (a) 3D rendering of instantaneous particle positions. A closeup of the interface between both the liquid (blue) and solid phases (red and white). The two layers of particles forming pyramyds of square base are clearly visible. (b) Phase diagram for the granular system, here $A = 0.15d$ and $f = 75$ Hz [9, 6].

5.2. Static structure function

All the results presented in this chapter were obtained from videos of approximately 3300 images taken at 10 fps using the thin ITO coated glass plates of 25 nm thickness, unless otherwise stated.

Particle positions $\vec{r}_j(t)$ in the plane (x, y) are determined for each time t. Experimentally, there is

no access to the z coordinate. Thus, the 2D microscopic density field Fourier components are

$$\widehat{\rho}(\vec{k},t) \;=\; \int d^2r\, e^{i\vec{r}\cdot\vec{k}}\rho(\vec{r},t) = \sum_{j=1}^{N} e^{i\vec{k}\cdot\vec{r}_j(t)}. \tag{5.2.1}$$

The static structure factor $S(\vec{k})$ measures the intensity of density fluctuations in Fourier space:

$$S(\vec{k}) \;=\; \frac{\langle|\widehat{\rho}(\vec{k},t) - \langle\widehat{\rho}(\vec{k},t)\rangle|^2\rangle}{N}, \tag{5.2.2}$$

where $\langle\ \rangle$ denotes time averaging. In general $\langle\rho(\vec{k})\rangle \neq 0$, due to inhomogeneities induced by boundary conditions. The wave vectors are computed from $\vec{k} = \pi(n_x\hat{\imath}+n_y\hat{\jmath})/L$, where $n_x, n_y \in \mathbb{N}$. In the liquid phase ($\Gamma < \Gamma_c$) we have verified that the system is isotropic, $S(\vec{k}) = S(k)$, where $|\vec{k}| \equiv k$. In the phase separated regime this quantity is not well defined as density fluctuations should in principle behave differently in each phase. However, as it is not easy to determine Γ_c precisely, we use this quantity as a possible relevant measurement in the vicinity of the solid-liquid phase separation, even above the critical amplitude.

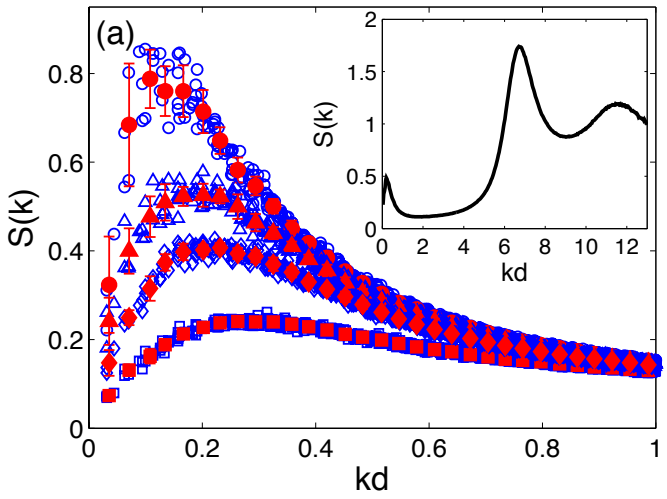

Figure 5.2.1.: $S(k)$ in the large wavelength limit for four different accelerations, $\Gamma = 2.13$, 2.74, 3.18 and 4.79 (C2). Open symbols correspond to raw $S(k)$ data, whereas solid symbols correspond to averages using windows $k \in [nk_{\min}, (n+1)k_{\min}]$ for integer $n \geqslant 1$, where $k_{\min} = \pi/L$. Error bars correspond to standard deviations. The inset shows $S(k)$ for a larger range of k for $\Gamma = 3.64$.

Fig. 5.2.1(a) presents $S(k)$ obtained for C2 (the qualitative features are the same for both configurations and their differences will pointed out explicitly later). The main figure presents the long-wavelength range, $kd \leqslant 1$, for four Γ below Γ_c. The inset presents $S(k)$ for a larger range of k. It has the usual form expected for liquids with short range order, but with a pre-peak located in the range $kd = 0.1 - 0.3$. The associated density fluctuations are indeed visible by simple visual inspec-

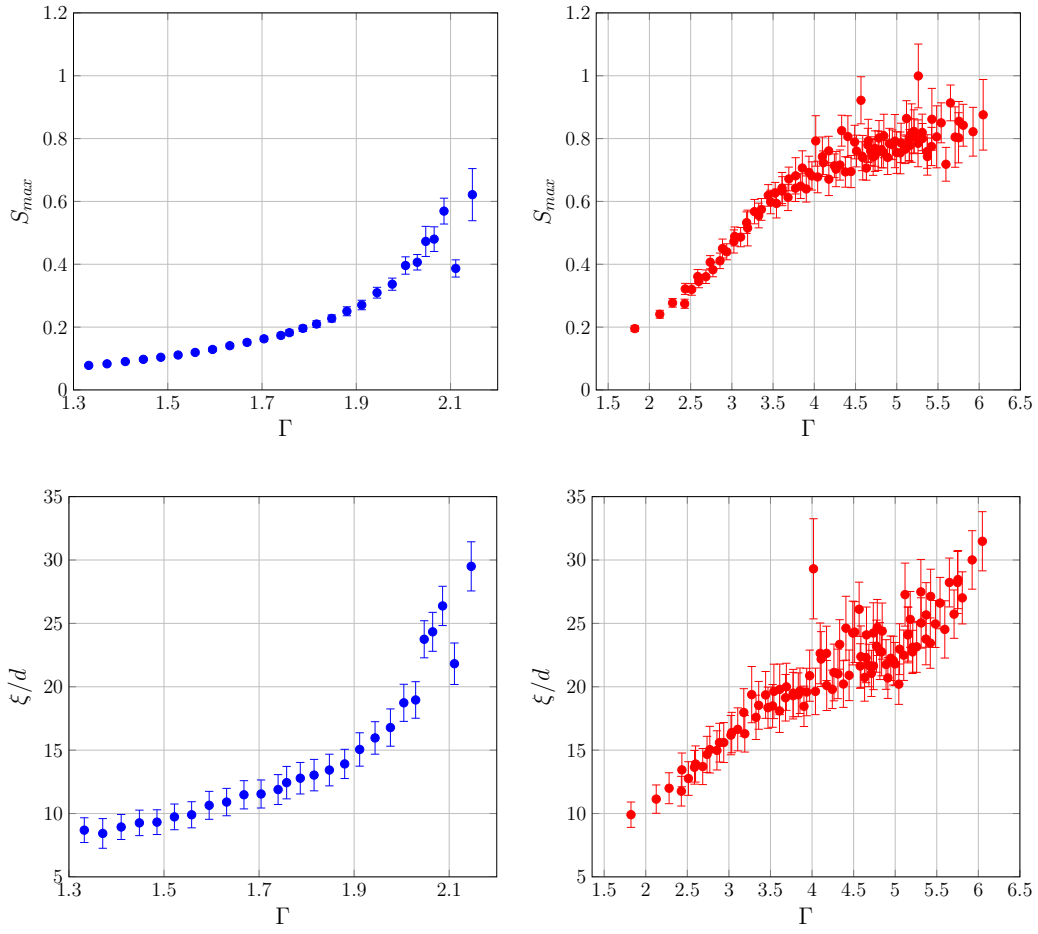

Figure 5.2.2.: Top: Pre-peak maximum $S_{\max} \equiv S(k = k^*)$, which occurs at $k = k^*$. Bottom: Associated length scale $\xi = \pi/k^*$ as functions of Γ for C1 (left) and C2 (right).

tion. The pre-peak is characterized by its maximum value at k^*, $S_{\max} \equiv S(k^*)$, and the associated characteristic length scale $\xi = \pi/k^*$. These quantities are plotted in Fig. 5.2.2(b-c) as functions of Γ for increasing amplitude ramps and for both configurations. They both increase as the transition is approached. The difference between configurations is mainly manifested in the shape of each curve, being their final values (near the transition) very similar, $S_{\max} \approx 0.5 - 0.8$ and $\xi/d \approx 20 - 30$. By observing visually the persistence of the solid clusters we conclude that for C1 the transition is located at $\Gamma_c \approx 2$. For C2 it is more difficult to determine with the same precision but it is found to be $\Gamma_c \sim 5$. However, neither $S_{\max}$ or ξ show evident changes at these values. Density fluctuations do not show critical behavior, but they are needed to create regions of high order. Similar density fluctuations have been observed in amorphous materials [76, 77], which have been consistently related to the existence of medium-range-crystalline-order. In our case, medium range order will be analyzed with an appropriate bond-orientational order parameter, which presents critical behavior.

5.3. Bond-orientational order parameter

In the vicinity of the transition, fluctuations of high density present the same square symmetry as the solid phase. In the quasi-2D geometry the solid phase consists of two square interlaced layers instead of the hexagonal layer that is characteristic of 2D systems [9]. The local order can be characterized through a fourfold bond-orientational order parameter. This is still valid in our quasi-2D geometry because the interlaced two-layer square lattices (with unit cell length d in each plane) result also in a square lattice when projected in two dimensions, with unit cell length $\sqrt{2}d/2$ when the grains are close packed. The fourfold bond-orientational order parameter per particle is defined as[1]

$$Q_4^j = \frac{1}{N_j} \sum_{s=1}^{N_j} e^{4i\alpha_s^j}, \tag{5.3.1}$$

where N_j is the number of nearest neighbors of particle j and α_s^j is the angle between the neighbor s of particle j and the x axis (see Fig. 5.3.1).

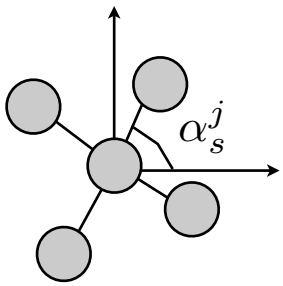

Figure 5.3.1.: Definition of the angle α_s^j.

In Fig. 5.3.2 we present representative $|Q_4^j|$ maps for two accelerations ($\Gamma = 2.00$, and 2.13) for configuration C1. For $\Gamma = 2.00 < \Gamma_c^{C1}$, solid ordered clusters are not observed. For $\Gamma = 2.13 > \Gamma_c^{C1}$ a large single solid cluster is observed, which presents some defects but is, comparatively, very stable. Single solid clusters are also present for intermediate Γ (for example, for $\Gamma = 2.09$ and 2.04) but they nucleate or migrate (depending on the acceleration ramp direction) at one of the cell borders, resting there for long times (not shown here for clarity). For this configuration, the large solid cluster that is present above the transition is extremely sensitive to small imperfections in the horizontal leveling of the cell. It is only for Γ not so close to Γ_c^{C1} and for long times that the solid, stable, large cluster remains in the vicinity of the cell's center.

As a comparison, we present in Fig. 5.3.3 representative $|Q_4^j|$ maps for four accelerations ($\Gamma = 2.74$, 4.18, 5.10 and 5.42) for configuration C2. Well below the transition, solid clusters are very unstable and small. As Γ is increased, solid clusters grow, become more ordered and persistent. For $\Gamma \approx \Gamma_c$

[1] A similar expression can be written for a sixfold bond- orientational parameter. We have verified that for the current system and forcing parameters its related global average and Fourier representation do not vary.

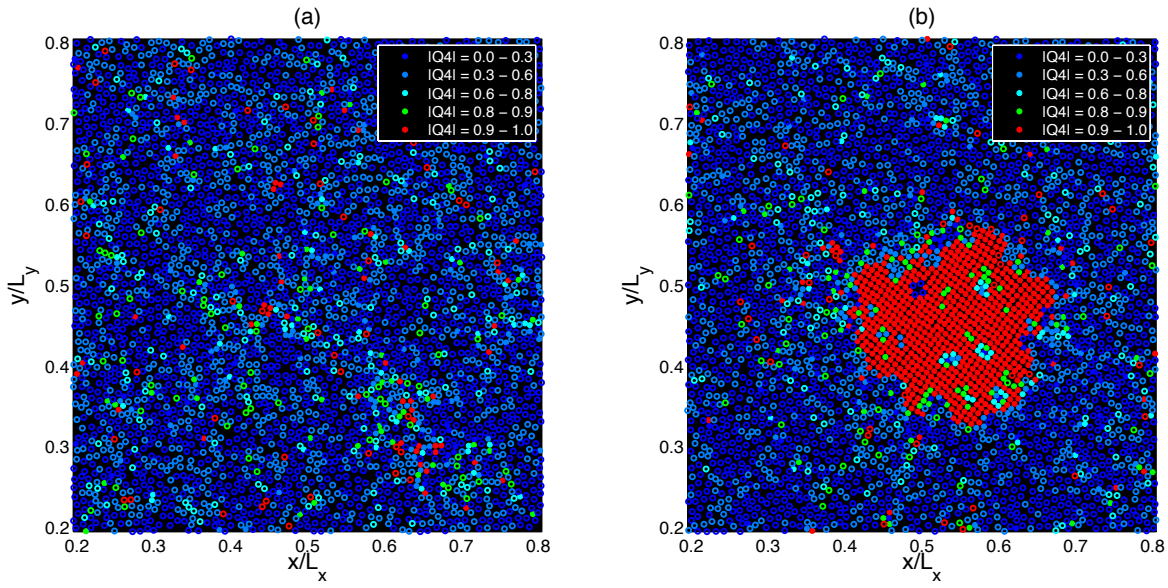

Figure 5.3.2.: Absolute value of 4-fold bond-orientational order parameter Q_4^j in real space for C1, $\Gamma = 2.00$ (a), and 2.13 (b). Color code is described in the legend of each figure. Particles in the solid (liquid) phase correspond to solid (open) symbols. Only a section of the whole area is shown ($0.6L_x \times 0.6L_y$).

solid clusters are still quite unstable, but with longer life times as Γ is increased further. However, the main solid cluster remain much less stable that its counterpart in configuration C1.

The corresponding global average and Fourier components of Q_4^j are

$$\langle |Q_4| \rangle = \left\langle \frac{1}{N} \sum_{j=1}^{N} \left| Q_4^j \right| \right\rangle, \qquad \hat{Q}_4 \left(\vec{k}, t \right) = \sum_{j=1}^{N} Q_4^j e^{i\vec{k}\cdot\vec{r}_j(t)}. \tag{5.3.2}$$

The average $\langle |Q_4| \rangle$ measures the fraction of particles in the ordered phase. This quantity is presented in Fig. 5.3.4 as function of Γ for both configurations. Results for increasing (decreasing) ramps are represented by open (solid) symbols. Two ramp rates are also reported: slow ramps, for which a quasistatic state has been reached, and fast ramps, for which it has not. The difference between both configurations is evidenced in the jump of about 10% that is measured for $\langle |Q_4| \rangle$ at the transition for C1.

Moreover, the position of this jump depends on the ramp rate: for the slow rate the increasing and decreasing ramp jumps coincide, whereas for faster ramps the increasing (decreasing) ramp jump occurs at higher (lower) Γ. We use the slow ramp data to obtain a measurement of the critical acceleration, $\Gamma_c^{C1} = 2.01 \pm 0.03$. By contrast, the results obtained for C2 show first a linear trend for low and a clear deviation around $\Gamma \approx 5.1$, with no measurable jump. In fact, the deviation from the linear behavior obeys a supercritical-like law. For $\Gamma > 5.2$ we have fitted the data with

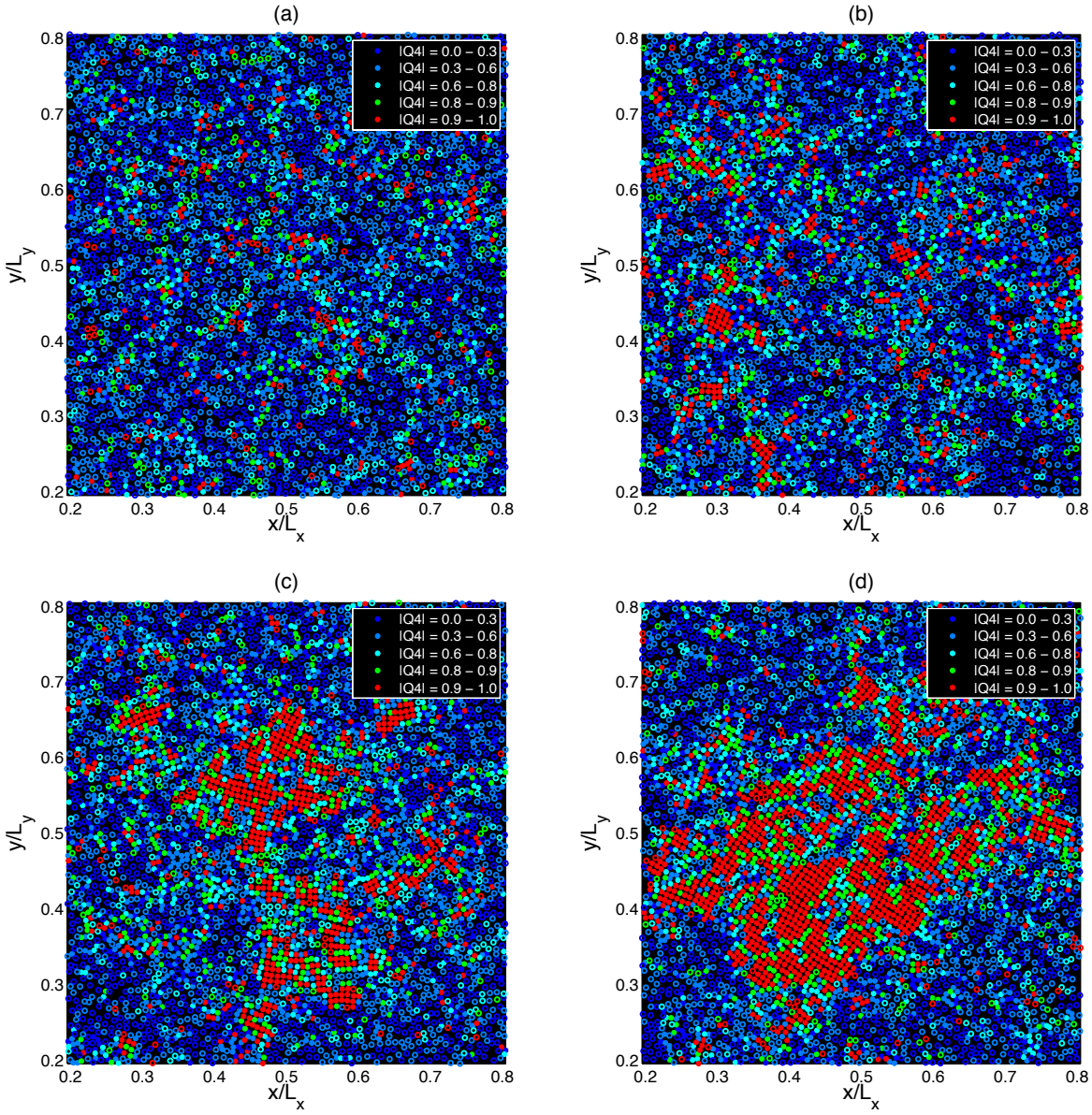

Figure 5.3.3.: Absolute value of 4-fold bond-orientational order parameter Q_4^j in real space for C2 and increasing acceleration, $\Gamma = 2.74$ (a), 4.18 (b), 5.10 (c) and 5.42 (d). Color code is described in the legend of each figure. Particles in the solid (liquid) phase correspond to solid (open) symbols. Only a section of the whole area is shown ($0.6L_x \times 0.6L_y$).

the function $\Delta Q_4 = \langle |Q_4| \rangle - Q_4^L = c\,(\Gamma - \Gamma_c)^\beta$, where Q_4^L is the extrapolation of the linear trend observed for lower . We obtain $c = 0.029 \pm 0.002$, $\Gamma_c^{C2} = 5.12 \pm 0.01$, and the exponent of the order parameter amplitude is $\beta = 1/2$. Within experimental error, the decreasing ramps also coincide with the increasing ramps in this configuration.

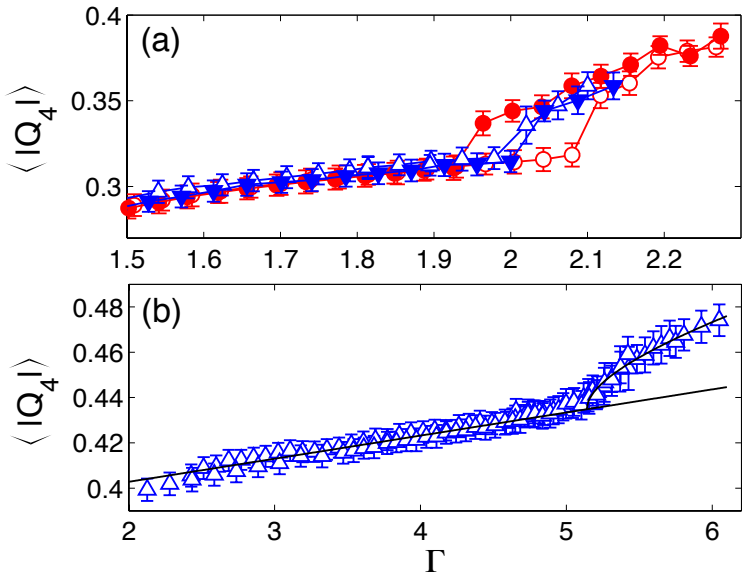

Figure 5.3.4.: Average global 4-fold bond-orientational order parameter $\langle |Q_4| \rangle$ versus Γ for C1 (a) and C2 (b). Open (solid) symbols represent data obtained for increasing (decreasing) Γ ramps, with the following rates: $\Delta\Gamma/\Delta t \approx 0.005$ min^{-1} ($\triangle$, $\blacktriangledown$) and $\Delta\Gamma/\Delta t \approx 0.02$ min^{-1} ($\circ$, $\bullet$). Continuous lines in (b) correspond to fits of the linear trend $Q_4^L = a\Gamma + b$ for $2.5 < \Gamma < 5$, with $a = 0.011 \pm 0.001$ and $b = 0.380 \pm 0.002$, and a supercritical-like behavior $\langle |Q_4| \rangle = Q_4^L + c(\Gamma - \Gamma_c)^\beta$, with $\beta = 1/2$, observed for $\Gamma \gtrsim 5$.

The curve ΔQ_4 versus Γ shown in Fig. 5.3.4(b) corresponds to a slowly increasing Γ ramp. Before verifying the reproducibility of this result for a slowly decreasing Γ ramp we run out of the 25 nm thick ITO coated glass plates. In order to show that the transition is indeed of second order type in the C2 configuration, we present in Fig. 5.3.5(a) the comparison of $\langle |Q_4| \rangle$ versus Γ for the thin and thicker ITO coated plates (25 and 750 nm respectively). For the latter, both increasing and decreasing Γ ramps are presented, showing good reproducibility. This figure indeed demonstrates that the C2 configuration presents a second order type transition, continuous and with no hysteresis.

The qualitative behavior is the same for both ITO coatings. $\langle |Q_4| \rangle$ has a linear dependence on Γ below the transition. For both cases there is a clear deviation from this linear trend above a given threshold. The critical acceleration for the thicker ITO coating case is lower ($\Gamma_c \approx 4.5$) than the one of the thin ITO coating case ($\Gamma_c \approx 5.1$), and also the initial linear slope below the transition is slightly larger for the thick ITO coating case. The deviation from the linear trend observed for $\Gamma < \Gamma_c$ is defined as $\Delta Q_4 = \langle |Q_4| \rangle - Q_4^L$, where Q_4^L is defined as the extrapolation of the linear trend over the complete range of Γ. Fig. 5.3.5(b) presents ΔQ_4 versus Γ for both cases. The continuous lines show the supercritical fits $\Delta Q_4 = c\sqrt{\Gamma - \Gamma_c}$ computed for $\Gamma \geqslant \Gamma_c$. Finally, as additional support for the supercritical law, in Fig. 5.3.6 we present ΔQ_4^2 (a) and ΔQ_4 (b) versus the reduced acceleration $\varepsilon = (\Gamma - \Gamma_c)/\Gamma_c$, in linear and log-log scales respectively. The fact that the constants c of the supercritical fits are different is manifested here from the difference between both slopes. We conjecture that both the differences in Γ_c and c between the ITO coatings reflects the difference

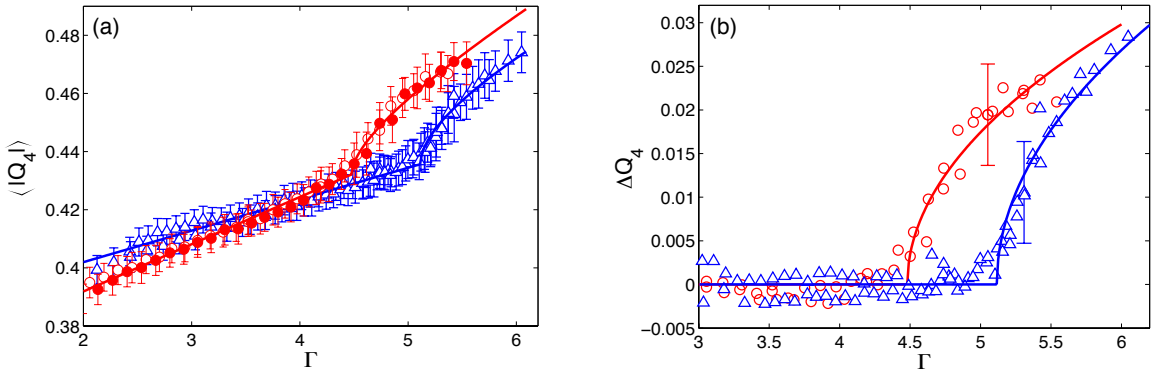

Figure 5.3.5.: (a) $\langle |Q_4| \rangle$ versus Γ for the two ITO coatings: 25 nm thickness (increasing Γ ramp: $\triangle$) and 750 nm thickness (increasing Γ ramp: $\circ$, decreasing Γ ramp: $\bullet$). Continuous lines show the linear trend fit for $2.5 < \Gamma < \Gamma_c$ and the supercritical deviation for $\Gamma \geqslant \Gamma_c$. (b) $\Delta Q_4 = \langle |Q_4| \rangle - Q_4^L$ versus Γ for each ITO coating thickness (25 nm: $\triangle$, 750 nm: $\circ$ for both increasing and decreasing Γ ramps), where $Q_4^L = a\Gamma + b$ is obtained from the linear trend below Γ_c. For the thin ITO coating, $a = 0.011 \pm 0.001$ and $b = 0.380 \pm 0.002$. For the thick ITO coating, $a = 0.016 \pm 0.001$ and $b = 0.359 \pm 0.002$. The continuous lines show the supercritical fits $\Delta Q_4 = c\sqrt{\Gamma - \Gamma_c}$ computed for $\Gamma \geqslant \Gamma_c$. The adjusted parameters are $c = 0.029 \pm 0.002$ and $\Gamma_c = 5.12 \pm 0.01$ (25 nm) and $c = 0.024 \pm 0.002$ and $\Gamma_c = 4.48 \pm 0.03$ (750 nm). In sake of clarity just one representative error bar is shown for each case.

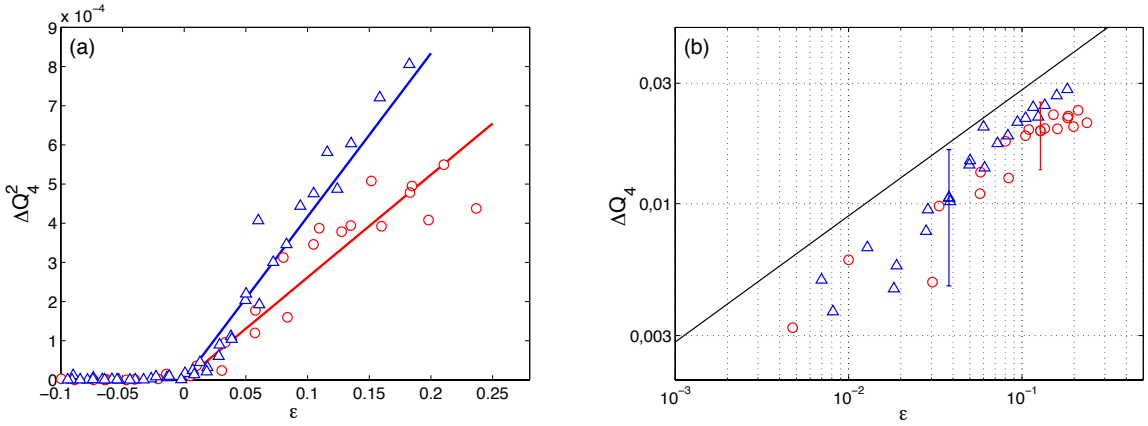

Figure 5.3.6.: (a) ΔQ_4^2 versus $\varepsilon = (\Gamma - \Gamma_c)/\Gamma_c$ for both ITO coatings. Error bars are not shown for clarity. The continuous lines correspond to the fitted supercritical laws $\Delta Q_4 = c\sqrt{\varepsilon \Gamma_c}$. (b) ΔQ_4 versus ε in log-log scale for both ITO coatings. The continuous line shows the supercritical law $\sim \sqrt{\varepsilon}$ for comparison. In sake of clarity just one representative error bar is shown for each case. In both figures ITO coatings are: 25 nm ($\triangle$) and 750 nm ($\circ$ for both increasing and decreasing Γ ramps).

of dissipation parameters that control del particle-wall collisions. The fact that Γ_c is lower for the thicker ITO coating would imply that both friction and normal restitution coefficients are lower

than those of the thin ITO coated glass plates. A more thorough analysis concerning this issue is presented in Sec. 5.6.

Consequently, we may say as a summary of this section, the transition for configuration C1 is abrupt, of first-order type, whereas for C2 it is continuous, of second-order type.

5.4. 4-fold bond-orientational structure factor $S_4(k)$

Local order can also be analyzed through its fluctuations in Fourier space by means of the 4-fold bond-orientational structure factor

$$S_4(\vec{k}) = \frac{\langle |\widehat{Q}_4(\vec{k},t) - \langle \widehat{Q}_4(\vec{k},t)\rangle|^2\rangle}{N}. \tag{5.4.1}$$

As shown in both configurations and for $\Gamma < \Gamma_c$, $S_4(k)$ shows an Ornstein-Zernike-like behavior in the limit $kd \ll 1$,

$$S_4(k) \approx \frac{S_4(0)}{1+(\xi_4 k)^2}, \tag{5.4.2}$$

where ξ_4 and $S_4(0)$ are the 4-fold bond-orientational correlation length and static susceptibility respectively.

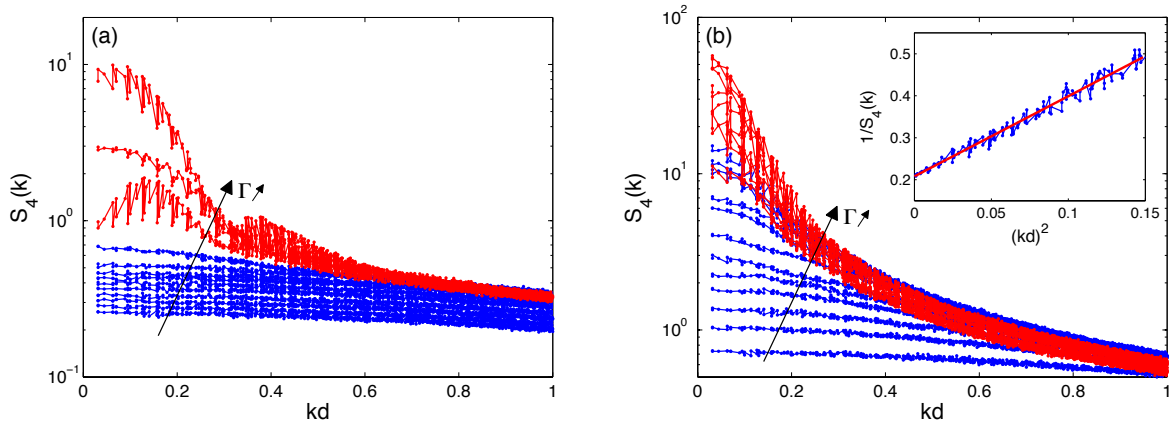

Figure 5.4.1.: 4-fold bond-orientational structure factor $S_4(k)$ for several Γ and for C1 (a) and C2 (b). The vertical axis is in $\log_{10}$ scale. Curves obtained for $\Gamma < \Gamma_c$ ($\Gamma > \Gamma_c$) are in blue (red). For both configurations and for $\Gamma < \Gamma_c$, all curves show an Ornstein-Zernike-like behavior in the limit $kd \ll 1$, $S_4(k) \approx S_4(0)/[1+(\xi_4 k)^2]$. An example is shown in the inset of (b). For $\Gamma > \Gamma_c$, there are clear differences between C1 and C2: for the former oscillations are observed, whereas for the latter curves tend to collapse together.

Fig. 5.4.1 presents $S_4(k)$ for several Γ for both configurations C1 (a) and C2 (b) in the low wavenumber limit ($kd < 1$). The acceleration increases in the direction of the arrow. We remind that $S(k)$ and $S_4(k)$ are not well defined at the solid-liquid coexistence. In particular they are not longer isotropic at the experimental time scale of measurements and fluctuations are different in each phase. Thus, care must be taken when analyzing this data above Γ_c.

An example of the Ornstein-Zernike-like behavior is shown in the inset of Fig. 5.4.1(b) for $kd < 0.15$, by rewriting $1/S_4(k) \approx (1 + (\xi_4 k)^2)/S_4(0)$. The continuous curve shows the linear fit between $1/S_4(k)$ and $(kd)^2$, from which ξ_4/d and $S_4(0)$ are measured. $S_4(k)$ obtained for C1 shows a weak Γ dependence. Above the transition it deviates strongly from Ornstein-Zernike law, showing oscillations which are reminiscent of the Fourier transform of a step function. For the C2 configuration the situation is quite different: the dependence on Γ is much stronger and curves tend to collapse together for $\Gamma \gtrsim \Gamma_c$.

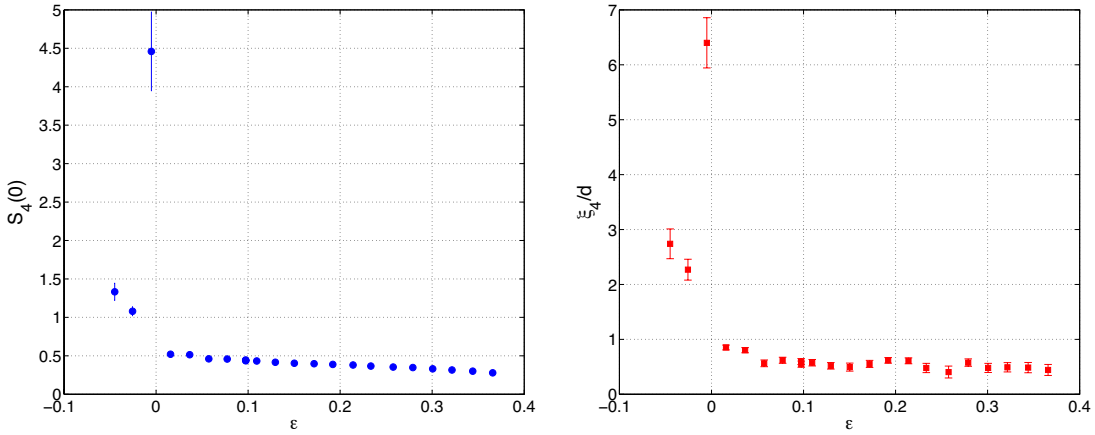

Figure 5.4.2.: $S_4(0)$ and ξ_4/d versus ε for C1 showing an abrupt change of behavior.

For configuration C1, the 4-fold bond-orientational susceptibility $S_4(0)$ and normalized correlation length ξ_4/d vary weakly as the transition is approached, as seen in Fig. 5.4.2. Defining the reduced acceleration $\varepsilon = (\Gamma_c - \Gamma)/\Gamma_c$, we obtain that for $0.005 < \varepsilon < 0.4$, $S_4(0)$ and ξ_4/d vary in the ranges $0.25 - 0.5$ and $0.5 - 0.7$ respectively. The fact that $S_4(0) < 1$ and $\xi_4/d < 1$ implies that fluctuations of the global 4-fold bond-orientational order parameter are weak and that there is practically no order correlation below the first-order-type transition. For C2 the situation is markedly different. Fig. 5.4.3 shows that $S_4(0)$ and ξ_4/d vary strongly as the transition is approached. In the limit $\varepsilon \to 0$ they both saturate, presumably due to the system's finite size. For $\varepsilon \lesssim 3 \times 10^{-2}$ they saturate to $S_4(0) \approx 20$ and $\xi_4/d \approx 10$ respectively. This figure also demonstrates that both quantities follow the critical-like behavior,

$$S_4(0) = \tilde{a}\varepsilon^{-\gamma}, \qquad \xi_4/d = \tilde{b}\varepsilon^{-\nu_\perp}, \tag{5.4.3}$$

with the critical exponents $\gamma = 1$ and $\nu_\perp = 1$. The critical divergence with ε makes it necessary to fit the Γ_c separately for each case. A detailed study of this is given in Sec. 5.7.

The adjusted critical accelerations are $\Gamma_c^{C2} = 5.09 \pm 0.07$ and $\Gamma_c^{C2} = 5.24 \pm 0.08$ respectively. Within

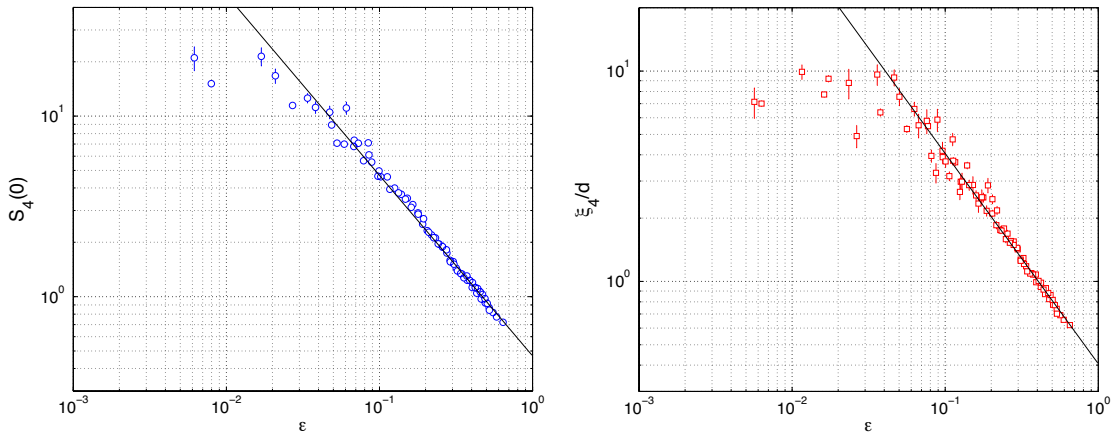

Figure 5.4.3.: $S_4(0)$ and ξ_4/d versus ε for C2. The fitted critical accelerations for each quantity are $\Gamma_c^{\mathrm{C2}} = 5.09 \pm 0.07$, $\Gamma_c^{\mathrm{C2}} = 5.24 \pm 0.08$ respectively

experimental errors both critical accelerations are very consistent, as well as with the value obtained from the supercritical behavior of ΔQ_4 ($\Gamma_c^{\mathrm{C2}} = 5.12 \pm 0.01$). Notice that now these are obtained from fits of measured quantities below the transition, whereas before, it was obtained with a fit of the order parameter above the transition.

In the hydrodynamic regime, $d/\xi_4 \lesssim kd \ll 1$, $S_4(k)$ is expected to present a power law decay

$$S_4(k) \approx \frac{C_\infty}{k^{(2-\eta)}}, \tag{5.4.4}$$

where η is the critical exponent related to the decay of the pair correlation function $g(r) \sim r^{D-2+\eta}$, with D the dimensionality. Fig. 5.4.4(a) presents $S_4(k)$ in log-log scale for various Γ. Indeed, as the transition is approached, curves tend to collapse for shorter wavelengths. They are clearly different for larger wavelengths as they converge to different static susceptibilities $S_4(0)$. In principle, η must be obtained for the Γ as close as possible to Γ_c. As the latter is not known with sufficient precision, we present in figures Fig. 5.4.4(b), Fig. 5.4.4(c) and Fig. 5.4.4(d) $S_4(k)$ for three accelerations close to Γ_c ($\Gamma = 5.04$, 5.10 and 5.12). For the highest Γ, it is not even certain that it is below the transition or not. The measured critical exponents are $\eta = 0.70 \pm 0.01$, $\eta = 0.67 \pm 0.01$ and $\eta = 0.59 \pm 0.01$ respectively. Thus, η varies rather strongly depending on $\Gamma_c - \Gamma$. Performing power law fits constraining k to the range $d/\xi_4 \leqslant kd \leqslant 1$ does not change much these results either: $\eta = 0.69 \pm 0.01$, $\eta = 0.67 \pm 0.01$ and $\eta = 0.59 \pm 0.01$ for $\Gamma = 5.04$, 5.10 and 5.12 respectively. In conclusion, there is clearly a hydrodynamic regime for which the power behavior is valid, even for a wider range than predicted. However, the measurement of η needs to be done extremely close to Γ_c. With the present data, we can state that $\eta = 2/3$ is a good estimation.

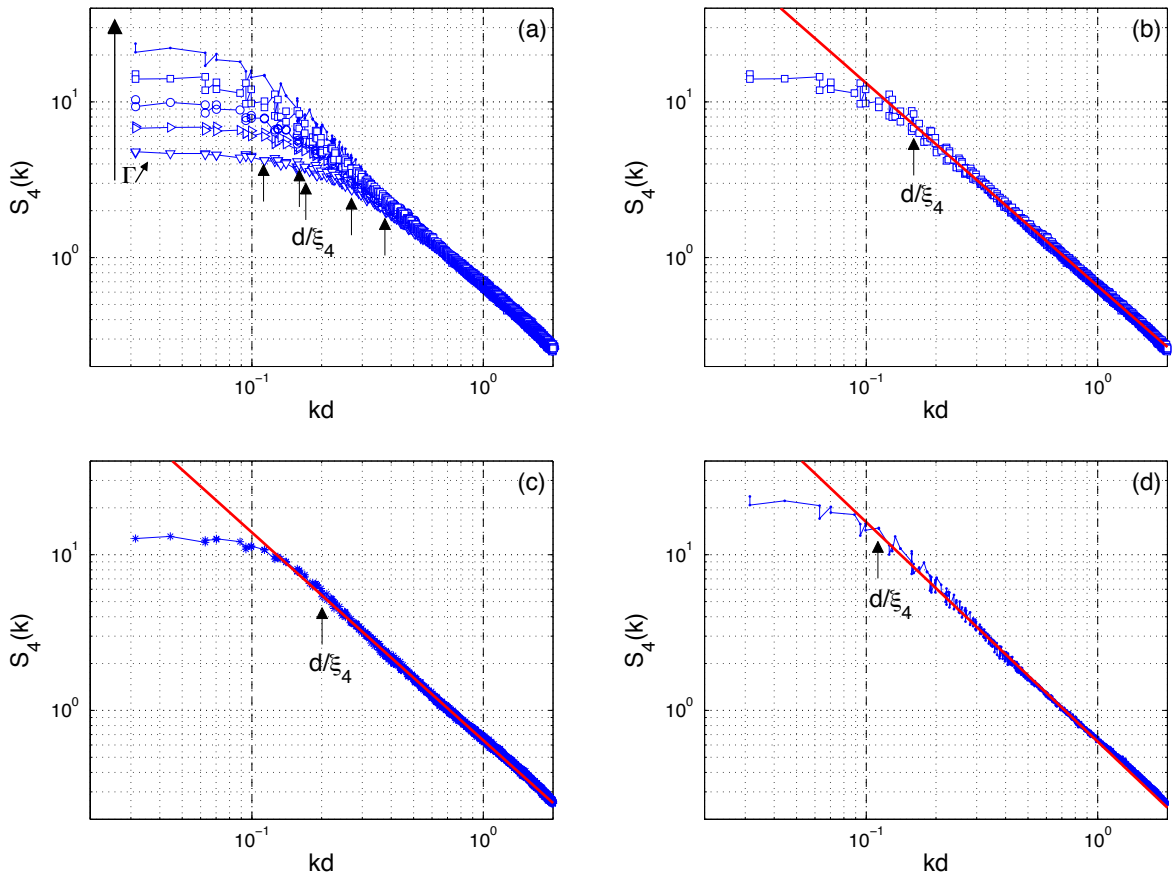

Figure 5.4.4.: (a) $S_4(k)$ in log-log scale for several Γ for C2. Acceleration increases in the direction of the long arrow, with values $\Gamma = 4.59$, 4.71, 4.84, 5.04 and 5.12. We recall that $\Gamma_c \approx 5.1$. The short arrows indicate the position of d/ξ_4 for each Γ (from right to left for increasing Γ). As expected, the hydrodynamic regime becomes wider as the transition is approached and $S_4(k)$ obeys a power law. (b), (c) and (d) present results for the three highest accelerations such that $\Gamma \lesssim \Gamma_c$, which are plotted separately for clarity ($\Gamma = 5.04$, 5.10 and 5.12 respectively, the second is not shown in (a) for clarity). Continuous lines show the power law fits $S_4(k) = C_\infty / k^{(2-\eta)}$, obtained for wave vectors in the range $0.1 \leqslant kd \leqslant 1$. The respective critical exponents are $\eta = 0.70 \pm 0.01$ (b), $\eta = 0.67 \pm 0.01$ (c) and $\eta = 0.59 \pm 0.01$ (d).

5.5. Dynamic 4-fold bond-orientational structure factor $F_4(k,\tau)$ and critical dynamics

As a final evidence of the observed criticality we now turn to the characterization of the relaxation time of the metastable solid clusters. The relaxation time is computed through the two-time bond-orientational correlation function

$$F_4(\vec{k},\tau) = \frac{\langle \delta\widehat{Q}_4(\vec{k},t+\tau)\delta\widehat{Q}_4(\vec{k},t)^* \rangle}{N}, \tag{5.5.1}$$

where * stands for the complex conjugate and $\delta\widehat{Q}_4(\vec{k},t) = \widehat{Q}_4(\vec{k},t) - \langle\widehat{Q}_4(\vec{k},t)\rangle$.

Fig. 5.5.1 presents the dynamic 4-fold bond-orientational structure factor $F_4(k,\tau)$ for $\Gamma = 4.8$ and for several wavelengths kd in semi-log scale. Indeed, this correlation function shows an exponential decay, $F_4(k,\tau) \approx F_4(k,0)\exp(-\tau/\tau_4)$, from which the relaxation time τ_4 is measured.

Here, we also obtain a critical-like behavior, which is presented in Fig. 5.5.2(a). The best fit is obtained for $\tau_4/T = \tilde{c}\varepsilon^{-\nu_{||}}$ with $\nu_{||} = 2$, for which the adjusted critical acceleration is $\Gamma_c^{C2} = 5.12 \pm 0.07$. The relaxation time also seems to saturate for small ε, which occurs at smaller ε for lower k, that is for fluctuations of larger size. Fig. 5.5.2(b) confirms that $\tau_4 \sim (\xi_4)^z$, with a dynamical exponent $z = \nu_{||}/\nu_\perp = 2$. As usual, there is critical slowing down in the dynamics. As a consequence, close to the critical point, stationary states are obtained after a long relaxation has taken place. Taken that into account, all Γ ramps for C2 are slow. Also, averages are taken for long times.

Five critical exponents have been obtained from the analysis of the order parameter. In the standard notation of critical phenomena these are: $\beta = 1/2$, $\gamma = 1$, $\eta = 0.67$, $\nu_\perp = 1$, and $z = 2$. In equilibrium, the scaling hypothesis predicts relations among the critical exponents. It is worth mentioning that the relation obtained in Sec. 2.3.3, $\gamma = (2-\eta)\nu_\perp$, is not satisfied; while $\alpha+2\beta+\gamma = 2$ and $\nu_\perp D = 2-\alpha$ ($D = 2$ is the spatial dimension) can be satisfied simultaneously if $\alpha = 0$. This exponent, associated in equilibrium to the specific heat divergence, has no interpretation out of equilibrium. The order parameter in the present case is a non-conserved complex scalar field. Its dynamics, however, is not expected to be autonomous even close to the critical point as density fluctuations are needed to create the ordered phase. Although it has been shown that the transition

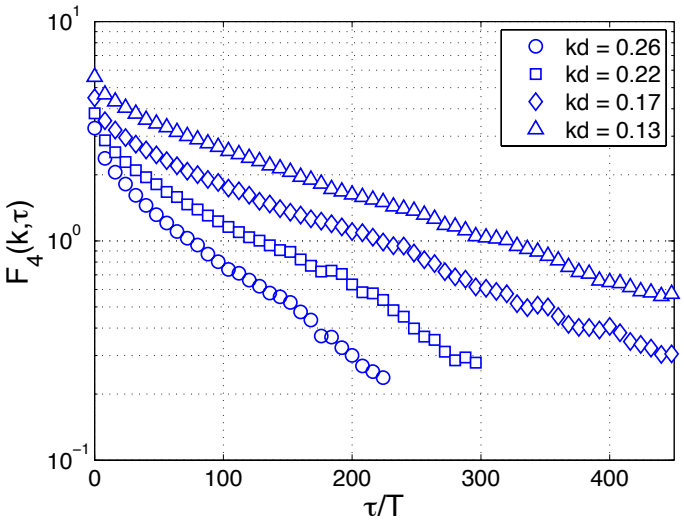

Figure 5.5.1.: Dynamic 4-fold bond-orientational structure factor $F_4(k,\tau)$ for several kd and $\Gamma = 4.8$, which shows an exponential decay. Only data above de noise threshold for this correlation function is shown for each kd.

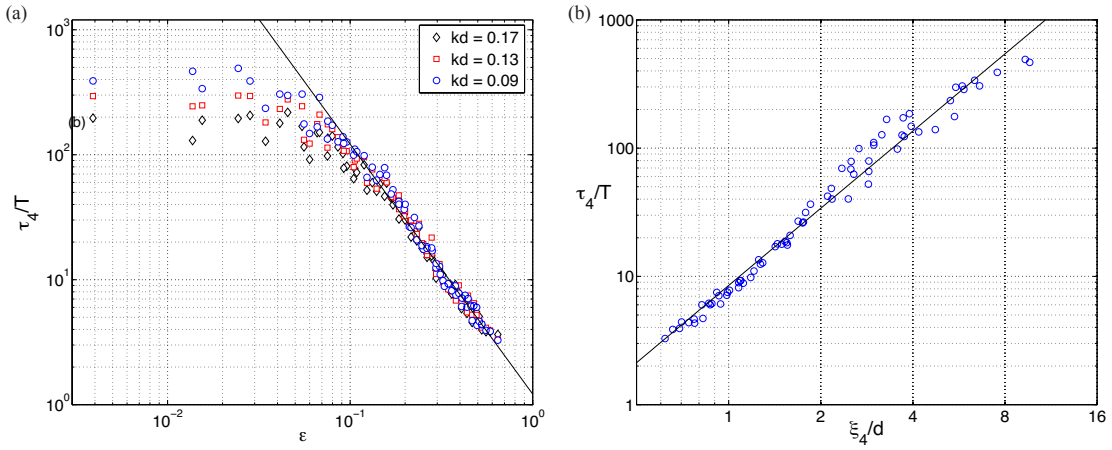

Figure 5.5.2.: (a) τ_4/T versus ε for C2, for three different low k. The continuous line shows the critical power law fit, with exponent $\nu_{||} = 2$ for τ_4. The fitted critical acceleration is $\Gamma_c^{C2} = 5.12 \pm 0.07$. (b) τ_4 versus ξ_4 for $\varepsilon > 0.03$. The continuous line shows a fit $\tau_4 \sim (\xi_4)^z$, with the dynamical exponent $z = \nu_{||}/\nu_\perp = 2$.

dynamics is mediated by waves [8], momentum density decays fast due to friction. Therefore, the most appropriate description in the theory of dynamical critical phenomena is model C, in which a non-conserved order parameter is coupled to a conserved non-critical density [49]. In this case [49, 62] and in extensions to non-equilibrium dynamics [78] the dynamical exponent is predicted to be $z = 2 + \alpha/\nu_\perp$, consistent with the measurements if $\alpha = 0$.

5.6. Universality

In this section we study whether the exponents presented above, in which the thin ITO coated glass plates (25 nm thickness) were used, are actually universal. That is, what happens if we change one or some of the microscopic parameters of our system? Do the critical exponents will turn out to be the same? As was already shown in Fig. 5.3.5, the order parameter $\langle |Q_4| \rangle$ that describes the transition studied actually presents a critical behavior, and whose critical exponent is $\beta = 1/2$. This was shown to be so for each ITO coating thickness (25 nm and 750 nm). The critical acceleration obtained for both sets of glasses are $\Gamma_c = 5.12 \pm 0.01$ and $\Gamma_c = 4.48 \pm 0.03$ respectively.

By looking at the 4-fold bond-orientational structure factor $S_4(k)$ we find that it also follows a Lorentzian described by the Ornstein-Zernike theory, from which we can extract the susceptibilty $S(0)$ and the correlation length ξ_4. These two quantities are shown in Fig. 5.6.1.

Hence, with the new set of glass plates we observe basically the same phenomenon. That is, both $S(0)$ and ξ_4 follow critical laws, and due to finite size effects, they saturate as the transition is approached. Accordingly, by doing the same kind of analysis explained earlier, it is possible to obtain the critical exponents as well as the critical acceleration Γ_c from each quantity independently.

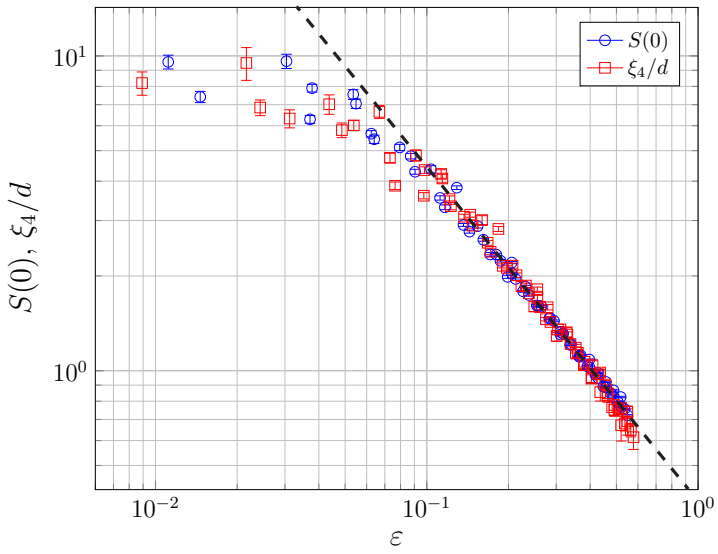

Figure 5.6.1.: $S(0)$ (○) and ξ_4 (□) versus $\varepsilon = (\Gamma_c - \Gamma)/\Gamma_c$ for configuration C2 using the ITO coated glass plates of 750 nm thickness. The fitted critical accelerations are $\Gamma_c = 4.43 \pm 0.06$ and $\Gamma_c = 4.58 \pm 0.06$ respectively.

The critical exponents turn out to be $\gamma = 1$ and $\nu_\perp = 1$, *i.e.* within experimental error, they are the *same* to the ones obtained using the thin glass plates. The adjusted critical accelerations are $\Gamma_c = 4.43 \pm 0.06$ and $\Gamma_c = 4.58 \pm 0.06$, obtained from $S(0)$ and ξ_4 respectively. Within experimental errors both critical accelerations are very consistent, as well as with the value obtained from the supercritical behavior of ΔQ_4 ($\Gamma_c = 4.48 \pm 0.03$). As noticed in Sec. 5.4, these critical accelerations are obtained from fits of measured quantities below the transition, whereas before, it was obtained with a fit of the order parameter above the transition.

By following the same procedure used in the previous section, it is possible to compute the dynamic 4-fold bond-orientational structure factor $F_4(k,\tau)$. Similarly to the results shown for the first set of glass plates, this correlation function shows an exponential decay, $F_4(k,\tau) \approx F_4(k,0)\exp(-t/\tau_4)$, from which the relaxation time τ_4 is measured. This time is shown in Fig. 5.6.2 for three different low wavenumbers k.

Here, we also obtain a critical-like behavior, in which the critical exponent is $\nu_\parallel = 2$ and the critical acceleration is $\Gamma_c = 4.46 \pm 0.03$. Once again, the value obtained for Γ_c is in good agreement with the values obtained from $S(0)$, ξ_4 and ΔQ_4. Moreover, τ_4 also shows a saturation for small ε, which occurs at smaller ε for lower k, that is for fluctuations of larger size.

Finally, by looking at the anomalous exponent η we need to analyze the behavior of $S_4(k)$ in the hydrodynamic regime when the system is very close to the critical point. Given that we can't know for sure where the critical point is, we study the behavior of $S_4(k)$ at three different $\Gamma \lesssim \Gamma_c$.

As it is clear from Fig. 5.6.3, $S_4(k)$ shows a power law decay in a hydrodynamic regime even wider than predicted. The measured critical exponents for the three accelerations close to Γ_c ($\Gamma = 4.29$,

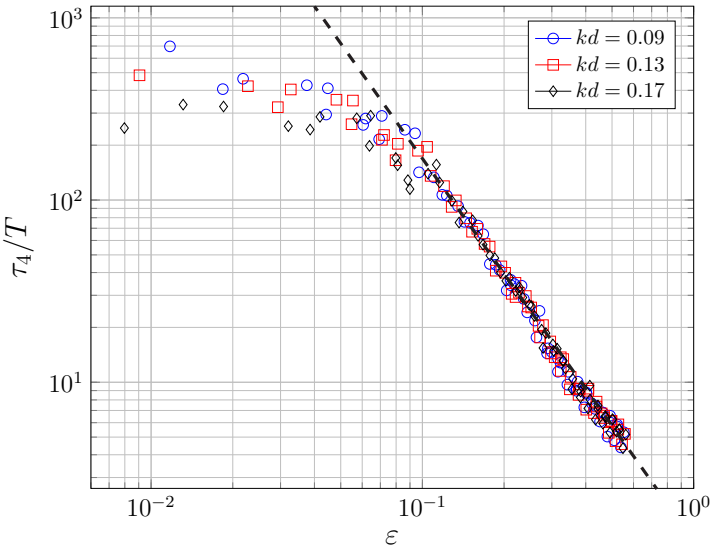

Figure 5.6.2.: τ_4/T versus $\varepsilon = (\Gamma_c - \Gamma)/\Gamma_c$ for three different low k using the ITO coated glass plates of 750 nm thickness. The fitted acceleration is $\Gamma_c = 4.46 \pm 0.03$. The value obtained for the critical exponent is $\nu_\parallel = 2$, which implies that $z = \nu_\parallel/\nu_\perp = 2$.

4.41 and 4.52) are $\eta = 0.87 \pm 0.01$, $\eta = 0.67 \pm 0.01$ and $\eta = 0.63 \pm 0.01$ respectively. Hence, with the existing data we can say that $\eta = 2/3$ is a good approximation. Moreover, it takes the same value obtained for the previous set of plates.

As a conclusion of this section, we can say that by changing the microscopic properties of our system (such as the friction coefficient) we in fact change the critical point ($\Gamma_c^{before} \approx 5.1$, $\Gamma_c^{after} \approx 4.5$). Nevertheless all the five exponents independently measured turn out to be the same. In other words, even though our system is out of equilibrium, it actually presents the property of universality.

5.7. Appendix: Determination of fittings parameters and error analysis

It has been shown that the solid-liquid-type transition for configuration C2 is continuous. It is straightforward to demonstrate that the susceptibility $S_4(0)$, correlation length ξ_4 and relaxation time τ_4 follow diverging critical-like behaviors

$$S_4(0) = \tilde{a}\,\varepsilon^{-\gamma}, \qquad \frac{\xi_4}{d} = \tilde{b}\,\varepsilon^{-\nu_\perp}, \qquad \frac{\tau_4}{T} = \tilde{c}\,\varepsilon^{-\nu_{||}}, \tag{5.7.1}$$

where $\varepsilon = (\Gamma_c - \Gamma)/\Gamma_c$ is the reduced acceleration and Γ_c is a critical acceleration. However, the precise determination of Γ_c, and therefore the corresponding power law exponents, is not simple. Initial fits give Γ_c in the range $5.1 - 5.6$ for the thin plates or $4.4 - 4.9$ for the thicker plates, and γ

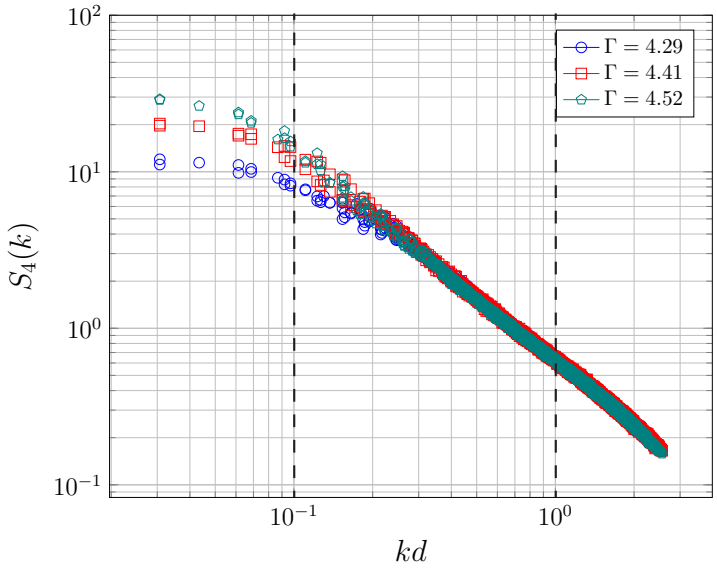

Figure 5.6.3.: $S_4(k)$ in log-log scale for three different values of Γ using the ITO coated glass plates of 750 nm thickness. As expected, the hydrodynamic regime becomes wider as the transition is approached and $S_4(k)$ obeys a power law. The fits $S_4(k) = C_\infty k^{2-\eta}$ are obtained for wave vectors in the range $0.1 \leqslant kd \leqslant 1$. The critical exponents obtained for $\Gamma = 4.29$, 4.41 and 4.52 are $\eta = 0.87 \pm 0.01$, $\eta = 0.67 \pm 0.01$ and $\eta = 0.63 \pm 0.01$ respectively.

between ≈ 1 and ≈ 1.8 and similar large variations for $\nu_\perp$ and $\nu_{||}$. Additionally, the fitted Γ_c can be quite different depending from which quantity they are obtained. The lack of precision is due to the arbitrariness in the choice of the range Γ to be used for the fit.

The most robust procedure that we have found is the analysis of the inverses of these quantities. Fig. 5.7.1 presents $S_4(0)^{-1}$, $(\xi_4/d)^{-1}$ and $(\tau_4/d)^{-1/2}$ as functions of Γ. They all seem to be linear functions of the acceleration, with some rounding at $\Gamma \sim 5$ (or $\Gamma \approx 4.5$, depending on the plates' thickness). Thus, considering the definitions given in equations 5.7.1, we expect $\gamma \approx \nu_\perp \approx 1$ and $\nu_{||} \approx 2$. In order to check the robustness of the critical-like behavior we perform two types of fits, one with an adjustable exponent and other with the exponent fixed to the expected value. These fits are performed between $\Gamma_i = 2.5$ and Γ_{fit}, which is varied between ≈ 2.9 and 5.5. This allows to obtain the fitted parameters as functions of Γ_{fit}, as well as the fit goodness R^2 for each adjustment. Fig. 5.7.2 presents the result of such procedure in the case of an adjustable exponent γ for $S_4(0)^{-1}$. Here, only results with high goodness parameter are shown, $R^2 > 0.98$. Fig. 5.7.3 presents the same but with a fixed exponent $\gamma = 1$. This procedure is realized for all three inverse quantities. The summary of the results, with adjustable and fixed exponents is presented in Tab. 5.1. Each parameter is computed as the average of the set of adjusted parameters obtained for the different Γ_{fit} values (for example by averaging the data shown in Fig. 5.7.2 and Fig. 5.7.3 for the parameters related to $S_4(0)$, with adjustable and fixed exponent γ respectively). The errors correspond to the standard deviation of these results. Our conclusion is that one can indeed fix the exponents to $\gamma = \nu_\perp = 1$ and $\nu_{||} = 2$.

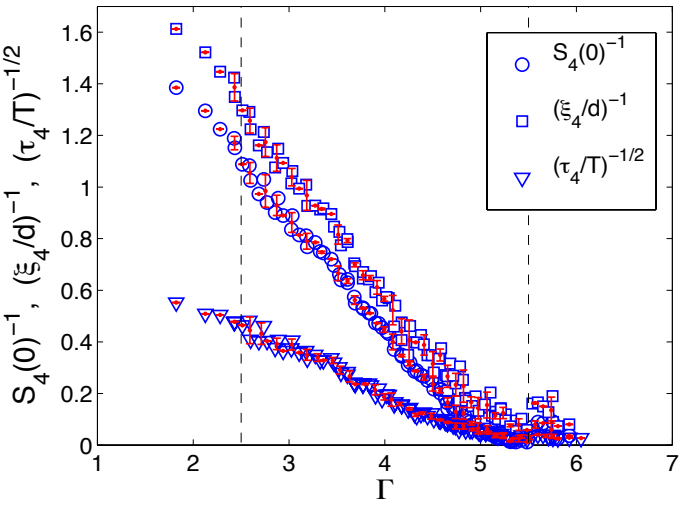

Figure 5.7.1.: Inverses of $S_4(0)$, ξ_4/d and $\sqrt{\tau_4/T}$ (for $kd = 0.09$) as functions of Γ for the thin plates. Raw data is represented by open circles. Window averaged data is shown by solid squares. The averaging windows are obtained by dividing the complete Γ range en 50 equal segments. The vertical dashed lines show the minimum Γ for each fit ($\Gamma_{\rm i} = 2.5$) and the maximum possible value ($\Gamma_{\rm fit} = 5.5$).

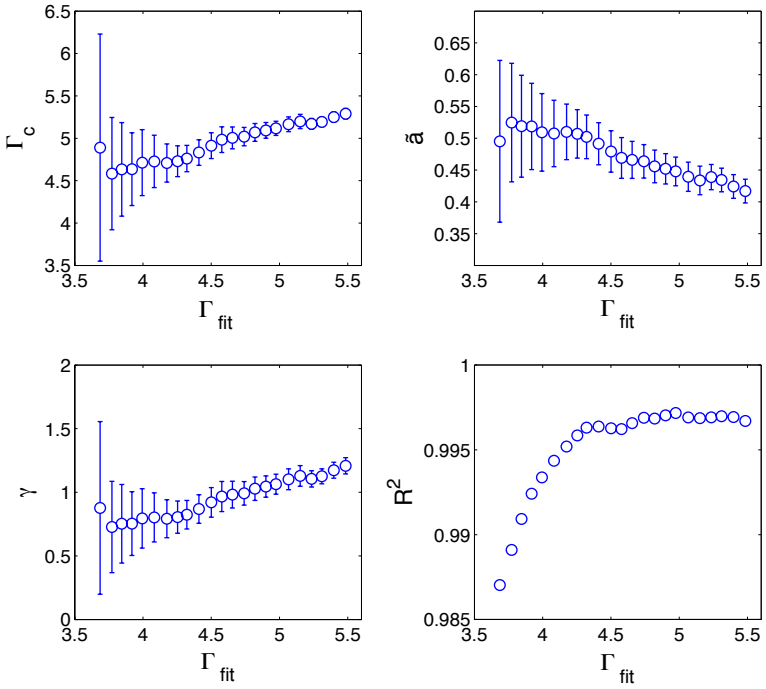

Figure 5.7.2.: Adjusted parameters for $1/S_4(0) = \tilde{a}^{-1}\varepsilon^{\gamma}$ as functions of Γ_{fit}, with Γ constrained to the range $\Gamma_{\text{i}} - \Gamma_{\text{fit}}$. Data presented for the thin plates case, the difference with the thicker plates is that there is a shifting in Γ_c. From these results, average values and their respective standard deviations are computed for each adjustable parameter.

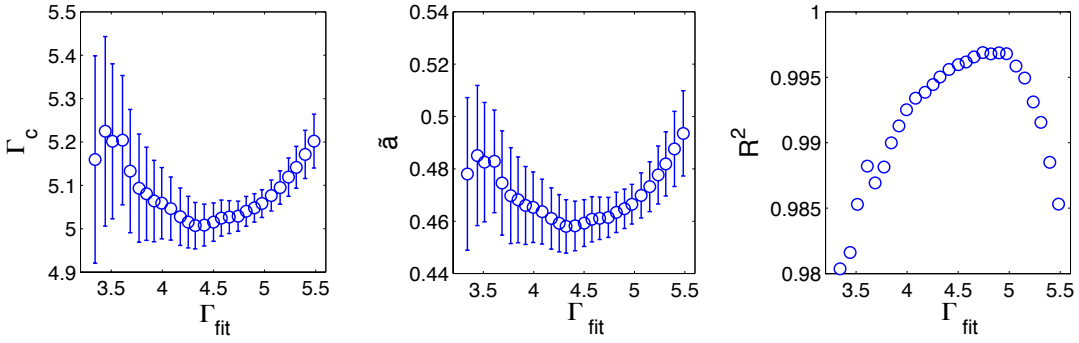

Figure 5.7.3.: Adjusted parameters for $1/S_4(0) = \tilde{a}^{-1}\varepsilon$ as functions of Γ_{fit}, with Γ constrained to the range $\Gamma_{\text{i}} - \Gamma_{\text{fit}}$. In this case the exponent is fixed ($\gamma = 1$). From these results, average values and their respective standard deviations are computed for each adjustable parameter. Data presented for the thin glass plates (25 nm thickness).

Thin ITO coated plates (25 nm)		
Free critical exponents		
$S_4(0)$	ξ_4/d	τ_4/T
$\gamma = 0.95 \pm 0.15$	$\nu_\perp = 0.97 \pm 0.21$	$\nu_\parallel = 1.98 \pm 0.50$
$\Gamma_c = 4.94 \pm 0.22$	$\Gamma_c = 5.11 \pm 0.35$	$\Gamma_c = 5.06 \pm 0.38$
$\tilde{a} = 0.47 \pm 0.03$	$\tilde{b} = 0.41 \pm 0.04$	$\tilde{c} = 1.11 \pm 0.13$
Fixed critical exponents		
$S_4(0)$	ξ_4/d	τ_4/T
$\gamma = 1$	$\nu_\perp = 1$	$\nu_\parallel = 2$
$\Gamma_c = 5.09 \pm 0.07$	$\Gamma_c = 5.24 \pm 0.08$	$\Gamma_c = 5.12 \pm 0.07$
$\tilde{a} = 0.47 \pm 0.01$	$\tilde{b} = 0.41 \pm 0.01$	$\tilde{c} = 1.10 \pm 0.03$

Thick ITO coated plates (750 nm)		
Free critical exponents		
$S_4(0)$	ξ_4/d	τ_4/T
$\gamma = 1.10 \pm 0.16$	$\nu_\perp = 1.10 \pm 0.03$	$\nu_\parallel = 1.98 \pm 0.21$
$\Gamma_c = 4.54 \pm 0.18$	$\Gamma_c = 4.73 \pm 0.03$	$\Gamma_c = 4.55 \pm 0.18$
$\tilde{a} = 0.39 \pm 0.03$	$\tilde{b} = 0.35 \pm 0.03$	$\tilde{c} = 1.14 \pm 0.07$
Fixed critical exponents		
$S_4(0)$	ξ_4/d	τ_4/T
$\gamma = 1$	$\nu_\perp = 1$	$\nu_\parallel = 2$
$\Gamma_c = 4.43 \pm 0.06$	$\Gamma_c = 4.58 \pm 0.06$	$\Gamma_c = 4.46 \pm 0.03$
$\tilde{a} = 0.41 \pm 0.01$	$\tilde{b} = 0.37 \pm 0.01$	$\tilde{c} = 1.17 \pm 0.01$

Table 5.1.: Average adjusted parameters with free and fixed critical exponents for both set of glass plates. Each parameter is computed as the average of the set of adjusted parameters obtained for the different Γ_{fit} values. The errors correspond to the standard deviation of these results. τ_4 corresponds to the relaxation times obtained for $kd = 0.09$.

6. Capillary-like fluctuations

« Science is facts; just as houses are made of stones, so is science made of facts; but a pile of stones is not a house and a collection of facts is not necessarily science. »

Henri Poincaré

One of the most noticeable collective motion of noncohesive granular matter is clustering under certain conditions. In particular, when a quasi-two-dimensional monolayer of monodispersed noncohesive particles is vertically vibrated, a solid-liquid-like transition occurs when the driving amplitude exceeds a critical value. Here the physical mechanism underlying particle clustering relies on the strong interactions mediated by grain collisions, rather than on grain-grain cohesive forces. In average, the solid cluster resembles a drop, with a striking circular shape. We experimentally investigate the coarse-grained solid-liquid interface fluctuations, which are characterized through the static and dynamic correlation functions in the Fourier space. These fluctuations turn out to be well described by the capillary wave theory, which allows us to measure the solid-liquid interface surface tension and mobility once the granular "thermal" kinetic energy is determined. Despite that the system is strongly out of equilibrium and that the granular temperature is not uniform, there is energy equipartition at the solid-liquid interface, for a relatively large range of angular wave numbers. Furthermore, both surface tension and mobility are consistent with a simple order of magnitude estimation considering the characteristic energy, length, and time scales, which is very similar to what can be done for atomic systems.

6.1. Overview

Dry granular systems are usually considered to have no surface tension. However, several recent studies show that non- cohesive or very weakly cohesive granular materials develop phenomena driven by surface tension, which can be low but not zero. Some remarkable examples are the Rayleigh-Taylor-like instability in tapped powders [79] and the interfacial instabilities in falling granular streams, in air [80], and in a vacuum [81]. In other cases, granular systems are shown to behave as a zero-surface-tension liquid, such as for particle sheets (analog to "water bells") created by a granular jet impacting a target [82] and fingering in a granular Hele-Shaw system [83]. In some cases, a hydrodynamic derivation taking the zero-surface- tension limit succeeds in describing the observations [82, 83], but in others a finite surface tension is needed [84]. Studying the spinodal

decomposition in a vibrated noncohesive granular media, recent experiments suggest that the cluster coalescence is consistent with a curvature driven force, and numerical simulation showed stress tensor anisotropies, linked to surface tension [85]. The point is to understand how capillary-like features can emerge out of collections of particles that are known to be almost or completely noncohesive. Considering either the flow of interstitial air [79, 80] or nano-Newton cohesion forces in the case of very low external forcing [81], a low effective surface tension depending on the granular system dynamics was estimated.

As was pointed out earlier, our system can present a transition from a completely fluidized state to the coexistence of a liquid state with solid (ordered) clusters [53, 8, 6]. It has been recently shown that such coexistence is triggered by a negative compressibility, as observed in a similar gas-liquid van der Waals granular transition [69, 73], and that density waves propagate in the system [8]. In Chapter 5 we showed that depending on the vertical height and filling density the transition can be of first- or second-order type. For both cases density fluctuations do not show strong variations at the transition, but local order varies strongly, either abruptly or continuously respectively, with a critical-like behavior in the second case.

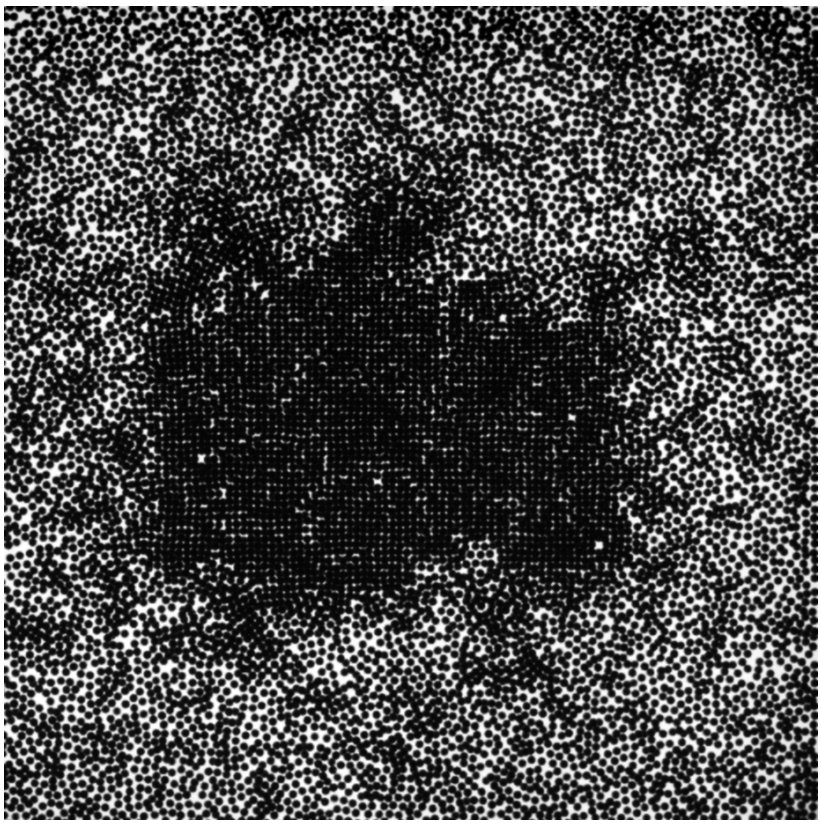

Figure 6.1.1.: Raw image showing both liquid and solid phases.

In this chapter we consider the stationary regime of phase coexistence for both the continuous and abrupt transitions. Above a critical driving amplitude a unique solid cluster is observed. For the continuous transition, as it is critical with an associated nonconserved order parameter, the system

spontaneously develops regions of one phase inside the other. For the abrupt case, some defects are present in the solid phase but, as shown before, it is much better defined. However for both cases, in average, the granular cluster exhibits a striking circular shape, like a drop (see Fig. 6.1.1). We focus on the characterization of the liquid-solid-like interface, which we make coarse-grained, becoming smooth and simply connected. Our approach is similar to the one proposed in [80], in analogy with condensed matter at a molecular scale where thermal agitation induces capillary waves that deform an interface. The coarse-graining procedure, which implementation is described below, limits the analysis of the capillary waves to large wavelengths and long time scales. Thus, in this coarse-grained description, we aim to discuss to what extent it is valid to use some of the concepts of effective surface tension and interface mobility.

For the results first presented below we use the configuration C2, *i.e.* $N = 11504$ stainless steel spherical particles in a shallow box with transverse dimensions $L_x = L_y = 100d$ and height $L_z = 1.94d \pm 0.02d$, where $d = 1$ mm is the particle diameter. Two videos were analyzed, with 3500 images acquired at 500 fps using the thin ITO coated glass plates (25 nm thickness). The filling fraction is $\phi = N\pi d^2/4L^2 = 0.904$, corresponding to 31% of volumetric filling. We used ITO coated glass plates 25nm thickness and $7.5\mu\Omega$m resistivity. As explained before, for this configuration, a second-order solid-liquid-like transition occurs when the dimensionless acceleration $\Gamma = A\omega^2/g$ reaches a critical value $\Gamma_c \approx 5.1$, at $f = 2\pi/\omega = 80$ Hz. In the framework of the solid cluster's characterization, the present study is done at $\Gamma = 6.30 \pm 0.03$ and $f = 80$ Hz.

Later, we present results with the thick ITO coated glass plates (750 nm thickness) and where the static quantities were obtained from videos acquired at 10 fps, whereas the dynamical quantities were obtained from videos at 500 fps.

To distinguish the liquid phase from the solid phase, which has square symmetry, we use a criterion based on Q_4, the 4-fold non-conserved local order parameter [53]

$$Q_4^j = \frac{1}{N_j} \sum_{s=1}^{N_j} e^{4i\alpha_s^j}. \tag{6.1.1}$$

Here N_j is the number of nearest neighbors of particle j and α_s^j is the angle between the neighbor s of particle j and the x axis. For a particle in a square lattice, $|Q_4^j| = 1$. If $|Q_4^j| \geqslant 0.7$, which has been determined empirically (see Sec. 4.2), the particle is considered in the solid phase; otherwise, it is in the liquid phase. Then, using coarse-grained polar coordinates ($\Delta\theta = 2°$), we detect 180 interfacial particles in each image. The origin of the polar coordinate system is fixed at the time-averaged center of mass of the solid-like particles. For C2 and $\Gamma = 6.3$ (ITO 25 nm thickness) the time-averaged interface exhibits a circular shape with a mean radius of $R_0/d = 22.7 \pm 0.4$. We have verified that a slightly different $\Delta\theta$, say between 1.5 and 2.4, gives the same results when the spectra of radius and kinetic energy fluctuations are analyzed (later in Sec. 6.5 for further details). For $\Delta\theta \sim 1°$, the interface detection presents errors due to the crystallographic order of the solid cluster: occasionally the corresponding angles are close to a plane direction implying that a particle can be detected near the center of mass, making the interface very noisy. Additionally, for $\Delta\theta \gtrsim 2.4°$ the detection acts as a filter for larger m numbers and affects the spectrum accordingly.

6.2. Non-equilibrium free energy

In this study, we consider a curve-driven interface behavior for the steady state cluster. In condensed matter, from the classical solid to liquid phases, any interface is microscopically rough due to the competition between thermal energy and minimization of surface area [86]. The grain-boundary or solid-liquid interface evolution is involved in processes such as crystallization in solution [87] or dendritic solidification [88], and controls structural and mechanical properties of many materials [89]. The first interfacial parameter studied is the solid-liquid interface stiffness, $\tilde{\gamma} = \gamma + \gamma''$, where γ is the surface tension and γ'' its second derivative with respect to the spatial coordinate. This is valid in the small slope approximation, as it is in our case (see Sec. 6.6). In our experiment, we actually measure $\tilde{\gamma}$, but for simplicity we will use γ and refer to it as surface tension. The correction γ'' is indeed usually small [88]. The second parameter is the solid-liquid interface mobility M, defined by $V = M\gamma\kappa$, with V the interface velocity and κ the interface curvature. Inspired by theoretical and numerical studies on interfacial properties of molecular systems [90, 91], and on an experimental study of colloidal crystals [92], we attempt to obtain these physical quantities applying a capillary wave description. In analogy to the capillary theory in condensed matter, we assume that there is a functional, analog to the free energy, that is minimized in the stationary state and allows to obtain the dynamics close to the stationary state. This assumption, although no fully justified in non-equilibrium systems, is made for simplicity and verified *a posteriori* as its predictions are consistent with the experimental results. To follow the analogy with equilibrium systems, this functional will be refered as *non-equilibrium free energy*.

First, we consider the interface contribution to the non-equilibrium free energy E_γ. In two dimensions, it is related to the cluster's arc length and by an effective surface tension γ such as

$$E_\gamma = \gamma \int_0^{2\pi} \sqrt{R^2 + (\partial_\theta R)^2}\, d\theta, \tag{6.2.1}$$

with $R(\theta, t)$ the cluster's radius.

The total non-equilibrium free energy has an additional term, because if we minimize the solid-liquid interface non-equilibrium free energy, the absolute minimum is at $R = 0$, that is, no droplet. In principle, this is solved by adding a Lagrange multiplier that fixes (in average) the total mass (or equivalently, the area). Then, the total non-equilibrium free energy should be

$$E = \gamma \int_0^{2\pi} \sqrt{R^2 + (\partial_\theta R)^2} d\theta - \mu \int_0^{2\pi} \frac{R^2}{2} d\theta. \tag{6.2.2}$$

where μ is the Lagrange multiplier, which apart from a proportional factor is equivalent to the effective chemical potential. The negative sign is arbitrary and it is there to further simplify the notation. The equilibrium droplet is obtained by minimizing the non-equilibrium free energy. First, non-uniformities in the radius increase the non-equilibrium free energy, so we assume a circular shape $R = R_0$. Then, the non-equilibrium free energy is

$$E = 2\pi\gamma R_0 - \mu\pi R_0^2. \tag{6.2.3}$$

To extreme E we take the derivative and equal it to zero. The solution is

$$R_0 = \frac{\gamma}{\mu}, \tag{6.2.4}$$

or equivalently $\mu = \gamma/R_0$. Note that this last expression shows that we have correctly chosen the sign for μ in 6.2.2. Now, we linearize about R_0. That is, $R(\theta) = R_0 + \epsilon\delta R(\theta)$ and keep up to quadratic terms in ϵ in the energy. Doing the expansion we obtain

$$E = \gamma \int_0^{2\pi} \left[R_0 + \epsilon\delta R + \epsilon^2 \frac{(\partial_\theta \delta R)^2}{2R_0} \right] d\theta - \frac{\mu}{2} \int_0^{2\pi} \left[R_0^2 + 2\epsilon R_0 \delta R + \epsilon^2 \delta R^2 \right] d\theta. \tag{6.2.5}$$

Recalling that $\mu = \gamma/R_0$ the linear terms cancel (as it always should happen when doing an expansion about an equilibrium state) and the final result is

$$E = \pi\gamma R_0 + \frac{\epsilon^2\gamma}{2R_0} \int_0^{2\pi} \left[(\partial_\theta \delta R)^2 - \delta R^2 \right] d\theta \tag{6.2.6}$$

This expression does not describe our system. Indeed, the non-equilibrium free energy increases due to deformations of the interface but is decreases when changing globally the radius. That is, R_0 is unstable under changes of the radius. In fact, this inconsistency could have been predicted when looking at 6.2.3: it is clear that R_0 is a maximum and, therefore, un unstable equilibrium.

The origin of the problem

The problem originates in the election of the thermodynamic ensemble. Indeed, when using μ we moved to the grand canonical ensemble in which the number of particles is not fixed. What we have found is what is called the Critical Nucleus in the *Homogeneous Nucleation Theory*. This is the size we have to overcome to create a droplet that, after reaching that size, will grow indefinitely. Droplets smaller than this radius will shrink again due to the energy cost of the free surface. The growth without bound is possible because we are in the grand canonical ensemble where we have fixed μ and, therefore, there are always available particles to change phase.

The solution

The solution consists of changing the ensemble to one in which we fix the total number of particles. This is a complicated ensemble to make calculations because we have to take into account the physical fact that when particles are moved from one phase to another, the *supersaturation* changes and therefore the chemical potential is dynamically adjusted. This is precisely what happens when, working in the canonical ensemble, we prepare the system with a density between the liquid and solid densities. Clusters of the solid phase will be created, decreasing the density of the remainder

part until it reaches the liquid density. To model this solution, we can write in the case of a circular droplet

$$E = 2\pi\gamma R_0 - \mu(R_0)\pi R_0^2. \tag{6.2.7}$$

If μ is a decreasing function of R_0, a second equilibrium appears (this time stable) at a larger value of R_0. This is the final equilibrium radius of the droplet.

6.3. Full model

Equivalently of using a chemical potential that depends on the radius, we modify 6.2.2 to have a non-linear dependence on the total mass of the cluster, expression that will be easier to manipulate

$$E = \gamma \int_0^{2\pi} \sqrt{R^2 + (\partial_\theta R)^2} d\theta - f\left(\int_0^{2\pi} \frac{R^2}{2} d\theta \right), \tag{6.3.1}$$

where f is a nonlinear function. For a cluster of area much smaller than the total system area, $f(x) = \mu x$ as in 6.2.2. Again, an expansion up to quadratic terms is done obtaining

$$\begin{aligned} E &= \gamma \int_0^{2\pi} \left[R_0 + \epsilon\delta R + \epsilon^2 \frac{(\partial_\theta \delta R)^2}{2R_0} \right] d\theta \\ &\quad - \left\{ f\left(\pi R_0^2\right) + \epsilon f'\left(\pi R_0^2\right) R_0 I_1 + \frac{\epsilon^2}{2} \left[f'\left(\pi R_0^2\right) I_2 + f''\left(\pi R_0^2\right) R_0^2 I_3 \right] \right\}, \end{aligned} \tag{6.3.2}$$

where

$$I_1 = \int \delta R d\theta \tag{6.3.3}$$

$$I_2 = \int (\delta R)^2 d\theta \tag{6.3.4}$$

$$I_3 = \left(\int \delta R d\theta \right)^2. \tag{6.3.5}$$

The equilibrium radius is such that the linear terms should cancel (as to have a global minimum). This condition gives

$$f'(\pi R_0^2) R_0 = \gamma, \tag{6.3.6}$$

that once substituted in 6.3.2 gives

$$E = E_0 + \frac{\epsilon^2 \gamma}{2R_0} \int_0^{2\pi} \left[(\partial_\theta \delta R)^2 - \delta R^2 \right] d\theta - \frac{\epsilon^2}{2} f''(\pi R_0^2) R_0^2 \left(\int_0^{2\pi} \delta R d\theta \right)^2. \tag{6.3.7}$$

Fourier-transforming the last expression gives

$$E = E_0 + \frac{\epsilon^2 \pi\gamma}{R_0} \sum_m |\widetilde{\delta R}_m|^2 (m^2 - 1) - \frac{\epsilon^2}{2} f''(\pi R_0^2)(2\pi R_0)^2 |\widetilde{\delta R}_0|^2, \tag{6.3.8}$$

where

$$\widetilde{\delta R}_m = \frac{1}{2\pi} \int \delta R \, e^{-im\theta} \, d\theta \tag{6.3.9}$$

In 6.3.8 all terms can be correctly interpreted. First, each mode contributes to the non-equilibrium free energy with a curvature dependence m^2, proportional to the surface tension. However, the modes $m = \pm 1$ do not contribute. This is indeed correct because when a circle is slightly (linear in ϵ) perturbed in the modes $m = \pm 1$, it is only translated but not deformed (this is related to the absence of dipolar perturbation of a circle or sphere) and can be directly checked as follows. Take the radius and do a $m = 1$ deformation, for example $R = R_0(1 + \epsilon \cos(\theta))$, then it is simple to check that $(x - \epsilon R_0)^2 + y^2 = R_0^2$, that is the circle is just translated. As there is translational symmetry these modes should not contribute to the energy. Finally, the last term corresponds to the increase of energy when the mass of the cluster is changed. To assure that the equilibrium is stable, the second derivative of f should be negative and its absolute value larger than the first term. Note, however, that its value is otherwise completely independent of γ, that is the mass fluctuations are independent of the shape fluctuations. In summary, the non-equilibrium free energy about the equilibrium droplet can be written as

$$E = E_0 + \frac{\pi\lambda}{R_0} |\widetilde{\delta R}_0|^2 + \frac{\pi\gamma}{R_0} \sum_{|m|\geq 2} |\widetilde{\delta R}_m|^2 (m^2 - 1), \tag{6.3.10}$$

where the formal expansion parameter ϵ has been suppressed and λ is a new parameter, which has the same units as γ. In experiments, the translational symmetry is not perfect and the cluster has a tendency to remain in the center of the box. Then, the non-equilibrium free energy should be modified to

$$E = E_0 + \underbrace{\frac{\pi\lambda}{R_0} |\widetilde{\delta R}_0|^2}_{\text{change in size}} + \underbrace{\frac{\pi\nu}{R_0} \left(|\widetilde{\delta R}_1|^2 + |\widetilde{\delta R}_{-1}|^2 \right)}_{\text{change in position}} + \underbrace{\frac{\pi\gamma}{R_0} \sum_{|m|\geq 2} |\widetilde{\delta R}_m|^2 (m^2 - 1)}_{\text{change in form}} \tag{6.3.11}$$

with ν a new parameter, with the same units as γ and λ. This expression is used to derive the equilibrium power spectrum and the time correlation functions. The parameters λ and ν have physical origins that are different from the surface tension parameter γ, so their three values do not have to be directly related. λ corresponds to a measure of solid cluster's size changes, either by expansion and contraction (at a fixed number of particles) or by the condensation and evaporation of particles in and out of the solid cluster. ν corresponds to a measure of how far from the ideal condition is the current experimental realization. Ideally, $\nu = 0$, which implies that this mode (translation) is a neutral mode, equivalent to the spatial average for a flat interface (limit $k \to 0$). If $\nu = 0$, the $m = 1$ mode would realize a simple random walk, as discussed in Sec. 6.9. In fact, we show below that this is not the case. We speculate that the origin of $\nu > 0$ is related to particle's vertical dynamics, and thus depends on surface roughness, friction, and top and bottom local wall

parallelism. In particular, it depends on the vertical dynamics of the whole solid cluster, which is still largely unknown.

6.4. Static power spectrum

Starting from 6.3.11, for equilibrium systems the equipartition theorem from statistical mechanics is invoked. Thus, each normal mode, when configurationally averaged (in our case when time averaged), contributes $k_BT/2$ of energy to the system. Thus, the power spectrum is

$$\langle|\widetilde{\delta R}_0|^2\rangle = \frac{k_BTR_0}{2\pi\lambda}, \tag{6.4.1}$$

$$\langle|\widetilde{\delta R}_{\pm1}|^2\rangle = \frac{k_BTR_0}{2\pi\nu}, \tag{6.4.2}$$

$$\langle|\widetilde{\delta R}_m|^2\rangle = \frac{k_BTR_0}{2\pi\gamma(m^2-1)}, \tag{6.4.3}$$

where the last line is valid for $|m| \geqslant 2$. In general, the equipartition theorem is used for the total kinetic and potential energies (if any) by defining the number of active modes n. Thus, in average

$$\langle K\rangle = \langle U\rangle = n\,\frac{1}{2}k_BT, \tag{6.4.4}$$

where K and U are the total kinetic and potential energies respectively. The idea is that active modes contribute with $k_BT/2$ to the total energy, whereas non-active modes do not contribute. The number of active modes n depends on the particular system, by the number of spatial dimensions and by the particular atom or molecule interactions (intramolecular and intermolecular). The most simple example is an ideal monoatomic gas in D_s dimensions, with no potential energy. In this case, $n = D_sN$, where N is the number of atoms. In our case, we consider that the granular system has an effective "granular" temperature T_{eff}. Although this quantity is commonly referred as a temperature it has units of energy. A simple version is to consider it equivalent to k_BT. But, our non-equilibrium system shows that this effective thermal energy, or granular temperature, has to be defined carefully, as well as the number of active modes. In our setup, the system is isotropic in the horizontal plane, but the horizontal thermal energy is different from the vertical one. For the following analysis we focus our attention to the projected 2D dynamics, which is what can be analyzed experimentally. In fact, Fig. 6.4.1(b) shows that equipartition can be applied for the horizontal kinetic energy, up to a given wavenumber (from $m = 2$ to $m \approx 30$). We now focus on the solid-liquid interface, as a subsystem of the complete granular system. We recall that the protocol used identifies one interface particle for each angle interval $\Delta\theta = 2°$. Therefore, the interface subsystem consists always in exactly $N_p = 180$ particles. The interface total potential energy is given by 6.3.11. We then consider equipartition for the total kinetic and potential energies,

$$\langle K\rangle = \langle E\rangle = n\,\frac{1}{2}T_{\text{eff}}, \tag{6.4.5}$$

where n is the number of active modes and T_{eff} is the effective granular temperature. The important issue is that we can measure $\langle K \rangle$ and express it as a sum of normal modes. Indeed,

$$\langle K \rangle = \frac{1}{2} \sum_{i=1}^{N_p} m_p \langle \vec{v}_i^2 \rangle = \frac{1}{2} N_p m_p \langle \vec{v}^2 \rangle \tag{6.4.6}$$

where $\langle \vec{v}^2 \rangle = \langle v_x^2 \rangle + \langle v_y^2 \rangle$ is the velocity variance. Here, we must stress that because $\vec{v}$ is function of both θ and t, the average $\langle\,\rangle$ is a double average, over angles and over time. Both velocity components can be expressed by Fourier series:

$$v_x = \sum_{m=-\infty}^{\infty} \tilde{v}_m^x e^{im\theta}, \qquad\qquad v_y = \sum_{m=-\infty}^{\infty} \tilde{v}_m^y e^{im\theta}, \tag{6.4.7}$$

where $\tilde{v}_m^x$ and $\tilde{v}_m^y$ are the Fourier components. In practice, because $\Delta\theta = 2^\circ$, then the summation is done for a finite number of modes, from $m = -m^*$ to $m = m^*$, with $m^* = N_p/2 - 1 = 89$. Thus,

$$\langle K \rangle = \frac{1}{2} N_p m_p \sum_{m=-m^*}^{m^*} \langle |\tilde{v}_m^x|^2 + |\tilde{v}_m^y|^2 \rangle, \tag{6.4.8}$$

which allows to define the kinetic granular energy per mode,

$$\langle K_m \rangle = \frac{1}{2} N_p m_p \langle |\tilde{v}_m^x|^2 + |\tilde{v}_m^y|^2 \rangle. \tag{6.4.9}$$

For the last two expressions, the angle average has already been performed, and $\langle\,\rangle$ is a configurational (time) average. Next, as we measure for each mode $\langle K_m \rangle$, we can apply $\langle K_m \rangle = \langle \delta E_m \rangle$, where $\langle \delta E_m \rangle$ corresponds to each mode contribution to

$$\langle \delta E \rangle = \frac{\pi\lambda}{R_0} \langle |\widetilde{\delta R}_0|^2 \rangle + \frac{\pi\nu}{R_0} \left(\langle |\widetilde{\delta R}_1|^2 \rangle + \langle |\widetilde{\delta R}_{-1}|^2 \rangle \right) + \frac{\pi\gamma}{R_0} \sum_{|m|\geq 2} \langle |\widetilde{\delta R}_m|^2 \rangle (m^2 - 1). \tag{6.4.10}$$

Thus, the final expressions for the static power spectrum for our system are

$$\langle |\widetilde{\delta R}_0|^2 \rangle = \frac{\langle K_0 \rangle R_0}{\pi\lambda}, \tag{6.4.11}$$

$$\langle |\widetilde{\delta R}_{\pm 1}|^2 \rangle = \frac{\langle K_1 \rangle R_0}{\pi\nu}, \tag{6.4.12}$$

$$\langle |\widetilde{\delta R}_{|m|\geq 2}|^2 \rangle = \frac{\langle K_{|m|\geq 2} \rangle R_0}{\pi\gamma(m^2 - 1)}. \tag{6.4.13}$$

Fig. 6.4.1(a) displays the probability density function (PDF) of particle velocities in the liquid (l) and solid (s) phases, as well as for the particles at the boundary (b). The PDFs are Gaussian for low velocities, while they present exponential tails at high velocities. Isotropy between the horizontal velocity components was verified. The granular temperature T_g, obtained from the variance of the velocity distributions, is not uniform. Indeed, because of the collisional and dissipative nature of

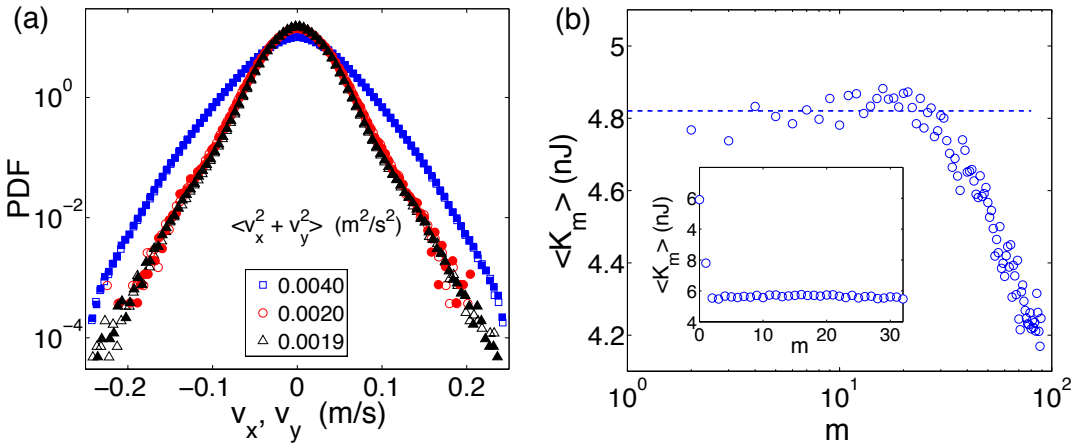

Figure 6.4.1.: (a) Probability density function (PDF) of velocity fluctuations. Open and solid symbols for x and y components respectively. In the liquid-like domain (■), for the solid-liquid boundary particles (●) and in the solid-like domain (▲). (b) Average horizontal kinetic energy spectrum, $\langle K_m \rangle$ versus m. The dashed line shows the equipartition value $K_{\rm eq}$. The inset shows the linear plot for $m = 0, ..., 35$.

particle interactions, higher particle volume fraction implies higher dissipation and lower T_g. As expected, we obtain $T_g^{\rm l} > T_g^{\rm b} \gtrsim T_g^{\rm s}$, although the temperature contrast between the phases is small as compared to [6] because in our case the solid cluster is soft. In Fig. 6.4.1(b) we present the average horizontal kinetic energy spectrum, $\langle K_m \rangle$ versus m. Although the system is strongly out of equilibrium and that temperature is not uniform, there is energy equipartition between $m = 2$ and $m \approx 30$, with an average value $K_{\rm eq} = 4.82 \pm 0.04$ nJ. For comparison, $T_g^{\rm b} \approx 4.5$ nJ. The two lowest modes have larger energy, $\langle K_0 \rangle = 8.0 \pm 4.7$ nJ and $\langle K_1 \rangle = 5.9 \pm 2.8$ nJ, and the energy components decrease for $m > 30$.

This is the quantity plotted in Fig. 6.4.1(b), which shows equipartition from $m = 2$ to $m \approx 30$ (corresponding to wavelengths $\approx 74d$ to $\approx 5d$). In fact, an average between $m = 2$ and $m = 30$ gives $\langle K_m \rangle \equiv K_{\rm eq} = 4.82 \pm 0.04$ nJ. The two lowest modes, which correspond to global radius fluctuations and center of mass translations, have higher energy: $\langle K_0 \rangle = 8.0^{+4.7}_{-4.6}$ nJ and $\langle K_1 \rangle = 5.9 \pm 2.8$ nJ. Their errors are slightly asymmetric due to their asymmetric (non-Gaussian) distribution functions, which are detailed in the last section of this document. Furthermore, the identity

$$\langle K \rangle = \frac{1}{2} N_p m_p \langle \vec{v}^2 \rangle = \frac{1}{2} N_p m_p \sum_{m=-m^*}^{m^*} \langle |\tilde{v}_m^x|^2 + \tilde{v}_m^y|^2 \rangle, \tag{6.4.14}$$

can be verified numerically. Indeed, from the particle velocity distributions (in x and y) and their variances, we obtain $\langle K \rangle \approx 0.80$ μJ, whereas from the velocity Fourier components we obtain $\langle K \rangle \approx 0.82$ μJ.

Fig. 6.4.2(a) shows a very satisfactory agreement for the experimental power spectrum 6.4.13 with a $1/(m^2-1)$ tendency, within a physically relevant range for the wavenumber $m = 6-54$, corresponding to wavelengths $2\pi R_0/m \approx 3d - 24d$. Fitting 6.4.13 to the experimental data gives an effective

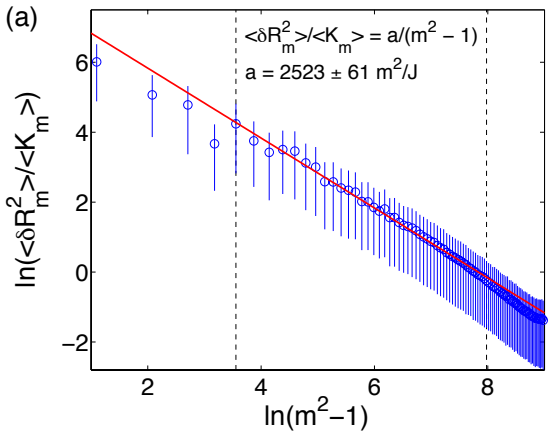

Figure 6.4.2.: Static and dynamic correlation analysis. The continuous lines show the fitted functions. (a) The ratio $\langle|\widetilde{\delta R}_m|^2\rangle/\langle K_m\rangle$ versus m^2-1 in ln-ln scale. The fits are performed within the range for the wavenumber $m = 6-54$, corresponding to wavelengths $2\pi R_0/m \approx 3d-24d$.

surface tension $\gamma = 2.9 \pm 0.1$ μN in two-dimensions, and using L_z as the third dimension, we get $\gamma_{3D} \equiv \gamma/L_z = 1.5 \pm 0.1$ mN/m. Additionally, λ and ν can be measured through the components $m = 0$ and $m = 1$ of $\langle|\widetilde{\delta R}_m|^2\rangle$ and $\langle K_m\rangle$, obtaining $\lambda = 0.23 \pm 0.21$ mN, and $\nu = 0.13 \pm 0.11$ mN. For comparison, our measured surface tension γ_{3D} is about 50 times smaller than pure water's surface tension, but it is much larger than the value 0.1 μN/m estimated for a freely falling dry granular material [81]. In fact, this latter work demonstrates that nano-Newton cohesive interaction forces, measured by AFM, are responsible for the surface tension. In our case, the physical mechanism is not originated by grain-grain cohesion, but from dissipative collisions between particles. Actually, the effective surface tension of our system can be estimated as $\gamma \sim T_g^b/d \approx 4.5$ μN, which implies $\gamma_{3D} \sim T_g^b/(dL_z) \approx 2.3$ mN/m. This result is consistent with the scaling found in a numerical study on 3D crystallization of hard spheres, where the fluid-solid surface tension is $\gamma_{3D} \sim k_B T/d^2$ [93].

6.5. Capillary-like spectrum for different interface detection conditions

In Sec. 4.2 we have presented the interface detection procedure, including the three different criteria used for the selection of particles in the solid cluster. In the main text we also discuss the validity of the capillary-like spectrum respect to the choice of the coarse-graining angle $\Delta\theta$. In Fig. 6.5.1 we present several fluctuation spectra $\langle|\widetilde{\delta R}_m|^2\rangle/\langle K_m\rangle$ versus m^2-1 using the three different criteria and several coarse-graining angles. The $1/(m^2-1)$ dependence is observed for all cases, with variations on the range of mode numbers m for which is it valid, depending on the specific details of the detection procedure. For $\Delta\theta = 2^\circ$ (Fig. 6.5.1(a)) we obtain that for the first criterion the fitted surface tension results $\gamma = 2.0 \pm 0.1$ μN. For the second and third criteria, within errors their result

are equal, $\gamma = 2.9 \pm 0.1$ μN. Fig. 6.5.1(b) and Fig. 6.5.1(c) present spectra for the second criterion with different coarse-graining angles. These results allow us to conclude that the description of the fluctuations by the capillary theory is very robust with respect to the details of the interface detection procedure. However, the numerical parameters of the theory (surface tension and mobility) are more sensible to the different criteria. In particular, the fact that γ is lower for criterion 1 can be explained recalling that the detection procedure adds a thin liquid-like skin to the solid cluster, as mentioned in Sec. 4.2. This layer is composed by particles with intermediate order ($|Q_4| \approx 0.55$) but with small Voronoi area ($2A_v/d^2 \approx 1.4$), thus with higher density.

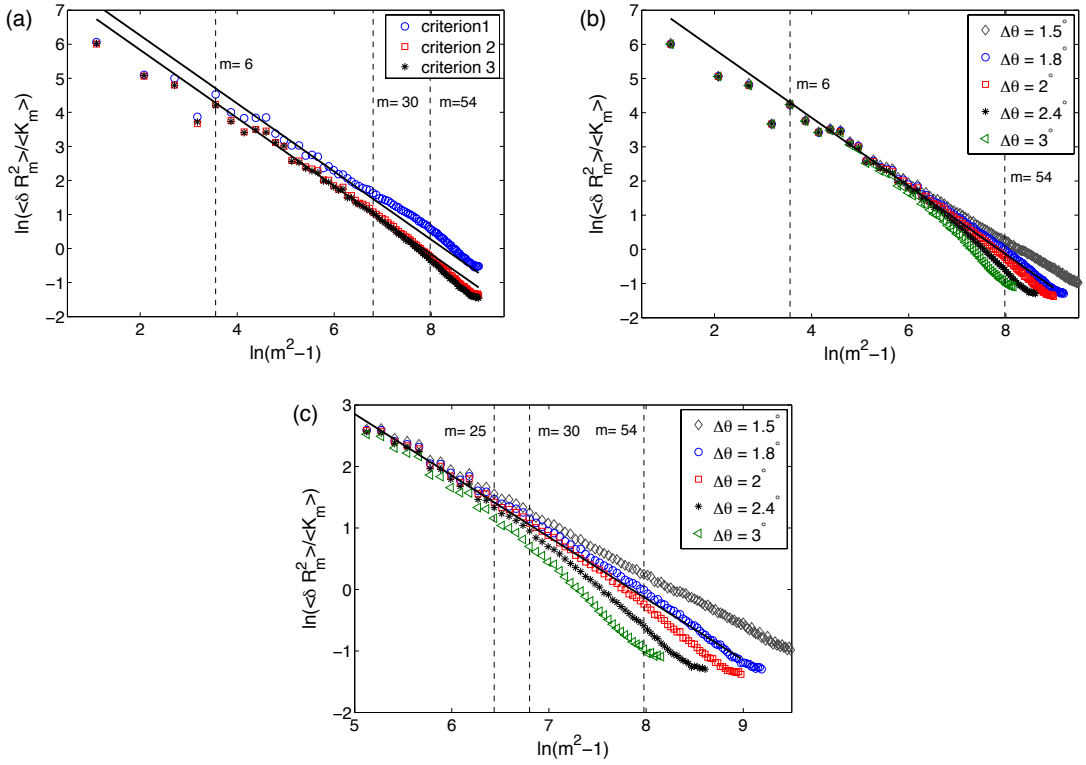

Figure 6.5.1.: (a) Fluctuation spectra $\langle|\widetilde{\delta R}_m|^2\rangle/\langle K_m\rangle$ versus $m^2 - 1$ for $\Delta\theta = 2°$ and the three cluster selection criteria presented in Sec. 4.2. The vertical dashed lines show the limit values used for the fits: $m = 6...30$ for criterion 1, and $m = 6...54$ for criteria 2 and 3. (b) Fluctuation spectra $\langle|\widetilde{\delta R}_m|^2\rangle/\langle K_m\rangle$ versus $m^2 - 1$ for several $\Delta\theta$ using criterion 2. For smaller $\Delta\theta$, noise contaminates the spectrum at higher m values. For larger $\Delta\theta$, the coarse-graining procedure acts as a filter at larger m. (c) Same as (b) for a smaller range of m, putting in evidence the discrepancies that appear for larger m.

6.6. About the small slope approximation

The small slope approximation is used explicitly in the Taylor expansion of $\sqrt{R^2+(\partial_\theta R)^2}$. In particular, the last two terms in

$$\sqrt{R^2+(\partial_\theta R)^2} = \sqrt{(R_0+\delta R)^2+(\partial_\theta \delta R)^2} \tag{6.6.1}$$

$$\approx R_0\left[1+\frac{\delta R}{R_0}+\frac{1}{2}\left(\frac{\partial_\theta \delta R}{R_0}\right)^2-\frac{1}{8}\left(\frac{\delta R}{R_0}\right)^4-\frac{1}{8}\left(\frac{\partial_\theta \delta R}{R_0}\right)^4+h.o.t\right], \tag{6.6.2}$$

are neglected, as well as the higher order terms (h.o.t) that are not shown. As discussed previously, the contribution of the linear term vanishes in the non-equilibrium free energy. Thus, we are left to show that the following conditions are indeed fulfilled by our experimentally determined solid-liquid interfaces:

$$\frac{1}{8}\left(\frac{\delta R}{R_0}\right)^4 \ll 1, \tag{6.6.3}$$

$$\frac{1}{8}\left(\frac{\partial_\theta \delta R}{R_0}\right)^4 \ll \frac{1}{2}\left(\frac{\partial_\theta \delta R}{R_0}\right)^2. \tag{6.6.4}$$

These terms contribute to the non-equilibrium free energy through the angle integral. Thus, by expanding δR in Fourier series, the above expressions become equivalent to show these conditions are satisfied:

$$\Psi_1 \equiv \frac{\langle|\widetilde{\delta R_m}|^4\rangle}{8R_0^4} \ll 1, \tag{6.6.5}$$

$$\Psi_2 \equiv m^2\frac{\langle|\widetilde{\delta R_m}|^2\rangle}{4R_0^2} \ll 1. \tag{6.6.6}$$

Here, the brackets $\langle\ \rangle$ represent an ensemble average, which in practice is done through time average of data from many images. These conditions are indeed satisfied, as shown in Fig. 6.6.1. The first parameter satisfies $\Psi_1 < 1.7\times10^{-6}$ for all m, whereas the second one, $\Psi_2 < 8\times10^{-3}$ for all m.

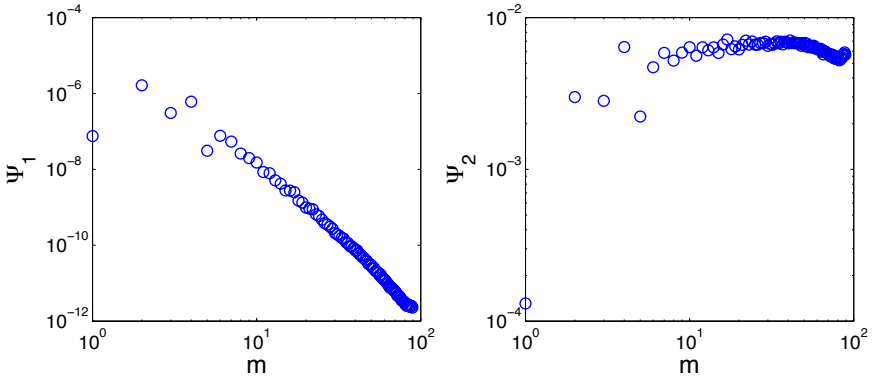

Figure 6.6.1.: Relative intensity of the correction terms, $\Psi_1 = \langle|\widetilde{\delta R_m}|^4\rangle/(8R_0^4)$ (left) and $\Psi_2 = m^2\langle|\widetilde{\delta R_m}|^2\rangle/(4R_0^2)$ (right), to the quadratic form of the non-equilibrium free energy in (6.6.2). Small values imply that the small slope approximation to the non-equilibrium free energy is valid and the quadratic form can be used.

6.7. Comparison between both configurations

In this section we present the results obtained for both configurations C1 and C2 using the thick ITO glass plates. The accelerations used for both cases are $\Gamma = 2.19 \pm 0.01$ and $\Gamma = 5.47 \pm 0.01$ for C1 and C2 respectively, while the critical accelerations for C1 and C2 are $\Gamma_c = 1.98$ and $\Gamma_c = 4.48 \pm 0.03$ respectively. For C1 the value of Γ_c is just approximated, given that it was obtained by eye observation, and not the method presented in Sec. 5.4. The normalized distance to the transition is $\varepsilon = 0.09$ and $\varepsilon = 0.22$ for C1 and C2 respectively. By doing the same procedure presented in Sec. 4.2 we detect the interfaces and then compute the power spectra $\left\langle\left|\widetilde{\delta R_m}\right|^2\right\rangle$ and $\langle K_m\rangle$. These are shown in Fig. 6.7.1.

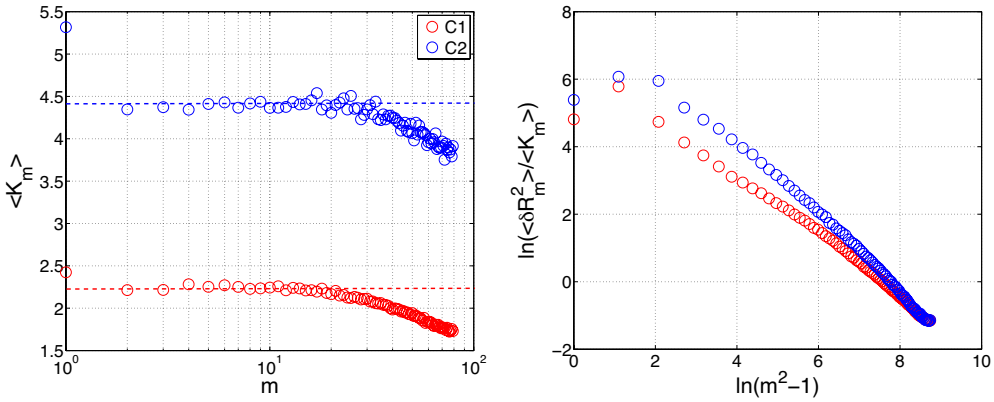

Figure 6.7.1.: Left: $\langle K_m\rangle$ versus m for both configurations. The dashed lines show the equipartion energy K_{eq} in each case. Right: The ratio $\left\langle\left|\widetilde{\delta R_m}\right|^2\right\rangle / \langle K_m\rangle$ versus $m^2 - 1$ in ln-ln scale.

From figure Fig. 6.7.1 left, we observe that both C1 and C2 show equipartition. Specifically between $m = 2$ and $m \approx 20$ for C1, versus between $m = 2$ and $m \approx 30$ for C2. The equipartition values obtained are $K_{eq} = 2.22 \pm 0.03$ nJ and $K_{eq} = 4.44 \pm 0.05$ nJ respectively. The right plot of Fig. 6.7.1 shows the ratio $\left\langle \left|\widetilde{\delta R_m}\right|^2 \right\rangle / \langle K_m \rangle$ versus $m^2 - 1$ where it is clear that there is an important difference between both configurations. As shown before, for C2 we observe that the spectrum actually follows the predicted power law $\left(m^2 - 1\right)^{-1}$ (6.4.13). However, for C1 we observe that the ratio $\left\langle \left|\widetilde{\delta R_m}\right|^2 \right\rangle / \langle K_m \rangle$ behaves as $\left(m^2 - 1\right)^{-1}$ at low and high values of m, but at intermediate values it presents a crossover between these two regimes. In order to clarify this, if we define the quantity a by $a \equiv \left\langle \left|\widetilde{\delta R_m}\right|^2 \right\rangle / \langle K_m \rangle \cdot \left(m^2 - 1\right)$, then a constant value of a would imply a surface tension $\gamma = R_0 / (a\pi)$. Thus, in Fig. 6.7.2 we plot $R_0 / (a\pi)$ versus $m^2 - 1$.

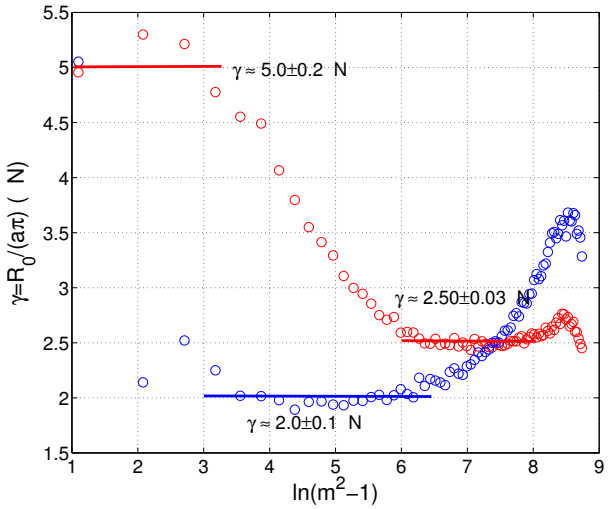

Figure 6.7.2.: Surface tension $\gamma = R_0 / (a\pi)$ for C1 and C2.

In Fig. 6.7.2 we observe that whereas C2 presents a constant value of a within a range for the wave number $m = 6 - 50$, resulting in a surface tension of $\gamma = 2.1 \pm 0.2\,\mu$N, the configuration C1 shows two relevant regimes; a small wavenumber regime ($m = 3 - 6$) with a surface tension approximately $\gamma = 5.0 \pm 0.2\,\mu$N, and a large wavenumber regime ($m = 20 - 55$) yielding a surface tension $\gamma = 2.5 \pm 0.03\,\mu$N. That is, we obtain two values for the surface tension depending on the scale we are looking at.

6.8. Surface tension as a function of Γ

Now, we perform the same analysis presented above as a function of Γ for the configuration C2. We study the system at 7 different $\Gamma = \{4.76, 4.87, 4.96, 5.08, 5.24, 5.32, 5.47\}$. We recall that $\Gamma_c = 4.48 \pm 0.03$. Unfortunately, the detection of the interface does not work properly at the lower Γ, because for this configuration the crystal is not so well defined near Γ_c, even though the system has crossed the critical point. Thus the detection of the interface only worked for the 4 largest Γ

($\varepsilon = \{0.13, 0.17, 0.19, 0.22\}$). Hence, we developed a method to extract the surface tension from the average of the images.

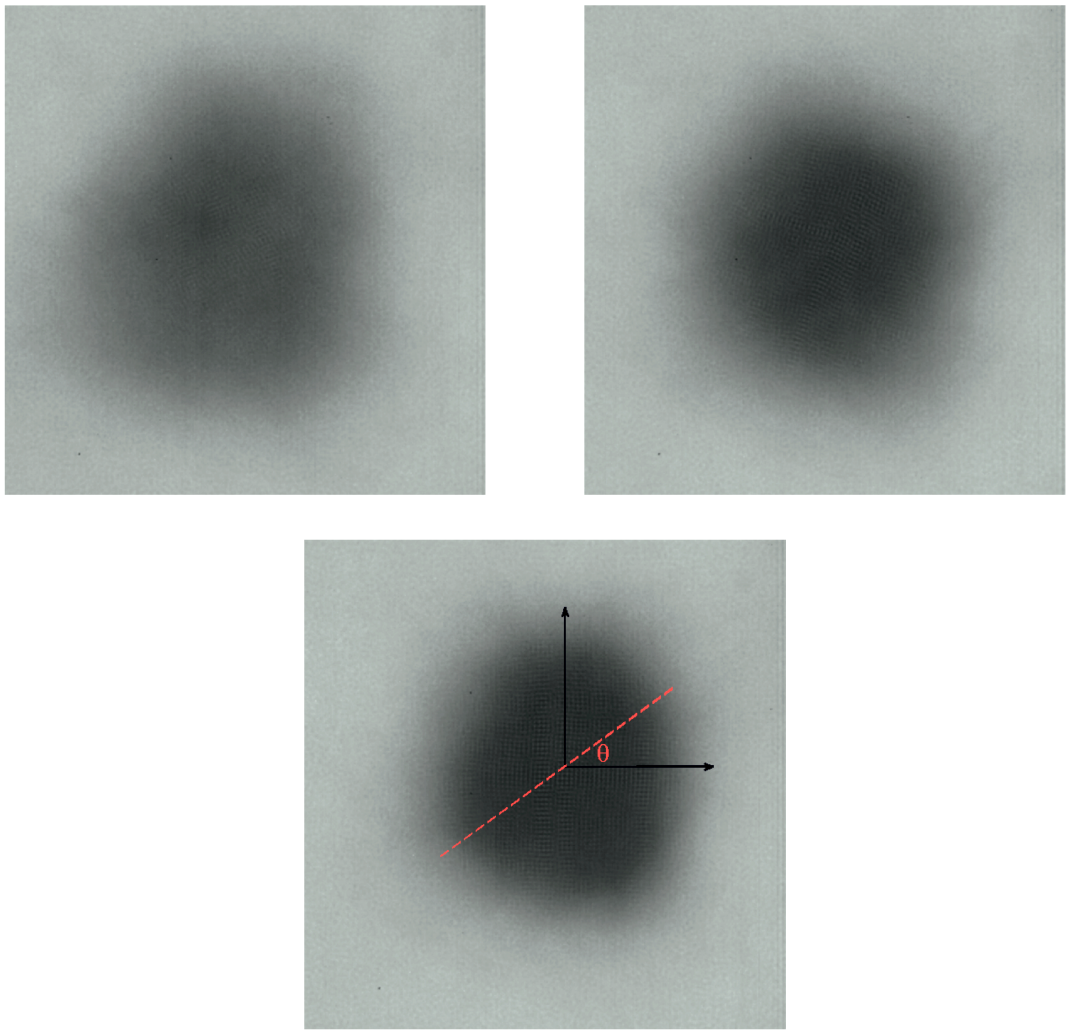

Figure 6.8.1.: Mean images obtained from 3270 images at $\Gamma = \{4.76, 5.08, 5.47\}$ from top to bottom.

From Fig. 6.8.1 we may notice that in average the crystal has a circular shape, thus if we fixed our reference system in the center of mass we can extract the intensity of the image by projecting at different angles. The intensity of the image for a value of the angle θ is shown in Fig. 6.8.2.

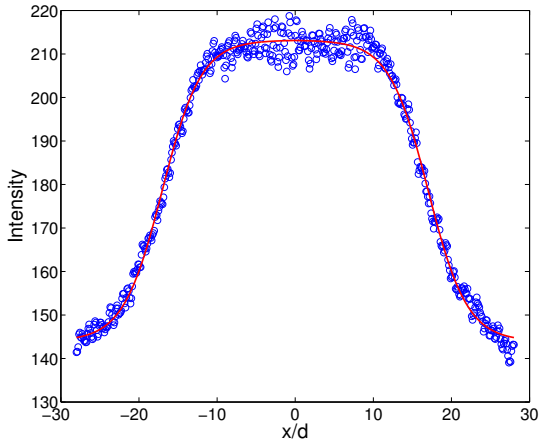

Figure 6.8.2.: Typical intensity profile of an image at a fixed angle θ. The red line corresponds to the fit $I(x) = I_{max}\left(1 - \tanh\left(\frac{|x|-D/2}{w}\right)\right) + I_{min}$, where D is basically the diameter of the crystal and w is related to how abrupt falls the intensity.

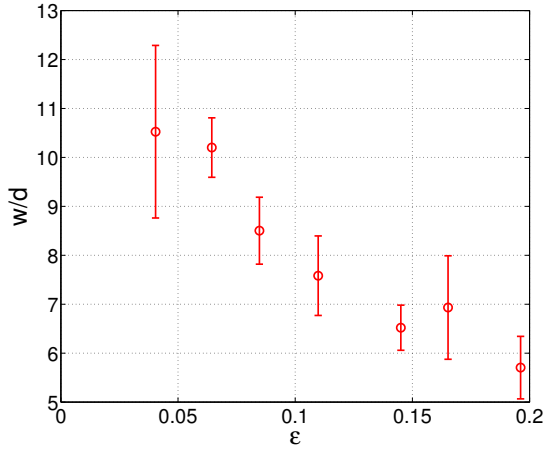

Figure 6.8.3.: Parameter w as a function of $\epsilon = \frac{\Gamma-\Gamma_c}{\Gamma_c}$ obtained by fitting the intensity to the curve $I(x) = I_{max}\left(1 - \tanh\left(\frac{|x|-D/2}{w}\right)\right) + I_{min}$ at 30 different angles equally spaced.

By fitting the curve $I(x) = I_{max}\left(1 - \tanh\left(\frac{|x|-D/2}{w}\right)\right) + I_{min}$ to the intensity of the mean image, we can extract the diameter of the crystal D and the width w, which indicates how abrupt is the change of intensity. In Fig. 6.8.3 we show w as a function of Γ obtained from fittings of the intensity at 30 different angles. For the smallest ε only 9 angles were analyzed because the crystal presents vacancies and an irregular shape, thus, only the angles where the fit works adequately are considered ($R^2 > 0.97$).

We observe from this figure that w decreases as we increase the distance to the transition. Thus, the

crystal becomes much well defined at higher values of Γ. Hence, we assume that the surface tension γ is related to w by $\gamma \sim 1/w$. That is, we assume that $w \cdot \gamma = \Upsilon = constant$. But, given that for the higher values of Γ we can actually detect the interface and thus calculate γ from the capillary fluctuations, we fixed the value of the constant with the cases where the detection of the interface works properly. In Fig. 6.8.4 we show $w/d \cdot \gamma$ as a function of Γ.

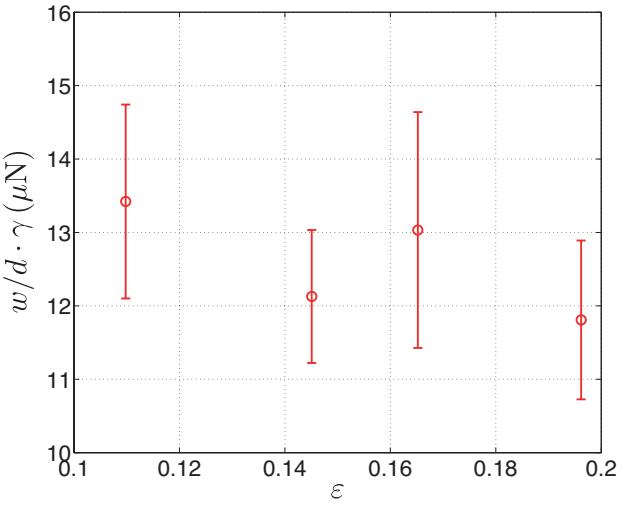

Figure 6.8.4.: $w/d \cdot \gamma$ for the cases when the detection of the interface actually works. With this four values we obtained that the value of the constant is $\Upsilon = 12.5 \pm 0.7\,\mu$N.

Accordingly, by impossing that $\gamma = \Upsilon/w$ we obtain the surface tension as a function of Γ. Besides, for the higher values of Γ we can compare the values of γ obtained from the assumption $\gamma \sim 1/w$ with the method of detecting the interface. This is shown in Fig. 6.8.5.

From this figure we observe that the surface tension decreases as we approach the critical point, which is expected, given that the crystal becomes less defined for accelerations near Γ_c. This is well known in the literature for normal liquids, and is known under the name of *Eötvös rule* [94]. It states that the surface tension of an arbitrary liquid is given by $\gamma V^{2/3} = k\,(T_c - T)$, where V is the liquid molar volume and k is a constant valid for all liquids $\left(k = 2.1 \cdot 10^{-7}\,\mathrm{J/K \cdot mol^{2/3}}\right)$.

We can also perform the analysis of fitting the intensity of the mean image in configuration C1. Unfortunately, for the set of data analized we do not have the dynamic information necessary to compute the spectrum of the kinetic energy $\langle K_m \rangle$, and hence we do not have a way to calibrate properly the constant Υ of the relation $\gamma = \Upsilon/(w/d)$. In Fig. 6.8.6 we show the parameter w as a function of Γ for C1.

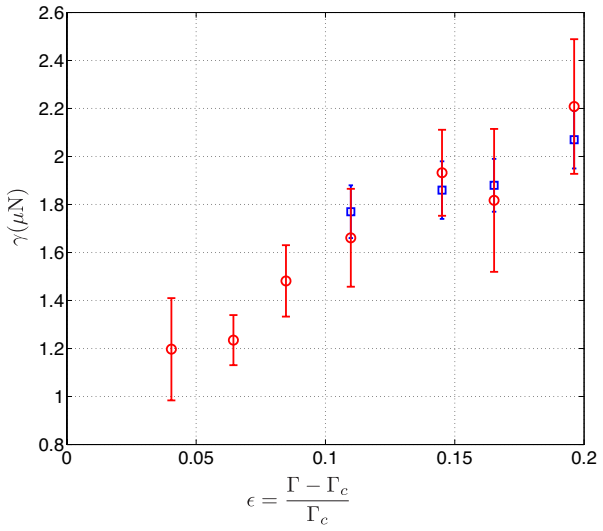

Figure 6.8.5.: γ as a function of Γ for C2. The red circles correspond to the surface tension obtained from the relation $\gamma = \frac{\Upsilon}{w}$, with $\Upsilon = 125 \pm 7$. The blue squares were obtained from the usual method of detecting the interface.

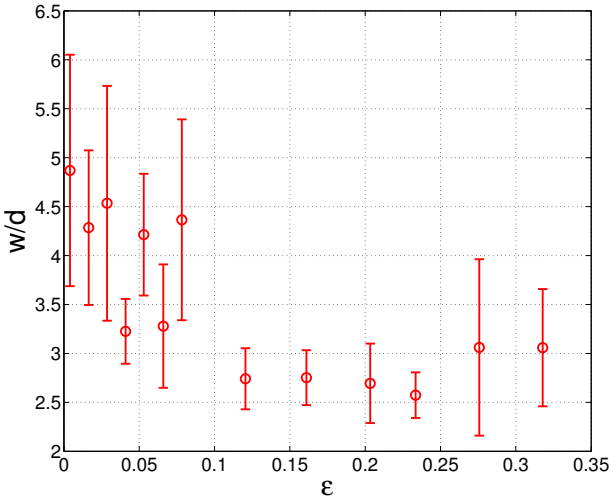

Figure 6.8.6.: Parameter w as a function of ϵ for configuration C1. We observe that w is almost constant, yielding a constant surface tension. By using the value obtained before for C1 at large wavelengths, we may say that the surface tension is constant and approximately $\gamma = 5.0 \pm 0.2\,\mu$N.

From Fig. 6.8.6 we observe that w is almost constant. For small values of ϵ we are very near the critical point, and the crystal turns out to be not so well defined, thus implying that the first points of Fig. 6.8.6 are not very reliable given that the crystal has an irregular shape and the value of w changes abruptly depending on what angles we use to fit the intensity.

6.9. Dynamic correlation function: Effective mobility

We now focus on the mobility parameter M and the interface dynamic correlation function. For an interface of flat geometry, with local height $h(x,t)$, the standard procedure is to consider the interface local velocity $V = \partial h/\partial t = M\gamma\kappa$, where κ is the interface's curvature ($\kappa = \partial_{xx}h$ for a flat interface in 2D). The Fourier transform of this equation leads to

$$\frac{\partial A_k}{\partial t} = -M\gamma k^2 A_k, \tag{6.9.1}$$

where we have used the Fourier representation

$$h(x,t) = \sum_k A_k(t) e^{ikx}. \tag{6.9.2}$$

When a noise term is included, Langevin equations are obtained, in real and Fourier space respectively:

$$\frac{\partial h(x,t)}{\partial t} = M\left(\gamma\frac{\partial^2 h(x,t)}{\partial x^2} + \eta(x,t)\right), \qquad \frac{\partial A_k}{\partial t} = M(-\gamma k^2 A_k + \eta_k(t)), \tag{6.9.3}$$

where

$$\eta(x,t) = \sum_k \eta_k(t) e^{ikx} \tag{6.9.4}$$

is modeled as a white noise term, which is delta correlated

$$\begin{aligned} \langle \eta(x,t)\rangle &= 0, & (6.9.5)\\ \langle \eta(x,t)\eta(x',t')\rangle &= C\delta(x-x')\delta(t-t'), & (6.9.6)\\ \langle \eta_k(t)\rangle &= 0, & (6.9.7)\\ \langle \eta_k(t)\eta_k^*(t')\rangle &= C\delta_{k,k'}\delta(t-t'). & (6.9.8) \end{aligned}$$

In 2D, if we consider an interface of length L between two semi-infinite phases, then the non-equilibrium free energy is

$$E = \gamma\int_0^L \sqrt{1+(\partial_x h)^2}dx \approx \gamma L + \frac{\gamma L}{2}\sum_k k^2|A_k|^2. \tag{6.9.9}$$

It is straightforward to show that 6.9.1 can be obtained by the general form

$$\frac{\partial A_k}{\partial t} = -\frac{M}{L}\frac{\delta E}{\delta A_k}, \tag{6.9.10}$$

where $\delta E/\delta A_k$ is the functional derivative of E. Applying the same formalism to our case, and

including noise, from 6.3.11 we obtain the following Langevin equations

$$\frac{\partial\widetilde{\delta R}_0}{\partial t} = M\left(-\frac{\lambda}{R_0^2}\widetilde{\delta R}_0 + \eta_0(t)\right), \tag{6.9.11}$$

$$\frac{\partial\widetilde{\delta R}_{\pm1}}{\partial t} = M\left(-\frac{\nu}{R_0^2}\widetilde{\delta R}_{\pm1} + \eta_{\pm1}(t)\right), \tag{6.9.12}$$

$$\frac{\partial\widetilde{\delta R}_{|m|\geqslant2}}{\partial t} = M\left(-\frac{\gamma}{R_0^2}(m^2-1)\widetilde{\delta R}_m + \eta_m(t)\right). \tag{6.9.13}$$

These Langevin equations have the form $\dot{x} = -x/\tau + M\eta(t)$, whose solution is

$$x(t) = x(0)e^{-t/\tau} + M\int_0^t e^{-(t-s)/\tau}\eta(s)ds. \tag{6.9.14}$$

The ensemble average results $\langle x(t)\rangle = \langle x(0)\rangle e^{-t/\tau}$, and $\langle x(t)\rangle \to 0$ for $t \to \infty$. The two time correlation function is

$$\langle x(t)x^*(t')\rangle = \langle|x(0)|^2\rangle e^{-(t+t')/\tau} + \frac{M^2C\tau}{2}\left(e^{-|t-t'|/\tau} - e^{-(t+t')/\tau}\right). \tag{6.9.15}$$

From here, the following expression for the dynamic correlation function in Fourier space is derived:

$$\langle\widetilde{\delta R}_m(t)\widetilde{\delta R}_m^*(0)\rangle = \langle|\widetilde{\delta R}_m|^2\rangle e^{-t/\tau_m}, \tag{6.9.16}$$

where $\tau_m = R_0^2/[M\gamma(m^2-1)]$ for $|m| \geqslant 2$, and $\tau_0 = R_0^2/(M\lambda)$ and $\tau_{\pm1} = R_0^2/(M\nu)$ for $m = 0$ and $m = \pm1$ respectively, are the relaxation times.

The inset of Fig. 6.9.1 displays an example of the good agreement for the predicted exponential decay. The data for $t > 0.2$ s and for $m > 18$ are very noisy and not considered for the analysis. Fig. 6.9.1(b) shows that τ_m^{-1} does increases linearly with (m^2-1). Using the value of γ, we obtain $M = 2.8 \pm 0.8$ m^{3}J^{-1}s^{-1}. We remark that for an atomic system simulation [90], the mobility in two-dimensions scales as $M \sim l_c^3/(k_BTt_c)$, with k_BT the thermal agitation, l_c and t_c characteristic length and time respectively. In our case, considering $k_BT = T_g^{\mathrm{b}}$, $l_c \sim d$ and $t_c \sim d/\sqrt{\langle\vec{v}_{\mathrm{b}}^2\rangle}$, yields the same order of magnitude for the mobility $M \approx 10$ m^{3}J^{-1}s^{-1}.

Now, evaluating 6.9.15 at $t = t'$, the static power spectrum is used in long time limit of

$$\langle|x(t)|^2\rangle = \langle|x(0)|^2\rangle e^{-2t/\tau} + \frac{M^2C\tau}{2}\left(1 - e^{-2t/\tau}\right), \tag{6.9.17}$$

which gives the constant $C = 2\langle K_m\rangle/(\pi R_0 M)$. Finally, the mean square displacement is

$$\langle|\Delta R|^2\rangle = \langle|x(t) - x(0)|^2\rangle. \tag{6.9.18}$$

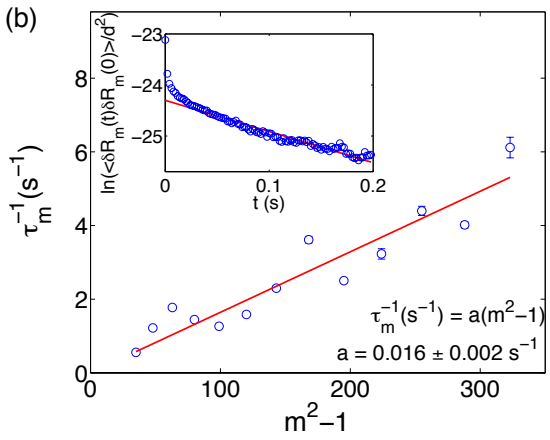

Figure 6.9.1.: Decay time τ_m^{-1} versus (m^2-1). Inset shows an example of $\langle \widetilde{\delta R}_m(t)\widetilde{\delta R}_m^*(0)\rangle$ $(m=18)$.

From 6.9.14 we obtain

$$x(t) - x(0) = x(0)(e^{-t/\tau} - 1) + M\int_0^t e^{-(t-s)/\tau}\eta(s)ds, \tag{6.9.19}$$

thus

$$\langle |x(t)-x(0)|^2\rangle = \langle |x(0)|^2\rangle(e^{-t/\tau}-1)^2 + M^2\int_0^t\int_0^t e^{-(2t-s-s')/\tau}\langle \eta(s)\eta^*(s')\rangle ds ds', \tag{6.9.20}$$

$$= \langle |x(0)|^2\rangle(e^{-t/\tau}-1)^2 + \frac{M^2C\tau}{2}\left(1-e^{-2t/\tau}\right), \tag{6.9.21}$$

where we have used the fact that $\langle x(0)\eta(s)\rangle = \langle x(0)\rangle\langle \eta(s)\rangle = 0$, for $s>0$, and the double integral is solved as before. We remind that the long time limit of 6.9.17 gives $M^2C\tau/2 = \langle |x(t)|^2\rangle = \langle |x(0)|^2\rangle$, allowing to simplify 6.9.21, leading to the following expression for the mean square displacement

$$\langle |x(t)-x(0)|^2\rangle = M^2C\tau\left(1-e^{-t/\tau}\right). \tag{6.9.22}$$

Finally, replacing the expression for C in terms of the energy per mode,

$$\langle |x(t)-x(0)|^2\rangle = \langle |\Delta R_m|^2\rangle = \frac{2\langle K_m\rangle M\tau_m}{\pi R_0}\left(1-e^{-t/\tau_m}\right). \tag{6.9.23}$$

The Langevin description can be studied considering the mean square-displacements for the $m=0,1$ modes. Indeed, from 6.9.23

$$\langle |\Delta R_{0,1}|^2\rangle = \frac{2M\langle K_{0,1}\rangle\tau_{0,1}}{\pi R_0}\left(1-e^{-t/\tau_{0,1}}\right), \tag{6.9.24}$$

where $\Delta R_{0,1} = \widetilde{\delta R}_{0,1}(t) - \widetilde{\delta R}_{0,1}(0)$. For short times $t \ll \tau_{0,1}$, a diffusive behavior is expected for each mode, $\langle|\Delta R_{0,1}|^2\rangle \approx 2D_{0,1}t$, with $D_{0,1} = M\langle K_{0,1}\rangle/(\pi R_0)$, which is the analog of the fluctuation-dissipation relation used in atomic simulations for flat geometries [90, 91]. Fig. 6.9.2 displays $\langle|\Delta R_m|^2\rangle$ as a function of time for $m = 0$ and $m = 1$. Fits are shown using $\langle|\Delta R_m|^2\rangle = A_m[1-\exp(-t/\tau_m)]+c_m$, where c_m reflects the fact that the Langevin equation does not capture the initial ballistic regime. The predicted saturation is observed for long times. From the fitted values we obtain $\lambda = 0.19 \pm 0.12$ mN, $\nu = 0.06 \pm 0.03$ mN, $M_0 = 1.3 \pm 0.9$ m^{3}J^{-1}s^{-1}, and $M_1 = 1.8 \pm 1.0$ m^{3}J^{-1}s^{-1}. The mean square-displacements are known to have poor convergent properties and the presented results were obtained using only two trajectories. Despite this numerical uncertainty, the qualitative shape of $\langle|\Delta R_m|^2\rangle$ is reproduced and the fitted values are in the correct order of magnitude, showing the that the interface dynamics is consistent with the Langevin model.

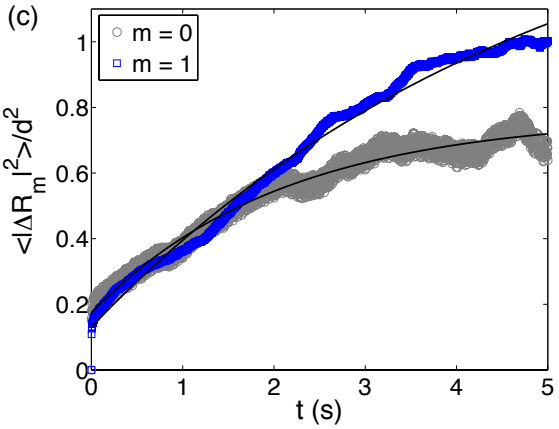

Figure 6.9.2.: Mean square displacement analysis for $m = 0$ (○) and $m = 1$ (□). Each curve is the result of the average of two realizations. The solid lines correspond to fits $\langle|\Delta R_m|^2\rangle = A_m[1-\exp(-t/\tau_m)]+c_m$. The fitted parameters are $A_0/d^2 = 0.599 \pm 0.005$, $c_0/d^2 = 0.175 \pm 0.004$, $\tau_0 = 2.09 \pm 0.06$ s, $A_1/d^2 = 1.47 \pm 0.03$, $c_1/d^2 = 0.131 \pm 0.004$, $\tau_1 = 5.03 \pm 0.17$ s.

6.10. Appendix: Error analysis

Both $|\widetilde{\delta R}_m|^2$ and K_m have large fluctuations. Their distributions are strongly non-Gaussian, which implies that the corresponding error analysis has to be realized carefully. For example, the measured average kinetic energy for $m = 0$ is 8.0 nJ, whereas its standard deviation is 7.9 nJ. Thus, the error related to this measurement is not its standard deviation. In fact, the associated error has to be computed with a generalized criterion. When a measurement of a quantity x is performed, the usual procedure is to assign the standard deviation σ_x as error to the average $\langle x\rangle$ of a set of data. For a Gaussian distribution, the range $[\langle x\rangle - \sigma_x, \langle x\rangle + \sigma_x]$ corresponds to a confidence interval of $\approx 68\%$, meaning that if a new measurement is performed, it has a 68% probability to be in this range.

Fig. 6.10.1(a) shows that K_0 obeys a Boltzmann distribution, strongly non-Gaussian. Fig. 6.10.1(b)

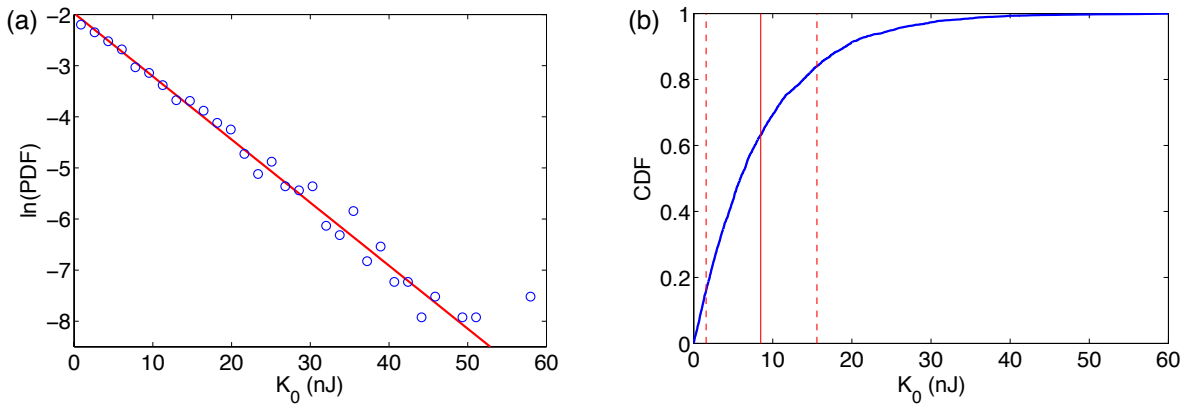

Figure 6.10.1.: (a) Probability density function, PDF, and (b) cumulative density function, CDF, of K_0 for one realization. In (a), the continuous line shows a Boltzmann distribution fit, $\mathrm{PDF}(K_0) = A\exp(-K_0/B)$, with $A = 0.14 \pm 0.02$ (nJ)$^{-1}$ and $B = 8.1 \pm 0.4$ nJ. In (b), the vertical solid line corresponds to the average $\langle K_0\rangle = 8.5$ nJ; the vertical dashed lines show the limits for which 16% of the data is below $\langle K_0\rangle - \sigma_-$, and 16% is above $\langle K_0\rangle + \sigma_+$, with $\sigma_- = 6.9$ nJ and $\sigma_+ = 7.1$ nJ. For the other realization, $\langle K_0\rangle = 7.5$ nJ, $\sigma_- = 6.2$ nJ and $\sigma_+ = 6.1$ nJ.

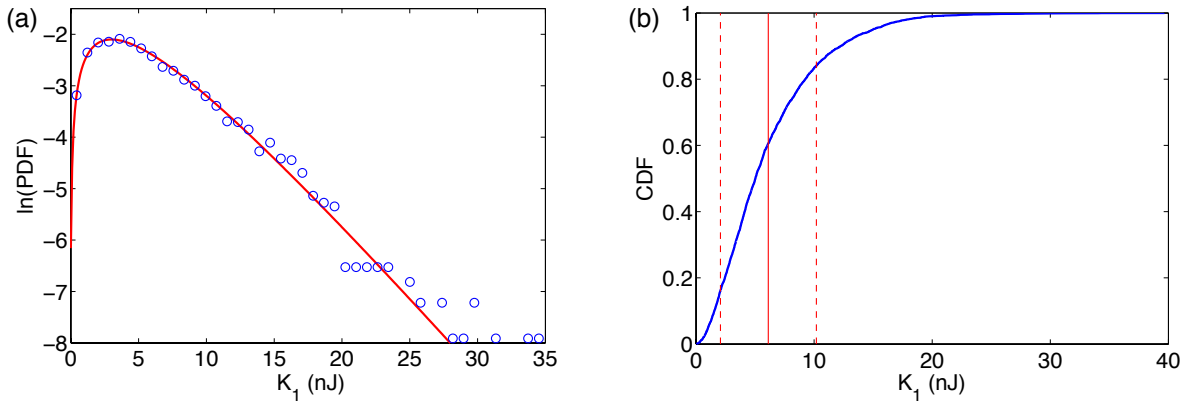

Figure 6.10.2.: (a) Probability density function, PDF, and (b) cumulative density function, CDF, of K_1 for one realization. In (a), the continuous line shows a generalized Poisson distribution fit, $\log[\mathrm{PDF}(K_1)/d] = -a(K_1 + b) + c\log[a(K_1 + b)]$, with $a = 0.32 \pm 0.04$ (nJ)$^{-1}$, $b = -0.02 \pm 0.60$ nJ, $c = 1.0 \pm 0.5$ and $d = 0.33 \pm 0.06$ (nJ)$^{-1}$. In (b), the vertical solid line corresponds to $\langle K_1\rangle = 6.1$ nJ; the vertical dashed lines show $\langle K_1\rangle - \sigma_-$ and $\langle K_1\rangle + \sigma_+$, with $\sigma_- = 4.1$ nJ and $\sigma_+ = 4.1$ nJ. For the other realization, $\langle K_1\rangle = 5.7$ nJ, $\sigma_- = 3.8$ nJ and $\sigma_+ = 3.8$ nJ.

presents the cumulative distribution function (CDF) of the data presented in Fig. 6.10.1(a). The adopted criterium is the following: errors σ_- and σ_+ are computed by estimating the values of the measured quantity that insure that 16% of the data is lower than $\langle K_0\rangle - \sigma_-$, and 16% is larger than $\langle K_0\rangle + \sigma_+$. Thus, 68% of the data lies in the range $[\langle K_0\rangle - \sigma_-, \langle K_0\rangle + \sigma_+]$. The same procedure

is realized for each mode m. Fig. 6.10.2(a) shows that K_1 obeys a generalized Poisson distribution, also strongly non-Gaussian. We have not yet a satisfactory explanation of why this fit seems to work very well, so it must be considered as a phenomenological fit. The distribution's asymmetry affects less the measured error bars. For the particular realization shown in this figure, $\sigma_- = 4.1$ nJ and $\sigma_+ = 4.1$ nJ, with $\langle K_1 \rangle = 6.1$ nJ. However, the average is clearly larger than the most probable value $K_1^{\rm mp} = 3.0$ nJ (also known as the maximum likelihood value). For $m \geqslant 2$, all K_m obey the generalized Poisson distribution. Furthermore, between $m = 2$ and $m \approx 30$ they all collapse on a single curve, which is consistent with the observed equipartition. The fluctuations of $|\widetilde{\delta R}_m|^2$ also obey similar non-Gaussian, asymmetric distributions. Their error bars are computed using the same procedure described above. For both $|\widetilde{\delta R}_m|^2$ and K_m the final asymmetric error bars are computed by averaging two independent realizations, thus reducing the total error. Because the asymmetries in the errors for both $|\widetilde{\delta R}_m|^2$ and K_m are small, the reported error bars in the paper correspond to the maximum of σ_- and σ_+, which allow an easier computation of errors when quantities with uncertainty are combined (sum, difference, multiplication or division) or when they are used for computing another quantity by means of a non-linear function.

7. Dynamic analysis and waves

« If your experiment needs statistics, you ought to have done a better experiment. »

Ernst Rutherford

In Chapter 5 we presented a thorough analysis on some of the static properties of the system, in particular we focus on the static structure factor $S(k)$ and the 4-bond orientational order parameter $S_4(k)$. We showed that the system may be described by a conserved field ρ coupled to a non-conserved order parameter ΔQ_4. But what about the dynamic properties? What is the dynamics of both density and order fluctuations? How are the dynamics of both solid and liquid domains once the transition has occured? In this chapter some experimental results on the dynamics of the system are presented. We characterize the time dependence of the fluctuations by means of dynamical correlation functions such as the *current correlation function* $J(\vec{k}, t)$, and the *intermediate coherent scattering function* $F(\vec{k}, t)$.

7.1. Overview

In a recent work by Clerc *et.al* [8], where a quasi-one dimensional system was studied, two main results were obtained. By measuring the effective granular pressure, they showed that macroscopically the solid-liquid granular transition is triggered by a negative compressibility, like in the van der Waals phase coexistence (see Sec. 2.3.1). The second important conclusion of this work is that the transition is mediated by waves, and that crystals in the system interact through them.

By a process of coarse-graining it is possible to obtain density ρ, as well as momentum $\rho\langle v\rangle$, as a function of time. Typical space-time diagrams are shown in Fig. 7.1.1. From space time diagrams they could show that momentum pulses are created from fluctuations, they propagate throughout the system, and then decay due to inelasticity and friction. By means of this coarse-graining procedure they reported that the group speed of waves is $c \approx 5 - 50$ cm/s. The large uncertainty comes from the difficulty to choose where exactly a pulse appears and where it decays.

Therefore, from these results, a natural step to follow would be to try to study these waves in a more quantitave way. Besides, by using the criterium explained in Sec. 4.2 to distinguish between the two phases, we can characterize these waves in each phase separately.

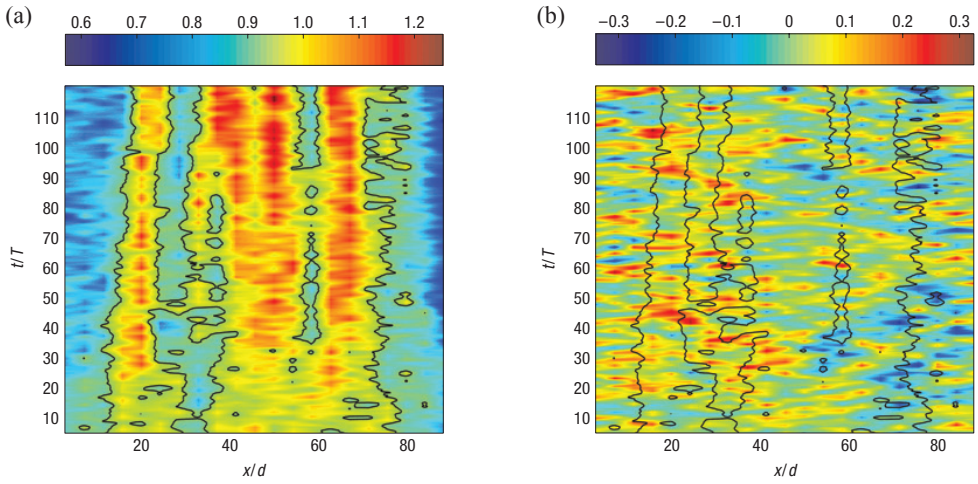

Figure 7.1.1.: Density (a) and momentum (b) space-time diagram respectively for a quasi-2D system ($L_x = 90d$, $L_y \approx 6d$ and $L_z = 1.8d$) vibrated at $f = 70$ Hz. Solid lines in (a) and (b) corresponds to $\rho = 1$ [8].

7.2. Intermediate coherent scattering function $F(\vec{k}, t)$

As a reminder, we define a particle to be in the solid phase whenever its 4-bond orientational order parameter $|Q_4^j|$ is larger than some critical value $|Q_4^c| \approx 0.7$, which depends on the forcing amplitude Γ. The results presented in this chapter come from videos taken at an acquisition rate of $f_{\text{acq}} = 500$ Hz, where each video has 3300 images. Besides, all the dynamical correlation functions presented below are calculated from an ensemble average of 45 videos, all of them acquired at the same acceleration Γ. We study 4 different situations; by using the two configurations C1 and C2 previously defined[1], we sudy the case when the system is in the homogeneous regime ($\Gamma < \Gamma_c$) and when the system presents both liquid and solid phases coexisting ($\Gamma > \Gamma_c$). In particular, we study the cases presented in Tab. 7.1 for the thick ITO glass plates.

	C1	C2
$\Gamma < \Gamma_c$	1.32 ± 0.01	2.60 ± 0.01
$\Gamma > \Gamma_c$	2.19 ± 0.00	5.23 ± 0.01

Table 7.1.: Cases studied. Each one of all the four cases are procesed by means of an ensemble average of 45 videos. In configuration C1, the critical acceleration is $\Gamma_c^{C1} = 1.98$, and was obtained by direct observation of the system, not by means of the method presented in Sec. 5.4. In C2 the critical acceleration is $\Gamma_c^{C2} = 4.48 \pm 0.03$.

Hence, the first quantity that we study is the intermediate scattering function $F(\vec{k}, t)$ which is defined as

$$F\left(\vec{k}, t\right) \equiv \frac{\langle \hat{\rho}\left(k, t\right) \hat{\rho}^*\left(k, 0\right)\rangle - \langle \hat{\rho}\left(k, t\right)\rangle \langle \hat{\rho}^*\left(k, 0\right)\rangle}{N}, \tag{7.2.1}$$

[1]Both configurations are defined such as C1: $N = 9878$, $L_z = 1.81d$ and C2: $N = 11504$, $L_z = 1.94d$.

where the brackets $\langle\,\rangle$ denote an ensemble average, and $\hat{\rho}\,(k,t)$ is the Fourier transform of $\rho\,(r,t)$. A typical behavior of $F\,(k,t)$ for a molecular liquid is shown in Fig. 7.2.1. Hence, we observe that at very low and large wavenumbers the function presents a pure exponential decay, whereas for intermediate kd, it shows some oscilations.

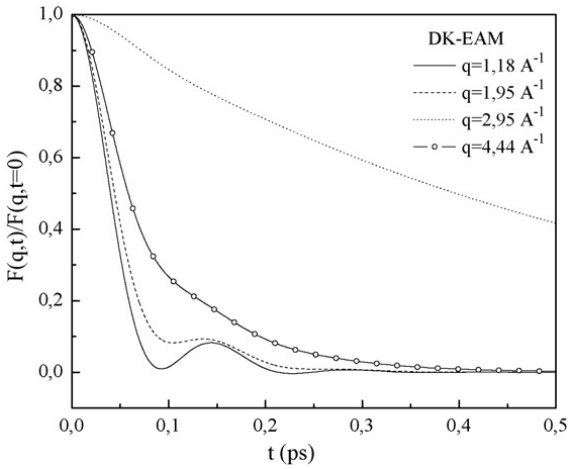

Figure 7.2.1.: Normalized intermediate scattering function $F\,(k,t)$ for liquid Cu at $T = 1453$ K [95]. At low wavenumbers (large wavelengths), oscillations are observed, indicative of propagation of sound waves.

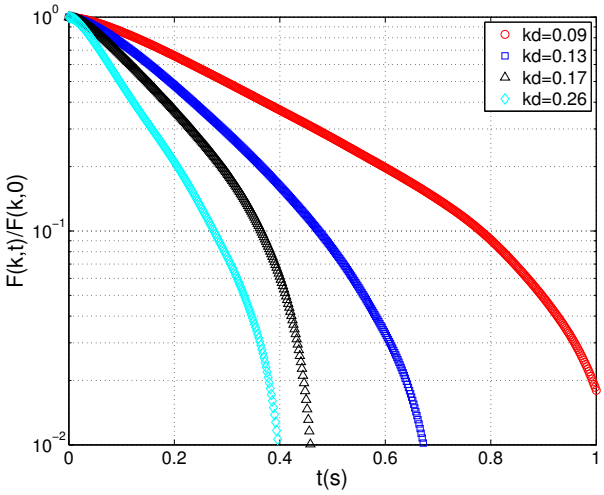

Figure 7.2.2.: $F\,(k,t)$ as a function of time for different low wavenumbers, for the case (C1, $\Gamma < \Gamma_c$). The situation is similar to the other cases. It is clear that $F\,(k,t)$ follows an exponencial decay law, $F\,(k,t) \approx F\,(k,0)\exp\left(-t/\tau_F\right)$, from which we can extract the characteristic time τ. Only data above de noise threshold for this correlation function is shown for each kd.

The behavior of $F\,(k,t)$ in our case is shown in Fig. 7.2.2 for C1 and C2, where there is no phase separation. As can be seen from this figure, we have that at short times, the intermediate scattering

function follows an exponential decay law $F(k,t) \approx F(k,0)\exp(-t/\tau_F)$. By fitting $F(k,t)$ with this exponential decay, we can extract the time τ_F for each wavenumber k. The results obtained for the 4 cases analyzed are presented in Fig. 7.2.3.

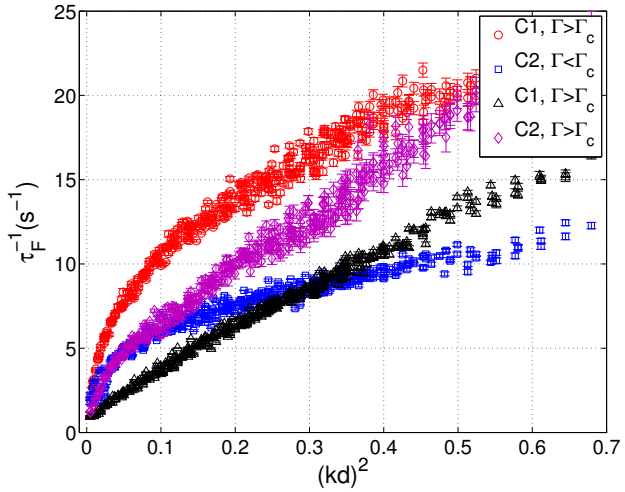

Figure 7.2.3.: Inverse of the decay time τ_F for the 4 cases studied. The fits were done in the region where $F(k,t)/F(k,0) \geq 9 \cdot 10^{-2}$. The errorbars come from errors derived from the fits.

We observe from Fig. 7.2.3 that τ_F^{-1} increases monotonically with k. Besides, for the case (C1, $\Gamma > \Gamma_c$) the time seems to behave like $\tau^{-1} \approx ak^2 + b$, whereas for the other cases such a simple behavior is less clear.

On the other hand, as was pointed out above, we can also distinguish whether a particle is the solid phase, or the liquid phase. By computing the histograms of $|Q_4^j|$ for each case, we detect the minimun that is between the 2 main peaks corresponding to each phase. This is depicted in Fig. 7.2.4. When the system is far below the critical point ($\Gamma < \Gamma_c$), this minimum is not so well defined, in particular for C1 configuration, given that the number of particles in the solid phase is small compared to the total number particles N. Besides, it is easy to notice that these solid particles are "isolated" from each other. Therefore, even though we can define a minimun in the histogram, it is not clear whether we can actually define the correlation functions for each phase separately.

Hence, with the computed $|Q_4|$ critical values, we can obtain the intermediate scattering functions for each phase, $F_{sol}(k,t)$ and $F_{liq}(k,t)$. These are shown in Fig. 7.2.5 along with $F(k,t)$. According to this figure, we observe that $F(k,t)$ follows a pure exponential decay $F(k,t) = F(k,0)\exp(-t/\tau_F)$ (see above), whereas both phases follow separately a "two-step" exponential decay. That is, there are two decay times τ_1 and τ_2, with $\tau_2 \ll \tau_1$, that are related to $F_{sol/liq}(k,t)$ through the relation

$$F_{sol/liq}(k,t) \approx A_1 \exp(-t/\tau_1(k)) + A_2 \exp(-t/\tau_2(k)). \tag{7.2.2}$$

One possible interpretation, is that the short time τ_1 is related to the fact that ρ is not conserved, that is, the particles change of identity or state (solid or liquid). The stay at an specific phase during a characteristic time τ_1, while τ_2 is related to a long time dominated by the hydrodynamics.

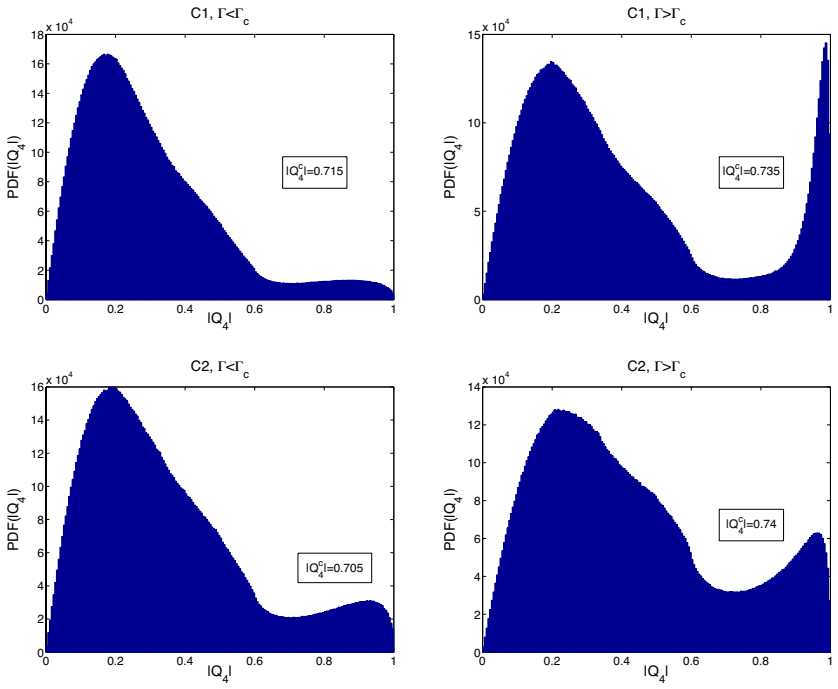

Figure 7.2.4.: Histograms of $|Q_4^j|$ for the 4 cases studied, obtained from statistics of 300 images. The critical values are $|Q_4^c| = 0.715$, $|Q_4^c| = 0.735$, $|Q_4^c| = 0.705$, $|Q_4^c| = 0.740$.

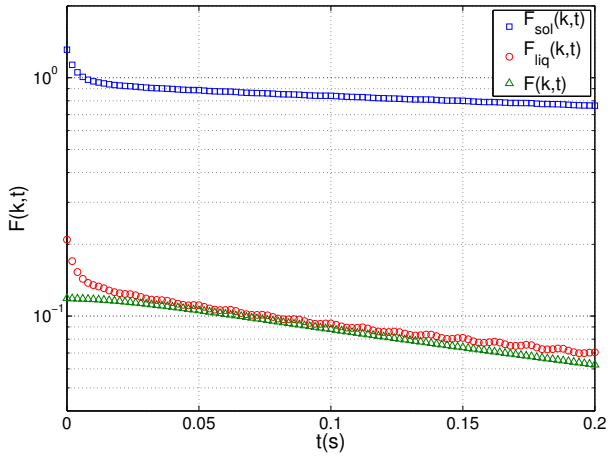

Figure 7.2.5.: Intermediate scattering functions for the case (C1, $\Gamma > \Gamma_c$) computed separetely for the solid phase, the liquid phase and the whole system ($F_{sol}(k,t)$, $F_{liq}(k,t)$ and $F(k,t)$ respectively) for $kd = 0.15$. The other cases show fundamentally the same behavior, that is, $F(k,t)$ decays with a pure exponential law, whereas both phases decay according to $F_{sol/liq}(k,t) \approx A_1 \exp(-t/\tau_1(k)) + A_2 \exp(-t/\tau_2(k))$.

As was stated before, it is not clear if the distinction between both phases when the system has not yet crossed the transition would lead to consistent physical results. On the other hand, there is something that should be noticed. That is, when $F(k,t)$ is computed for one phase only, it presents this "two-time" decay. However, when computed using all the particles, the contribution of all of them seems to cancel out, yielding a pure exponential decay.

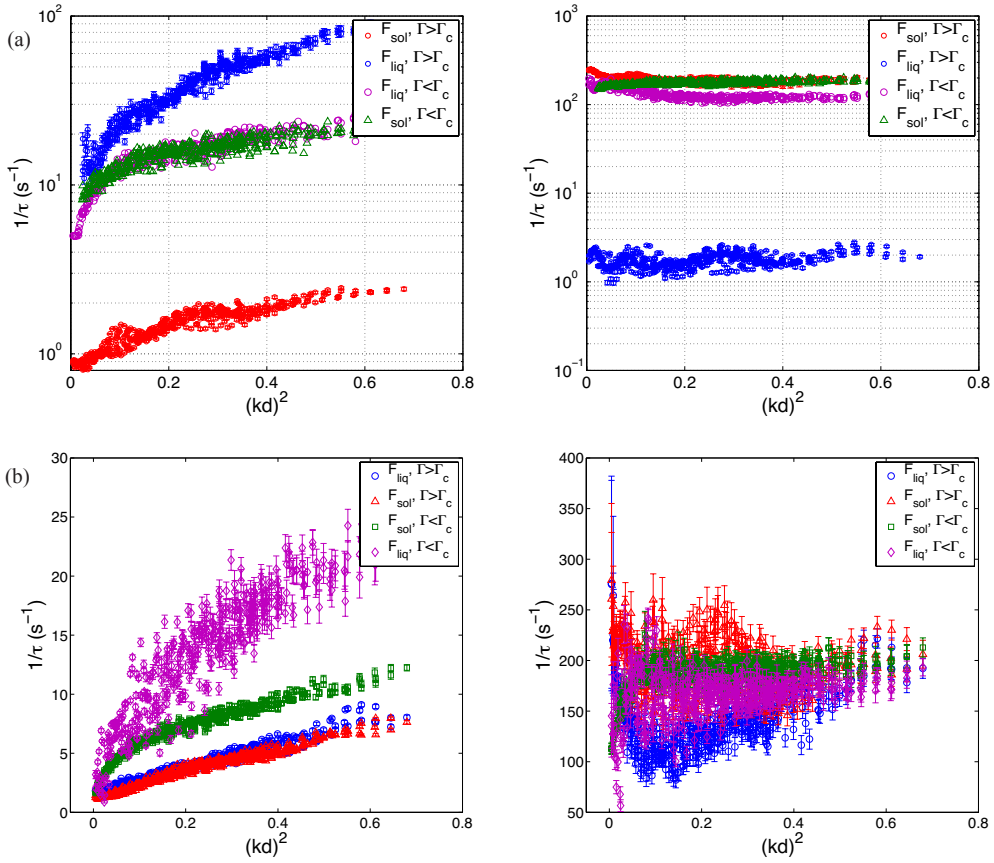

Figure 7.2.6.: (a)-(b) Decaay times τ_1(left) and τ_2(right) obtained from fits of equation 7.2.2 for both phases in configurations C1(top) and C2(bottom), respectively. For configuration C1 we present the data in a semilog scale, given that there is a difference of almost two orders of magnitude between the different times.

The decay times τ_1 and τ_2 obtained from the fits of $F_{sol}(k,t)$ and $F_{liq}(k,t)$ are presented in Fig. 7.2.6. We observe that when the system is above the transition ($\Gamma > \Gamma_c$), the long times τ_1 are vey similar between the two phases in C2, while in C1 there is a factor ≈ 10 between them. Besides, they seem to follow a cuadratic behavior $1/\tau \sim \nu k^2 + \mu$. In the literature it is well known that this kind of behavior is expected for the decay time of some dynamical correlation functions, in which the coefficient μ is associated to the friction, whereas the term $\sim \nu k^2$ comes from the viscosity term in the hydrodynamic equations (see [40] and references therein). In Sec. 7.4.1 we give a brief and simple derivation of this relation for the case of the transverse current correlation function $J_t(k,t)$, given that the transverse current is uncoupled from all the other transport properties. Hence, in this

scheme the results presented imply that in C1, $\mu_s < \mu_l$; whereas in C2 we have the opposite: $\mu_s > \mu_l$. Regarding the short times τ_2, we can see that in all the cases they seem to be constant throughout k, except for very low k, where in some cases the intermediate scatering function is "contaminated" by the forcing frequency of $f = 80$ Hz. This is more noticeable at low modes, making the fits not very reliable at short times in this region.

7.3. Dynamic 4-fold bond-orientational structure factor $F_4(k,t)$

We now turn to the characterization of the relaxation time of the metastable solid clusters. The two-time bond-orientational correlation function is defined by

$$F_4(\vec{k},\tau) = \frac{\langle \delta\widehat{Q}_4(\vec{k},t+\tau)\delta\widehat{Q}_4(\vec{k},t)^*\rangle}{N}, \tag{7.3.1}$$

where * stands for the complex conjugate and $\delta\widehat{Q}_4(\vec{k},t) = \widehat{Q}_4(\vec{k},t) - \langle\widehat{Q}_4(\vec{k},t)\rangle$. Given the property of the 4-fold orientational order paramter, $|Q_4^j| = 1$ for particles in a square symmetry, the main contribution in $F_4(k,t)$ comes from the solid particles. At the frequency we acquired the images (500 Hz), we are not able to see any significant behavior in $F_4(k,t)$ for the liquids particles alone, because it decays too fast to be captured at 500 Hz, and hence with our capabilities we see that it is governed by noise. In Fig. 7.3.1 we show the behavior of $F_4(k,t)$. Within experimental error, both $F_4^{sol}(k,t)$ and $F_4^{all}(k,t)$ follow the same laws, except by some proportionality constant. Therefore, in the analysis of $F_4(k,t)$ we will not make the distinction between both phases, and we just compute it by adding up all the terms in the equation 7.3.1.

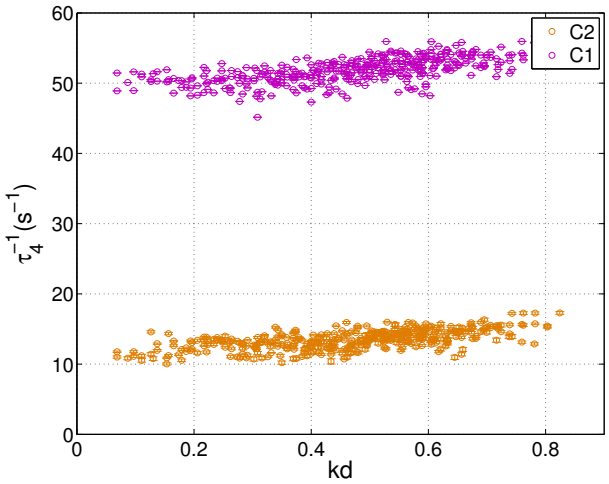

Figure 7.3.2.: Characteristic time τ_4 for configurations C1 and C2 when $\Gamma < \Gamma_c$.

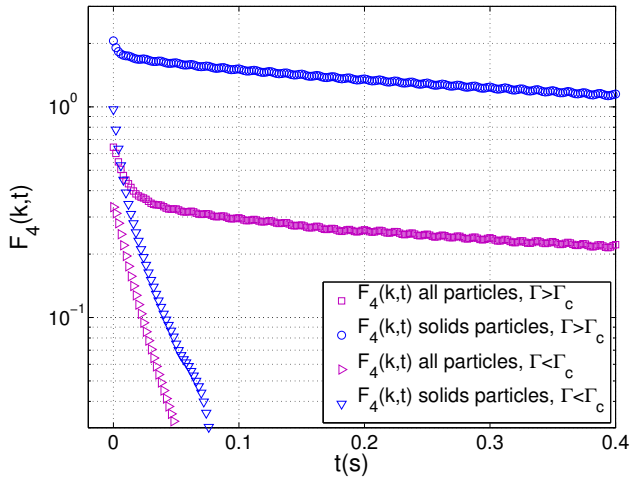

Figure 7.3.1.: Typical $F_4(k,t)$ for all the particles, and only the solid particles for $kd = 0.11$. We present here the results for the configuration C1, but C2 is analogous. We see that if $\Gamma < \Gamma_c$, we have a pure exponential decay, whereas when $\Gamma > \Gamma_c$, $F_4(k,t)$ shows the same feature of a "two-time" exponential decay presented in $F(k,t)$. Unlike the results shown in Sec. 5.5, here we can see a rapid decay time which is not visible in $F_4(k,t)$ for Fig. 5.5.1. This is because now we acquired the images at 500 Hz, and not at 10 Hz as for the data presented in Sec. 5.5 and [53].

From Fig. 7.3.1, when $\Gamma < \Gamma_c$, we fit an exponential decay law and obtain the characteristic time for $F_4(k,t)$. This is shown in Fig. 7.3.2. We observe that τ_4 is roughly a constant for both configurations, besides we obtain $\tau_4^{C1} < \tau_4^{C2}$. Meanwhile, when the system is above the critical point ($\Gamma > \Gamma_c$), for the two-time decay we fit $F_4(k,t)$ as the sum of two exponential functions, $F_4(k,t) \approx A_1 \exp(-t/\tau_1) + A_2 \exp(-t/\tau_2)$. We then can extract both times τ_1 and τ_2, which are shown in Fig. 7.3.3.

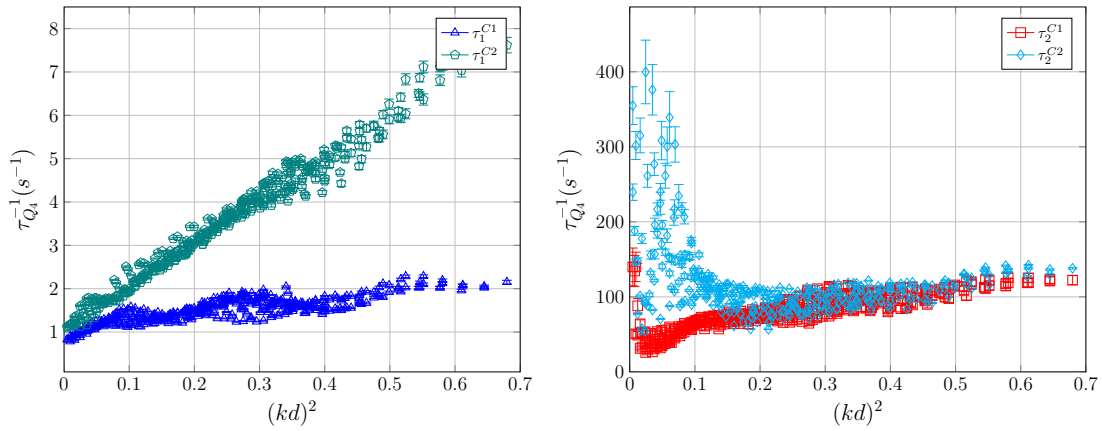

Figure 7.3.3.: Characteristic times τ_1(left) and τ_2(right) extracted from the fit $F_4(k,t) \approx A_1 \exp(-t/\tau_1) + A_2 \exp(-t/\tau_2)$ for C1 and C2.

Again, we have that the short times τ_2, the fits are not very reliable at the very low k, especially for C2. But, with some certainty we obtain that τ_2 is approximately a constant. On the other hand, we have that τ_1^{C1} seems to follow a law like $\tau^{-1} \sim ak^2 + b$, but just for very low k. However, for C2 the situation is markedly diferent, τ_2^{C2} follows in very good aggrement $\tau_2^{C2} \sim \nu k^2 + \mu$ in the whole range of kd studied.

7.4. Current correlation function $J(k,t)$

Finally we focus our attention to the current correlation function. We start by defining the current density

$$\mathbf{j}(\mathbf{r},t) = \sum_{l=1}^{N} \mathbf{v}_l(t)\,\delta(\mathbf{r} - \mathbf{r}_l(t)). \tag{7.4.1}$$

With this, the *current correlation function*, is defined as

$$J_{\alpha\beta}\left(\left|\mathbf{r} - \mathbf{r}'\right|, t\right) = \frac{\langle j_\alpha(\mathbf{r}',0)\, j_\beta(\mathbf{r},t)\rangle}{N}, \tag{7.4.2}$$

where α and β denote cartesian indices. For a system with spherical symmetry (radial in our case), only the pure longitudinal and transverse components J_l and J_t are relevant. By Fourier transforming $J_{\alpha\beta}(r,t)$ we obtain

$$J_{\alpha\beta}(k,t) = \frac{\langle j^*_{\mathbf{k}\alpha}(0)\, j_{\mathbf{k}\beta}(t)\rangle}{N}, \tag{7.4.3}$$

with

$$j_{\mathbf{k}\alpha} = \sum_{l=1}^{N} v_{l\alpha}(t)\, e^{i\mathbf{k}\cdot\mathbf{r}_l(t)}. \tag{7.4.4}$$

From 7.4.3 it is possible to extract the longitudinal and transverse parts of the current correlation by means of

$$J_{\alpha\beta}(k,t) = \frac{k_\alpha k_\beta}{k^2} J_l(k,t) + \left(\delta_{\alpha\beta} - \frac{k_\alpha k_\beta}{k^2}\right) J_t(k,t). \tag{7.4.5}$$

where $\delta_{\alpha\beta}$ is the Kronecker delta function. Hence, the standard definitions for $J_l(k,t)$ and $J_t(k,t)$ are

$$\begin{aligned} J_l(\mathbf{k},t) &= \left\langle \frac{1}{N} \sum_{i,j=1}^{N} \left(\hat{\mathbf{k}}\cdot\mathbf{v}_i\right)(t) \left(\hat{\mathbf{k}}\cdot\mathbf{v}_j\right)(0)\, e^{i\mathbf{k}\cdot(\mathbf{r}_i(t) - \mathbf{r}_j(0))} \right\rangle, \\ J_t(\mathbf{k},t) &= \left\langle \frac{1}{N} \sum_{i,j=1}^{N} \left(\hat{\mathbf{k}}\times\mathbf{v}_i\right)(t) \left(\hat{\mathbf{k}}\times\mathbf{v}_j\right)(0)\, e^{i\mathbf{k}\cdot(\mathbf{r}_i(t) - \mathbf{r}_j(0))} \right\rangle. \end{aligned} \tag{7.4.6}$$

Besides, it is straightforward to show that

$$J_l(\mathbf{k},t) = -\frac{1}{k^2}\partial_t^2 F(\mathbf{k},t), \tag{7.4.7}$$

where $F(k,t)$ is the intermediate scattering function previously defined. This last equation implies that the content of information is the same in both functions, however it will be clear that some spectral properties, such as the collective modes in the system, are more easily obtained in $J_l(k,\omega)$ rather in $F(k,\omega)$[2] [96, 97].

7.4.1. Transverse current correlation function $J_t(k,t)$

A phenomenological relation between current and gradient of the density, which plays the same role as the Fick's rule of difussion, is the Newtonian form of the stress tensor:

$$\tau_{\alpha\beta}(\mathbf{r},t) = \delta_{\alpha\beta}p(\mathbf{r},t) - \frac{\eta}{\rho}\left(\frac{\partial j_\alpha(\mathbf{r},t)}{\partial r_\beta} + \frac{\partial j_\beta(\mathbf{r},t)}{\partial r_\alpha}\right) - \delta_{\alpha\beta}\nabla\cdot\mathbf{j}(\mathbf{r},t)\left(\frac{\eta_B}{\rho} + \frac{2}{3}\frac{\eta}{\rho}\right), \tag{7.4.8}$$

where p is the local pressure, η the shear viscocity, and η_B the bulk viscocity. Combining this with the momentum conservation, one obtains the Navier-Stokes equation of fluid dynamics

$$\frac{\partial}{\partial t}\mathbf{j}(\mathbf{r},t) + \nabla p(\mathbf{r},t) - \frac{\eta}{Mn}\nabla^2\mathbf{j}(\mathbf{r},t) - \frac{1}{Mn}\left(\eta_B + \frac{1}{3}\eta\right)\nabla\nabla\cdot\mathbf{j}(\mathbf{r},t) = 0, \tag{7.4.9}$$

where $\nu = \eta/Mn$ is the kinematic viscocity.

Given that we are only interested in the shear viscocity, it is sufficient to consider only the transverse part of the current. We therefore divide $\mathbf{j}(\mathbf{r},t)$ into longitudinal and transverse parts

$$\mathbf{j}(\mathbf{r},t) = \mathbf{j}_l(\mathbf{r},t) + \mathbf{j}_t(\mathbf{r},t), \tag{7.4.10}$$

where,

$$\begin{aligned} \nabla\cdot\mathbf{j}_t(\mathbf{r},t) &= 0, \\ \nabla\times\mathbf{j}_l(\mathbf{r},t) &= 0. \end{aligned} \tag{7.4.11}$$

Thus, inserting $\mathbf{j}_t(\mathbf{r},t)$ into the Navier-Stokes equations we get

$$\frac{\partial}{\partial t}\mathbf{j}_t(\mathbf{r},t) = \frac{\eta}{Mn}\nabla^2\mathbf{j}_t(\mathbf{r},t). \tag{7.4.12}$$

From this, one finds that the transverse current correlation function is given by

$$J_t(k,t) = v_0^2\exp\left(-\nu k^2 t\right). \tag{7.4.13}$$

[2] $J_l(k,\omega)$ and $F(k,\omega)$ are the temporal Fourier transfom of $J_l(k,t)$ and $F(k,t)$ respectively.

It should be kept in mind that these last equations are valid only at long times and small k. This last equation is the hydrodynamic expression for the transverse current correlation function. Its form indicates that $J_t(k,t)$ dissipate exponentially in time at a rate equal to $\tau_k^{-1} = \nu k^2$, which is also the half-width at half maximum of $J_t(k,\omega)$.

By introducing a dissipative term $-\mu\mathbf{j}$ in 7.4.9, the solution for $J_t(k,t)$ becomes

$$J_t(k,t) = v_0^2 \exp\left(-\left(\nu k^2 + \mu\right) t\right), \tag{7.4.14}$$

and hence, the dissipative time is now

$$\tau(k) = \frac{1}{\nu k^2 + \mu}. \tag{7.4.15}$$

In Fig. 7.4.1 we show the transverse current correlation function for a hard-sphere system. We observe that for the low wavenumber, the function decays exponentially. However, at the high value of kd, $J_t(k,t)$ is negative at an intermediate time, implying that the relation expressed in 7.4.13 for $J_t(k,t)$ is an inadequate description, given that according to it, $J_t(k,t)$ should always be positive. Therefore, viscoelastic effects should be taken into account, and hence we conclude that the kinematic viscosity ν must depend on the wavelength and the frequency [98, 99]. In other word, in order to have transverse current waves we need to add an inertial term (second derivative) to the equation 7.4.12.

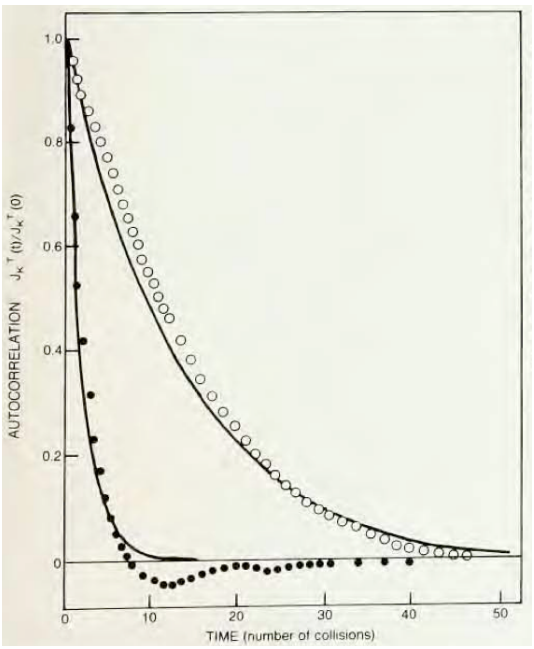

Figure 7.4.1.: Transverse current correlation function for a hard-sphere fluid at a density corresponding to $V/V_0 = 1.6$ and for wavenumbers $kd = 0.76$ (open symbols), and $kd = 2.28$ (closed circles) using molecular dynamics. The solid lines represent the hydrodynamic calculations [98].

We will focus in the meantime on the case where the system is far from the critical point ($\Gamma < \Gamma_c$)

for both configurations C1 and C2. In this regime, we surprinsingly have the same kind of behavior of viscoelasticity, as it is evident in Fig. 7.4.2.

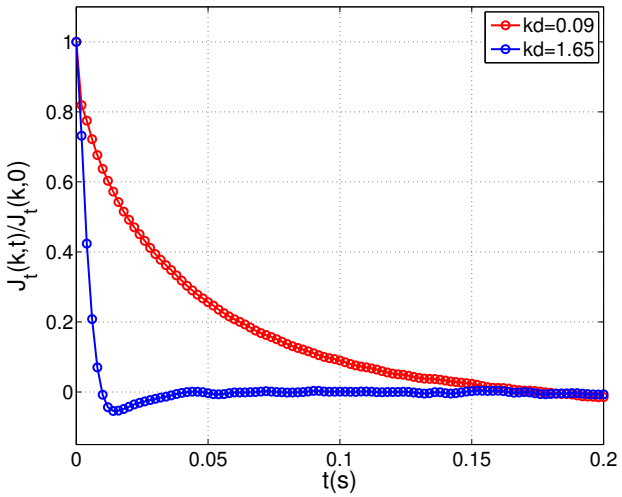

Figure 7.4.2.: Transverse current correlation function $J_t(k,t)$ for our system in the case (C1, $\Gamma < \Gamma_c$). In the case (C2, $\Gamma < \Gamma_c$), the situation is the same.

It is clear from Fig. 7.4.2 that at the low wavenumber $kd = 0.09$, $J_t(k,t)$ shows a pure exponential decay, whereas at $kd = 1.65$ it clearly crosses through zero and then has some damped oscilations. These oscilations at high wavenumbers become manifest in the Fourier transform of $J_t(k,t)$ shown in Fig. 7.4.3.

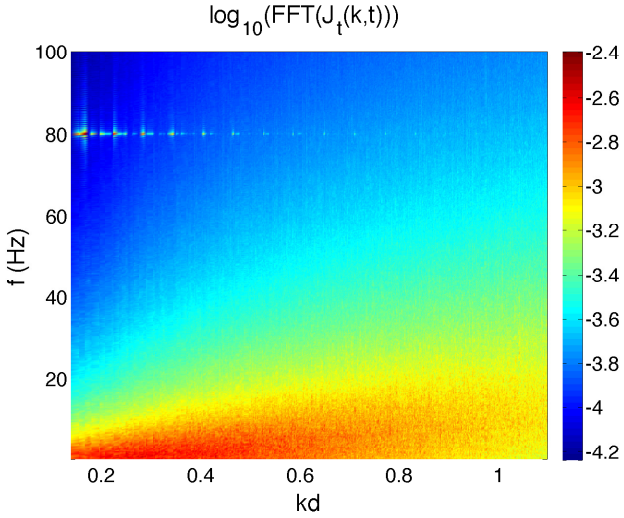

Figure 7.4.3.: Fourier transform of the transverse current correlation function $J_t(k,t)$ in the case (C1, $\Gamma < \Gamma_c$). The case (C2, $\Gamma < \Gamma_c$) presents the same basic features.

In Fig. 7.4.3 we observe clearly the forcing frequency of $f = 80$ Hz, specially at low k. Besides, we can also notice that for wavenumbers approximately $kd \lesssim 0.7$ the Fourier transform of $J_t(k,t)$ takes very high values, but there is not a well defined peak, but instead a maximum value at $f = 0$. However, for larger wavenumbers ($kd \gtrsim 0.7$), the Fourier transform does present a peak that has moved away from zero, showing the same phenomenon of viscoelasticy presented before.

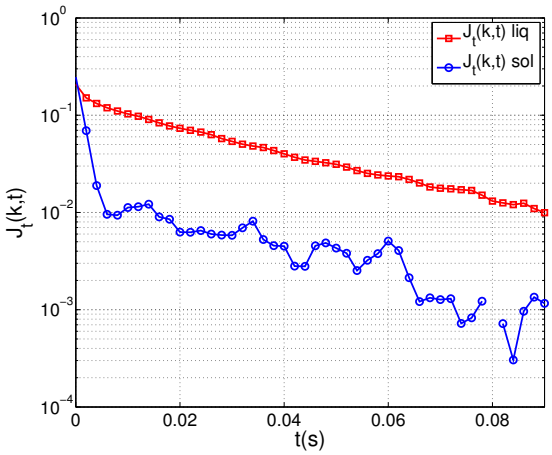

Figure 7.4.4.: Transverse current correlation function $J_t(k,t)$ showing the "two-time" decay for the solid phase, while the liquid phase shows a pure exponential decay.

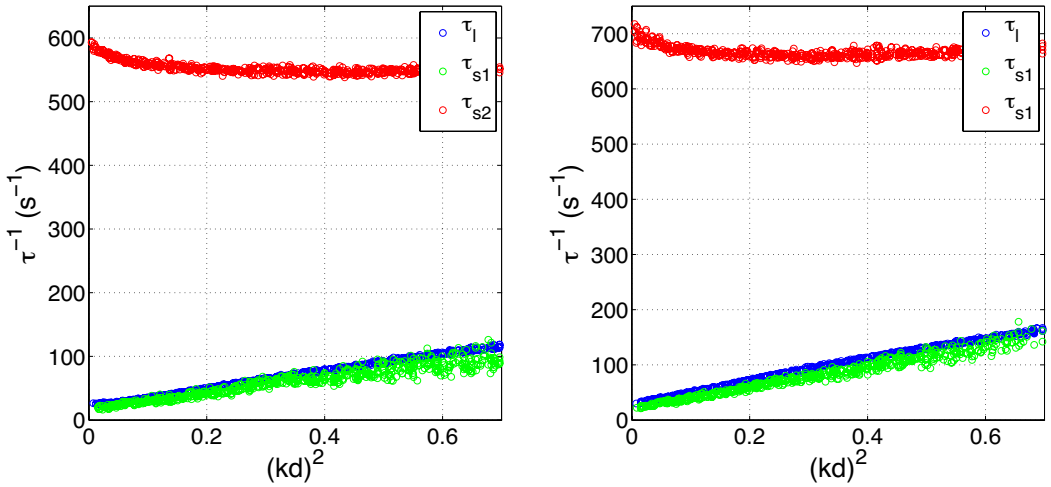

Figure 7.4.5.: Decay time of the transverse current correlation function $J_t(k,t)$ for the two configurations (left: C1, right: C2). For the solid particles showing the "two-time" exponential decay, and the liquid phase which shows a pure exponential decay.

By computing $J_t(k,t)$ for each solid and liquid phases separately we obtain Fig. 7.4.4. Again, we observe this same "two-time" decay feature for $J_t(k,t)$ for the solids particles, whereas for the liquids

particles we have a pure exponential decay. By fitting $J_t^{sol}(k,t) = A_1 \exp(-t/\tau_{s1}) + A_2 \exp(-t/\tau_{s2})$ and $J_t^{liq}(k,t) = B_1 \exp(-t/\tau_l)$, for both the liquids and solids particles respectively we obtain the results presented in Fig. 7.4.5.

From this figure, while τ_l and τ_{s1} show in excellent agreement a behavior according to $\tau \sim \nu k^2 + \mu$, the short time τ_{s2} for the solid phase is nearly a constant. Thus, a possible interpretation is that while the solid particles are trapped by the their neighbors, its characteristic time τ_2 is dominated by the friction μ. However in the hydrodynamic regime, it is dominated by an effective viscosity.

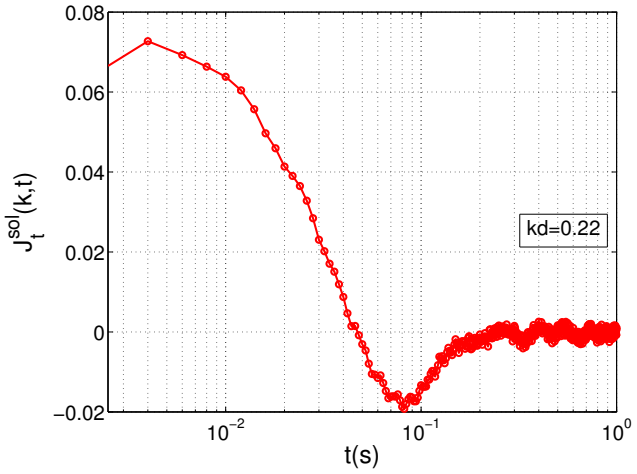

Figure 7.4.6.: Transversal current correlation function for the solids particles $J_t^{sol}(k,t)$ when $\Gamma > \Gamma_c$ at $kd = 0.22$.

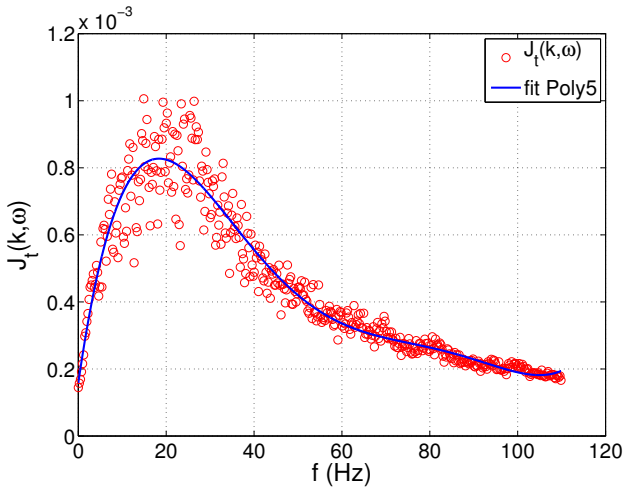

Figure 7.4.7.: Example of $J_t(k,\omega)$ for $kd = 0.43$. The continuous blue line is obtained by fitting a degree 5-polynomial in order to obtain ω_{max}.

In contrast to what we have just shown, when the system has already crossed the transition ($\Gamma > \Gamma_c$), *i.e.* the system is no longer homogeneous but it presents the two phases coexisting, the transverse

current correlation function $J_t(k,t)$ does actually presents oscilations in the solid phase. This is shown in Fig. 7.4.6. Hence, we from Fig. 7.4.6 by computing the fourier transform to $J_t(k,t)$ we obtain $J_t(k,\omega)$. An example of $J_t(k,\omega)$ for $kd = 0.43$ is shown in Fig. 7.4.7.

Therefore, by extracting the frequency where $J_t(k,\omega)$ is maximum, we obtain the speed of the sound waves along with its dispersion relation. These relations are shown in Fig. 7.4.8. We can conclude that approximately the dispersion relation for the waves in the solid seems to obey a linear law $\omega \sim k$. Besides, the speeds found ($c \sim 8 - 20$ cm/s depending on k) are in very good agreement with the results found by Clerc *et.al* in [8].

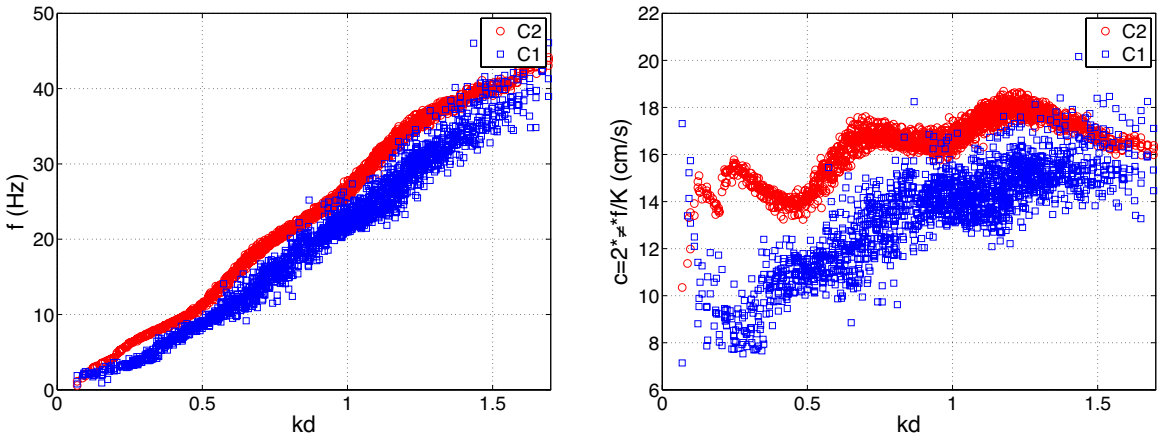

Figure 7.4.8.: Dispersion relation and sound speed for the transverse waves in the solid when $\Gamma > \Gamma_c$ in both configurations.

7.4.2. Longitudinal current correlation function $J_l(k,t)$

Lets take a look now at the longitudinal current correlation function $J_l(k,t)$. It is well known in the literature that it presents damped oscilations in a wide range of wavenumbers [40, 97]. In Fig. 7.4.9 we show $J_l(k,t)$ obtained from molecular dynamics simulations for a granular system of $N = 2 \cdot 10^5$ spherical particles with periodic boundary conditions.

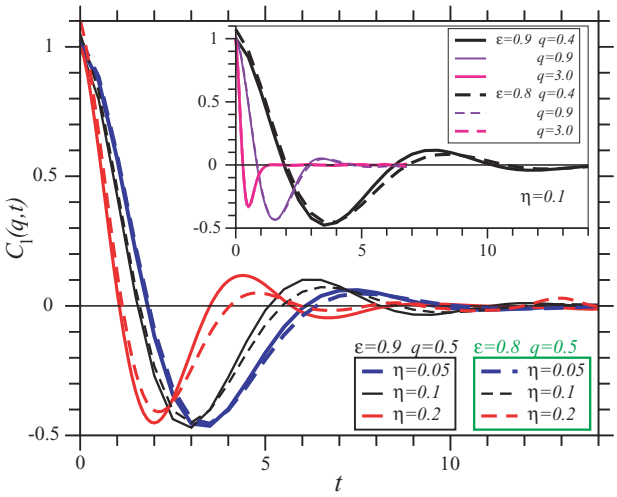

Figure 7.4.9.: Longitudinal current correlation function for a hard-sphere granular fluid. Several packing fractions η, and different normal restitution coefficients ε are studied [96].

In our system, we observe that $J_l(k,t)$ basically does not show significant differences between the two configurations C1 and C2. Hence, in Fig. 7.4.10 we show the behavior of $J_l(k,t)$ for C1 only.

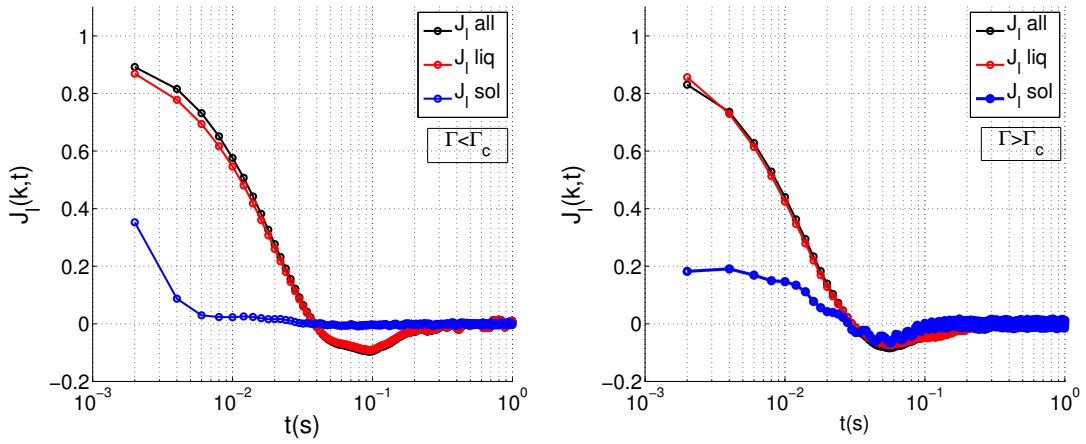

Figure 7.4.10.: $J_l(k,t)$ in our system for C1 computed for all the particles, and each phase separately at $kd = 0.26$. Left: $\Gamma < \Gamma_c$. right: $\Gamma > \Gamma_c$.

We observe from Fig. 7.4.10 that both $J_l^{all}(k,t)$ and $J_l^{liq}(k,t)$ do not change much between the two regimes. However $J_l^{sol}(k,t)$ shows a rapid decay for $\Gamma < \Gamma_c$, whereas for $\Gamma > \Gamma_c$ it shows damped oscilations. Therefore, just as we did before, we can obtain the Fourier transform of $J_l(k,t)$. The Fourier transform of $J_l^{liq}(k,t)$ is shown in Fig. 7.4.11.

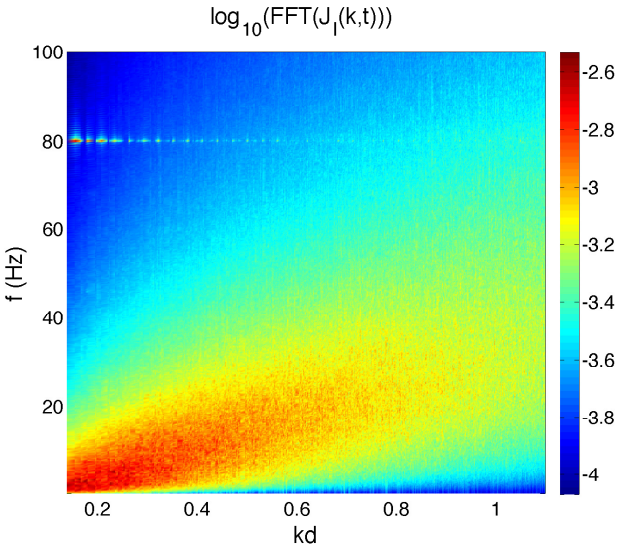

Figure 7.4.11.: Fourier transform of the longitudinal current correlation function $J_l^{liq}J(k,t)$ for (C1,$\Gamma > \Gamma_c$). The other cases show basically the same.

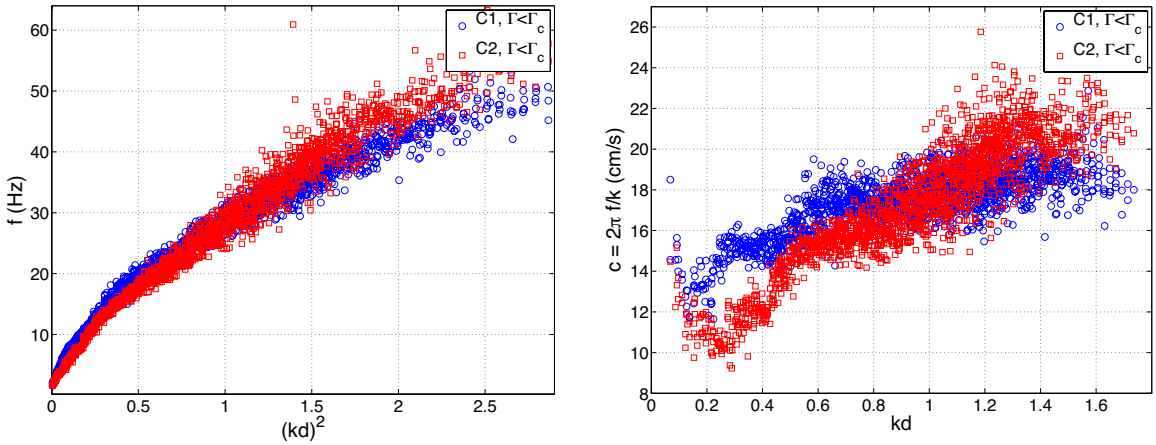

Figure 7.4.12.: Left: Dispersion relation of the sound waves for both configurations C1 and C2 when $\Gamma < \Gamma_c$. Right: Longitudinal sound speed of the waves in the liquid.

Again, we can observe from Fig. 7.4.11 the forcing frequency ($f = 80$ Hz), along with a low frequency peak which is related to the sound waves in the system [40, 96, 97, 100]. Hence, a rough estimate of the sound speed may be obtained from the maximum of $J_l(k,\omega)$.

Therefore, by extracting the frequency where $J_l(k,\omega)$ is maximum, we obtain the speed of the longitudinal sound waves along with its dispersion relation. They are both shown in Fig. 7.4.12.

From Fig. 7.4.12 we can say that in both configurations, at low wavenumbers $(kd)^2 < 0.5$, the frequency seems to obey a law $\omega \sim \nu k^2 + \mu$. In consideration of the sound speed c_l, it seems to have some different regimes. The velocity decreases with kd up to $kd \approx 0.3$, and an opposite slope is observed above, with a change about $kd \approx 0.5$, where it becomes more difficult to say something due to the large dispersion of the data. Nevertheless, these observations are intimately related to a relaxation scenario. Finally, when the system has already approached the transition ($\Gamma > \Gamma_c$), we have the two phases well differentiated and we can compute the sound waves for each phase separately. This is shown in Fig. 7.4.13.

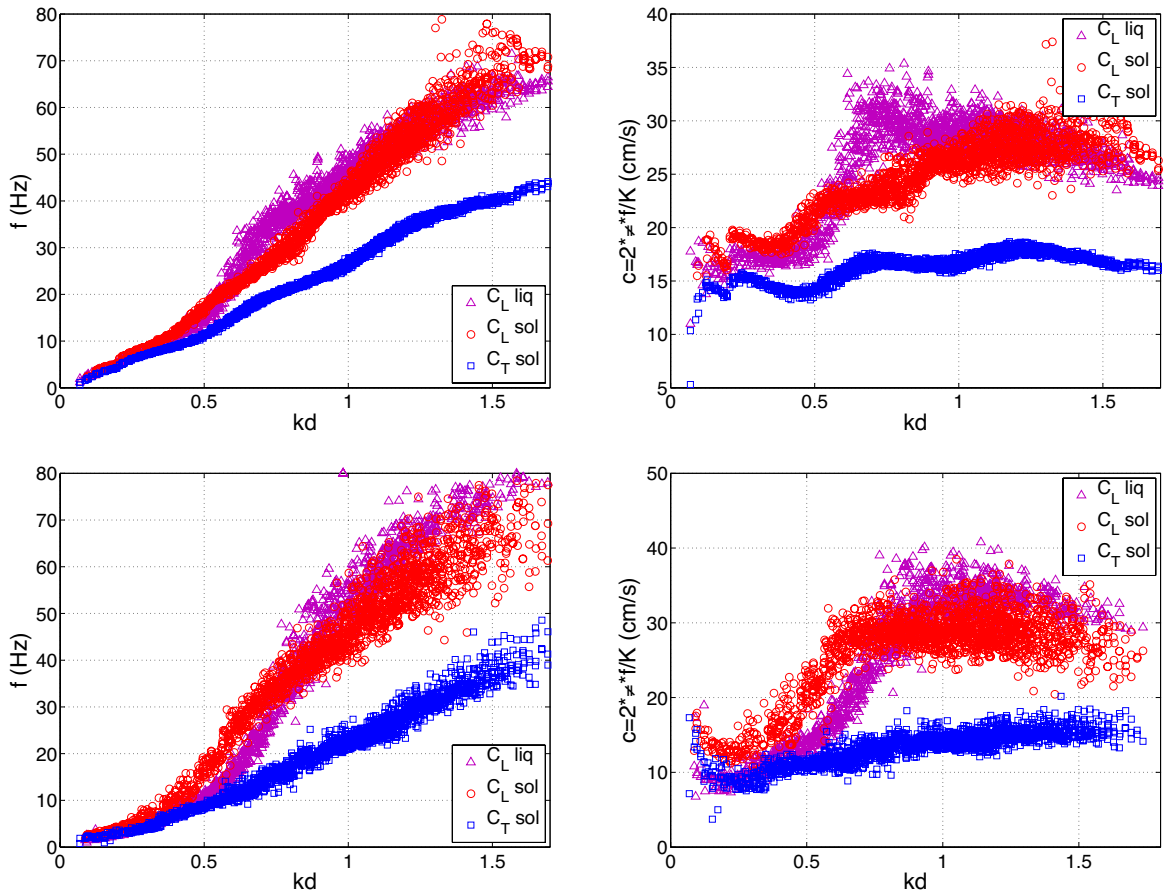

Figure 7.4.13.: Dispersion relation and phase speed of the waves in both solid and liquid phases. Top: configuration C1. Bottom: configuration C2. We added the case of the transverse waves in the solid for its comparison.

Hence, from this figure we may conclude that the longitudinal waves seem to follow a law $\omega_l \sim \nu k^2 + \mu$ in both phases, whereas the trasverse waves obey $\omega \sim k$. Nevertheless, to conclude about these dispersion relations still require more analysis given that the data are still very noisy and at low kd

is difficult to distinguish between linear and quadratic behaviors. However, we have that at low kd,

$$\begin{aligned} c_l^{sol} &> c_l^{liq} \\ c_l^{sol} &> c_t^{sol} \\ c_l^{liq} &\gtrsim c_t^{sol}, \end{aligned} \tag{7.4.16}$$

which is also satisfied in molecular systems [13]. From the dispersion relations we can obtain the group speed of the waves for both configurations, which are shown in Fig. 7.4.14. Given that the data for the dispersion relations are noisy, we computed the group speeds by smoothing the curves shown in Fig. 7.4.13. This was done by averaging $f(k)$ in 100 windows $k \in [nk_{min}, (n+1)k_{min}]$ for integer $n \geq 1$, where $k_{min} = \pi/L$. From Fig. 7.4.14 we observe that in C1, the group velocity is almost constant $c_g \sim 5 - 10$ cm/s, except at very low kd where it increases by a factor ~ 5. In C2 the situation is somewhat different given that c_g does not vary much as a function of kd. However, the data are much more noisy and hence, there is not a clear tendency.

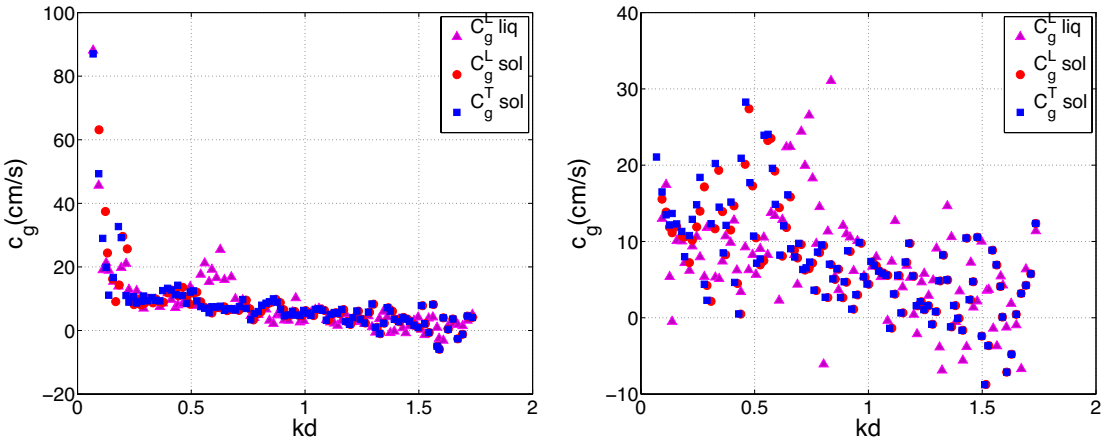

Figure 7.4.14.: Group speed of the waves in both solid and liquid phases. Left: Configuration C1. Right: Configuration C2.

Accordingly, in this chapter we presented several results dealing with the dynamics of some correlations functions. We extract the characteristic times associated for each phase separately. Besides, we can also obtain dispersion relations as well as the phase and group speed of the waves that propagate in the system in both phases, though a more detailed interpretation of these results will be matter of future work.

Conclusions and future perspectives

« Research is what I'm doing when I don't know what I'm doing. »

Wernhern von Braun

In this thesis we have studied the density, order and capillary fluctuations in the vicinity of the solid-liquid-like transition that occurs in a quasi-two-dimensional vibrated granular monolayer. By means of the experimental setups presented in Chapter 3, and the widely used tools of statistical mechanics and hydrodynamics we investigated the role of the fluctuations and the static and dynamics properties of the system.

In the first part of this thesis we have demonstrated that the non-equilibrium solid-liquid transition that occurs in a shallow, quasi-two-dimensional granular system can be of either first- or second-order type depending on the vertical height and filling density. This seems counterintuitive, because it is widely believed that a solid-liquid phase transition can only be of first-order. However, motivated by observations inside carbon nanotubes recent molecular dynamic simulations show that in confined water nanofilms the transition to a solid phase can be either of first or second order, depending on the filling density [50].

In our experiments, for both cases, density fluctuations do not show strong variations at the transition. In fact, we showed that the static structure factor $S(k)$ actually presents a peak at low wavenumbers, called the *first sharp diffraction peak* (FSDP) in the amorphous materials community, which is related to the existence of medium range crystalline order [76]. In our case, the characteristic length ξ of the these structures in the system do not show critical behavior.

On the contrary, local order varies strongly, either abruptly in the first-order type transition, or continuously in the second-order type configuration. This is characterized through the bond-orientational order parameter Q_4, which in Fourier space shows an Ornstein-Zernike-like behavior. When the transition is a second-order type, the associated correlation length ξ_4, the relaxation time τ_4, the zero k limit of Q_4 fluctuations (static susceptibility), the pair correlation function of Q_4, and the amplitude of the order parameter obey critical power laws, with saturations due to finite size effects. Their respective critical exponents are $\nu_\perp = 1$, $\nu_\parallel = 2$, $\gamma = 1$, $\eta = 0.67$ and $\beta = 1/2$, whereas the dynamical critical exponent $z = \nu_\parallel/\nu_\perp = 2$. The five static exponents were measured independently of each other. Hence, the continuous transition presents critical-like behavior, with

dynamic exponent z consistent with model C of dynamical critical phenomena, valid for a non-conserved critical order parameter (bond-orientation order) coupled to a conserved field (density). Aditionally, by changing both bottom and top lids of the cell, we show that these static exponents, as well as the dynamic exponent z, are indeed universal, because within experimental error they do not vary as we change the microscopic properties of the system (dissipation).

In the second part of our results we present an experimental study of the coarse-grained solid-liquid interface fluctuations, which are characterized through the static and dynamic correlation functions in Fourier space. We have demonstrated that these fluctuations turn out to be well described by the capillary wave theory, which allows us to measure the solid-liquid interface surface tension γ, and mobility M once the granular "thermal" kinetic energy is determined. Both quantities are consistent with a simple order of magnitude estimation considering the characteristic energy, length, and time scales, which is very similar to what can be done for atomic systems. The scaling of the effective surface tension with the granular temperature T_g^b suggests that the particles' kinetic energy plays the role of the cohesive energy that originates the capillary-like phenomenon in molecular liquids. It would be interesting to relate the kinetic energy to a collisional pressure in each phase. For this purpose, the unexpected result of energy equipartition of the surface Fourier modes should be included in any theoretical approach. By doing so, we could handle the surface tension concept by thinking in terms of pressure difference, as defined by the hydrodynamic law of Laplace. This would allow to couple a particle's scale study (e.g., by accounting for collisions, cross section, and contact duration) to a macroscopic description and would raise the question of particle pressure in granular media, well known for homogeneous gas fluidized beds [101], but still open for dense granular flows. We also show that in configuration C1 the system presents two well defined regimes; a small wavenumber regime ($m = 3 - 6$) with a surface tension γ_1, and a large wavenumber regime ($m = 20 - 55$) with a surface tension γ_2, where $\gamma_1 > \gamma_2$. On the other hand, by analyzing directly the images, we showed that in C1 the surface tension is almost constant as a function of Γ, whereas in C2 it increases as we increase Γ.

In the third and final part of this thesis we show that the dynamical correlation functions *density-density* and *order-order*, present exponential decays. We have demonstrated that the inverse of the characteristic times either follow a quadratic law or are roughly constant, depending on the temporal scale we observe. On the other hand, the current correlation function, in its transverse and longitudinal parts, shows a rather richer behavior. We showed by means of its Fourier transform that it actually presents oscilations, confirming in a more quantitave way some results previously found [8]. By handling the current correlation function for each phase separately, we obtained dispersion relations as well as phase and group wave speeds for each phase and for each component of the current. We obtained that the longitudinal waves in both phases seem to obey $\omega \sim ak^2 + b$, while the transverse waves in the solid the dispersion relation is linear $\omega \sim ak$. An interesting result that we found is that at high wavenumbers, the transverse part of the current does present waves in the liquid phase, thus indicating a viscoelastic behavior as it is found in some molecular fluids [98].

In order to further extend our work, one way would be to study other correlation functions. That is, so far we have explored *density-density*, *order-order* and *current-current* correlations functions, but it would be interesting to study correlations such as of *density-order* or even to study higher order correlations such as the susceptiblities functions that are widely used in other systems to study dynamical heterogeneities [102, 103, 104, 105].

Another possibility is to study the phase of the imaginary 4-bond orientational order parameter Q_4^j, and not just its absolute value. This quantity because would provide information about the relative orientation between the crystals, something that could be crucial when $\Gamma > \Gamma_c$ and the system has not yet reached its stationary state, while the crystals are still moving and interacting until they coalesce into one big cluster.

For the future, an interesting thing to do would be to study what happens for other heights of the cell, *i.e.* to explore a more extended region in the phase space. Under some other conditions of frequency, filling density and height, is already known that the system presents structures different than the squared studied by us. Hence, the order parameter would not be ΔQ_4 as in our case, but probably the global parameter ΔQ_6. For heights of the cell larger than $2d$, some new experimental methods would have to be used, given that with the actual setup it would not be possible to observe particles in the bottom layers.

Bibliography

[1] Igor S Aranson and Lev S Tsimring. Patterns and collective behavior in granular media: Theoretical concepts. *Reviews of Modern Physics*, 78:641, April 2006.

[2] HM Jaeger, SR Nagel, and RP Behringer. Granular solids, liquids, and gases. *Reviews of Modern Physics*, 68(4):1259–1273, 1996.

[3] Leo P. Kadanoff. Built upon sand: Theoretical ideas inspired by granular flows. *Rev.Mod.Phys.*, 71:435–444, 1999.

[4] S. Lübeck. Universal Scaling Behavior of Non-Equilibrium Phase Transitions. *International Journal of Modern Physics B*, 18:3977–4118, 2004.

[5] Kazumasa A. Takeuchi, Masafumi Kuroda, Hugues Chaté, and Masaki Sano. Directed percolation criticality in turbulent liquid crystals. *Phys. Rev. Lett.*, 99:234503, Dec 2007.

[6] Alexis Prevost, Paul Melby, David A Egolf, and Jeffrey S Urbach. Nonequilibrium two-phase coexistence in a confined granular layer. *Phys. Rev E*, 70:050301, Nov 2004.

[7] PM Reis, RA Ingale, and MD Shattuck. Crystallization of a quasi-two-dimensional granular fluid. *Physical Review Letters*, 96(25):258001, 2006.

[8] M G Clerc, P Cordero, J Dunstan, K Huff, N Mujica, D Risso, and G Varas. Liquid-solid-like transition in quasi-one-dimensional driven granular media. *Nature Physics*, 4:249, March 2008.

[9] P Melby, F Vega Reyes, A Prevost, R Robertson, P Kumar, D A Egolf, and J S Urbach. The dynamics of thin vibrated granular layers. *Journal of Physics: Condensed Matter*, 17:2689, June 2005.

[10] J S Olafsen and J S Urbach. Two-Dimensional Melting Far from Equilibrium in a Granular Monolayer. *Physical Review Letters*, 95:98002, August 2005.

[11] Kurt Binder, Surajit Sengupta, and Peter Nielaba. The liquid-solid transition of hard discs: first-order transition or Kosterlitz-Thouless-Halperin-Nelson-Young scenario? *Journal of Physics: Condensed Matter*, 14(9):2323, 2002.

[12] Katherine J. Strandburg. Two-dimensional melting. *Reviews of Modern Physics*, 60(1):161–207, January 1988.

[13] Landau, L. D. and Lifshitz, E. M. *Theory of Elasticity*. Pergamon Press, Oxford, 2nd edition, 1970.

[14] H. Hertz. Über die berührung fester elastischer körper. *J. reine angewandte Matematik*, 92:156–171, 1882.

[15] Brillantov, N. V. and Pöschel, T. *Kinetic Theory of Granular Gases*. Oxford University Press, New York, 2004.

[16] Phil Attard and John L. Parker. Deformation and adhesion of elastic bodies in contact. *Physical Review A*, 46(1):7959–7971, December 1992.

[17] Landau, L. D. and Lifshitz, E. M. *Electrodynamics of Continuous Media*. Pergamon Press, Oxford, 1960.

[18] S McNamara and WR Young. Dynamics of a freely evolving, two-dimensional granular medium. *Physical Review E*, 53(5):5089–5100, 1996.

[19] Thomas Schwager and Thorsten Pöschel. Coefficient of normal restitution of viscous particles and cooling rate of granular gases. *Physical Review E*, 57(1):650–654, January 1998.

[20] HM Jaeger, CH LIU, SR Nagel, and TA Witten. Friction in Granular Flows. *Europhysics Letters*, 11(7):619–624, 1990.

[21] Francois Chevoir, Jean-Noël Roux, Frédéric da Cruz, Pierre G Rognon, and Georg Koval Jr. Friction law in dense granular flows. *Powder Technology*, 190(1-2):264–268, March 2009.

[22] Dowson D. *History of tribology*. Professional Engineering Publishing, New York, 1997.

[23] Halsey T. and Mehta A. *Challenges in Granular Physics*. World Scientific, London, 2002.

[24] Gurtin M. *Configurational forces as basics concepts of continuum physics*. Springer, New York, 2000.

[25] S Luding. Granular materials under vibration: Simulations of rotating spheres. *Physical Review E*, 52(4):4442, 1995.

[26] S McNamara and S Luding. Energy nonequipartition in systems of inelastic, rough spheres. *Physical Review E*, 58(2):2247–2250, 1998.

[27] J S Olafsen and J S Urbach. Velocity distributions and density fluctuations in a granular gas. *Physical Review E*, 60:2468, September 1999.

[28] W Losert, DGW Cooper, J Delour, A Kudrolli, and J P Gollub. Velocity statistics in excited granular media. *Chaos*, 9(3):682–690, 1999.

[29] A Puglisi, V Loreto, U Marini Bettolo Marconi, A Petri, and A Vulpiani. Clustering and Non-Gaussian Behavior in Granular Matter. *Physical Review Letters*, 81:3848, November 1998.

[30] Chapman S. and Cowling T. G. *The Mathematical Theory of Non-Uniform Gases*. Cambridge University Press, Cambridge, third edition, 1970.

[31] G Gradenigo, A Sarracino, D Villamaina, and A Puglisi. Non-equilibrium length in granular fluids: From experiment to fluctuating hydrodynamics. *Europhysics Letters*, 96(1):14004, October 2011.

[32] Alexis Prevost, David Egolf, and Jeffrey Urbach. Forcing and Velocity Correlations in a Vibrated Granular Monolayer. *Physical Review Letters*, 89(8):084301, August 2002.

[33] R Soto and M Mareschal. Statistical mechanics of fluidized granular media: Short-range velocity correlations. *Physical Review E*, 63(4), March 2001.

[34] R Soto, J Piasecki, and M Mareschal. Precollisional velocity correlations in a hard-disk fluid with dissipative collisions. *Physical Review E*, 64(3):031306, August 2001.

[35] TPC van Noije, M H Ernst, and R Brito. Ring kinetic theory for an idealized granular gas. *Physica A: Statistical Mechanics and its Applications*, 251:266–283, 1998.

[36] TPC van Noije, M H Ernst, and R Brito. Spatial correlations in compressible granular flows. *Physical Review E*, 57(5):R4891–R4894, 1998.

[37] TPC vanNoije, M H Ernst, R Brito, and JAG Orza. Mesoscopic theory of granular fluids. *Physical Review Letters*, 79(3):411–414, 1997.

[38] David K Yoon and James T Jenkins. Kinetic theory for identical, frictional, nearly elastic disks. *Physics of Fluids*, 17(8):083301, 2005.

[39] H Grad. On the kinetic theory of rarefied gases. *Communications on Pure and Applied Mathematics*, 2(4):331–407, 1949.

[40] Hansen J. P. and McDonald I.R. *Theory of Simple Liquids*. Academic Press, San Diego, second edition, 1990.

[41] James W. Dufty. Statistical mechanics, kinetic theory, and hydrodynamics for rapid granular flow. *Journal of Physics: Condensed Matter*, 12(8):47–56, February 2000.

[42] I Goldhirsch. Introduction to granular temperature. *Powder Technology*, 182(2):130–136, 2008.

[43] N Sela and I Goldhirsch. Hydrodynamic equations for rapid flows of smooth inelastic spheres, to Burnett order. *Journal of Fluid Mechanics*, 361:41–74, April 1998.

[44] Norman F Carnahan. Equation of State for Nonattracting Rigid Spheres. *The Journal of Chemical Physics*, 51(2):635, 1969.

[45] S Luding, M Lätzel, W Volk, S Diebels, and H J Herrmann. From discrete element simulations to a continuum model. *Computer Methods in Applied Mechanics and Engineering*, 191:21–28, November 2001.

[46] HM Jaeger and SR Nagel. Physics of the granular state. *Science*, 255(5051):1523, 1992.

[47] Aranson I. S and Tsimring L. S. *Granular Patterns*. Oxford University Press, New York, 2009.

[48] Isaac Goldhirsch. Rapid Granular Flows. *Annual Review of Fluid Mechanics*, 35(1):267–293, January 2003.

[49] Hohenberg, P.C. and B.I. Halperin. Theory of dynamic critical phenomena. *Reviews of Modern Physics*, 49(3):435–479, July 1977.

[50] S Han, M Choi, P Kumar, and H Stanley. Phase transitions in confined water nanofilms. *Nature Physics*, 2010.

[51] E. Stanley. *Introduction to Phase Transition Dynamics and Critical Phenomena*. Oxford University Press, New York, 1971.

[52] HE Stanley. Scaling, universality, and renormalization: Three pillars of modern critical phenomena. *Reviews of Modern Physics*, 71(2):S358–S366, 1999.

[53] Gustavo Castillo, Nicolás Mujica, and Rodrigo Soto. Fluctuations and Criticality of a Granular Solid-Liquid-Like Phase Transition. *Physical Review Letters*, 109(9), August 2012.

[54] J. Sethna. *Entropy, Order Parameters, and Complexity*. Oxford University Press, New York, 2010.

[55] Cardy J. *Scaling and renormalization in statistical physics*. Cambridge University Press, Cambridge, 1996.

[56] Akira Onuki. *Phase Transition Dynamics*. Cambridge University Press, Cambridge, 2002.

[57] A Einstein. Theorie der opaleszens von homogenen fluessigkeiten und fluessigkeitsgemischen in der naehe des kritischen zustandes. *Annalen der Physik*, 33, 1910.

[58] Th Voigtmann. Fragility measures and mode-coupling theory. *Journal of Non-Crystalline Solids*, 352(42-49):4826–4829, November 2006.

[59] B.I. Halperin, Hohenberg, P.C., and Shang-keng Ma. Renormalization-group methods for critical dynamics: 1. Recursion relations and effects of energy conservation. *Physical Review B*, B10:139–153, 1974.

[60] Géza Ódor. Universality classes in nonequilibrium lattice systems. *Rev. Mod. Phys.*, 76:663–724, Aug 2004.

[61] R. Folk and G. Moser. Critical dynamics of model c resolved. *Phys. Rev. Lett.*, 91:030601, Jul 2003.

[62] R Folk and G Moser. Critical dynamics of stochastic models with energy conservation (model C). *Physical Review E*, 69(3):36101, March 2004.

[63] B. I. Halperin, P. C. Hohenberg, and Shang-keng Ma. Renormalization-group methods for critical dynamics: Ii. detailed analysis of the relaxational models. *Phys. Rev. B*, 13:4119–4131, May 1976.

[64] E. Brézin and C. de Dominicis. Field-theoretic techniques and critical dynamics. II. Ginzburg-Landau stochastic models with energy conservation. *Physical Review B*, 12(1):4954–4962, December 1975.

[65] M Shattuck. *http://gibbs.engr.ccny.cuny.edu/technical.php.*

[66] J Silva and M Cerda. *http://www.dfi.uchile.cl/nmujica/PTrack2/.*

[67] J Silva. *Optimización de proceso de detección de partículas a partir de imágenes de video mediante paralelización*. Computer Science Engineer thesis, Universidad de Chile, 2012.

[68] J S Olafsen and J S Urbach. Clustering, Order, and Collapse in a Driven Granular Monolayer. *Physical Review Letters*, 81:4369, November 1998.

[69] M Argentina, M G Clerc, and R Soto. van der Waals-Like Transition in Fluidized Granular Matter. *Physical Review Letters*, 89:44301, July 2002.

[70] Rui Liu, Yinchang Li, Meiying Hou, and Baruch Meerson. van der waals–like phase-separation instability of a driven granular gas in three dimensions. *Phys. Rev. E*, 75:061304, Jun 2007.

[71] J. Javier Brey, M. J. Ruiz-Montero, F. Moreno, and R. García-Rojo. Transversal inhomogeneities in dilute vibrofluidized granular fluids. *Phys. Rev. E*, 65:061302, Jun 2002.

[72] M. V. Sapozhnikov, Y. V. Tolmachev, I. S. Aranson, and W.-K. Kwok. Dynamic self-assembly and patterns in electrostatically driven granular media. *Phys. Rev. Lett.*, 90:114301, Mar 2003.

[73] C Cartes, M G Clerc, and R Soto. van der Waals normal form for a one-dimensional hydrodynamic model. *Physical Review E*, 70:31302, September 2004.

[74] P M Reis, R A Ingale, and M D Shattuck. Caging Dynamics in a Granular Fluid. *Physical Review Letters*, 98:188301, May 2007.

[75] Keiji Watanabe and Hajime Tanaka. Direct Observation of Medium-Range Crystalline Order in Granular Liquids Near the Glass Transition. *Physical Review Letters*, 100:158002, April 2008.

[76] S R Elliott. Medium-range structural order in covalent amorphous solids. *Nature*, 354:445, December 1991.

[77] H Tanaka. Two-order-parameter model of the liquid glass transition. II. Structural relaxation and dynamic heterogeneity. *Journal of Non-Crystalline Solids*, 351:3385, November 2005.

[78] Vamsi K. Akkineni and Uwe C. Täuber. Nonequilibrium critical dynamics of the relaxational models c and d. *Phys. Rev. E*, 69:036113, Mar 2004.

[79] Jacques Duran. Rayleigh-taylor instabilities in thin films of tapped powder. *Phys. Rev. Lett.*, 87:254301, Nov 2001.

[80] Yacine Amarouchene, Jean-François Boudet, and Hamid Kellay. Capillarylike fluctuations at the interface of falling granular jets. *Phys. Rev. Lett.*, 100:218001, May 2008.

[81] John R Royer, Daniel J Evans, Loreto Oyarte, Qiti Guo, Eliot Kapit, Matthias E Möbius, Scott R Waitukaitis, and Heinrich M Jaeger. High-speed tracking of rupture and clustering in freely falling granular streams. *Nature*, pages 1–4, June 2009.

[82] Xiang Cheng, German Varas, Daniel Citron, Heinrich Jaeger, and Sidney Nagel. Collective Behavior in a Granular Jet: Emergence of a Liquid with Zero Surface Tension. *Physical Review Letters*, 99(18):188001, November 2007.

[83] Xiang Cheng, Lei Xu, Aaron Patterson, Heinrich Jaeger, and Sidney Nagel. Towards the zero-surface-tension limit in granular fingering instability. *Nat. Phys.*, 4:234–237, Mar 2008.

[84] Stephan Ulrich and Annette Zippelius. Stability of freely falling granular streams. *Phys. Rev. Lett.*, 109:166001, Oct 2012.

[85] James P. D. Clewett, Klaus Roeller, R. M. Bowley, Stephan Herminghaus, and Michael R. Swift. Emergent surface tension in vibrated, noncohesive granular media. *Phys. Rev. Lett.*, 109:228002, Nov 2012.

[86] J M Howe. *Interfaces in Materials*. Wiley, New York, 1997.

[87] Denis Mangin, Francois Puel, and Stephane Veesler. Polymorphism in Processes of Crystallization in Solution: A Practical Review. *Organic Process Research & Development*, 13(6):1241–1253, November 2009.

[88] J Hoyt. Atomistic and continuum modeling of dendritic solidification. *Materials Science and Engineering: R: Reports*, 41(6):121–163, September 2003.

[89] Sidney Yip. Nanocrystals: The strongest size. *Nature*, 391(6):532–533, February 1998.

[90] Z T Trautt, M Upmanyu, and A Karma. Interface Mobility from Interface Random Walk. *Science*, 314(5799):632–635, October 2006.

[91] J J Hoyt, Z T Trautt, and M Upmanyu. Fluctuations in molecular dynamics simulations. *Mathematics and Computers in Simulation*, 80(7):1382–1392, March 2010.

[92] Thomas O. E. Skinner, Dirk G. A. L. Aarts, and Roel P. A. Dullens. Grain-boundary fluctuations in two-dimensional colloidal crystals. *Phys. Rev. Lett.*, 105:168301, Oct 2010.

[93] L. A. Fernández, V. Martín-Mayor, B. Seoane, and P. Verrocchio. Equilibrium fluid-solid coexistence of hard spheres. *Phys. Rev. Lett.*, 108:165701, Apr 2012.

[94] S.R. Palit. Thermodynamic interpretation of the eötvös constant. *Nature*, 177:1180, 6 1956.

[95] S Dalgõç. The EAM based effective pair potentials for the dynamic properties of liquid Cu. *Materials Chemistry and Physics*, 103(1):183–189, May 2007.

[96] Katharina Vollmayr-Lee, Timo Aspelmeier, and Annette Zippelius. Hydrodynamic correlation functions of a driven granular fluid in steady state. *Physical Review E*, 83(1):011301, 2011.

[97] Boon, J. P. and Yip, S. *Molecular Hydrodynamics*. Dover Publications Inc., New York, 1980.

[98] W Edward Alley and Berni J Alder. Generalized transport coefficients for hard spheres. *Physical Review A*, 27(6):3158–3173, June 1983.

[99] R Vogelsang and C Hoheisel. Computation and analysis of the transverse current autocorrelation function, Ct(k,t), for small wave vectors: A molecular-dynamics study for a Lennard-Jones fluid. *Physical Review A*, 35(4):1786–1794, February 1987.

[100] G Gradenigo, A Sarracino, D Villamaina, and A Puglisi. Fluctuating hydrodynamics and correlation lengths in a driven granular fluid. *Journal of Statistical Mechanics: Theory and Experiment*, 2011(08):P08017, August 2011.

[101] G. K. Batchelor. A new theory of the instability of a uniform fluidized bed. *Journal of Fluid Mechanics*, 193:75–110, 7 1988.

[102] N Lačević, F W Starr, T B Schrøder, and S C Glotzer. Spatially heterogeneous dynamics investigated via a time-dependent four-point density correlation function. *Journal of Chemical Physics*, 119:7372, October 2003.

[103] Ludovic Berthier. Dynamic heterogeneity in amorphous materials. *Physics*, 4:42, May 2011.

[104] L O Hedges, R L Jack, J P Garrahan, and D Chandler. Dynamic Order-Disorder in Atomistic Models of Structural Glass Formers. *Science*, 323(5919):1309–1313, March 2009.

[105] Walter Kob, Claudio Donati, Steven J Plimpton, Peter H Poole, and Sharon C Glotzer. Dynamical Heterogeneities in a Supercooled Lennard-Jones Liquid. *Physical Review Letters*, 79:2827, October 1997.

[106] Hinrichsen H. and Wolf D., editors. *The Physics of Granular Media*. Wiley-VCH, Berlin, 2004.

Appendices

A. Hertzian contact force

By defining the strain tensor

$$u_{ij}\left(\vec{r}\right) \equiv \frac{1}{2}\left(\frac{\partial u_i}{\partial x_j} + \frac{\partial u_j}{\partial x_i}\right), \tag{A.0.1}$$

where $u_i\left(\vec{r}\right)$ is the displacement field at the point $\vec{r}$, the simplest relationship between strain and stress is[1]

$$\sigma^{ij}\left(\vec{r}\right) = E_1\left(u_{ij}\left(\vec{r}\right) - \frac{1}{2}\delta_{ij}u_{ll}\left(\vec{r}\right)\right) + E_2\delta_{ij}u_{ll}\left(\vec{r}\right) \tag{A.0.2}$$

which is just the well know Hooke's law. Where $\sigma^{ij}\left(\vec{r}\right)$ describes the i-component of the force acting on a unit surface which is normal to the direction j. The constants E_1 and E_2 are related to Y and ν by

$$E_1 = \frac{Y}{1+\nu} \qquad\qquad E_2 = \frac{Y}{3\left(1-2\nu\right)} \tag{A.0.3}$$

Now, if we call $P\left(x,y\right)$ the pressure acting on the surface of the semi-space $z > 0$, the displacement field in the bulk is (see [106] and references therein)

$$u_i = \iint G_{ik}\left(x-x', y-y', z\right) P_k\left(x', y'\right)\, \mathrm{d}x'\mathrm{d}y', \tag{A.0.4}$$

where G_{ik} is the corresponding Green function. For the problem that we want to solve now we only need the z-component of the displacement on the surface $z = 0$. Thus, the only component needed is [13]

$$G_{zz}\left(x,y,z=0\right) = \frac{1-\nu^2}{\pi Y}\frac{1}{\sqrt{x^2+y^2}} = \frac{\left(1-\nu^2\right)}{\pi Y}\frac{1}{r}. \tag{A.0.5}$$

[1] Einstein convention is used. Repeated indices are implicitly summed over.

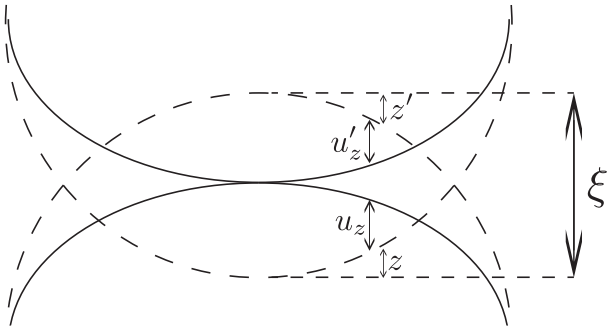

Figure A.0.1.: Two colliding bodies in the Hertz scheme. Dashed lines represent the original shape of the bodies, whereas continuous lines correspond to the actual shape of the particles when they are in contact.

As we can see from Fig. A.0.1 that the equation

$$(u_z + z) + \left(u'_z + z'\right) = \xi, \tag{A.0.6}$$

holds in the region of contact. If we choose the axis to be the principal axis of the system, equation A.0.6 becomes

$$A_1 x^2 + A_2 y^2 + u_{z1}(x, y) + u_{z2}(x, y) = \xi, \tag{A.0.7}$$

where the constants A_1 and A_2 are related to the radii of curvature of the surfaces in contact [13]

$$\begin{aligned} 2(A_1 + A_2) &= \frac{1}{R_1} + \frac{1}{R_2} + \frac{1}{R'_1} + \frac{1}{R'_2} \\ 4(A_1 - B_2)^2 &= \left(\frac{1}{R_1} - \frac{1}{R_2}\right)^2 + \left(\frac{1}{R'_1} - \frac{1}{R'_2}\right)^2 + 2\cos 2\varphi \left(\frac{1}{R_1} - \frac{1}{R_2}\right)\left(\frac{1}{R'_1} - \frac{1}{R'_2}\right) \end{aligned} \tag{A.0.8}$$

Here R_1, R_2 and R'_1, R'_2 are respectively the principal radii of curvature of both bodies in contact and φ is the angle between the planes corresponding to the curvature radii R_1 and R'_1.

From A.0.4 and A.0.5, A.0.7 becomes

$$\frac{1}{\pi}\left(\frac{1-\nu_1^2}{Y_1} + \frac{1-\nu_2^2}{Y_2}\right) \iint \frac{P_z(x', y')}{r} \mathrm{d}x' \mathrm{d}y' = \xi - A_1 x^2 - A_2 y^2, \tag{A.0.9}$$

where $r = \sqrt{(x-x')^2 + (y-y')^2}$. This is an integral equation for the unknown variable $P_z(x,y)$. We can notice now that the left-hand side of this equation is commonly found in potential theory. Actually, by using the identity

$$\iint \frac{\mathrm{d}x'\mathrm{d}y'}{r}\sqrt{1-\frac{x'^2}{a^2}-\frac{y'^2}{b^2}} = \frac{\pi ab}{2}\int_0^\infty \left[1-\frac{x^2}{a^2+t}-\frac{y^2}{b^2+t}\right]\frac{\mathrm{d}t}{\sqrt{(a^2+t)(b^2+t)\,t}} \tag{A.0.10}$$

whose domain of integration is the elliptical area $x'^2/a^2 + y'^2/b^2 = 1$, which just comes from calculating the potential from a uniformly charged ellipsoid [13]. By looking at equations A.0.9 and A.0.10 we can see that both equations contain integrals of the same type, while the right-hand sides contain quadratic forms of the same type also. Therefore, we can conclude that the contact area is an ellipse with semi-axis a and b and that the pressure is of the form $P_z(x,y) = const\sqrt{1-x^2/a^2-y^2/b^2}$. But we also know that the total force acting between the bodies is $F_{el} = \iint P_z(x',y')\,\mathrm{d}x'\mathrm{d}y'$, thus the constant may be found from this, resulting

$$P_z(x,y) = \frac{3F_{el}}{2\pi ab}\sqrt{1-\frac{x^2}{a^2}-\frac{y^2}{b^2}}. \tag{A.0.11}$$

By inserting equation A.0.11 into equation A.0.9 we obtain

$$\frac{F_{el}D}{\pi}\int_0^\infty \left(1-\frac{x^2}{a^2+\xi}-\frac{y^2}{b^2+\xi}\right)\frac{\mathrm{d}\xi}{\sqrt{(a^2+\xi)(b^2+\xi)\,\xi}} = \xi - A_1x^2 - A_2y^2 \tag{A.0.12}$$

Where the constant D is defined as $D \equiv \frac{3}{4}\left(\frac{1-\nu_1^2}{Y_1}+\frac{1-\nu_2^2}{Y_2}\right)$. For the equality in A.0.12 to be true, the coefficients of each term of the polynomial must be equal on both sides of the equation. Hence,

$$\xi = \frac{F_{el}D}{\pi}\int_0^\infty \frac{\mathrm{d}\xi}{\sqrt{(a^2+\xi)(b^2+\xi)\,\xi}} \tag{A.0.13}$$

$$A_1 = \frac{F_{el}D}{\pi}\int_0^\infty \frac{\mathrm{d}\xi}{(a^2+\xi)\sqrt{(a^2+\xi)(b^2+\xi)\,\xi}} \tag{A.0.14}$$

$$A_2 = \frac{F_{el}D}{\pi}\int_0^\infty \frac{\mathrm{d}\xi}{(b^2+\xi)\sqrt{(a^2+\xi)(b^2+\xi)\,\xi}} \tag{A.0.15}$$

And from these, it is possible to determine the semi-axis a and b of the contact surface.

So far we have solved completely the problem of two bodies of convex surfaces when put into contact. The previous analysis made us possible to determine the shape of the surface of contact and to obtain the semi-axis a and b, the displacement u_z and u'_z within each body, as well as obtain the pressure

$P_z(x, y)$ on the surface of contact. Now, we focus on the particular case of two spheres of the same material of radii R_1 and R_2. In this case, $A_1 = A_2 = 1/2R_1 + 1/2R_2$. And from symmetry it is clear that $a = b$. From equation A.0.15 it is possible to obtain a, which reads

$$a = F^{1/3} \left(\frac{DR_1R_2}{R_1 + R_2} \right)^{1/3}. \tag{A.0.16}$$

Inserting this into A.0.13 we obtain

$$F_{el} = \rho \xi^{3/2}, \tag{A.0.17}$$

where $\rho \equiv \frac{2Y}{3(1-\nu^2)}\sqrt{R^{eff}}$ and $R^{eff} \equiv \frac{R_1R_2}{R_1+R_2}$. Using similarity arguments it is also possible to conclude that for two bodies of any shape[2], the relation $F_{el}\,\alpha\,\xi^{3/2}$ still holds, but now with a different constant of proportionality. This contact problem was solved for the first time by Heinrich Hertz in 1882 [14].[3]

[2] Always under the assumption of arbitrary shaped convex bodies.
[3] A similar analysis can be made for the 2D case yielding $F_{el}\,\alpha\,\xi$.

B. Publications

1. Gustavo Castillo, Nicolás Mujica, and Rodrigo Soto. **Fluctuations and criticality of a granular solid-liquid-like phase transition**. *Physical Review Letters*, 109(9), 2012.

   We present an experimental study of density and order fluctuations in the vicinity of the solid-liquid-like transition that occurs in a vibrated quasi-two-dimensional granular system. The two-dimensional projected static and dynamic correlation functions are studied. We show that density fluctuations, characterized through the structure factor, increase in size and intensity as the transition is approached, but they do not change significantly at the transition itself. The dense, metastable clusters, which present square symmetry, also increase their local order in the vicinity of the transition. This is characterized through the bond-orientational order parameter Q_4, which in Fourier space obeys an Ornstein-Zernike behavior. Depending on filling density and vertical height, the transition can be of first or second order type. In the latter case, the associated correlation length ξ_4, relaxation time τ_4, zero k limit of Q_4 fluctuations (static susceptibility), the pair correlation function of Q_4, and the amplitude of the order parameter obey critical power laws, with saturations due to finite size effects. Their respective critical exponents are $\nu_\perp = 1$, $\nu_{||} = 2$, $\gamma = 1$, $\eta = 0.67$, and $\beta = 1/2$, whereas the dynamical critical exponent $z = \nu_{||}/\nu_\perp = 2$. These results are consistent with model C of dynamical critical phenomena, valid for a non-conserved critical order parameter (bond-orientation order) coupled to a conserved field (density).

2. Li-Hua Luu, Gustavo Casillo, Nicolás Mujica and Rodrigo Soto. **Capillarylike fluctuations of a solid-liquid interface in a noncohesive granular system**. *Physical Review E*, 87 040202(R), 2013.

   One of the most noticeable collective motion of non-cohesive granular matter is clustering under certain conditions. In particular, when a quasi-two-dimensional monolayer of monodisperse non-cohesive particles is vertically vibrated, a solid-liquid-like transition occurs when the driving amplitude exceeds a critical value. Here, the physical mechanism underlying particle clustering relies on the strong interactions mediated by grain collisions, rather than on grain-grain cohesive forces. In average, the solid cluster resembles a drop, with a striking circular shape. We experimentally investigate the coarse-grained solid-liquid interface fluctuations, which are characterized through the static and dynamic correlation functions in the Fourier space. These fluctuations turn out to be well described by the capillary wave theory, which allows us to measure the solid-liquid interface surface tension and mobility once the granular "thermal" kinetic energy is determined. Despite the system is strongly out of equilibrium and that the granular temperature is not uniform, there is energy equipartition at the solid-liquid

interface, for a relatively large range of angular wave-numbers. Furthermore, both surface tension and mobility are consistent with a simple order of magnitude estimation considering the characteristic energy, length and time scales, which is very similar to what can be done for atomic systems.